Synthesis and characterisation of metal-organic framework materials with carboxylate ligands

by

Alexis Siân Munn

Supervisor, Richard I. Walton

Thesis submitted for the degree of

Doctor of Philosophy in Chemistry

University of Warwick, Department of Chemistry

July 2013

Contents

Acknowledgements

The first acknowledgement has to go to my supervisor Richard Walton, who has helped and guided me through the entire process. His support has defined these four years as years that will be looked back at fondly, for that, I would like to thank him wholeheartedly. He has also provided many opportunities to learn different techniques and given me the opportunity to travel and collaborate internationally, giving this work an extra level of enjoyment.

I would like to thank the whole of the Walton research group, past and present, for all of their help. With special mentions to Peter Dunne and Luke Daniels who have collected many TG data over the years, and lastly to Helen Playford who has gone above and beyond the role of colleague. For all her help, collecting and analysing neutron data, fixing broken equipment and for generally being a good friend, I would like to say thank you.

A special thank you goes to Guy Clarkson who has been invaluable to the completion of Chapter 5. I am extremely grateful for the crystal structures he has solved for me.

I would also like to thank Matt Tucker from ISIS for all his help with the GEM instrument and the interpretation of the data. To all the other beam scientists from DIAMOND and ISIS, who have helped with data collection and analysis, I would like to express my gratitude. A special mention also goes to Racha El Osta who was a very welcome distraction from the long boring hours spent collecting data at the HASYLAB on the dark snowy nights in the middle of November.

I am grateful to the European 7th framework community project, MACADEMIA, for funding this research and to all of the MACADEMIA research partners. We have

collaborated with many groups from various countries who have collected and analysed data which has supported the work in this thesis, to all of them I owe my appreciation.

To everyone who proof read this work, particularly my family who have little interest in chemistry, I am very grateful for your help.

And lastly, I would like to thank my fiancé, Adam. His support and patience has been tireless and I cannot imagine what these last few months would have been like without him.

Declaration

This thesis is submitted to the University of Warwick in support of my application for the degree of Doctor of Philosophy. It has been composed by myself and has not been submitted in any previous application for any degree.

The work presented (including data generated and data analysis) was carried out by the author except in the cases outlined below:

Various contributions have been made to this work by other researchers and MACADEMIA partners. These have been indicated clearly within the text.

Parts of this thesis have been published by the author:

R. I. Walton, A. S. Munn, N. Guillou and F. Millange, "Uptake of Liquid Alcohols by the Flexible Fe(III) Metal-Organic Framework MIL-53 Observed by Time-Resolved in situ X-ray Diffraction" Chem. Eur. J., 2011, ***17****, 7069-7079*

B. Van de Voorde, A. S. Munn, N. Guillou, F. Millange, D. E. De Vos and R. I. Walton, "Adsorption of N/S heterocycles in the flexible metal-organic framework MIL-53(Fe^{III}*) studied by in situ energy dispersive X-ray diffraction" PCCP, 2013,* ***15****, 8606-8615*

A. S. Munn, A. J. Ramirez-Cuesta, F. Millange and R. I. Walton, "Interaction of Methanol with the Flexible Metal-Organic Framework MIL-53(Fe) Observed by Inelastic Neutron Scattering" Chem. Phys., 2013, ***In Press****.*

A. S. Munn, G. J. Clarkson, F. Millange, Y. Dumont and R. I. Walton, "M(II) (M = Mn, Co, Ni) Variants of the MIL-53-Type Structure with Pyridine-N-Oxide as a Co-Ligand" CrystEngComm, 2013, DOI: 10.1039/C3CE41268G

A. S. Munn, G. J. Clarkson, R. I. Walton, "Distortions of a Flexible Metal-Organic Framework From Substituted Pendant Ligands" Acta Cryst. B, 2013, ***In Press***

Abstract

The adsorption of various guest molecules by the flexible 1,4-benzenedicarboxylate metal-organic framework (MOF), MIL-53, has been followed using *in situ* diffraction techniques. This crystalline MOF displays a structural expansion upon the adsorption of guest molecules, evident by a change in unit cell parameters, which allows adsorption to be followed using diffraction techniques.

Adsorption studies were performed with the Fe(III) form of MIL-53 using both liquid- and gas-phase guest molecules. The results from *in situ* X-ray diffraction (XRD) studies show that small aliphatic-alcohols give rise to a two-step expansion whereas branched-alcohols and larger aromatic molecules result in only a one-step expansion. The solvent used for liquid phase studies was shown to affect guest adsorption; benzothiophene and benzothiazole were adsorbed more quickly from a solution of heptane than from a solution of isopropanol. Gas phase studies were used to investigate the effect of occluded water molecules inside the pores of the framework upon the adsorption of methanol. A combination of XRD, thermogravimetry and inelastic neutron scattering studies were used to show that methanol does not displace water when hydrated MIL-53(Fe) is used as an adsorbent. Two equivalents of methanol can be packed inside the pores of the framework, irrespective of the adsorbent being hydrated or dehydrated.

Eight linker-modified MIL-53(Al) materials were supplied by research partners and *in situ* XRD studies were performed to reveal the effect of the modifications upon the adsorption of gas-phase molecules. The results show that the linkers change the behaviour of the material towards certain guest molecules and the most dramatic effect was seen when the benzene ring of the linker was replaced by cyclohexane.

A series of cobalt (II) MOFs synthesised with carboxylate and pyridine-*N*-oxide linkers is presented. The effect of functionalising the pyridine ring upon the topology of the resulting framework was studied. Resonance and steric effects were found to influence the structure of the final product. One of the new materials has the potential to be used as an adsorbent due to a 3D porous structure.

Chapter 1

Introduction

1 Metal-Organic Frameworks

The synthesis and characterisation of metal-organic frameworks is an area of coordination chemistry that has grown rapidly in recent years.[1-11] This chapter describes briefly the different types of framework that already exist, focussing on carboxylate-containing frameworks, which are the focus of this thesis. The variation of framework components and their effect on the framework topology and the pore size and shape is discussed. Also explored are the possible applications for these unique materials and how these materials can be tuned for specific applications. Throughout the work presented in this thesis a metal-organic framework known as MIL-53 and related materials have been investigated. The structure and properties of MIL-53 are described and relevant characterisation techniques and the corresponding results that have been reported in the literature are reviewed. This chapter is concluded with an outline of the aims of the work presented in the succeeding chapters.

1.1 Nomenclature

In 2012 the International Union of Pure and Applied Chemistry (IUPAC) defined the recommended terminology to be used when publishing reports on the type of materials that will be discussed in this work.[12] The term *coordination polymer* is recommended as the general term to describe all materials that extend in 1, 2 or 3- dimensions through coordination bonds. Battern *et al.*[12] defined two subsets to the term coordination polymer which are: *coordination network* and *metal-organic framework*. A coordination network is defined as having cross links between two or more chains. A metal-organic framework is either a coordination polymer or network that is connected in such a way as to create "potential voids" within the framework; the porosity of a framework does

not have to be proven prior to the material being classified as a metal-organic framework.

In 2006, Cheetham *et al.*[13] proposed a system to categorise the dimensionality of organic, inorganic and mixed inorganic-organic coordination polymers. The proposal is simple; it defines the type of connectivity as either M-ligand-M (organic connectivity, *O*) or M-X-M (inorganic connectivity, *I*), where X = oxide, hydroxide, floride *etc*. The dimensionality of the connectivity is described using a superscript 1, 2 or 3 for each type of connectivity. For example, chain coordination polymers with only M-ligand-M connectivity are given the classification I^0O^1 and purely inorganic chains are described as I^1O^0. In the same way, 3-D coordination polymers made from organic connections are classified as I^0O^3 and 3-D inorganic materials, such as zeolites, are described as I^3O^0. However, MOF-type materials can contain 1-dimensional chains with M-X-M connectivity cross-linked by organic molecules in 2-dimensions, which gives an overall 3-dimensional system with the classification I^1O^2. This nomenclature does not provide any information about the porosity of the material but it does give an indication of the connectivity of the different components in the mixed inorganic-organic materials.

Although various authors have made attempts to describe the framework connectivity of these materials, at present, there are no rules on how to name the thousands of frameworks that exist. Many research groups have chosen to identify their own materials using a short acronym which usually relates to the location of the laboratory in which the materials were synthesised, such as MIL; Matériaux Institut Lavoisier, STAM; St Andrews MOF, and HKUST; Hong Kong University of Science and Technology. Other groups have chosen to use the chemical formula to identify new materials and some have included the IUPAC recommended nomenclature for

coordination compounds *e.g.* poly[cobalt(II)-μ^2-*N*,*N*-dimethylformamide-κ^2O:O-μ^4-terephthalato- κ^4O:O':O'':O''']. [14] Each type of nomenclature has its advantages. Simple acronyms allow for quick identification of materials and structural analogues, but no information about the structure can be gained from this system. Using the chemical formula and IUPAC recommendations provides instant information about the framework composition but structural analogues are not immediately obvious and literature searches can be difficult. These different approaches to the naming of these materials have led to confusion and multiple publications of the same material, as discussed in Chapter 5. There is as yet no standard classification defined for the naming of these materials, and therefore the new materials synthesised as part of the work in this thesis will be identified by their chemical formulae.

1.2 A Brief History

The history of metal-organic frameworks begins back in 1897 when Hofmann *et al.*[15] reported a coordination network bonded via CN groups with the formula $Ni(CN)_2(NH_3).C_6H_6$. However, its crystal structure was not confirmed until 1952 when Rayner *et al.*[16] reported that the Hofmann structure was a layered, square network of $Ni(CN)_2(NH_3)$ groups with benzene sitting in the channels, recognising the structure as an extended network. Since 1897 many similar extended network-type materials have been described in the literature. In 1990, Hoskins and Robson published a speculative article regarding the design of 3-dimensional frameworks using octahedral and tetrahedral metal centres linked by "rod-like units".[17] They described the range of possible frameworks that could be achieved if the synthesis of these types of materials could be perfected.

Over the past one hundred years these types of materials have been defined as coordination polymers, coordination networks, inorganic-organic coordination polymers, porous coordination polymers and many other similar terms. It was not until 1995 that the term metal-organic framework was first used by Yaghi and co-workers to describe these materials.[18] They reported the successful design and synthesis of a layered material constructed from 1,3,5-benzenetricarboxylate, pyridine and octahedral Co centres which was capable of reversibly and selectively binding aromatic compounds such as benzene. This paper focussed on the conclusion that the functionality of these types of materials could be altered by changing the different framework components. Since this publication this area of materials science has grown rapidly, demonstrating the versatility of the linkages between inorganic and organic moieties. Various research groups around the world have demonstrated the vast range of different metals and ligands which can be used to produce these materials. Work has mostly focused on the transition metals and some p-block elements, although more recently the rare-earths have been shown to produce similar frameworks. While many authors have adopted the use of the term "metal-organic frameworks" to describe these materials, the various terms discussed above have continued to be used interchangeably, leading to confusion. Recently an attempt was made to standardise the terminology used for these types of materials, as described in Section 1.1; clarifying the differences between the most commonly used terms.

1.3 The Building Blocks of MOF Structures

The skeletal structure of a metal-organic framework (MOF) can be simply described as an arrangement of rigid units such as spheres and rods that are connected in 1, 2 or 3-dimensions (Figure 1.1). As defined by IUPAC, the components must be constructed in

such a way as to create an ‘open’ framework (porosity), which has the potential to host guest-molecules. This potential porosity is one reason why these materials are being extensively researched.[11, 19, 20] The structure of MOFs has been compared to that of aluminosilicate type zeolites, because they have a similar open network with microporous pores (less than 2 nm in dimension). However, MOFs can also have much larger pores in the mesoporous range (2 – 50 nm). The configuration in which the building blocks of both zeolites and MOFs are bonded is greatly dependent on the conditions during synthesis. Zeolites, aluminosilicates comprised entirely of corner-shared, inorganic, tetrahedral units of AlO_4 and SiO_4, generally require an additional molecule or ion to act as a template whereas, in general, no extra reagents are needed for the production of metal-organic frameworks. This is the major difference between the two materials as the building blocks for MOFs can differ enormously and contain both inorganic and organic components which define the connectivity with no need for templating species. This difference is also important as it means MOFs may include regions of hydrophobic (aliphatic or aromatic areas) or hydrophilic functions, which can affect the adsorption properties of the crystal lattice. MOFs are constructed via a self-assembly, supramolecular process known as the “bottom-up” approach. In contrast to supramolecular chemistry, the organic and inorganic building blocks are covalently bonded, giving rise to structures which have been shown to be stable up to 500 °C and are chemically resistant to most solvents.[21]

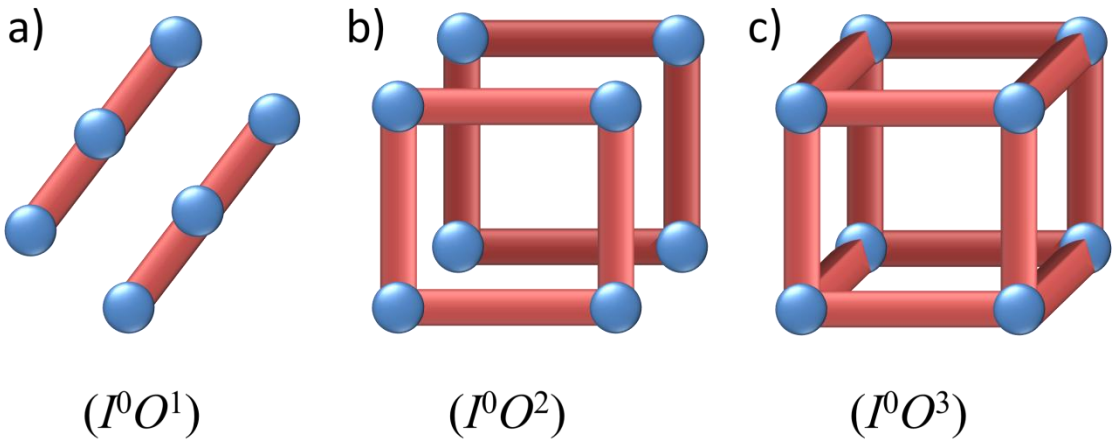

Figure 1.1: Simple rod and sphere representation of MOF structures with different dimensionalities a) 1-dimensional, b) 2-dimensional and c) 3-dimensional

A simple rod and sphere representation of a MOF can be used to simplify the description of the connectivity between the two building units (Figure 1.1). The rods represent organic molecules that can have a range of carbon backbones and functional groups and the spheres represent metal cations that are capable of coordinating to these organic molecules with various coordination geometries. The number of possible organic molecules that can be used as ligands is enormous; the only restrictions being that the molecule must contain functional groups capable of coordinating to metal centres in either 1-, 2- or 3-dimensions. Some of the most common functional groups shown to be successfully used in the synthesis of these materials are carboxylates,[11, 22, 23] pyridyls,[24] phosphonates[25, 26] and pyrazoles.[27] Bifunctional molecules such as those containing tetrazoles and carboxylates,[28] and tetrazoles and pyridyls[29] have also been used for MOF synthesis.

The sphere, which is used to represent the metallic component of the MOF, can symbolise either a single metal cation or a cluster of metal cations coordinated to a heteroatom *e.g.* Zn_4O.[30] There are a large number of metal cations that can be used for MOF synthesis. Most of these cations can have various oxidation states and a variety of

coordination numbers. Some common transition metals used for MOF synthesis are Zn, Cu and Fe.[27, 31-39] It is not always clear prior to the synthesis of the MOF whether the metal cations will form clusters or remain as single cations. The large numbers of organic molecules and metal cations can, theoretically, lead to an infinite number of possible combinations that can result in the formation of MOFs. It is for this reason and their porosity that MOFs have been extensively studied and been recognised as promising alternatives to current adsorbents, *e.g.* activated carbons and zeolites, in a large number of industrial applications, such as hydrogen and methane storage. [9, 40]

1.4 Carboxylate-containing MOFs

As described above, there is a huge variation in the different types of organic linkers that can be used for MOF synthesis. The new work presented in this thesis uses primarily carboxylate-containing organic linkers. Therefore the remainder of this review will focus on these types of ligands.

1.4.1 Ligand Variation

The carboxylate functional group is able to either bridge between two metal centres or act as a chelating ligand where both the oxygens coordinate to the same metal. It is the ability to bridge between metal centres that makes this functional group an important component of MOF synthesis. To enable the formation of 3-dimensional frameworks, ligands with two or more carboxylate groups are used, which allows the ligands to bridge in more than one dimension. Two possible coordination modes of a single carboxylate group and a molecule containing two bridging carboxylate groups are shown in Figure 1.2.

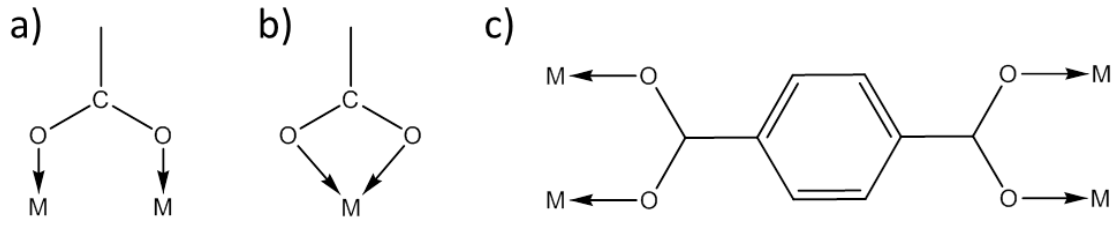

Figure 1.2: Coordination modes of carboxylate functional groups a) single carboxylate bridging two metal cations, b) single carboxylate chelating to one metal cation and c) an example of a molecule containing two bridging carboxylate groups.

Organic carboxylate-containing molecules, used for MOF synthesis, are not restricted to two carboxylate groups and molecules containing three or four are quite common. Considering the variety of organic functionalities and possible carbon backbones, there is, in theory, an infinite number of organic components that can make up the non-coordinating part of the molecule. This section of the molecule can be linear, bent or branched and either rigid or include some inherent flexibility. The variation in the number of carboxylate groups and the shape and size of the ligand leads to a wide variation in framework topologies. Figure 1.3 highlights the effect of increasing the length of the ligand. The series shown here was first reported by Yaghi and co-workers.[30] The ligands in these examples are based on the rigid and linear 1,4-benzenedicarboxylate linker where additional phenyl groups only have the effect of increasing the size of the pores, but do not affect the topology of the structure. These structures are described as *isoreticular*.

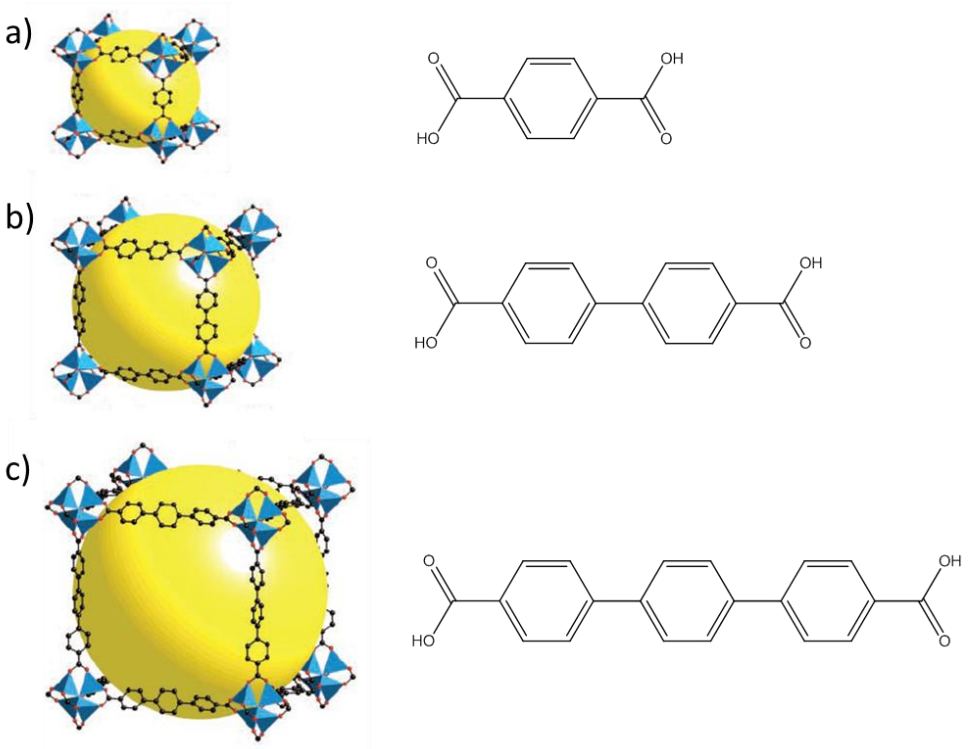

Figure 1.3: Isoreticular frameworks using different carboxylate linkers a) MOF-5, H_2bdc, b) IRMOF-10, H_2bpdc and c) IRMOF-16, H_2tpdc.[30]

Ligands can contain two carboxylate groups and either have a straight or bent geometry, for example, 1,4-benzendicarboxylic acid and 1,3-benzendicarboxylic acid (H_2bdc), respectively. They can also contain three carboxylate groups and have a rigid conformation such as, 1,3,5-benzenetricarboxylic acid (H_2btc), or have a degree of flexibility, *i.e.* 4,4',4''-benzene-1,3,5-triyl-tribenzoic acid (H_3btb). Figure 1.4 shows four different MOFs: Figure 1.4a and b show MOFs that were synthesised using Fe^{3+} but with different organic linkers containing two carboxylate groups and Figure 1.4c and d show MOFs synthesised using Cu^{2+} and organic ligands containing three carboxylate groups. This figure highlights the variation in framework topology due to changes of the organic linker.

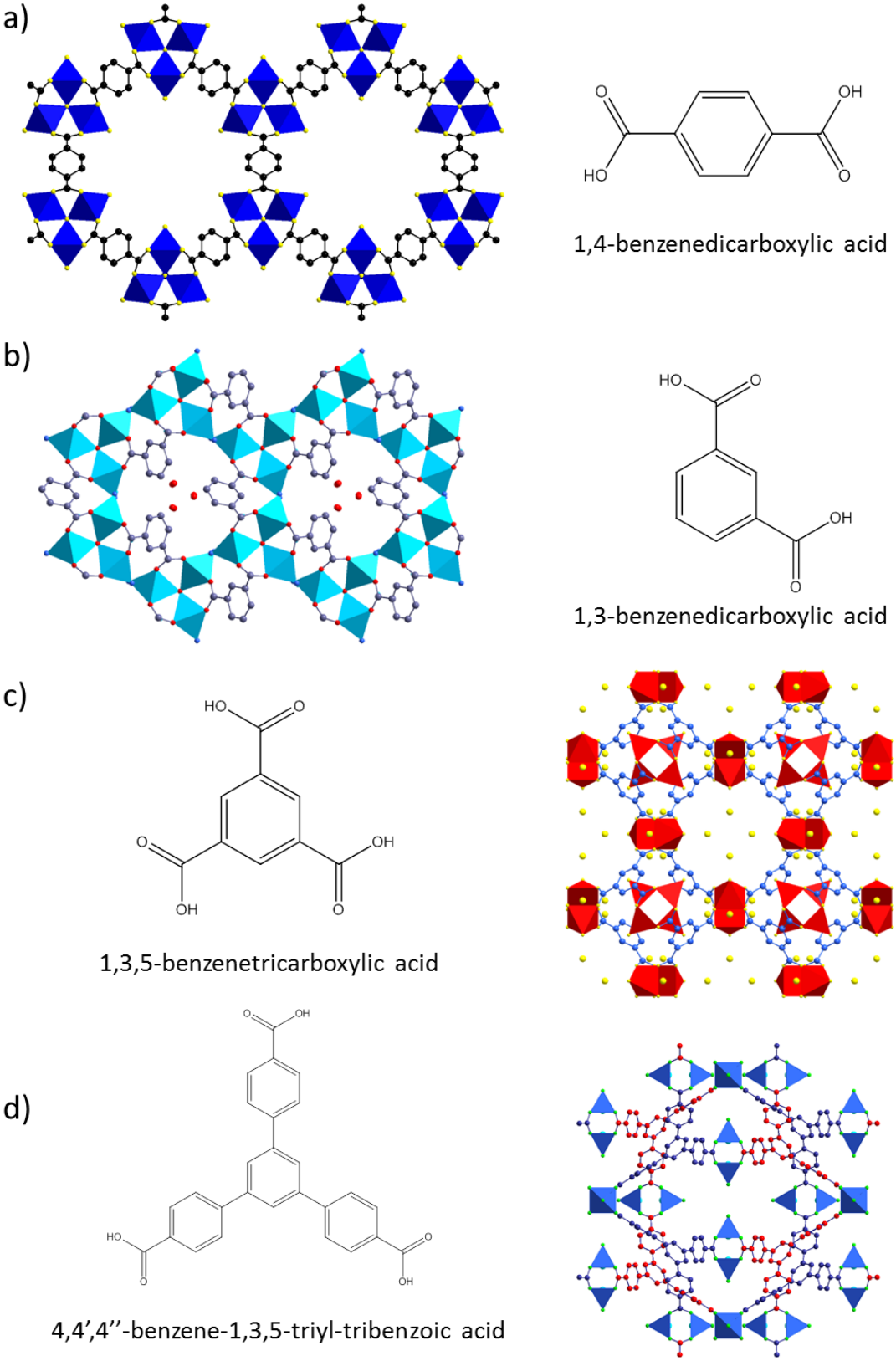

Figure 1.4: Changes in framework topology with changing ligand geometry a) MIL-88b (Fe3+) [41]*, b) MOF-236 (Fe^{3+}),*[42] *c) HKUST-1 (Cu^{2+})*[43] *and d) MOF-14 (Cu^{2+}).*[44]

1.4.2 Metal Cation Variation

Various coordination environments around the metal centres are also possible. As expected from classical coordination chemistry, the choice of metal cation and its oxidation state can create several geometries, *e.g.* Pt^{2+}: square planar (four-coordinated), Fe^{3+}: octahedral (six-coordinated), Cu^{2+} (Jahn-Teller distorted six-coordinate). As described in Section 1.3 the metal nodes are not restricted to single metal cations; they can also form clusters *e.g.* $Zn_4O(CH_3CO_2)_6$ (the zinc acetate cluster). Other common cluster geometries for carboxylate ligands are shown in Figure 1.5, $M_2(CO_2)_4(O)_2$ and $M_3O(CO_2)_6(O)_3$.

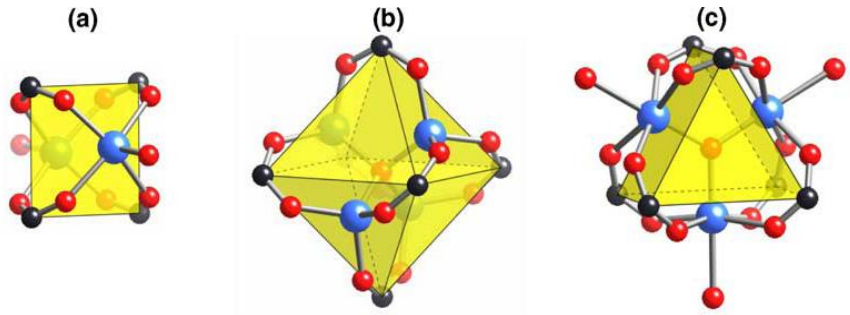

Figure 1.5 [11] *"a) the square "paddlewheel", with two terminal ligand sites b) the octahedral "basic zinc acetate" cluster and c) the trigonal prismatic oxo-centred trimer, with three terminal ligand sites." The black spheres indicate the position of the linking ligands, blue spheres show the metal ions and the red spheres highlight the bridging and terminal oxygen atoms.*

There are few restrictions on the cations that be used to create a metal-organic framework, transition metals are a common choice, however, more recently the lanthanides have been experimented with and shown to form similar structures.[45] Due to the larger ionic radii of the lanthanides they are able to coordinate to a larger number of ligands leading to topologies that are specific to these types of cations. Figure 1.6 shows three MOFs that have been synthesised with the 1,4-benzenedicarboxylic acid ligand

and various metal cations in varying oxidation states. This figure highlights the effect of the metal cation in framework design.

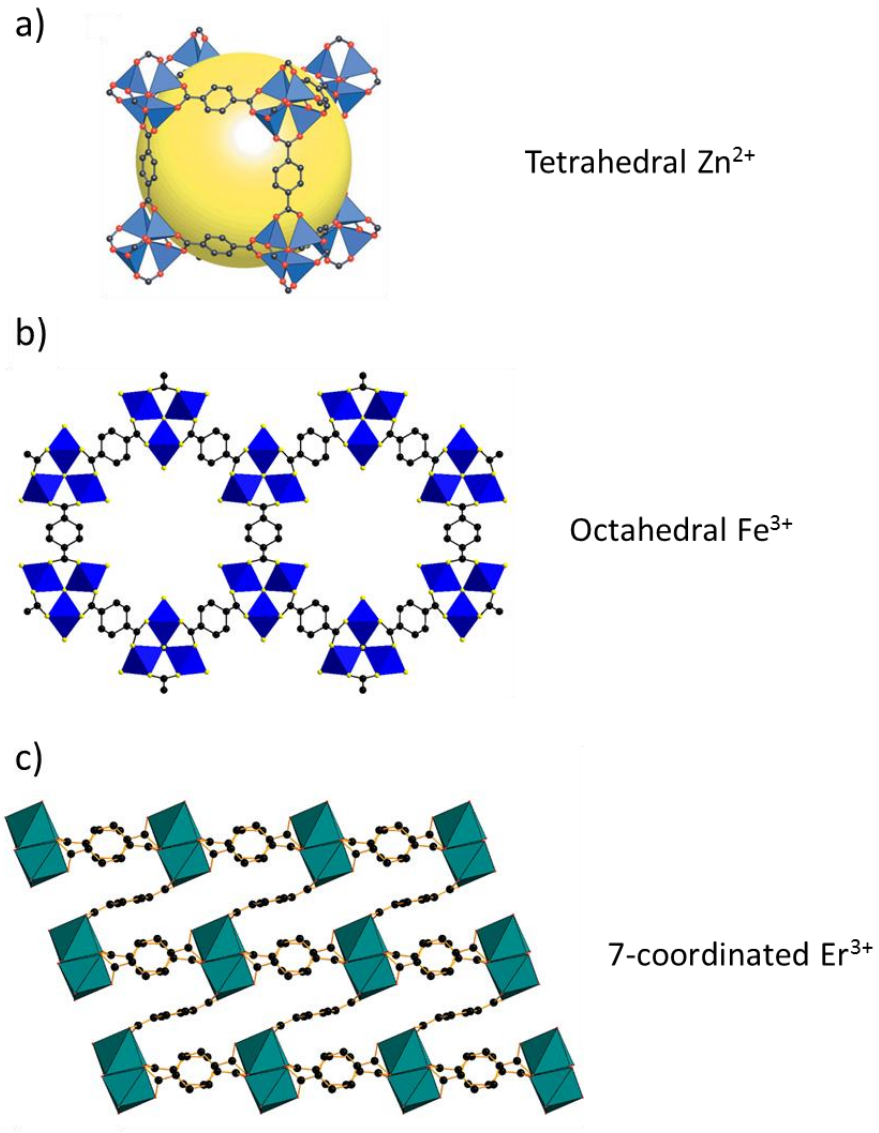

Figure 1.6: Changing the metal source while keeping the organic linker the same results in very different framework topologies a) MOF-5,[30] b) MIL-88b(Fe),[41] and c) $Er_2(bdc)_3$.[46]

1.4.3 Synthesis Conditions

As described in the previous sections the metal cations and organic ligands chosen for MOF synthesis define the resultant framework structure. However, the synthetic conditions have been shown to play a major role in defining the outcome of a given reaction. The metal salt used as the source for a particular metal cation can affect how a

reaction proceeds. Ahnfeldt *et al.*[47] reported in 2009 that keeping the synthesis conditions constant, but changing the metal salt from $Al(NO_3)_3.9H_2O$ to $AlCl_3.6H_2O$, gave two very different frameworks, MIL-53-NH_2 and CAU-1, respectively (Figure 1.7a).

The choice of solvent has also been shown to have an effect on the final topology of the framework. Liu *et al.*[48] published the structure of two different MOFs for which they used the same metal salts and organic linkers but they changed the solvent from DMF to MeOH. This small change in the synthetic conditions resulted in the production of two different frameworks (Figure 1.7b); one where the two ligands lined different walls of the pores and the other where the two ligands alternated along each pore wall.

Millange *et al*.[49] reported that the duration and temperature of their reaction was crucial to the outcome of their experiment. If the synthesis was too short or the temperature too low then the resulting product was a MOF known as MOF-235 and not the desired MOF, MIL-53 (Figure 1.7c).

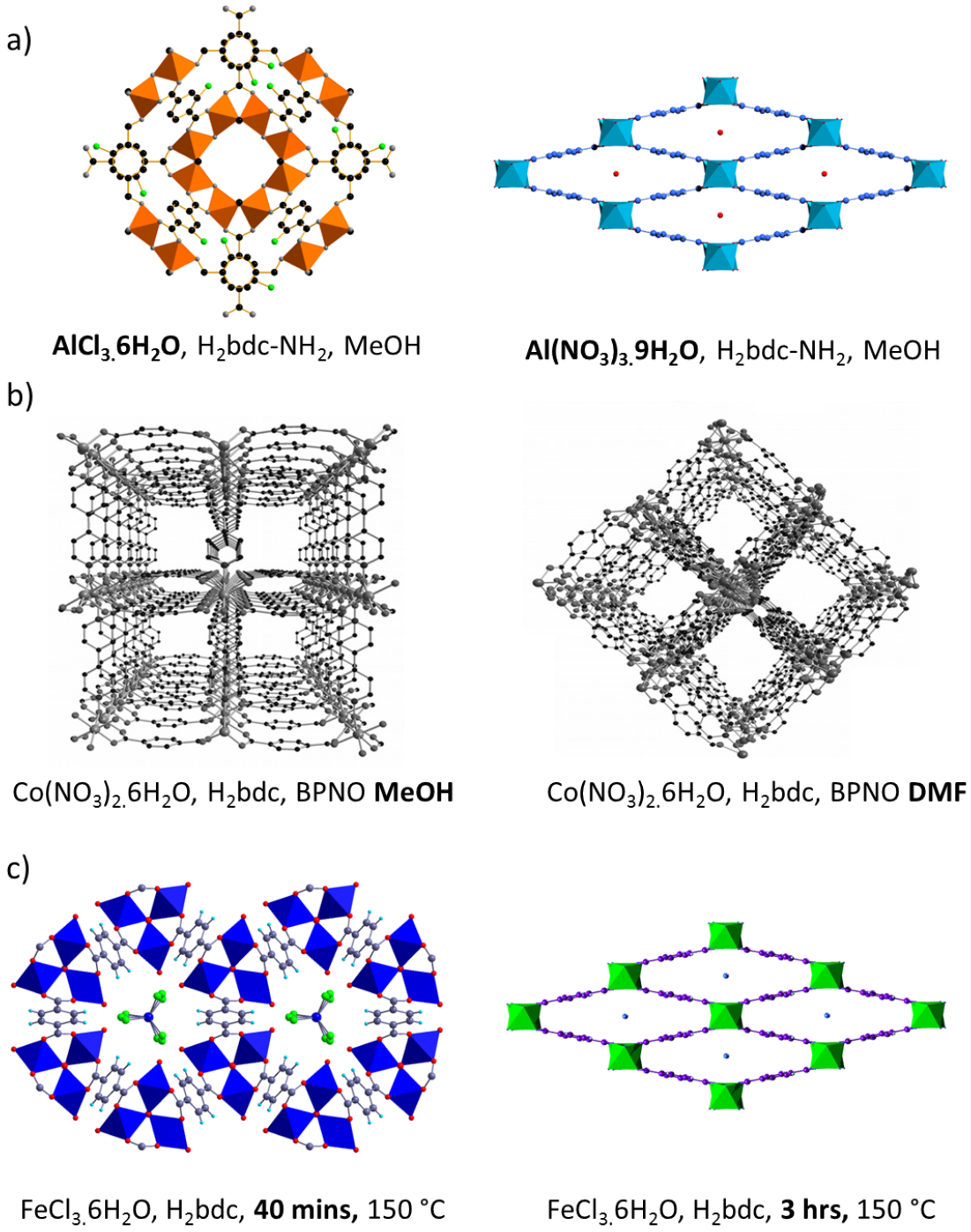

Figure 1.7: Effect of the synthesis conditions upon framework topology a)changing the metal salt, b) changing the solvent, and c) changing the duration.

1.4.4 Dynamic Frameworks

The majority of metal-organic frameworks are rigid *i.e.* where the framework dimensions remain unchanged after the removal of any occluded molecules. However, it has been shown that some frameworks have a structure that can reversibly *breathe*

under the influence of external stimuli *e.g.* temperature, pressure, gas sorption, and these frameworks are termed dynamic.[50-53] This breathing phenomenon is described as a reversible contraction or expansion of the structure upon the application of the external stimuli where the topology of the structure is usually retained.[54] This phenomenon is not exclusive to these hybrid materials it has previously been witnessed in purely inorganic compounds such as zeolites[55] and perovskites.[56, 57]

The excitement associated with metal-organic frameworks is the extent to which they expand and contract. In general, atomic displacements seen in conventional solid state materials are very small (<0.8 Å), whereas atomic displacements of several Ångströms have been recorded in MOFs. There are a small number of examples of dynamic carboxylate-containing metal-organic frameworks in the literature. Serre *et al.*[41] reported a series of MOFs with the formula $M_3O(H_2O)_2X(dicarbox)_3]\cdot guest$, where X(dicarbox) = fumurate (MIL-88a), terephthalate (MIL-88b), 2,6-naphthalenedicarboxylate (MIL-88c) and 4-4'-biphenyldicarboxylate (MIL-88d) (where M = $Cr^{(III)}$ or $Fe^{(III)}$), which show a very large breathing effect comprising a 270% increase in pore volume. The degree of this increase is dependent upon the adsorbed molecules. Férey and co-workers also demonstrated that a framework known as MIL-53, $[M(OH)(CO_2\text{-}C_6H_4\text{-}CO_2).H_2O]$ (where M = $Cr^{(III)}$, $Fe^{(III)}$, $Al^{(III)}$)[52, 54] shows a reversible pore expansion of 30% when the material is dehydrated at moderate temperatures.

1.4.5 Potential Applications

The porosity of MOFs has led to the properties of these frameworks being extensively researched.[45, 58-66] As mentioned previously, MOFs have similar, but potentially superior, properties to zeolites and as a consequence have been found to be useful in the

same industrial areas. As well as porosity, other properties have been studied, including magnetism,[7] ferroelectricity[67] and catalysis.[62] There are a large number of studies into the uses of MOFs, therefore only those most applicable to the work presented in this thesis are described below:

Adsorption and storage- Adsorption of various molecules is a highly researched area that exploits the molecular-scale porosity and the ability of the frameworks to reversibly adsorb molecules.[9, 68-71] The adsorption of H_2 gas by MOFs has been researched extensively for the purpose of providing efficient energy storage materials.[27, 65, 72-74] The adsorption of hydrogen gas within the pores of metal-organic frameworks has been shown to be influenced by the shape and size of the pores,[75, 76] the presence of any coordinatively unsaturated sites (CUS),[77, 78] and the functionality of the framework ligands.[79] The same principles have been used to enhance the adsorption of various guest molecules including H_2S,[80] sulfur-containing heterocycles,[81-83] medicinal molecules,[84] small alcohols[85, 86]and small gas molecules such as methane[30, 71] and carbon dioxide.[87-89]

Separation- The separation of guest molecules based on size, shape or chemical affinity can lead to new low energy alternatives to industrial problems. Separation is closely related to adsorption; however it requires the selective adsorption of specific guest molecules from a mixture of compounds either in the liquid or gas phase. The removal of harmful compounds from industrial flue gas (CO_x, C_xH_y, NO_x, SO_x) is one application that has been studied. Various research groups have used adsorption isotherms to study the separation of carbon dioxide from gas mixtures using MOFs *e.g.* Finsy *et al.*[90] found that MIL-53(Al) preferentially adsorbed CO_2 over CH_4 and Liu *et al.*[91] reported that CPO-27(Ni) preferentially adsorbed CO_2 over N_2. Separation can be

achieved by either the favourable adsorption of specific guest molecules or the framework favourably retaining a specific guest. Various compounds can be adsorbed by a framework, but a stronger interaction with a specific guest, due to size, shape or chemical reactivity, can lead to longer retention times when exposed to specific conditions, such as different eluents and temperatures. This process has been used for the separation of the xylene isomers, a process that is very challenging since the boiling points of the three isomers differ by only 6 °C. Examples of MOFs that have been used for this type of separation are MIL-53(Al),[92] and MOF-5.[93]

Sensors- MOFs can be used as chemical sensors as some frameworks show structural changes upon the uptake or removal of guest molecules or exhibit changes in their phosphorescent properties.[4, 61] Allendorf *et al*.[94] reported the use of Cu-BTC (BTC = 1,3,5-benzenetricarboxylate) as a chemical sensor for the presence of H_2O, MeOH and EtOH. Piezoelectric materials were used to detect small structural changes in a thin film of Cu-BTC. Xie *et al*.[95] reported the synthesis of a phosphorescent Ir MOF that displayed quenching of the phosphorescence upon the adsorption of O_2. This process was shown to be completely reversible.

1.5 Modifications of MOF Structures

In an attempt to improve the properties of MOFs, functionalisation of the organic linkers has been identified as a promising technique to allow greater control over the properties of the structures. Two methods have been used to create functionalised MOFs; 1) modifications are made to the reaction mixtures and 2) the linkers or frameworks are modified using post-synthetic methods, such as nitration.[96, 97] Studies have shown that these modified frameworks can exhibit improvement, if particular

functional groups are added, for applications such as separation,[98] catalysis,[96] and gas adsorption.[99]

1.5.1 Pre-Synthetic Design

Modifications at the synthesis stage can be used to alter the properties of certain frameworks with the view of improving specific interactions towards certain types of guest molecules. These pre-synthetic modifications can take two forms; changes to the organic linkers or changes to the metal centres.

1.5.1.1 Ligand modification

Ligand modification of specific frameworks can be achieved by adding functional groups to the molecules used as framework linkers. Functionalisation is normally achieved through organic synthesis techniques. The added groups can dramatically change the functionality of the MOF; for example the hydrophobicity of the pores can be adjusted by introducing either polar or non-polar groups. It has been shown that this type of modification works for various ligands and introduces significant improvements in properties.

Yaghi and co-workers performed a comprehensive study on pre-synthetic design using carboxylate ligands.[30] The results show that a series of MOFs can be synthesised using a range of functionalised carboxylate ligands. Functional groups such as $-NH_2$ and $-C_2H_4$ were shown to produce a series of isoreticular MOFs which were related to the unmodified carboxylate material, MOF-5. The study also showed that the effect of functionalising the ligands was to change the behaviour of the original framework; the methane capacity of each framework was 9.2 mmol g^{-1} (MOF-5), 7.9 mmol g^{-1} ($-NH_2$) and 10.0 mmol g^{-1} ($-C_2H_4$). Zlotea *et al.*[99] studied the effect of functional groups on H_2 gas adsorption by functionalising three carboxylate containing materials with two

different functional groups. The MOFs used in this study were; MIL-53(Fe)-$(CF_3)_2$, MIL-125(Ti)-NH_2, UiO-66(Zr)-$(CF_3)_2$ and UiO-66(Zr)-(NH_2) and the unmodified materials. Table 1.1 shows the results of the H_2 adsorption isotherms. The results show that the functionalisation had a mixed effect on the three frameworks. The modified MIL-53 material showed an improved H_2 capacity, the modified MIL-125 material showed a decrease in H_2 capacity and the UiO-66 material showed an increase when modified with $–NH_2$ but a decrease when modified with $-(CF_3)_2$ (Table 1.1). It is concluded that in this case the resultant behaviour towards small gas molecules was less affected by the chemistry of the functional group and more by the resultant size and texture of the pores after functionalisation.

Table 1.1: Hydrogen capacity of functionalised carboxylate MOFs.[99]

Framework	H_2 capacity at 77 K and 4 MPa	
	wt%	mmol g^{-1}
MIL-53(Fe)	< 0.1	0.5
MIL-53(Fe)-$(CF_3)_2$	0.6	3.0
MIL-125(Ti)	3.4	16.9
MIL-125(Ti)-NH_2	2.5	12.4
UiO-66(Zr)	2.3	11.4
UiO-66(Zr)-$(CF_3)_2$	1.2	6.0
UiO-66(Zr)-NH_2	2.5	12.4

Mixed-ligand modifications are also possible. A mixed carboxylate ligand framework which is isoreticular to the MOFs MOF-5 [Zn_4O-$(C_8H_4O_4)_3$] and IRMOF-3 [Zn_4O-$(C_8H_3O_4$-$(NH_2))_3$] was successfully synthesised by Kleist *et al.*[96]. The MOF contained a mixture of 1,4-benzenedicarboxylate (bdc) and the amino modified bdc (bdc-NH_2) and

was synthesised with varying ligand ratios. This study showed that this MOF could be used for the catalysis of propylene oxide and carbon dioxide to give propylene carbonate. It was also shown that the catalytic activity could be related to the number of NH_2 groups present. Chun *et al.*[31] synthesised a mixed ligand framework which was also isoreticular with the two parent frameworks, Zn_2(bdc)(dabco) and Zn_2(tmbdc)(dabco) (dabco = 1,4-diazabicyclo[2.2.2]octane, and tmbdc = 2,3,5,6-tetramethyl-1,4-benzenedicarboxylate). The two ligands, bdc and tmbdc, were randomly distributed through the mixed-ligand framework. The study showed that the smaller pores created by the bigger ligand, tmbdc, improved the adsorption of H_2. However, the uptake of the mixed-ligand framework was significantly higher than the Zn_2(tmbdc)(dabco) material.

1.5.1.2 Mixed-Metal Frameworks

Modification of the metal content or valency is a relatively new area of MOF synthesis to be investigated, nevertheless, there are several successful examples of these different types of modification. A report by Kozachuk *et al.*[100] in 2012 showed the successful synthesis of a series of frameworks with the empirical formula $Cu^{II}_{1-x}Zn^{II}_x$(bdc)(dabco)$_{0.5}$, with the metal ratios of 5:95, 25:75, 50:50, 75:25, 95:5 (Cu:Zn). The mixed-metal frameworks were shown to be isoreticular to the parent frameworks. H_2 adsorption isotherms were performed which show that in general the higher the Zn content the greater the amount of H_2 that can be adsorbed, and that even a small amount of Cu (5%) results in a higher H_2 adsorption than the pure Zn material. Interestingly, a linear trend between H_2 adsorption and metal ratio is not seen suggesting that mixed-metal frameworks can give rise to some interesting properties not previously seen for single-metal MOFs. In 2013, Wang *et al.*[101] reported the synthesis of a series of MOFs with the empirical formula $Mn^{II}_{1-x}Fe^{II}_x$(cmpc)(N_3)·H_2O (cmpc =

carboxymethylpyridinium-4-carboxylate) using the metal ratios 1:1, 2:3 and 1:4 (Mn:Fe). Magnetic studies on these materials showed that the resultant behaviour was a combination of the ferromagnetic behaviour of the Fe(II) centres and the antiferromagnetic behaviour of the Mn(II) centres and as the Fe(II) content increased there was a gradual evolution from antiferromagnetic to ferromagnetic behaviour. It was also reported that further investigation was needed to understand the origins of the complex relaxation processes seen for the Fe(II) rich materials.

1.5.2 Post-Synthetic Modification

Post-synthetic modification has been shown to be an effective way to alter the functionality of MOFs. This can be achieved through chemical reactions to alter the framework ligands[102, 103] or the removal of terminating ligands from metal centres which results in coordinatively unsaturated sites (CUS).

1.5.2.1 Ligand Modification

Post-synthetic modification of framework ligands can take two routes; the substitution of relatively weakly coordinating ligands directly bonded to the metal centres or the covalent modification of functional groups coordinated to the framework linkers. There are various reports that show that auxiliary ligands, *e.g.* H_2O, which are directly coordinated to the metal centres such as those found in HKUST-1 and MIL-100(Cr), can be removed or replaced by various other ligands such as pyridine[43] and MeOH.[104] Dietzel *et al.*[77] reported improved H_2 gas uptake for CPO-27 (Ni, Co, Mg) after the removal of the auxiliary H_2O ligands. It was concluded that the resulting coordinatively unsaturated sites on the metal centres gave a stronger interaction with the adsorbed H_2 molecules. Hwang *et al.*[105] reported that the auxiliary H_2O ligands of MIL-101 could be easily replaced with ethylenediamine (ED) by refluxing in a solution of ethylenediamine

and toluene. This modified framework was investigated for its catalytic activity towards the condensation of benzaldehyde and ethyl cyanoacetate and it was found that conversion was improved to >96% compared to the 35% conversion rate seen for the unmodified material.

Reports by Wang *et al.*[106, 107] describe the covalent modification of three frameworks, UMCM-1, MOF-5 and DMOF-1, which had previously been synthesised in their isoreticular forms using $–NH_2$ functionalised bdc ligands. These amino containing frameworks were treated with acetic anhydride in $CDCl_3$ which resulted in the addition of the acetyl group and gave materials with amide functional groups on the linkers. The authors concluded that this type of modification can facilitate the generation of functional properties that are not directly accessible from conventional MOF synthetic schemes.

1.6 MIL-53: $M^{III}(CO_2\text{-}C_6H_4\text{-}CO_2)(OH)$

The MIL-53 structure was first published in 2002 by the Férey research group from the Institut Lavoisier (IL) in Versailles.[52] The organic and inorganic components of MIL-53 are 1,4-benzenedicarboxylate (bdc) and M^{III} (first published using Cr^{III}), which is octahedrally coordinated to two hydroxy groups and four bdc linkers. This particular MOF has been extensively studied in recent years. Since 2007 the number of papers that have been published relating to the MIL-53 structure has dramatically increased (Figure 1.8). The unique properties of this framework are the cause of the interest in this material. Understanding and manipulating these properties has been the focus of much research into these materials.

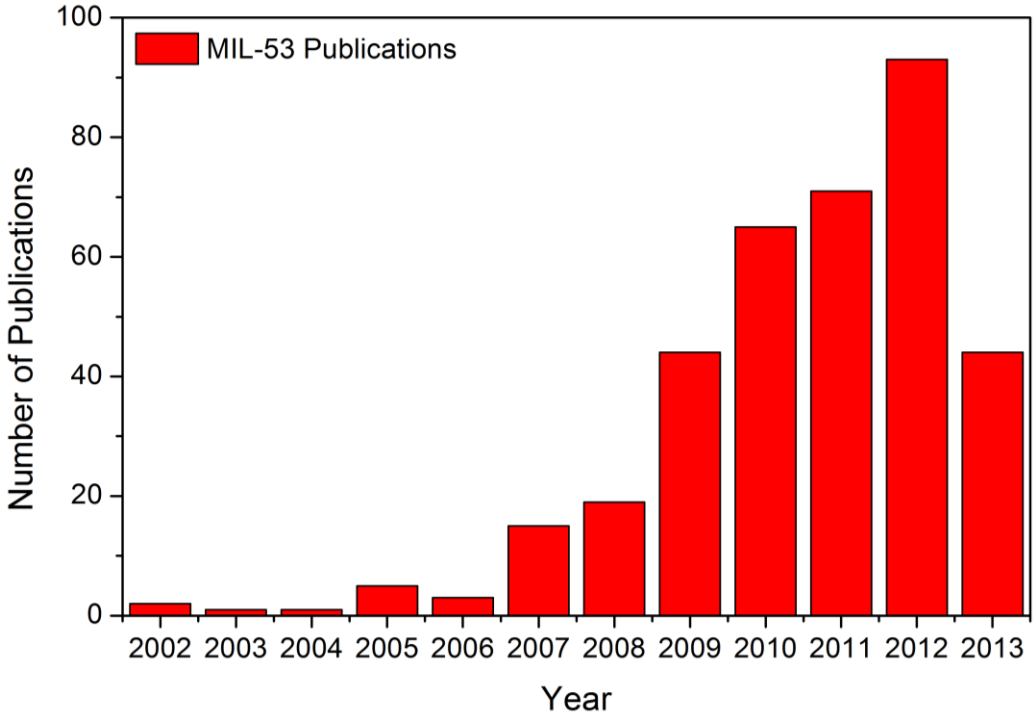

Figure 1.8: Number of publications related to MIL-53.Data obtained from Web of Knowledge search for Topic: MIL-53. Data for 2013 accurate on 15-07-13.

1.6.1 Structure and Properties

The components of MIL-53, bdc linkers and M^{III} octahedra, coordinate to form a highly-ordered three-dimensional framework, which has a one-dimensional lozenge-shaped pore system along the *c*-axis (Figure 1.9a).[54] The framework is formed from *trans*-chains of $M^{III}O_4(OH)_2$ octahedra where the metal centres are bridged by hydroxyl groups (Figure 1.9b). These chains are cross-linked by 1,4-benzenedicarboxylate anions coordinated via the two oxygens in the carboxylate groups (Figure 1.9c). Figure 1.9 shows the hydrated phase of MIL-53, which contains water molecules inside the pores. The structure was solved with monoclinic symmetry, *C2/c*, to give a refined unit cell volume of ~950 $Å^3$.[52] The hydrated phase is obtained by activating the sample, isolated from the reaction mixture, to remove unreacted reagents and solvent molecules from the pores and allowing equilibration (at ambient conditions) where the framework adsorbs water from the atmosphere.

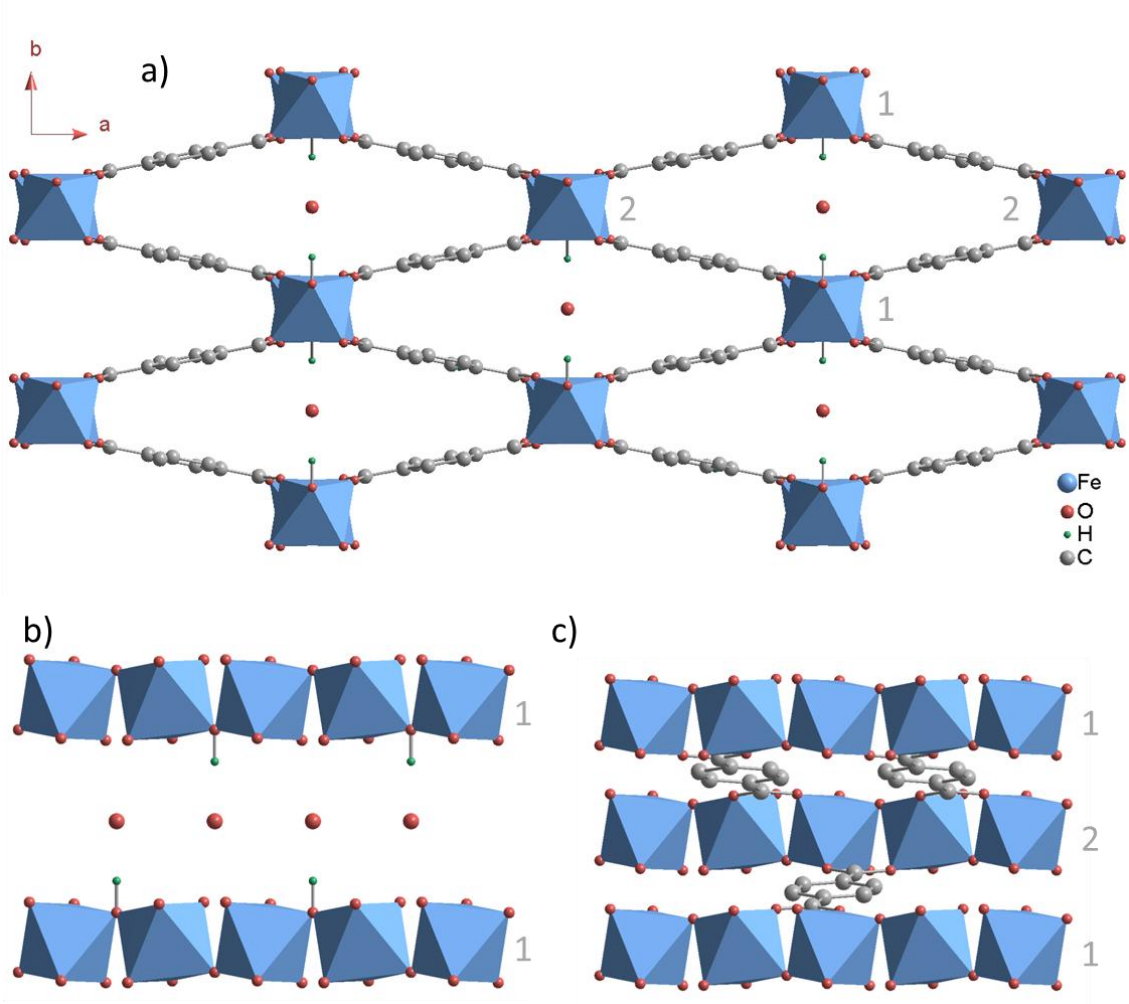

Figure 1.9: Hydrated MIL-53 viewed along a) the c-axis, b) the a-axis showing the trans chains, the bridging hydroxy groups and occluded water molecules (bdc linkers and the metal oxide chain labelled "2" have been omitted for clarity), and c) the a-axis showing the cross-linked bdc ligands (hydroxy groups and occluded water molecules have been omitted for clarity)

The main interest in this material is the ability of the framework to expand and contract without making or breaking bonds while remaining highly crystalline.[52] The original MIL-53 framework was synthesised with Cr^{3+}. This framework was found to expand in response to increasing temperature and the introduction of various guest molecules *e.g.* CO_2, 1,4-benzenedicarboxylic acid. The structure of the dehydrated expanded phase, achieved using temperatures above 150 °C, was solved using powder X-ray diffraction (PXRD). The unit cell volume was shown to increase to 1486.1 $Å^3$ and the unit cell was refined using the orthorhombic space group, *Imcm*.[52] This shows an increase in the framework volume of approximately 50% while the crystallinity of the framework is

maintained (Figure 1.10). A similar degree of expansion was found when CO_2 guest molecules were adsorbed.[108]

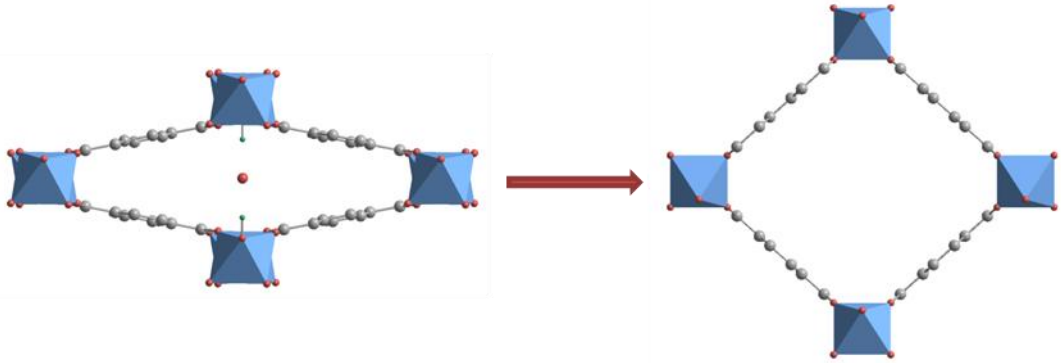

Figure 1.10: Expansion of MIL-53(Cr) upon dehydration [52]

This unique flexibility is assumed to arise from the particular connectivity of the framework linkers and metal oxide chains. The O-C-O group of the carboxylate that bridges between metal centres creates a hinge-like component and allows a certain degree of rotation, which is sometimes referred to as the *knee-cap* (Figure 1.11).[109] The carbon-phenyl bond allows a certain amount of rotation, adding complexity to the way the framework can adjust during expansion and contraction.

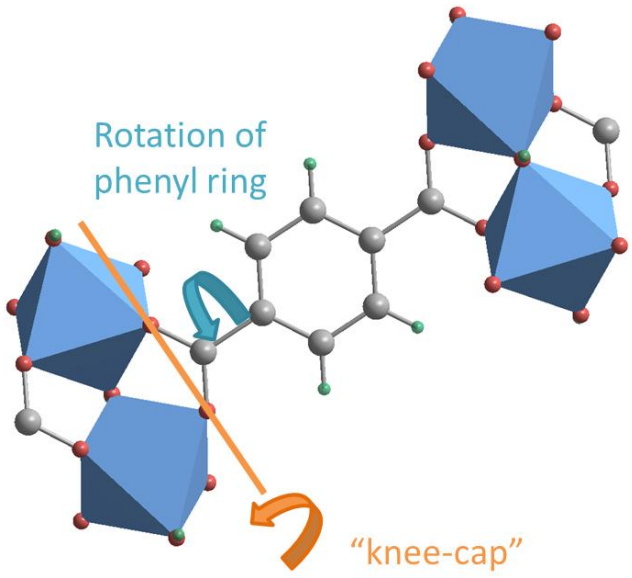

Figure 1.11: The knee-cap of MIL-53

1.6.1.1 The Effect of Metal Centres on the Breathing Phenomenon

Various analogues of MIL-53 have been reported. The different metal cations that have been successfully used to synthesise MIL-53 are; Cr^{III},[54] Al^{III},[58] In^{III},[110] Fe^{III},[111] Ga^{III},[51] V^{III}[112] and Sc^{III}.[113] Owing to the difficulty in growing single crystals only the structures of the as-made phases of the Sc[113] and In[110] forms and a pyridine containing phase of the Fe[114] form have been solved from single crystals. The structures of the other analogues and the other phases seen for these materials were determined using high-resolution powder X-ray diffraction and structural refinement analysis. Each analogue displays the breathing property in varying degrees. The chromium, aluminium and gallium forms contract when molecules are adsorbed into their pores and expand upon desorption of these molecules under thermal treatment (Figure 1.10). In contrast, the iron structure contracts slightly upon the complete removal of occluded molecules under thermal treatment and only expands when guest molecules are adsorbed (Figure 1.12).[70, 111, 115] The scandium is a unique case due to the hydrated phase only containing water in half the available pores, resulting in a very distorted structure at room temperature. When thermal treatment is used, the water molecules are removed and the framework reorders to give a structure very similar to the dehydrated iron structure.[116] Structural changes were not reported for the In framework, therefore this analogue will not be discussed further.

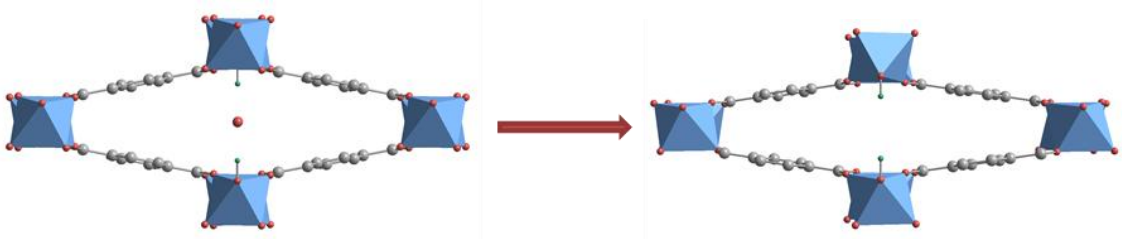

Figure 1.12: Contraction of the framework (Fe^{3+} and Sc^{3+}) upon dehydration

There are three distinct forms of MIL-53 that can be characterised for each of the metal centres: 1) The as-synthesised form (denoted in the literature as 'MIL-53as'), which is a room temperature phase isolated from the reaction vessel, where the pores contain unreacted 1,4-benezenedicarboxylic acid (H_2bdc) and solvent molecules from the reaction mixture, 2) the hydrated phase (referred to as 'hydrated MIL-53' in this work[*]), which can be collected by either washing in a volatile solvent or heating to remove the H_2bdc molecules (water molecules are adsorbed from the air) and, 3) the dehydrated phase (referred to as 'dehydrated MIL-53' in this work[†]), which is heated to remove water from the pores. The three phases are distinct but the pore volumes of each phase are dependent upon the metal centres.

It has been shown that there is a fourth phase that occurs for MIL-53(Fe) and MIL-53(Ga), which is 'int-MIL-53' and this appears as a transient phase during the transition from the hydrated phase to the dehydrated phase. The pore volumes of int-MIL-53 are similar in volume to the hydrated phases, but they contain no guest molecules.

The scheme below (Figure 1.13) shows the change in pore volume at varying temperature for three of the six possible metal centres: Al, Ga and Fe. The Cr form behaves in a similar way to the Al material but the temperature range at which the transformation occurs is between 100 – 150 °C which is higher than is seen for Al, 40 – 60 °C. Figure 1.13 illustrates that the aluminium framework has a high thermal stability, the framework only collapses above 500 °C.[21] The thermal stability of the frameworks not shown in Figure 1.13 is ~350 °C and ~500 °C for Cr and Sc respectively.

[*] Has been denoted in the literature as lt-MIL-53 or np-MIL53

[†] Has been denoted in the literature as ht-MIL-53 or lp-MIL53

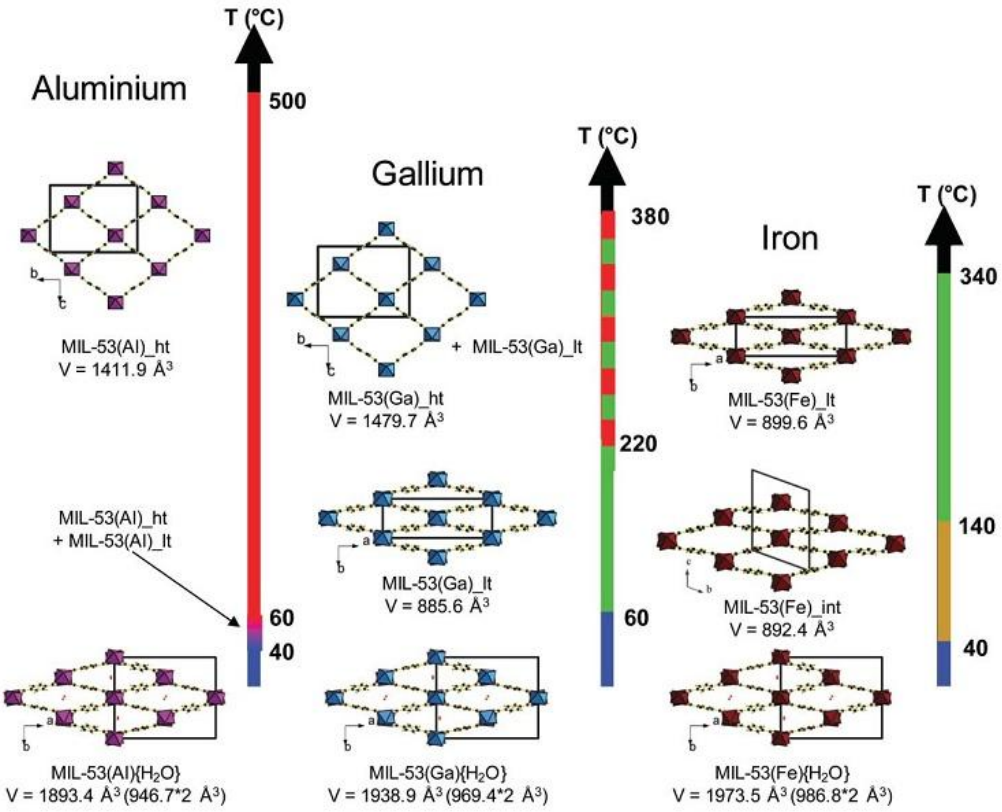

Figure 1.13 "Evolution of the different channel openings in the different members of MIL-53 (Al, Ga or Fe) as a function of temperature above RT (blue: hydrated form, green: low temperature form of the anhydrous solid; red: high temperature form; orange: intermediate form)."[51]

It is believed that the structural changes upon hydration and dehydration in the framework are due to host-guest, guest-guest and also host-host interactions. The reasons for the differences in behaviours are unclear. Férey[117] has proposed that the iron framework contracts upon heating (in direct contrast to the chromium and aluminium structures) due to stronger π-π interactions between the phenyl rings within the framework. The larger number of unpaired d electrons in Fe^{III} (d^5) compared to Cr^{III} (d^3) were thought also to contribute to the differences. However, neither statement has been confirmed experimentally.

Computational studies on the various forms of MIL-53 have shown that the different phases observed experimentally, upon exposure to various stimuli such as temperature and guest adsorption, can be rationalised by considering the thermodynamics of each

phase of the structure. These studies have shown that the MIL-53 structure will adopt the most energetically favourable phase; the fully-open phase was shown to be most favourable for dehydrated MIL-53(Cr)[68, 118, 119] and MIL-53(Al)[120] whereas contracted forms of the structure were shown to be most energetically favourable for dehydrated MIL-53(Sc).[121] Theories, based on experimental and computational methods, have been proposed that describe the various factors that can induce framework flexibility. Liu *et al.*[122] used inelastic neutron scattering studies to suggest that low energy librational motions of the 1,4-benzenedicarboxylate linker are the driving force behind the opening/closing of the structure. These librational motions affect the disorder of the system; as the framework pores open the amplitude of these motions increases, which in turn increases the entropy within the system. The introduction of guest molecules results in both entropic and enthalpic contributions to the free energy of the system, where the enthalpic contributions will be dependent upon the range of possible interactions that can occur *e.g.* guest-guest, guest-host and host-host.[86] Experimental[108] and computational[120] studies performed for the adsorption of CO_2 and CH_4 by MIL-53(Al) showed that if the host framework exhibits a strong affinity towards the guest molecules then it is energetically more favourable for the framework to contract in the presence of the adsorbate at low pressures before reopening at higher pressures. However, if a strong interaction between host and guest is not present then this contraction at low pressure is not seen. A computational study by Ortiz *et al.*[123] suggests that the flexibility of MIL-53(Al) can be characterised by highly anisotropic elastic properties (Young's and shear moduli and Poisson's ratios) and directions of negative compressibility. However, these studies are not able to show why the various metal cations affect the breathing of the MIL-53 framework differently; this phenomenon is still not fully understood.

1.6.1.2 Interactions with Guest Molecules

The various analogues of MIL-53 expand or contract upon the removal of water molecules, as described above. These frameworks have also been shown to expand and contract in response to different guest molecules. An additional monoclinic, *C2/c*, phase has been observed during the adsorption of particular guest molecules and has a unit cell volume between the hydrated and fully-open phases of approximately 1200 $Å^3$. This phase has been seen for lutidine, pyridine and xylene.[115, 124]

Figure 1.14 shows the crystal structures of representative expanded forms of MIL-53 with the unit cells depicted. This figure highlights that the volume of each phase can be directly compared as each unit cell contains an equivalent number of atoms, with the exception of hydrated MIL-53 (Figure 1.14a) which crystallises with a superstructure where the unit cell contains double the equivalent number of atoms.

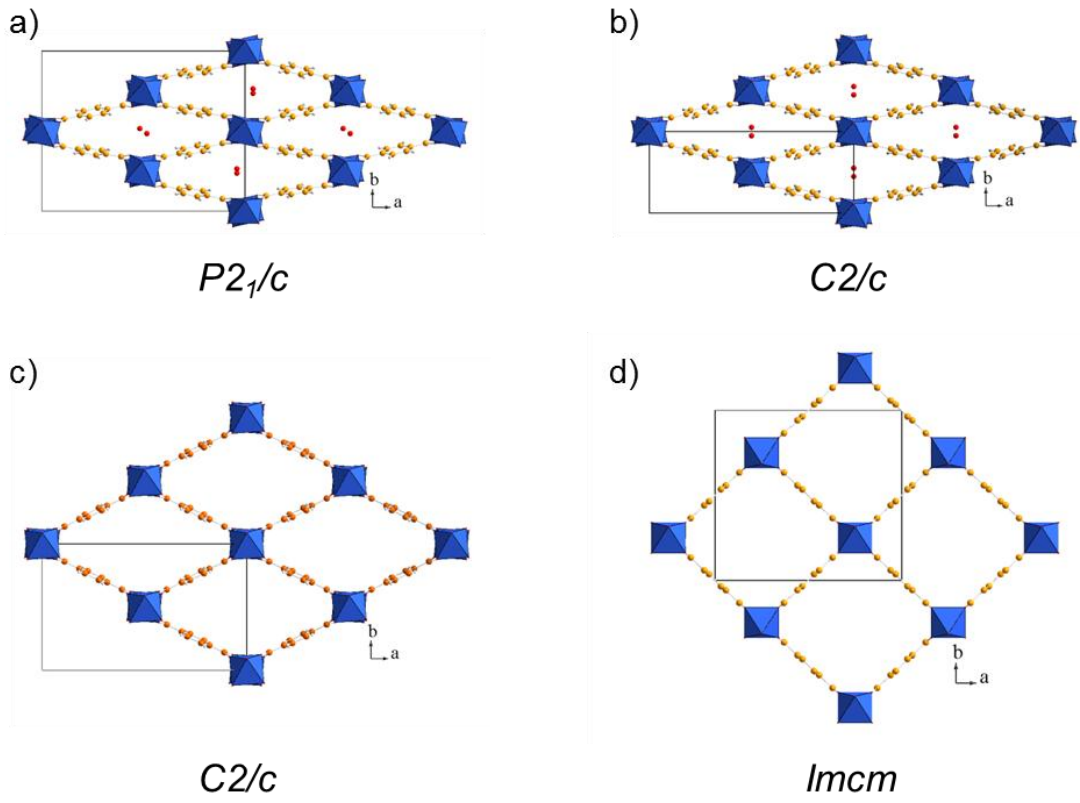

Figure 1.14: The structure of MIL-53 in various expanded forms showing the relationship of unit cell volume to the framework topology.(a) Closed $P2_1/c$ form seen for hydrated MIL-53 (b) closed C2/c form seen for partially fluorinated hydrated MIL-53(Fe,F,OH), described in Section 1.6.1.3, (c) partially open C2/c form seen for MIL-53 (Fe,F,OH) [pyridine] and (d) fully open Imcm form seen for dehydrated MIL-53(Cr/Al). Guest molecules are omitted from c) and d).

The positions of some guest molecules inside the pores of the MIL-53 frameworks have been determined using high-resolution XRD. Location of the guest molecules is only possible when they form an ordered array inside the pores. The strength of the interactions between the guest molecules and the host framework can be predicted from their relative positions. Figure 1.15 shows four examples where it was possible for the guest molecules to be located. The co-adsorption of lutidine and water was seen for the partially fluorinated MIL-53(Fe) framework. The crystal structure shows that the framework is fully-open with the orthorhombic, *Imcm*, structure and the relative distances indicate that the water molecules are hydrogen-bonded to the μ^2OH groups along the metal oxide chains and the lutidine molecules are hydrogen bonded to the

water molecules.[124] A monoclinic phase was observed during heating of the lutidine/water phase which corresponds to the loss of the water molecules. Due to the bulky methyl groups on either side of the nitrogen atom lutidine is unable to hydrogen-bond to the framework OH groups. Therefore, lutidine adopts an orientation which was concluded to be the consequence of space-filling, as the distances between molecules were considered too great for any interactions to occur.[124] It was also possible to locate pyridine inside the pores of MIL-53(Fe)(OH,F) and Figure 1.15c shows that the guest molecules are hydrogen bonded to the framework OH groups with the distances between pyridine rings found to be indicative of π-π interactions.[124] The fourth example shown below is the result of suspending hydrated MIL-53(Cr) in water. The material adsorbs additional water molecules, which were shown to form a highly ordered hydrogen-bonded array inside the pores, this phase has the fully-open, *Imcm*, structure and was described as superhydrated MIL-53(Cr).[125]

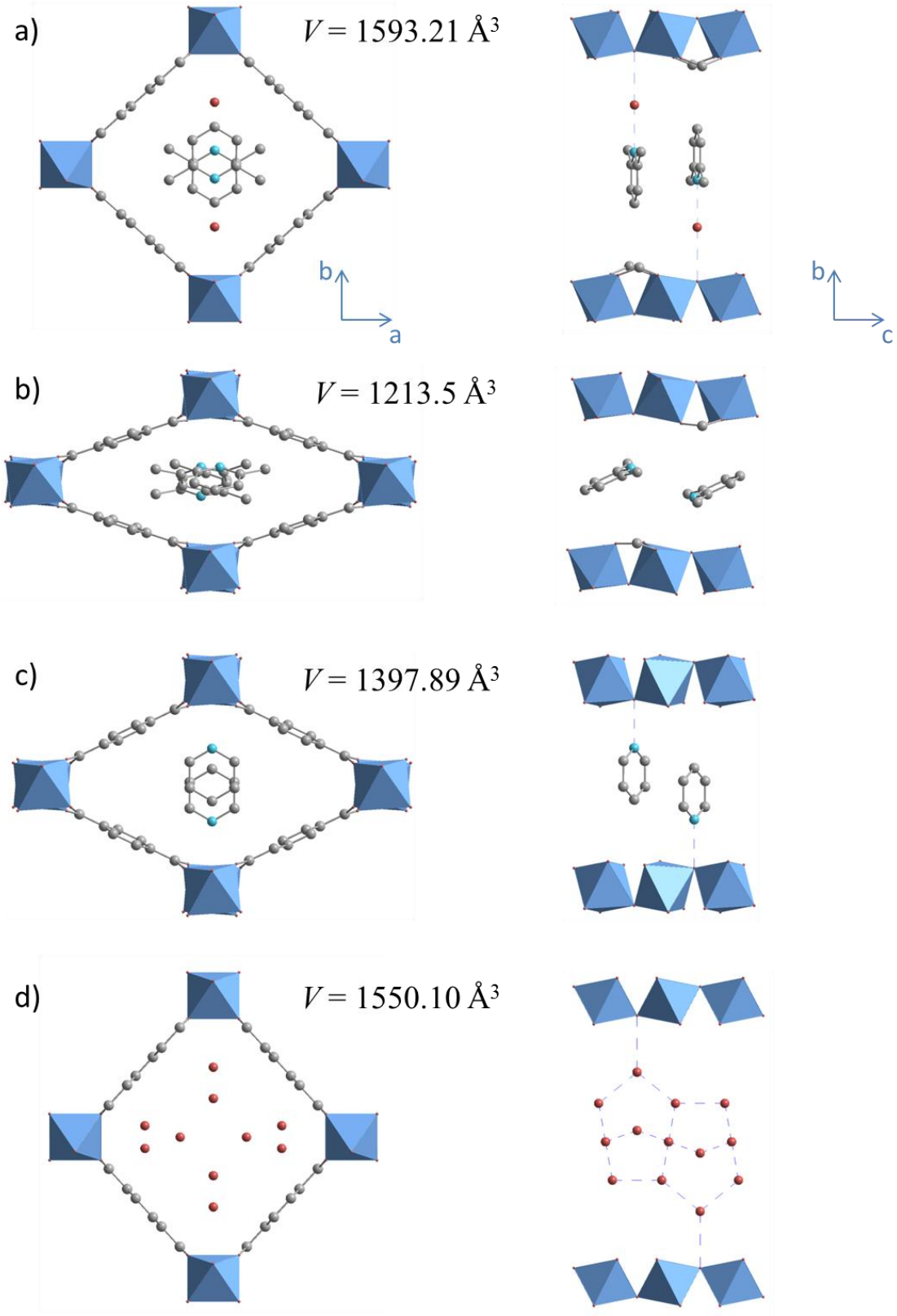

Figure 1.15: Crystal structures of a) MIL-53(Fe)(OH,F) and lutidine+H_2O, b) MIL-53(Fe)(OH,F) and lutidine, c) MIL-53(Fe)(OH,F) and pyridine, and d) MIL-53(Cr) and H_2O (superhydrated)

1.6.1.3 Modifications to the MIL-53 framework

As described in Section 1.5, modification pre- or post-synthesis can be used to tune the properties of metal-organic frameworks. Various types of modification have been investigated to improve the properties of the different MIL-53 analogues for various applications.

1.6.1.3.1 Fluorinated MIL-53

Liu *et al.*[126] reported the synthesis of a MIL-53(Al) type material where all the μ^2-OH groups were replaced with μ^2-F, which was achieved by reaction of the AlF_3 salt with H_2bdc in DMF. This material was found not to absorb water at ambient conditions as is seen for MIL-53(Al) and the framework did not exhibit similarly large breathing effects upon guest adsorption. The synthesis of a partially fluorinated form of MIL-53(Fe) has also been published.[127] This was accomplished by including aqueous hydrofluoric acid at the synthesis stage. Fluoride replaces some of the μ^2-OH groups in the framework, but the degree of replacement is hard to determine using X-ray diffraction techniques due to the similarities between the electron density of F^- and OH^-. The fluorine atoms in the structure have been shown to affect the properties of the framework. They are believed to make the pores of the framework more hydrophobic, as was seen by Liu *et al.* for the AlF material, and they have been shown to affect the flexibility of the framework. Walton *et al.*[128] reported that in response to various alcohol guest molecules the hydroxylated material expanded straight from the contracted hydrated phase to a fully-expanded phase whereas initial studies of the partially fluorinated material showed that the framework expanded via a transient crystalline phase. Further investigations into this transient crystalline phase are presented in this thesis (Chapter 3).

1.6.1.3.2 Mixed-Metal MIL-53

Mixed metal and mixed valent analogues of MIL-53 have been successfully synthesised. Nouar *et al.*[129] reported that a mixed Fe^{3+}/Cr^{3+} MIL-53 framework could be synthesised and diffraction studies determined that the hydrated room temperature phase gave the same monoclinic, *C2/c*, structure as both the parent frameworks. However upon heating, the framework initially contracted to a volume similar to the dehydrated MIL-53(Fe) material before opening, upon further heating, to a volume similar to the dehydrated MIL-53(Cr). CO_2 adsorption isotherms were also performed which indicated that the step in the isotherm, which indicates the opening of the framework, occurred at a pressure between that recorded for the two parent frameworks. This report concludes that the behaviour of MIL-53 towards the adsorption of guest molecules can be successfully tuned.

Breeze *et al.*[130] reported the synthesis of iron-vanadium analogues of MIL-53 which display varying degrees of flexibility, dependent upon the ratio of Fe/V. They reported materials that were partially fluorinated, as seen for MIL-53(Fe) above, with the empirical formula $(Fe,V^{III})(bdc)(OH,F)$. They found that Fe-rich analogues could reversibly expand upon thermal dehydration, which is in contrast to the pure Fe materials that contract. However, the Fe:V 1:1 materials were shown to expand irreversibly after thermal treatment, which was concluded to be due to domains of V^{III} oxidising to V^{IV}. This is comparable to the pure V^{III} material, MIL-47, which is oxidised to V^{IV} upon calcination. Upon calcination the framework μ^2OH^- groups are reduced to μ^2O^{2-} groups which has the effect of removing the flexibility of the framework.[131] This report shows that the breathing behaviour of MIL-53 can be affected dramatically by cation mixing.

Medina *et al.*[132] reported the synthesis of a mixed-valent MIL-53 framework. The framework contains a regular distribution of Fe^{III} and Fe^{II} cations where the charge is balanced by DMA^+ molecules. This structure has the same topology as MIL-53(Fe^{III}) but the hydrated phase at room temperature has a more expanded framework due to the occluded DMA^+ guest molecules. It was shown that upon heating, the DMA^+ molecules are removed from the framework as the Fe^{II} cations are oxidised to Fe^{III} to give the dehydrated MIL-53(Fe^{III}) material.

1.6.1.3.3 Ligand Modified MIL-53

Presented here are two reports of pre-synthetically modified MIL-53(Al) which have been subsequently post-synthetically modified. Reimer *et al.*[133] reported that the pre-synthetically modified MIL-53(Al)-COOH, where an additional carboxylate group has been substituted onto the benzene ring of the organic linker, could be post-synthetically modified using thermal treatment. They used IR studies to show that upon heating to 400 °C the condensation of neighbouring –COOH groups occurred. The result was the formation of cyclic anhydride functionalities. No adsorption studies were reported for this new material. Ahnfeldt *et al.*[47] investigated the post-synthetic modification of the amino ($–NH_2$) modified MIL-53(Al). The reaction of MIL-53(Al)–NH_2 with formic acid resulted in the corresponding amide functionalised framework, MIL-53(Al)–NHCOH. Their work shows that the functionality of the framework ligands can be modified to change the properties of the material.

1.6.2 Characterisation Techniques

A number of different applications have been proposed for the family of MIL-53 frameworks such as molecular storage,[84] molecular separation[90, 134] molecular sensors[135] and catalysis.[136] Work published on the use of the MIL-53 frameworks as adsorbents is

extensive and a range of characterisation techniques have been used to investigate these materials, therefore, only a few of the most relevant studies are summarised below. The details of the techniques used in this work are described in Chapter 2.

1.6.2.1 Studies using Adsorption Isotherms and X-ray Diffraction Techniques

Owing to the interest in the porosity of metal-organic frameworks, adsorption studies are commonly used to quantify the superiority of these frameworks over similar materials in adsorbing various guest molecules. These studies are used to investigate the number of guest molecules that are adsorbed by materials as a function of pressure (gas phase) or concentration (liquid phase). X-ray diffraction techniques have also been used widely due to the crystalline nature of the MIL-53 frameworks. Large changes in the unit cell parameters of these materials are observed upon the addition/removal of guest molecules. The crystallinity of the materials is retained throughout these transitions therefore the process can be studied *ex situ* or followed *in situ* using X-ray diffraction techniques.

Gas phase adsorption isotherms have been used to study various small molecules such as H_2,[70] CO_2,[108, 137] CH_4,[90, 108, 137] H_2S[80] and xylene isomers.[92] These studies have shown that the flexibility of the MIL-53 frameworks gives rise to a unique isotherm profile where a step corresponds to a change in the pore volume. This technique also provides quantitative results which can be used to compare the performance of the MIL-53 analogues.

Ex situ diffraction techniques, such as high-resolution XRD, have been used to study the change in unit cell parameters after the addition of liquid or gas phase guest molecules. Solutions or vapours of guest molecules are added to glass capillaries containing MIL-53 powder and the XRD patterns are recorded. This technique is used to obtain the unit

cell parameters for various phases of MIL-53. If high-resolution data is collected then the structures of the different guest-host phases can be solved *ab initio* which also allows the position of the guest molecules to be determined. This technique has been used for pyridine and lutidine in MIL-53(Fe),[124] xylene isomers in MIL-53(Fe),[138] and excess water in MIL-53(Cr).[125]

In situ XRD techniques have also been used to investigate the expansion and contraction of MIL-53. Serre *et al*.[52] reported *in situ* thermo-diffraction of MIL-53(Cr) showing that the expansion of the framework in response to dehydration could be followed. It was observed in this study that the expansion from the hydrated phase to the dehydrated phase was not due to a gradual opening of the pores but that in a defined temperature range the contracted pores sporadically open until all the pores are fully-open. This is confirmed by the observation that the Bragg peaks of the initial phase gradually decrease as the Bragg peaks of the final phase gradually increase. The two phases co-exist rather than there being a gradual transformation from on to the other.

Similar techniques have been used to follow the uptake of liquid and gas phase guest molecules. Serre *et al.*[109] reported the results for the *in situ* adsorption of CO_2 gas at various pressures in MIL-53(Cr) and their results showed that the framework reversibly expanded to give the *Imcm* structure at high pressures but at low pressures the framework had a structure that resembled hydrated MIL-53(Cr) with *C2/c* symmetry. Llewellyn *et al.*[115] reported that a similar method using variable pressure was used to study the uptake of C1-C4 hydrocarbons in dehydrated MIL-53(Cr). This report found that at higher pressures (e.g. > 1 bar) all the guest molecules that were studied forced the framework into the fully-open *Imcm* structure. It was also seen that ethane, propane

and butane showed evidence for a contraction of the pores to a half-open phase (~1200 Å^3, *C2/c*) at lower pressures.

Energy dispersive XRD techniques have been used to perform similar *in situ* studies in the liquid phase. Millange *et al.*[124] followed the uptake of solutions of pyridine, lutidine and a mixture of pyridine/lutidine in water using partially fluorinated MIL-53(Fe). The results show that the expansion of the framework in response to both guests, when studied individually, occurred in a single step. However, when the mixture was studied, it revealed that both molecules were taken up simultaneously before the pyridine was displaced in favour of the lutidine. *In situ* thermodiffraction results showed that the fully-open lutidine phase contracts via a half-open phase. Studies of the uptake of the xylene isomers in the liquid phase using partially fluorinated MIL-53(Fe) were performed by El Osta *et al.*[138] These results also show that the guest molecules were taken up in one step and *in situ* thermodiffraction of the fully-loaded samples reveals that the framework contracts via a half-open phase.

1.7 Aims of this work

The objectives of this thesis are to use various X-ray diffraction techniques and other complementary studies to investigate the adsorption behaviour of MIL-53 and MIL-53-type materials in both the liquid and gas phases. MIL-53 exhibits a large expansion and contraction upon the adsorption of different guest molecules, although many adsorption studies have been reported for MIL-53 the work presented in this thesis intends to follow the structural changes of the framework using *in situ* diffraction and spectroscopic techniques to understand better the cause and nature of these transitions. Modifications to MOF frameworks have been shown to be beneficial for improving the usefulness of these materials and the work presented here aims to investigate the effect

of pre-synthetic modification upon the adsorption behaviour of MIL-53. The synthesis and characterisation of some new MIL-53-type materials will explore the inherent flexibility of the diamond-shape pores and the effect of ligand modification upon the topology of the final product will be investigated.

Some of the work presented in this thesis was performed as part of the MACADEMIA project. MACADEMIA, MOFs as Catalysts and Adsorbents: Discovery and Engineering of Materials for Industrial Applications, was part of the European Community's Seventh Framework Programme (FP7/2007-2013). This project aimed to bring together academic research and industrial experience to develop the use of MOFs for industrial applications. The Walton research group at the University of Warwick was responsible for the synthesis and characterisation of new MOF materials. New MOF materials synthesised by the Stock research group at Christian-Albrechts-Universitaet Kiel were characterised at the University of Warwick using X-ray diffraction techniques; the results of this study are presented in this thesis. New MOFs have also been synthesised as part of this work, some of which have been characterised by other members of the MACADEMIA project, collaborations have included; computational studies at the University of Edinburgh and adsorption studies performed at the Aix-Marseille Université, France, the Faculté Polytechnique Mons, Belgium and the Katholieke Universiteit Leuven, Belgium. The results of these studies have been summarised where relevant.

1.8 References

1. S. T. Meek, J. A. Greathouse and M. D. Allendorf, *Adv. Mater.*, 2011, **23**, 249-267.

2. D. Farrusseng, S. Aguado and C. Pinel, *Angew. Chem. Int. Ed.*, 2009, **48**, 7502-7513.

3. S. Kitagawa, R. Kitaura and S.-i. Noro, *Angew. Chem. Int. Ed.*, 2004, **43**, 2334-2375.

4. M. D. Allendorf, C. A. Bauer, R. K. Bhakta and R. J. T. Houk, *Chem. Soc. Rev.*, 2009, **38**, 1330-1352.

5. G. Ferey, *Chem. Soc. Rev.*, 2008, **37**, 191-214.

6. S. L. James, *Chem. Soc. Rev.*, 2003, **32**, 276-288.

7. M. Kurmoo, *Chem. Soc. Rev.*, 2009, **38**, 1353-1379.

8. J.-R. Li, R. J. Kuppler and H.-C. Zhou, *Chem. Soc. Rev.*, 2009, **38**, 1477-1504.

9. L. J. Murray, M. Dinca and J. R. Long, *Chem. Soc. Rev.*, 2009, **38**, 1294-1314.

10. D. Zacher, O. Shekhah, C. Woll and R. A. Fischer, *Chem. Soc. Rev.*, 2009, **38**, 1418-1429.

11. J. L. C. Rowsell and O. M. Yaghi, *Microporous Mesoporous Mater.*, 2004, **73**, 3-14.

12. S. R. Batten, N. R. Champness, X. M. Chen, J. Garcia-Martinez, S. Kitagawa, L. Ohrstrom, M. O'Keeffe, M. P. Suh and J. Reedijk, *IUPAC Provisional Recommendations*, 2012.

13. A. K. Cheetham, C. N. R. Rao and R. K. Feller, *Chem. Commun.*, 2006, **0**, 4780-4795.

14. Y.-L. Fu, J.-L. Ren and S. W. Ng, *Acta Crystallogr. Sect. Sect. E: Struct. Rep. Online*, 2004, **60**, m1507-m1509.

15. K. A. Hofmann and F. Küspert, *Z. Anorg. Chem*, 1897, **15**, 204-207.

16. J. H. Rayner and H. M. Powell, *J. Chem. Soc.*, 1952, **0**, 319-328.

17. B. F. Hoskins and R. Robson, *JACS*, 1990, **112**, 1546-1554.

18. O. M. Yaghi, G. Li and H. Li, *Nature*, 1995, **378**, 703-706.

19. N. L. Rosi, M. Eddaoudi, J. Kim, M. O'Keeffe and O. M. Yaghi, *CrystEngComm*, 2002, **4**, 401-404.

20. J. Kim, B. Chen, T. M. Reineke, H. Li, M. Eddaoudi, D. B. Moler, M. O'Keeffe and O. M. Yaghi, *JACS*, 2001, **123**, 8239-8247.

21. J. H. Cavka, S. Jakobsen, U. Olsbye, N. Guillou, C. Lamberti, S. Bordiga and K. P. Lillerud, *JACS*, 2008, **130**, 13850-13851.

22. M. J. Rosseinsky, *Microporous Mesoporous Mater.*, 2004, **73**, 15-30.

23. C. N. R. Rao, S. Natarajan and R. Vaidhyanathan, *Angew. Chem. Int. Ed.*, 2004, **43**, 1466-1496.

24. M.-X. Li, Z.-X. Miao, M. Shao, S.-W. Liang and S.-R. Zhu, *Inorg. Chem.*, 2008, **47**, 4481-4489.

25. M. Plabst and T. Bein, *Inorg. Chem.*, 2009, **48**, 4331-4341.

26. M. V. Vasylyev, E. J. Wachtel, R. Popovitz-Biro and R. Neumann, *Chem. Eur. J.*, 2006, **12**, 3507-3514.

27. H. J. Choi, M. Dinca, A. Dailly and J. R. Long, *Energy Environ. Sci.*, 2010, **3**, 117-123.

28. F. Nouar, J. F. Eubank, T. Bousquet, L. Wojtas, M. J. Zaworotko and M. Eddaoudi, *JACS*, 2008, **130**, 1833-1835.

29. L. Sun, L. Ma, J.-B. Cai, L. Liang and H. Deng, *CrystEngComm*, 2012, **14**, 890-898.

30. M. Eddaoudi, J. Kim, N. Rosi, D. Vodak, J. Wachter, M. O'Keeffe and O. M. Yaghi, *Science*, 2002, **295**, 469-472.

31. H. Chun, D. N. Dybtsev, H. Kim and K. Kim, *Chem. Eur. J.*, 2005, **11**, 3521-3529.

32. A. Dailly, J. J. Vajo and C. C. Ahn, *J. Phys. Chem. B*, 2006, **110**, 1099-1101.

33. K. Gedrich, I. Senkovska, I. A. Baburin, U. Mueller, O. Trapp and S. Kaskel, *Inorg. Chem.*, 2010.

34. C. G. Carson, K. Hardcastle, J. Schwartz, X. Liu, C. Hoffmann, R. A. Gerhardt and R. Tannenbaum, *Eur. J. Inorg. Chem.*, 2009, **2009**, 2338-2343.

35. Y. Cui, Q. Gao, C.-Y. Zhang and Y.-B. Xie, *Acta Crystallogr. Sect. Sect. E: Struct. Rep. Online*, 2009, **65**, m850.

36. B. O. Patrick, C. L. Stevens, A. Storr and R. C. Thompson, *Polyhedron*, 2005, **24**, 2242-2249.

37. P. Horcajada, S. Surble, C. Serre, D.-Y. Hong, Y.-K. Seo, J.-S. Chang, J.-M. Greneche, I. Margiolaki and G. Ferey, *Chem. Commun.*, 2007, **0**, 2820-2822.

38. M. Märcz, R. E. Johnsen, P. D. C. Dietzel and H. Fjellvåg, *Microporous Mesoporous Mater.*

39. A. Mesbah, R. Sibille, T. Mazet, B. Malaman, S. Lebegue and M. Francois, *J. Mater. Chem.*, 2010, **20**, 9386-9391.

40. W. Zhou, *The Chemical Record*, 2010, **10**, 200-204.

41. C. Serre, C. Mellot-Draznieks, S. Surble, N. Audebrand, Y. Filinchuk and G. Férey, *Science*, 2007, **315**, 1828-1831.

42. A. C. Sudik, A. P. Côté and O. M. Yaghi, *Inorg. Chem.*, 2005, **44**, 2998-3000.

43. S. S.-Y. Chui, S. M.-F. Lo, J. P. H. Charmant, A. G. Orpen and I. D. Williams, *Science*, 1999, **283**, 1148-1150.

44. B. Chen, M. Eddaoudi, S. T. Hyde, M. O'Keeffe and O. M. Yaghi, *Science*, 2001, **291**, 1021-1023.

45. S. Qiu and G. Zhu, *Coord. Chem. Rev.*, 2009, **253**, 2891-2911.

46. C. Daiguebonne, N. Kerbellec, O. Guillou, J.-C. Bünzli, F. Gumy, L. Catala, T. Mallah, N. Audebrand, Y. Gérault, K. Bernot and G. Calvez, *Inorg. Chem.*, 2008, **47**, 3700-3708.

47. T. Ahnfeldt, N. Guillou, D. Gunzelmann, I. Margiolaki, T. Loiseau, G. Férey, J. Senker and N. Stock, *Angew. Chem. Int. Ed.*, 2009, **48**, 5163-5166.

48. D. Liu, Y. Liu, G. Xu, G. Li, Y. Yu and C. Wang, *Eur. J. Inorg. Chem.*, 2012, **2012**, 4413-4417.

49. F. Millange, M. I. Medina, N. Guillou, G. Férey, K. M. Golden and R. I. Walton, *Angew. Chem. Int. Ed.*, 2010, **49**, 763-766.

50. C. Yang, X. P. Wang and M. A. Omary, *Angew. Chem. Int. Ed.*, 2009, **48**, 2500-2505.

51. C. Volkringer, T. Loiseau, N. Guillou, G. Férey, E. Elkaim and A. Vimont, *Dalton Transactions*, 2009, 2241-2249.

52. C. Serre, F. Millange, C. Thouvenot, M. Nogues, G. Marsolier, D. Louer and G. Férey, *JACS*, 2002, **124**, 13519-13526.

53. C. Mellot-Draznieks, C. Serre, S. Surble, N. Audebrand and G. Ferey, *JACS*, 2005, **127**, 16273-16278.

54. F. Millange, C. Serre and G. Férey, *Chem. Commun.*, 2002, 822-823.

55. N. Khosrovani and A. W. Sleight, *J. Solid State Chem.*, 1996, **121**, 2-11.

56. G. Férey and J. Pannetier, *Eur. J. Solid State Inorg. Chem.*, 1994, **31**, 697.

57. R. H. Mitchell, *Perovskites Modern and Ancient*, Almaz Press Inc., Thunderbay, Canada, 2002.

58. T. Loiseau, C. Serre, C. Huguenard, G. Fink, F. Taulelle, M. Henry, T. Bataille and G. Férey, *Chem. Eur. J.*, 2004, **10**, 1373-1382.

59. G. Férey, *Hybrid porous solids* in *Studies in Surface Science and Catalysis*, eds. J. Čejka, H. Van Bekkum, A. Corma and F. Schüth, Elsevier, 2007, vol. 168, pp. 327-374.

60. G. K. Kole and J. J. Vittal, *Chem. Soc. Rev.*, 2013.

61. L. E. Kreno, K. Leong, O. K. Farha, M. Allendorf, R. P. Van Duyne and J. T. Hupp, *Chem. Rev.*, 2011, **112**, 1105-1125.

62. J. Lee, O. K. Farha, J. Roberts, K. A. Scheidt, S. T. Nguyen and J. T. Hupp, *Chem. Soc. Rev.*, 2009, **38**, 1450-1459.

63. J. Liu, P. K. Thallapally, B. P. McGrail, D. R. Brown and J. Liu, *Chem. Soc. Rev.*, 2012, **41**.

64. M. Meilikhov, K. Yusenko, D. Esken, S. Turner, G. Van Tendeloo and R. A. Fischer, *Eur. J. Inorg. Chem.*, 2010, **2010**, 3701-3714.

65. J. Sculley, D. Yuan and H.-C. Zhou, *Energy Environ. Sci.*, 2011, **4**, 2721-2735.

66. O. Shekhah, J. Liu, R. A. Fischer and C. Woll, *Chem. Soc. Rev.*, 2011, **40**, 1081-1106.

67. C. Pan, J. Nan, X. Dong, X.-M. Ren and W. Jin, *JACS*, 2011, **133**, 12330-12333.

68. F. Salles, A. Ghoufi, G. Maurin, R. G. Bell, C. Mellot-Draznieks and G. Ferey, *Angew. Chem. Int. Ed.*, 2008, **47**, 8487-8491.

69. B. Xiao, P. J. Byrne, P. S. Wheatley, D. S. Wragg, X. B. Zhao, A. J. Fletcher, K. M. Thomas, L. Peters, J. S. O. Evans, J. E. Warren, W. Z. Zhou and R. E. Morris, *Nature Chem.*, 2009, **1**, 289-294.

70. G. Férey, M. Latroche, C. Serre, F. Millange, T. Loiseau and A. Percheron-Guegan, *Chem. Commun.*, 2003, 2976-2977.

71. P. S. Barcia, L. Bastin, E. J. Hurtado, J. A. C. Silva, A. E. Rodrigues and B. L. Chen, *Sep. Sci. Technol.*, 2008, **43**, 3494-3521.

72. N. L. Rosi, J. Eckert, M. Eddaoudi, D. T. Vodak, J. Kim, M. O'Keeffe and O. M. Yaghi, *Science*, 2003, **300**, 1127-1129.

73. J. L. C. Rowsell, A. R. Millward, K. S. Park and O. M. Yaghi, *JACS*, 2004, **126**, 5666-5667.

74. S. Ma and H.-C. Zhou, *Chem. Commun.*, 2010, **46**, 44-53.

75. J. L. C. Rowsell and O. M. Yaghi, *Angew. Chem. Int. Ed.*, 2005, **44**, 4670-4679.

76. X. Lin, J. Jia, X. Zhao, K. M. Thomas, A. J. Blake, G. S. Walker, N. R. Champness, P. Hubberstey and M. Schröder, *Angew. Chem. Int. Ed.*, 2006, **45**, 7358-7364.

77. P. D. C. Dietzel, P. A. Georgiev, J. Eckert, R. Blom, T. Strassle and T. Unruh, *Chem. Commun.*, 2010, **46**, 4962-4964.

78. J. G. Vitillo, L. Regli, S. Chavan, G. Ricchiardi, G. Spoto, P. D. C. Dietzel, S. Bordiga and A. Zecchina, *JACS*, 2008, **130**, 8386-8396.

79. X. Lin, I. Telepeni, A. J. Blake, A. Dailly, C. M. Brown, J. M. Simmons, M. Zoppi, G. S. Walker, K. M. Thomas, T. J. Mays, P. Hubberstey, N. R. Champness and M. Schröder, *JACS*, 2009, **131**, 2159-2171.

80. L. Hamon, C. Serre, T. Devic, T. Loiseau, F. Millange, G. Férey and G. D. Weireld, *JACS*, 2009, **131**, 8775-8777.

81. K. A. Cychosz, A. G. Wong-Foy and A. J. Matzger, *JACS*, 2008, **130**, 6938-6939.

82. N. A. Khan, J. W. Jun, J. H. Jeong and S. H. Jhung, *Chem. Commun.*, 2011, **47**, 1306-1308.

83. D. Britt, D. Tranchemontagne and O. M. Yaghi, *Proceedings of the National Academy of Sciences*, 2008, **105**, 11623-11627.

84. P. Horcajada, C. Serre, G. Maurin, N. A. Ramsahye, F. Balas, M. Vallet-Regí, M. Sebban, F. Taulelle and G. Férey, *JACS*, 2008, **130**, 6774-6780.

85. J. Gee, J. Chung, S. Nair and D. S. Sholl, *J. Phys. Chem. C*, 2013.

86. S. Bourrelly, B. Moulin, A. Rivera, G. Maurin, S. Devautour-Vinot, C. Serre, T. Devic, P. Horcajada, A. Vimont, G. Clet, M. Daturi, J.-C. Lavalley, S. Loera-Serna, R. Denoyel, P. L. Llewellyn and G. Férey, *JACS*, 2010, **132**, 9488-9498.

87. S. Cavenati, C. A. Grande, A. E. Rodrigues, C. Kiener and U. Müller, *Ind. Eng. Chem. Res.*, 2008, **47**, 6333-6335.

88. S. R. Caskey, A. G. Wong-Foy and A. J. Matzger, *JACS*, 2008, **130**, 10870-10871.

89. A. R. Millward and O. M. Yaghi, *JACS*, 2005, **127**, 17998-17999.

90. V. Finsy, L. Ma, L. Alaerts, D. E. De Vos, G. V. Baron and J. F. M. Denayer, *Microporous Mesoporous Mater.*, 2009, **120**, 221-227.

91. J. Liu, J. Tian, P. K. Thallapally and B. P. McGrail, *J. Phys. Chem. C*, 2012, **116**, 9575-9581.

92. V. Finsy, C. E. A. Kirschhock, G. Vedts, M. Maes, L. Alaerts, D. E. De Vos, G. V. Baron and J. F. M. Denayer, *Chem. Eur. J.*, 2009, **15**, 7724-7731.

93. Z.-Y. Gu, D.-Q. Jiang, H.-F. Wang, X.-Y. Cui and X.-P. Yan, *J. Phys. Chem. C*, 2009, **114**, 311-316.

94. M. D. Allendorf, R. J. T. Houk, L. Andruszkiewicz, A. A. Talin, J. Pikarsky, A. Choudhury, K. A. Gall and P. J. Hesketh, *JACS*, 2008, **130**, 14404-14405.

95. Z. Xie, L. Ma, K. E. deKrafft, A. Jin and W. Lin, *JACS*, 2009, **132**, 922-923.

96. W. Kleist, M. Maciejewski and A. Baiker, *Thermochimica Acta*, 2010, **499**, 71-78.

97. S. Bernt, V. Guillerm, C. Serre and N. Stock, *Chem. Commun.*, 2011, **47**, 2838-2840.

98. S. Couck, J. F. M. Denayer, G. V. Baron, T. Rémy, J. Gascon and F. Kapteijn, *JACS*, 2009, **131**, 6326-6327.

99. C. Zlotea, D. Phanon, M. Mazaj, D. Heurtaux, V. Guillerm, C. Serre, P. Horcajada, T. Devic, E. Magnier, F. Cuevas, G. Ferey, P. L. Llewellyn and M. Latroche, *Dalton Transactions*, 2011, **40**, 4879-4881.

100. O. Kozachuk, K. Khaletskaya, M. Halbherr, A. Bétard, M. Meilikhov, R. W. Seidel, B. Jee, A. Pöppl and R. A. Fischer, *Eur. J. Inorg. Chem.*, 2012, **2012**, 1688-1695.

101. Y.-Q. Wang, Q. Yue, Y. Qi, K. Wang, Q. Sun and E.-Q. Gao, *Inorg. Chem.*, 2013, **52**, 4259-4268.

102. K. K. Tanabe and S. M. Cohen, *Chem. Soc. Rev.*, 2011, **40**, 498-519.

103. Z. Wang and S. M. Cohen, *Chem. Soc. Rev.*, 2009, **38**, 1315-1329.

104. G. Férey, C. Serre, C. Mellot-Draznieks, F. Millange, S. Surblé, J. Dutour and I. Margiolaki, *Angew. Chem. Int. Ed.*, 2004, **43**, 6296-6301.

105. Y. K. Hwang, D.-Y. Hong, J.-S. Chang, S. H. Jhung, Y.-K. Seo, J. Kim, A. Vimont, M. Daturi, C. Serre and G. Férey, *Angew. Chem. Int. Ed.*, 2008, **47**, 4144-4148.

106. Z. Wang, K. K. Tanabe and S. M. Cohen, *Inorg. Chem.*, 2009, **48**, 296-306.

107. Z. Wang and S. M. Cohen, *JACS*, 2007, **129**, 12368-12369.

108. S. Bourrelly, P. L. Llewellyn, C. Serre, F. Millange, T. Loiseau and G. Ferey, *JACS*, 2005, **127**, 13519-13521.

109. C. Serre, S. Bourrelly, A. Vimont, N. A. Ramsahye, G. Maurin, P. L. Llewellyn, M. Daturi, Y. Filinchuk, O. Leynaud, P. Barnes and G. Férey, *Adv. Mater.*, 2007, **19**, 2246-2251.

110. E. V. Anokhina, M. Vougo-Zanda, X. Wang and A. J. Jacobson, *JACS*, 2005, **127**, 15000-15001.

111. F. Millange, N. Guillou, R. I. Walton, J. M. Greneche, I. Margiolaki and G. Férey, *Chem. Commun.*, 2008, 4732-4734.

112. H. Leclerc, T. Devic, S. Devautour-Vinot, P. Bazin, N. Audebrand, G. Férey, M. Daturi, A. Vimont and G. Clet, *J. Phys. Chem. C*, 2011, **115**, 19828-19840.

113. J. P. S. Mowat, S. R. Miller, A. M. Z. Slawin, V. R. Seymour, S. E. Ashbrook and P. A. Wright, *Microporous Mesoporous Mater.*, 2011, **142**, 322-333.

114. T. R. Whitfield, X. Wang, L. Liu and A. J. Jacobson, *Solid State Sci*, 2005, **7**, 1096-1103.

115. P. L. Llewellyn, P. Horcajada, G. Maurin, T. Devic, N. Rosenbach, S. Bourrelly, C. Serre, D. Vincent, S. Loera-Serna, Y. Filinchuk and G. Férey, *JACS*, 2009, **131**, 13002-13008.

116. J. P. S. Mowat, V. R. Seymour, J. M. Griffin, S. P. Thompson, A. M. Z. Slawin, D. Fairen-Jimenez, T. Duren, S. E. Ashbrook and P. A. Wright, *Dalton Transactions*, 2012, **41**, 3937-3941.

117. G. Férey and C. Serre, *Chem. Soc. Rev.*, 2009, **38**, 1380-1399.

118. D. S. Coombes, F. Cora, C. Mellot-Draznieks and R. G. Bell, *J. Phys. Chem. C*, 2009, **113**, 544-552.

119. A. Ghoufi, A. Subercaze, Q. Ma, P. G. Yot, Y. Ke, I. Puente-Orench, T. Devic, V. Guillerm, C. Zhong, C. Serre, G. Férey and G. Maurin, *J. Phys. Chem. C*, 2012, **116**, 13289-13295.

120. F. X. Coudert, M. Jeffroy, A. H. Fuchs, A. Boutin and C. Mellot-Draznieks, *JACS*, 2008, **130**, 14294-14302.

121. L. Chen, J. P. S. Mowat, D. Fairen-Jimenez, C. A. Morrison, S. P. Thompson, P. A. Wright and T. Düren, *JACS*, 2013.

122. Y. Liu, J.-H. Her, A. Dailly, A. J. Ramirez-Cuesta, D. A. Neumann and C. M. Brown, *JACS*, 2008, **130**, 11813-11818.

123. A. U. Ortiz, A. Boutin, A. H. Fuchs and F.-X. Coudert, *The Journal of Chemical Physics*, 2013, **138**, 174703-174708.

124. F. Millange, N. Guillou, M. E. Medina, G. Férey, A. Carlin-Sinclair, K. M. Golden and R. I. Walton, *Chem. Mater.*, 2010, **22**, 4237-4245.

125. N. Guillou, F. Millange and R. I. Walton, *Chem. Commun.*, 2011, **47**, 713-715.

126. L. Liu, X. Wang and A. J. Jacobson, *Dalton Transactions*, 2010, **39**, 1722-1725.

127. N. Guillou, R. I. Walton and F. Millange, *Z. Kristallogr. - Cryst. Mater.*, 2010, **225**, 552-556.

128. R. I. Walton, A. S. Munn, N. Guillou and F. Millange, *Chem. Eur. J.*, 2011, **17**, 7069-7079.

129. F. Nouar, T. Devic, H. Chevreau, N. Guillou, E. Gibson, G. Clet, M. Daturi, A. Vimont, J. M. Greneche, M. I. Breeze, R. I. Walton, P. L. Llewellyn and C. Serre, *Chem. Commun.*, 2012, **48**, 10237-10239.

130. M. I. Breeze, G. Clet, B. C. Campo, A. Vimont, M. Daturi, J.-M. Grenèche, A. J. Dent, F. Millange and R. I. Walton, *Inorg. Chem.*, 2013, **52**, 8171-8182.

131. K. Barthelet, J. Marrot, D. Riou and G. Férey, *Angew. Chem. Int. Ed.*, 2002, **41**, 281-284.

132. M. E. Medina, Y. Dumont, J.-M. Greneche and F. Millange, *Chem. Commun.*, 2010, **46**, 7987-7989.

133. N. Reimer, B. Gil, B. Marszalek and N. Stock, *CrystEngComm*, 2012, **14**, 4119-4125.

134. M. A. Moreira, J. C. Santos, A. F. P. Ferreira, J. M. Loureiro and A. E. Rodrigues, *Ind. Eng. Chem. Res.*, 2011, **50**, 7688-7695.

135. J. Jia, F. Xu, Z. Long, X. Hou and M. J. Sepaniak, *Chem. Commun.*, 2013, **49**, 4670-4672.

136. T. Ishida, M. Nagaoka, T. Akita and M. Haruta, *Chem. Eur. J.*, 2008, **14**, 8456-8460.

137. L. Hamon, P. L. Llewellyn, T. Devic, A. Ghoufi, G. Clet, V. Guillerm, G. D. Pirngruber, G. Maurin, C. Serre, G. Driver, W. Van Beek, E. Jolimaître, A. Vimont, M. Daturi and G. Férey, *JACS*, 2009, **131**, 17490-17499.

138. R. El Osta, A. Carlin-Sinclair, N. Guillou, R. I. Walton, F. Vermoortele, M. Maes, D. de Vos and F. Millange, *Chem. Mater.*, 2012, **24**, 2781-2791.

Chapter 2

Experimental Techniques

2 Experimental Procedures and Techniques

The details of all experimental procedures and characterisation techniques that were used throughout this work are summarised in this Chapter. Some details presented here are brief where further information is provided in later chapters.

2.1 Sample Preparation

This section describes the solvothermal and reflux techniques used to synthesis samples. The method used for activating the samples for adsorption studies is also explained.

2.1.1 Solvothermal Synthesis

Solvothermal synthesis is a method widely used for the low temperature synthesis of inorganic and hybrid inorganic-organic solids.[1-6] Solvents are heated to or above their boiling points in a sealed vessel to generate autogenous pressure; these conditions are used to induce a chemical reaction between dissolved or suspended chemical reagents. Solvothermal synthesis has been beneficial for controlling particle size and morphology of a wide range of oxide materials such as zeolites[7], perovskites[8] and pyrochlores.[9] Also the functionalization of carbon nanotubes has been shown to be possible using this type of synthesis.[10] In the work described in this thesis, a 20 mL Teflon-lined autoclave was used for the majority of experiments. Approximately 10–12 mL of solvent can be used in these reaction vessels. The maximum temperature for these vessels is 250 °C due to Teflon having a much larger coefficient of thermal expansion than the materials that surround it; at or below this temperature a spring-loaded closure is able to maintain a constant pressure on the liner. A 125 mL Teflon-lined autoclave was used to scale up

the reactions; approximately 70 mL of solvent was used in this reaction vessel. Figure 2.1 shows a schematic of a typical Teflon-lined autoclave.

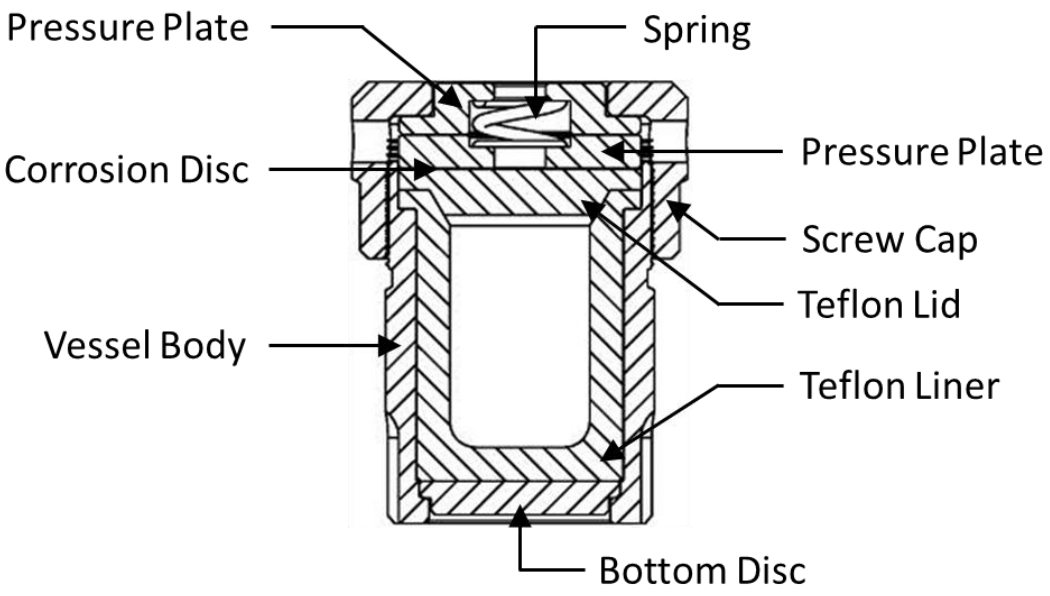

Figure 2.1: Diagram of a Teflon-lined autoclave

All reagents were obtained from chemical vendors and were used without any further purification.

Aluminium perchlorate, $Al(ClO_4)_3 \cdot 9H_2O$, was used for the synthesis of one series of MOFs. Extra care was taken not to expose this salt to shock or heat, outside of the autoclave, as it is known to be explosive. However, no problems were found with the small amounts that were used for these syntheses.

Aqueous hydrofluoric acid, 40% HF in H_2O, was used in the synthesis of various MOFs throughout this work. Caution was always taken when handling this chemical. A solution of calcium gluconate was used to neutralise any acid residues and a calcium gluconate gel was always kept within reach in case of accidental skin contact. All experiments were performed within a plastic tray to contain potential spillages.

2.1.2 Reflux

Reflux was used to scale-up reactions to the 100 mL scale in glass round-bottomed flasks. This method was only possible for syntheses that did not require the increase in pressure created inside the autoclave.

2.1.3 MOF Cleaning and Activation

As MOFs are porous by definition they tend to contain unreacted reagents and solvent molecules within the pores of the framework when initially isolated. To remove these it is necessary for the samples to be *cleaned*. The cleaning process takes the form of either stirring the material in a large excess of a volatile solvent where the solvent replaces any molecules that are trapped within the pores or the material is heated below its decomposition temperature to burn off any trapped organic molecules. The *activation* of a MOF can be defined as the removal of any occluded molecules to give the empty framework, *i.e.* the pores are free from any unreacted reagents or solvent molecules. The activation of a MOF maximises the capacity of the pores for the subsequent adsorption of guest molecules and allows for the behaviour of the framework to be studied without the complication of considering the interactions between different guest molecules.

To clean samples of MIL-53(Fe) and (Cr), the samples (~1.5 g) were stirred in a large excess of methanol (~500 mL) at room temperature for approximately 12 hrs; methanol displaces any solvent and unreacted reagents inside the pores. The samples were filtered and dried in air; the methanol in the pores is replaced by water from the air to give the hydrated phases. This method was applied to most of the porous frameworks that were synthesised throughout this project.

Some samples required heating, typically above 150 °C, to burn off any organic compounds that were trapped within the pores; thermogravimetric analysis (Section 2.4.2) was used to assess the maximum temperature that could be used. The samples were then washed in a volatile solvent which displaces any remaining molecules and dried in air to give the hydrated phases.

2.2 Characterisation Using X-rays

Various X-ray diffraction and spectroscopy techniques were used to characterise the structural properties of the metal-organic frameworks investigated in this work, under both static and dynamic conditions.

2.2.1 Powder X-ray Diffraction

Powder X-ray diffraction (PXRD) is a technique used to investigate the structures of crystalline materials. A crystalline material has an ordered arrangement of atoms or ions in three-dimensional space. The simplest representation of this arrangement that can be repeated by translation to give the full structure is defined as the *unit cell*. Two examples of a unit cell for a two-dimensional array are shown in Figure 2.2, both A and B can be repeated by applying translational symmetry to give the complete array. However, A would be chosen as the representative unit cell as it has the smallest area.

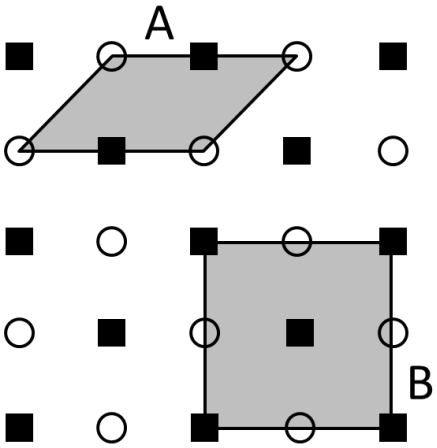

Figure 2.2: Two-dimensional representation of a crystalline material demonstrating the choice of unit cell, A and B.[11]

A three-dimensional unit cell can be defined by a parallelepiped with the side lengths denoted as *a*, *b* and *c* and the internal angles denoted as α, β and γ, these are known as the *unit cell parameters*. No relationship between cell parameters is necessary, however increasing levels of symmetry produce varying relationships which lead to the seven *crystal classes*. These classes are summarised in Table 2.1.

Table 2.1: Summary of crystal classes.[11]

Unit cell dimensions		Crystal Class
$a = b = c$	$\alpha = \beta = \gamma = 90\ °$	Cubic
$a = b \neq c$	$\alpha = \beta = \gamma = 90\ °$	Tetragonal
$a \neq b \neq c$	$\alpha = \beta = \gamma = 90\ °$	Orthorhombic
$a \neq b \neq c$	$\alpha = \gamma = 90\ ° \beta \neq 90\ °$	Monoclinic
$a \neq b \neq c$	$\alpha \neq \beta \neq \gamma \neq 90\ °$	Triclinic
$a = b \neq c$	$\alpha = \beta = 90\ ° \gamma = 120\ °$	Hexagonal
$a = b = c$	$\alpha = \beta = \gamma \neq 90\ °$	Trigonal/Rhombohedral

The ordered arrangement of atoms or ions that the unit cell describes is known as a *lattice*. A lattice is defined as an array of equivalent points in one, two or three dimensions. The lattice provides no information about the actual positions of the atoms

or molecules in space it only shows the translational symmetry of the material; the environment of an atom placed on a lattice point would be identical to an atom placed on any other equivalent point.

For three-dimensional crystal structures there are four types of lattice (Figure 2.3). The simplest lattice is known as *primitive* (P). A unit cell with a primitive lattice contains a single lattice point *i.e.* the only purely translational symmetry is that of the unit cell; lattice points are normally located at the corners of the unit cell.

The remaining three types of lattice contain translational symmetry within the unit cell. The second lattice type is *body centred* (I). The additional lattice point is at the cell's centre, which has the fractional coordinates (½, ½, ½). This means that for any atom given the fractional coordinates (x, y, z) this lattice will generate an identical atom with the fractional coordinates (x+½, y+½, z+½).

The third lattice type is known as *face centred* (F), this lattice has additional lattice points at the centre of each face with the fractional coordinates (½, ½, 0), (0, ½, ½), and (½, 0, ½). Therefore, for an atom with the general position (x, y, z) three additional identical atoms will be generated with the coordinates (x+½, y+½, z), (x, y+½, z+½) and (x+½, y, z+½).

The final lattice type is similar to the face centred lattice however it only has points on one of the faces. This lattice is still known as face centred but is given the symbol C. The lattice point is normally placed at the centre of the face delineated by a and b, which has the fractional coordinates (x+½, y+½, z). Hence, only one additional atom is generated in this lattice. The A and B face centred lattices can be obtained if the lattice points sit at the centre of the bc or ac planes, respectively. Conventionally, the C

description is always used as redefinition of the *a*, *b* and *c* directions will always produce the C centred description.

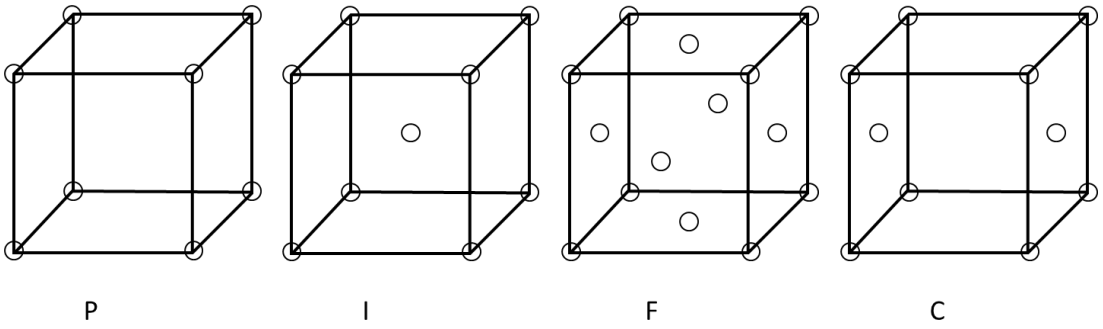

Figure 2.3: The four lattice types; Primitive, P, Body centred, I, Face centred, F and Face centred, C.

These lattice types can be combined with the seven crystal classes giving rise to all the possible variations which are known as the *Bravais lattices* (Table 2.2). There are only fourteen possibilities as not all combinations give rise to a unique lattice *i.e.* a face centred tetragonal unit cell can be redefined as a body centred tetragonal unit cell.

Table 2.2: The fourteen Bravais lattices.[11]

Crystal Classes	Bravais lattices
Cubic	P, I, F
Tetragonal	P, I
Orthorhombic	P, C, I, F
Monoclinic	P, C
Triclinic	P
Hexagonal	P
Triganol/Rhombohedral	P

Additional symmetry operations such as rotation axes and mirror planes can be applied to the Bravais lattice descriptions to produce 230 distinct lattices; these are known as

space groups. Due to the number of variations and the difficulty in determining them using powder XRD, space groups will not be discussed further.

For each unit cell a set of equally spaced parallel planes can be defined and labelled using *Miller indices*. These indices are conventionally designated as *h*, *k* and *l* which relate to the unit cell directions *a*, *b* and *c*. The Miller indices are given by the reciprocals of the fractional intercepts along each of the cell directions *i.e*. the fractional intercept along the unit cell *a* direction gives *h*, along *b* gives *k* and along *c* gives *l*. The *h*, *k* and *l* values are always integers; they can be positive, negative or zero. For planes that are parallel to one of the unit cell directions the intercept is at infinity, the reciprocal of which is equal to zero. These indices define the Miller index for a set of parallel planes, which includes one that passes through the origin. An example of a set of lattice planes is shown in Figure 2.4, where the intercepts are at ½ × *a*, ∞ × *b* and 1 × *c* therefore the Miller indices for these planes are (201).

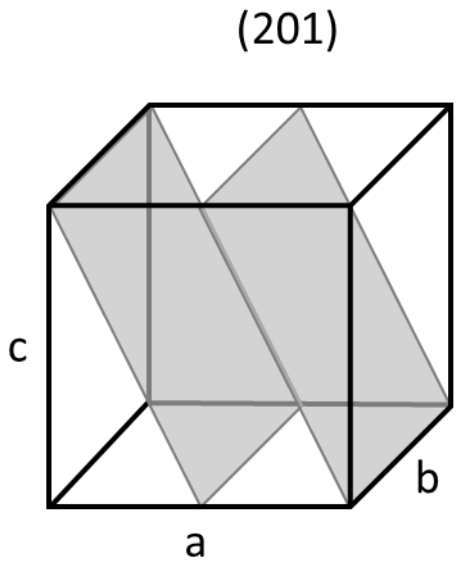

Figure 2.4: Two of the set of lattice planes with Miller indices (201)

The distance between a set of lattice planes is known as the *d-spacing* and is normally denoted as d_{hkl}. The relationship between *d*-spacing and the lattice parameters can be determined geometrically but is dependent upon the crystal class. The relationships between the *d*-spacing and the Miller indices are shown in Table 2.3.

Table 2.3: Expressions for d-spacings for the different crystal classes.[11]

Crystal Class	Expression for d_{hkl} in terms of lattice parameters and Miller indices
Cubic	$\frac{1}{d^2} = \frac{h^2 + k^2 + l^2}{a^2}$
Tetragonal	$\frac{1}{d^2} = \frac{h^2 + k^2}{a^2} + \frac{l^2}{c^2}$
Orthorhombic	$\frac{1}{d^2} = \frac{h^2}{a^2} + \frac{k^2}{b^2} + \frac{l^2}{c^2}$
Hexagonal	$\frac{1}{d^2} = \frac{4}{3}\left(\frac{h^2 + hk + k^2}{a^2}\right) + \frac{l^2}{c^2}$
Monoclinic	$\frac{1}{d^2} = \frac{1}{\sin^2\beta}\left(\frac{h^2}{a^2} + \frac{k^2\sin^2\beta}{b^2} + \frac{l^2}{c^2} - \frac{2hl\cos\beta}{ac}\right)$
Triclinic	$\frac{1}{d^2} = \frac{\left[\begin{array}{l}\frac{h^2}{a^2\sin^2\alpha} + \frac{2kl}{bc}(\cos\beta\cos\gamma - \cos\alpha) + \\ \frac{k^2}{b^2\sin^2\beta} + \frac{2hl}{ac}(\cos\alpha\cos\gamma - \cos\beta) + \\ \frac{l^2}{c^2\sin^2\gamma} + \frac{2hk}{ab}(\cos\alpha\cos\beta - \cos\gamma)\end{array}\right]}{(1 - \cos^2\alpha - \cos^2\beta - \cos^2\gamma + 2\cos\alpha\cos\beta\cos\gamma)}$

The distances between atoms or ions in solids are typically a few Ångströms which are comparable to the wavelength of X-rays. When X-rays collide with solid materials they interact with the atomic electrons and are scattered in various directions. Since the atoms are separated by distances comparable to the wavelength of the X-rays,

interference between scattered waves can occur. For an ordered array of atoms this scattering can give rise to interference maxima and minima which can provide information about the structure of the solid, providing a useful technique for the study of crystalline solids. This type of interference is known as *diffraction*.

Figure 2.5 demonstrates diffraction from points on a set of lattice planes. When the X-rays leave the source they are *in phase* but after they have been scattered by points B and D on different lattice planes they will only remain in phase (constructive interference) if the additional path difference, equal to AB + BC, is an integral number of wavelengths *i.e.* AB + BC = $n\lambda$. The path difference is dependent upon the lattice spacing, d_{hkl}, and the angle of incidence of the X-ray beam, θ. For constructive interference the following relationship can be obtained,

$$n\lambda = 2d \sin\theta$$

Equation 2.1: The Bragg equation.

where n is an integer which is related to the order of the diffracted beam and λ is the X-ray wavelength. This expression is known as the Bragg equation, first derived by W. H. and W. L. Bragg in 1913. The derivation of this expression is shown in Figure 2.5, given that the angle of incidence is equal to the angle ADB.

$$\sin\theta = \frac{AB}{BD} = \frac{BC}{BD}$$

$$BD = d$$

$$2\sin\theta = \frac{AB + BC}{d}$$

$$\boldsymbol{n\lambda = 2d \sin\theta}$$

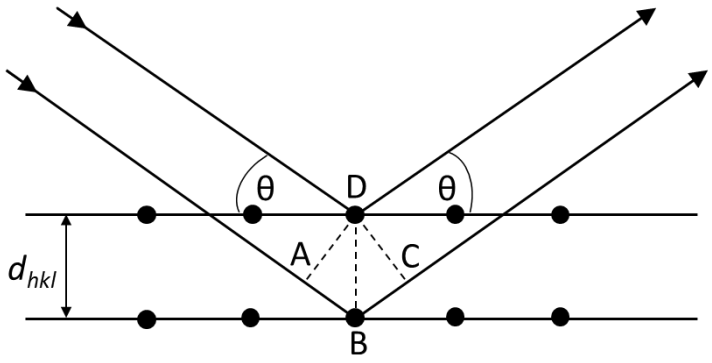

Figure 2.5: Schematic showing Bragg diffraction.[12]

An X-ray *diffractometer* is used to study the diffraction of X-rays by crystalline samples. An X-ray diffractometer consists of three essential components; a source of radiation, a detector and a goniometer.

A source of X-rays may be generated using an X-ray tube, in which a high energy beam of electrons is accelerated towards a metal target. The target is excited and emits energy in the X-ray range.

There are two main types of detector; *gas-filled* and *scintillation detectors*. Gas-filled detectors work on the principle that X-ray photons can ionise inert gases *e.g.* xenon. These ions are then accelerated towards a detector which converts the electrical signal into voltage allowing it to be interpreted computationally. Scintillation detectors require a two-step process; the X-ray photons initially strike a phosphor screen which emits photons in the visible region. These photons strike a detector and are then converted to voltage pulses which are interpreted computationally. This type of detector has a poorer resolution due to the energy losses during the process however it benefits from rapid data collection.

The goniometer allows for the precise angle at which Bragg diffraction occurs to be calculated.

The basic relationship between the X-ray source, the sample and the detector is shown in Figure 2.6. The schematic highlights the connection between the incident and reflected beams; the reflected beam will always be reflected at the angle of incidence therefore the angle between the incident beam and the reflected beam will always be equal to 2θ. Consequently, the detector will always need to be positioned at an angle of 2θ to record the Bragg diffraction for a given set of lattice planes.

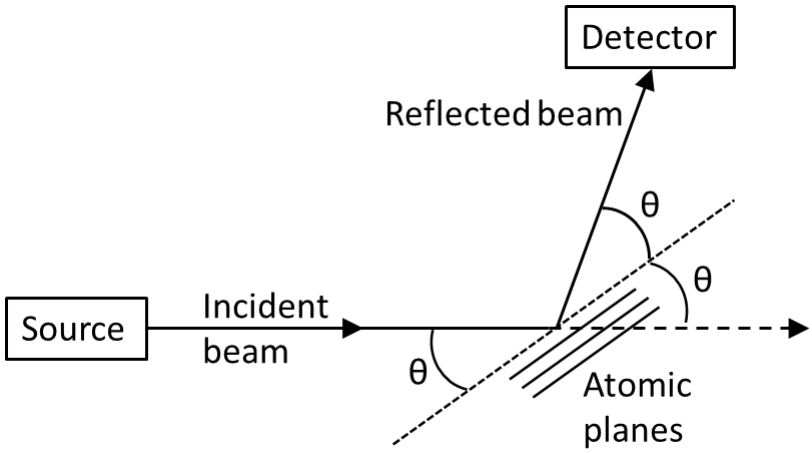

Figure 2.6: Bragg reflection from a set of lattice planes

The output produced by this method is the intensity of the X-rays detected as a function of the detector angle, 2θ. X-ray diffraction (XRD) can be used to analyse both single crystals and crystalline powders. The remainder of this section will focus on powder X-ray diffraction. Figure 2.7 shows an example of a typical powder X-ray diffraction pattern.

The positions of the reflections (2θ) and the X-ray wavelength can be used to determine the Miller indices for a given XRD pattern using the relationship between the Bragg equation and the expressions for the different crystal classes. The simplest example is for a cubic unit cell. Equation 2.2 shows the result of rearranging the Bragg equation to solve for *d* and substituting this into the expression for the cubic crystal class.

$$\sin^2\theta = \frac{\lambda^2}{4a^2}\{h^2 + k^2 + l^2\}$$

Equation 2.2

Equation 2.2 can be simplified to give Equation 2.3.

$$\sin^2\theta = A\{h^2 + k^2 + l^2\}$$

Equation 2.3

The $\sin^2\theta$ values for a sample can be calculated using the 2θ positions observed in the diffraction pattern. The ratio between these values can be used to identify the Miller indices *h*, *k* and *l*. The Miller indices can then be used to indicate the lattice planes responsible for each reflection in a diffraction pattern. Figure 2.7 shows an indexed powder XRD pattern for Cu_2O.

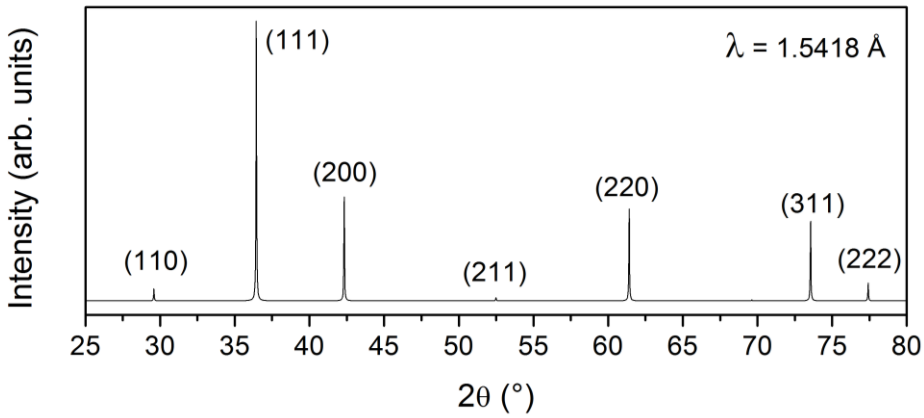

Figure 2.7: Indexed PXRD pattern for the cubic structure of Cu_2O.

A powder diffraction pattern can be used in various ways, it can be used for identification purposes if a reference crystal structure is already known; for confirming the purity of a sample as any crystalline materials within the powder sample will contribute reflections to the diffraction pattern; it can also be used for determining or refining the unit cell parameters of a sample; refining the atomic parameters if a structural model is known; and for solving structures *ab initio* if high-resolution data are available.

Refinement of PXRD patterns can be performed using structure analysis software which can process and analyse structural data. These types of software can be used to calculate

an ideal diffraction pattern from existing crystal structure information which is then compared with experimental data. Through a series of parameter refinements (*i.e.* unit cell dimensions, peak intensities and widths), the comparison between the two can be improved. This type of refinement can simply provide a profile fit which contains information about the unit cell parameters but no information about atom positions, or atomic positions may be included if the peak intensities have been determined accurately.

2.2.1.1 Laboratory PXRD

Two diffractometers were used to collect XRD data in the laboratory; a Siemens D5000 and a Bruker D8 Advance.

2.2.1.1.1 D5000

A Siemens D5000 diffractometer was used primarily for sample identification purposes. The X-ray source position is fixed and the sample and detector positions vary to maintain the 2θ angle. The instrument uses Cu Kα radiation with a weighted average wavelength of 1.54184 Å (Cu Kα1 = 1.54056 Å and Cu Kα2 = 1.54439 Å). The JCPDS[13] structural database supplied by Bruker as part of the EVA software was used to identify the composition of any crystalline impurities that were present and simulated patterns from published crystallographic data were used to identify any frameworks that had been reported previously.

2.2.1.1.2 D8

A Bruker D8 Advance diffractometer was used to collect time-resolved and temperature-resolved powder X-ray diffraction data. The breathing property of flexible MOFs, such as MIL-53, means that as the framework expands the position and the

intensity of the Bragg peaks change, which can be followed using X-ray diffraction. Some of these changes can be fast therefore the ability to collect data quickly is crucial. The D8 diffractometer is fitted with a VÅNTEC solid-state detector which benefits from rapid data collection (on the time scale of minutes). However, the disadvantage of this is the resolution of the data is reduced. Most scans were collected over a 2θ range of 6 – 30 ° for a total of approximately 210 seconds. This allowed for sufficient information about the unit cell parameters to be obtained to enable the different phases of framework breathing to be distinguished. This instrument uses a fixed sample position where the X-ray source (Cu Kα radiation with a weighted average wavelength of 1.54184 Å) and detector positions are varied to maintain the 2θ angle.

These time- and temperature-resolved experiments were designed to follow the breathing of flexible MOFs *in situ*. The flexible MOFs studied were able to expand in volume by approximately 50%. This presented problems for data collection as the diffractometer has a ceramic flat-plate sample holder. The disadvantage to using a flat-plate sample holder packed with powder is that the sample is only able to expand upwards, destroying the flatness of the sample which is required for data collection. To enable the whole breathing process to be followed it was necessary for the sample to remain flat throughout the entire data collection. The solution used to reduce this problem was to pack the sample only in the centre of the circular holder leaving free space around the edges of the powder. If expansion of the framework was slow and controlled then this solution allowed for an experiment to be completed satisfactorily.

The D8 advance diffractometer is equipped with a sample chamber (Anton Paar XRK900) which can be pressurised to 10 bar. The chamber was modified to allow for a gas flow to pass over the sample in a continuous flow without a pressure build-up.

Organic vapours were created by passing nitrogen gas through a Drechsel bottle containing an organic liquid; hydrated atmospheres were also created by passing nitrogen gas through water. The resulting vapour was then passed over the sample while the expansion/contraction of the framework was studied *in situ*. The gas flow could be controlled to adjust the rate of response of the solid if necessary.

2.2.1.2 High-Resolution Powder X-Ray Diffraction

High-resolution XRD data were collected using two different synchrotron facilities, beamline I11 at the DIAMOND Light source located in Oxfordshire in the UK and also beamline ID31 at the ESRF in Grenoble, France. Data were collected while the samples were spun continuously in borosilicate glass capillaries. Data collection performed using this method removes the effects of preferred orientation; a true average diffraction pattern can be obtained.

2.2.1.2.1 Beamline I11

Beamline I11 uses high energy X-rays, ~15 keV (λ = 0.82599 Å for the work presented in this thesis) and has an angular range of 3-150 ° (2θ). The finely ground samples were loaded into capillaries with a diameter of between 0.5- 0.7 mm and mounted onto a brass tip which fits directly on to the instrument. The standard time taken for data collection was 30 minutes. For cases where quick data collection were necessary (where beam degradation of the samples was seen) the position sensitive detector (PSD) was used. The PSD (based on Mythen-2 modules) is specified to perform fast data collection (e.g. 1 powder pattern/ms) with a 90º aperture and an intrinsic angular resolution of 0.01º.

2.2.1.2.2 Beamline ID31

Data collected using this beamline was done so by F. Millange. Beamline ID31 covers a large energy range from 5 keV to 60 keV (2.48 Å. to 0.21 Å in wavelength). The X-ray beam is monochromated by a cryogenically cooled double Si (111) crystal monochromator. For this work, data were recorded at room temperature using a wavelength of 0.7998 Å from samples loaded into the same capillaries as were used for the I11 experiments.

2.2.1.3 PXRD Refinement

Refinement of PXRD patterns was performed using the General Structure Analysis System (GSAS)[14] which uses the graphical user interface EXPGUI[15]. Profile parameter fits were used to obtain refined unit cell parameters for powder samples. The profile fit involves empirical fitting of peak intensities and the method used in this thesis was that developed by Le Bail.[16]

2.2.1.4 Energy Dispersive X-Ray Diffraction

Energy dispersive X-ray diffraction (EDXRD) uses a *white beam* of X-rays to collect data over a wide range of energies. The higher energy and intensity of the beam allows the X-rays to penetrate a reaction vessel, which means solid/liquid reactions that involve crystalline samples can be followed *in situ*, giving invaluable insight into the way a reaction proceeds. Laboratory-sized vessels can be used for this method. This type of *in situ* technique has allowed for the crystallisation of different materials to be followed from nucleation to completion leading to a better understanding of the mechanisms involved.[17] Materials studied using this method include metal oxides,[9, 18] zeolites[19, 20] and MOFs.[21, 22] In this thesis, the technique allowed for the breathing behaviour of MIL-53(Fe) when different guest molecules are adsorbed from the liquid phase to be studied

in real-time. Beamline F3 at the HASYLAB synchrotron facility in Hamburg, Germany was used to record all EDXRD data. The diagram of beamline F3, Figure 2.8, highlights how the sample and detector positions are adjustable but fixed for a given experiment. Beamline F3 receives white-beam radiation with energy 13.5–65 keV and the incident X-ray beam is collimated to dimensions 20 × 20 μm^2. The scattered X-rays are detected using a fixed single-element germanium solid-state detector. Because the detector is fixed, each pattern can be accumulated in a short period of time, typically one minute, allowing kinetic measurements to be made. The use of white beam radiation means that the data is collected as a function of energy. By substituting Equation 2.4, which relates energy, *E*, to the wavelength, λ, into the Bragg equation, Equation 2.5 can be obtained. Where *h* is Planck's constant and *c* is the speed of light.

$$E = \frac{hc}{\lambda}$$

Equation 2.4

$$E = \frac{hc}{2d \sin\theta}$$

Equation 2.5

Equation 2.5 can be simplified to give,

$$E = \frac{6.19926}{d\sin\theta}$$

Equation 2.6

If *E* is expressed in keV and *d* is in Ångströms.

The precise angle of the detector was calibrated using the Bragg peaks of a solid polycrystalline sample of MIL-53(Fe)[H_2O] and the detector energy was calibrated

using a glass containing heavy elements with well-separated fluorescence lines. These calibrations were performed on each visit to the beamline. Data were collected over several visits to this beamline therefore several detector angles were used.

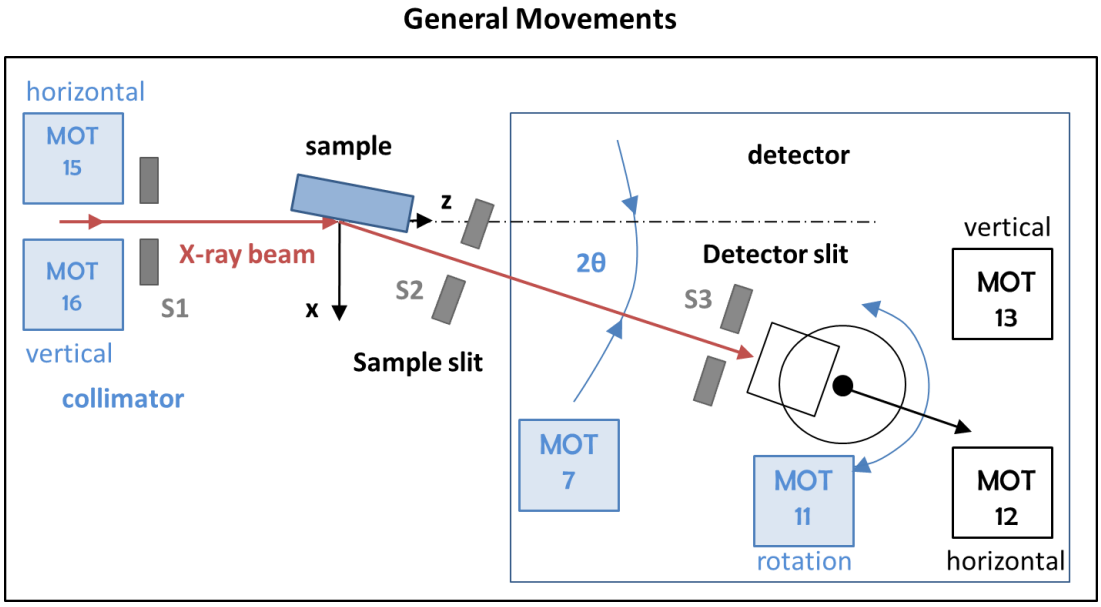

Figure 2.8: Schematic of the F3 beamline at HASYLAB, Hamburg.

A Pyrex test tube filled with 400 mg of MIL-53(Fe) was used for all of the liquid sorption experiments. The powder was either used in its hydrated form or it was dehydrated in an oven for several hours above 100 °C and sealed while hot, using a Suba-Seal septa. Solvent (3 mL) was added directly to the test tube. Anhydrous solvents were used for the dehydrated samples. The suspensions were constantly stirred throughout the experiment using a magnetic stirrer. The addition of the guest molecules to the MIL-53 suspension was controlled using a 10 mL syringe and an electric syringe pump. The syringe pump was programmed to slowly dispense liquid at a predefined rate. The syringe was filled with either a pure solvent (the same as that in the test tube) or a solution of guest molecules dissolved in solvent. Data collection began as soon as the syringe pump was started. Data were recorded every 60 seconds for a minimum of 1 hour. Due to the quick data collection time and the large range of wavelengths in the X-

ray beam the resolution is poor meaning only the strongest Bragg peaks are visible. This is, however, sufficient to be able to follow the changes in symmetry as the framework expands in response to the guest molecules.

The analysis of the data was performed using several methods: 1) Comparisons were made between the experimental data and the crystallographic data obtained using high-resolution XRD. After converting to *d*-spacing, using Equation 2.6, the positions of the observed Bragg peaks can be compared to the positions expected based on the results obtained from high-resolution XRD. The phases observed during framework breathing have distinct Bragg peak positions therefore each phase can be unambiguously identified in this way. 2) Contour plots were made to show the growth and decay of the characteristic Bragg peaks as a function of time. These allow the expansion and contraction of the framework throughout the entire experiment to be observed. 3) Extent-of-conversion graphs were used to plot the change in the area of the strongest Bragg peaks as a function of time or concentration of guest molecules. Integration of the individual peaks was performed using the software X-fit-Koalariet.[23] The decay of the initial phase was compared against the growth of the final phase to elucidate information about the kinetics of framework opening and the effect of guest concentration.

2.2.2 Single Crystal X-ray Diffraction

Single crystal X-ray diffraction operates using the same basic principles described for powder X-ray diffraction in Section 2.2.1. The technique differs in the instrumentation used to collect the data and the size of the sample to be studied. This technique collects data from a single unfractured, optically-clear crystal between 30 – 300 microns in size. The advantage of single-crystal XRD is that the data can be used to determine, through

analysis and refinement techniques, the full crystal structure of unknown materials; this includes the location and identity of all the atoms, the bond distances and angles, and also the space group and unit cell dimensions.

Single crystal diffraction was performed using a Gemini R diffractometer from Oxford Diffraction equipped with an Oxford Cryosystems Cobra which allows for low temperature (>8 K) experiments to be performed. The EPSRC National Crystallography Service (NCS) was also used for data collection.[24] Data analysis and structure refinement was performed by G. J. Clarkson. The structures were solved by direct methods using SHELXS and refined using SHELXL 97.[25]

2.2.3 X-Ray Absorption Near-Edge Spectroscopy

Beamline B18 at the DIAMOND synchrotron facility in Oxfordshire was used to perform X-ray absorption near-edge spectroscopy (XANES). B18 has an energy range of 4–35 keV. This type of spectroscopy can be used to gain electronic and geometrical information about the absorbing element allowing details such as an element's oxidation state to be elucidated.[26] In this work, only the Co K-edge was studied. Structural information is obtained from spectra by comparison with reference spectra. Therefore it is important to choose reference spectra that have comparable coordination environments and oxidation states. Three reference samples were chosen for this work: $Co(NO_3)_2 \cdot 6H_2O$, $Co(acac)_3$ and Co_3O_4. Comparisons between the oxidation states and coordination environments of these reference samples and the experimental samples are given in Section 5.2.3. Samples were investigated by preparing 12 mm pellets with a thickness of 1-2 mm using polyethylene powder as the binder. Data were collected by M. I. Breeze, C. I. Hiley and M. Harun Sani. The data were processed by R. I. Walton.

2.3 Characterisation Using Neutrons

Neutron diffraction and spectroscopy techniques were used to characterise the structural properties of MIL-53(Fe) and (Cr) in response to changing external stimuli.

2.3.1 Inelastic Neutron Scattering

Inelastic neutron scattering (INS) studies were performed using the instrument TOSCA at the neutron source facility, ISIS, located in Oxfordshire, UK. INS experiments were performed to investigate the local interactions between guest molecules and the framework. The addition of methanol to the MIL-53(Fe) framework was studied *ex situ* to identify key vibrations that were characteristic of framework expansion.

TOSCA is a crystal-analyser inverse-geometry spectrometer, where the final neutron energy is selected by two sets of pyrolytic graphite crystals placed in forward scattering (at around 42.6° with respect to the incident beam) and in backscattering (at about 137.7° with respect to the incident beam). This arrangement sets the nominal scattered neutron energy to $E_1 = 3.35$ meV (forward scattering) and to $E_1 = 3.32$ meV (backscattering). Higher-order Bragg reflections are filtered out by 120 mm-thick beryllium rods, wrapped in cadmium and cooled down to a temperature lower than 30 K. The incident neutron energy, E_0, spans a broad range allowing it to cover an extended energy transfer ($E = E_0 - E_1$) region: 3 meV < E < 500 meV.

Approximately 1 g of accurately weighed MIL-53(Fe) was loaded into an aluminium foil packet which was placed inside an aluminium sample holder where it was subject to a number of different conditions. Table 2.4 outlines the various experiments that were performed. To dehydrate the sample the hydrated powder was loaded into the sample holder and then heated to ~150 °C before tightly sealing the sample holder while hot.

Methanol or d3-methanol was introduced by injecting the liquid directly into the holder, tightly sealing and then gently heating to allow equilibrium to be reached.

Data collection was performed at 15 K and accumulated for ~6 hours per experiment. For comparison, the INS spectra for CH_3OH and CD_3OH were recorded. All of the INS data were reduced using the MANTID platform.[27] INS spectra were plotted as a function of energy and normalised to the mass of sample used in each experiment. The reduction and normalisation of the data was performed by A. J. Ramirez-Cuesta.

Table 2.4: Summary of the different experiments performed on TOSCA.

Experiment Number	MIL-53(Fe)[H_2O] / g	MIL-53(Fe) / g	CH_3OH / g (molar eq.)	CD_3OH / g (molar eq.)
1	0.9	-	-	-
2	-	0.82	-	-
3	-	1.055	0.18 (1.27)	-
4	-	0.867	-	0.14 (1.10)
5	-	0.979	-	0.31 (2.15)
6	1.0	-	-	0.19 (1.39)
7	-	-	~0.5	-
8	-	-	-	~0.5

2.3.2 Total Neutron Scattering

Total neutron scattering experiments were performed using the instrument GEM at the neutron source facility, ISIS, located in Oxfordshire, UK. GEM has been optimised for high-intensity, high-resolution experiments to study the structures of both disordered materials and crystalline powders.[28]. Approximately 3 g of sample was loaded into a cylindrical vanadium can with an inner diameter of 7.62 mm. The closed cycle refrigerator (CCR) sample holder was used for the entire experiment to allow the

sample to be cooled to low temperatures. The experiment was started at 5 K after equilibration at this temperature for several hours. Data were then collected as a sample of MIL-53(Cr) was gradually heated to 300 K. After reaching 300 K the sample can was then removed from the CCR and heated in an oven to 400 K. This step was necessary to ensure that the material had expanded completely to the fully-open phase before the sample was cooled. After returning the sample to the CCR, data were collected as the sample was cooled to 50 K. Table 2.5 shows the different temperatures at which data were collected. Longer data collection times were used for five of the temperatures investigated; data were collected for approximately 6 – 8 hours.

Table 2.5: Temperatures chosen for data collection during the heating and cooling runs for the GEM experiment. At the temperatures shown in bold, longer data collection times were used, these datasets were used to produce correlation functions.

Heating Run	Cooling Run
5 K	**300 K**
50 K	275 K
100 K	250 K
150 K	225 K
200 K	200 K
250 K	175 K
300 K	**150 K**
Sample heated to 400 K in oven	125 K
	100 K
	75 K
	50 K

Neutrons are scattered strongly and incoherently by hydrogen so any water or hydrogen in the sample affects the quality of the recorded spectra. Therefore, for these experiments the sample was deuterated as much as possible to reduce the background in the spectra due to the incoherent scattering of hydrogen; deuterated terephthalic acid was used in the synthesis but the framework μ-OH groups are still present. To synthesise deuterated MIL-53(Cr) $Cr(NO_3)_3 \cdot 9H_2O$, d4-terephthalic acid, hydrochloric acid and *N*,*N*-dimethylformamide (DMF) were heated to 120 °C in a 125 mL Teflon-lined autoclave. After filtration the sample was washed in a large quantity of fresh DMF (~500 mL), dried and then heated to 150 °C to remove any residual DMF or terephthalic acid molecules. IR spectroscopy was used to confirm that the sample had been successfully deuterated.

The diffraction data were analysed using the GSAS[14, 15] software to identify the unit cell parameters and phase fractions at each temperature. The GudrunN[29] software was used to normalise and correct the data. GudrunN and ATLAS[30] were then used to produce the

atomic pair correlation functions for the experimental datasets indicated in Table 2.5. Simulated correlation functions were produced from crystal structure data using the *xtal* software provided by A. C. Hannon. Data analysis was carried out with the help and guidance of H. Y. Playford (the simulated correlation function for terephthalic acid was produced by H. Y. Playford). Interpretation of the correlation functions has been done with the assistance of H. Y. Playford and M. G. Tucker.

2.4 Other Characterisation Techniques

Described here briefly are the various other characterisation techniques used throughout this work.

2.4.1 Infrared Spectroscopy

Infrared spectroscopy was measured using a PerkinElmer® Spectrum™ 100 FTIR with an Attenuated Total Reflectance (ATR) attachment. Spectra were acquired at 4 cm^{-1} resolution in the range 4000-550 cm^{-1}.

2.4.2 Thermogravimetric Analysis

Thermogravimetric (TG) data were recorded using a Mettler Toledo TGA/DSC1 instrument. Approximately 10 mg of powder were loaded into an alumina crucible; the sample was heated in air to 1000 °C at a rate of 10 °C min^{-1}. Room temperature experiments were also performed where the adsorption of volatile organic vapours was followed *in situ*. Nitrogen gas was passed through a Drechsel bottle containing a liquid organic which was then passed through the sample chamber.

For all of the TGA results where the empirical formula was known the first order and second order difference curves were used to identify small plateaus and inflection points in the data. The first order difference is calculated using Equation 2.7.

$$y'[n] = y[n+1] - y[n]$$

Equation 2.7

When the first order difference is close to zero it indicates that there is little change in the mass of the sample. The second order difference curve, calculated using Equation 2.8, was used to identify the inflection points in the data.

$$y''[n] = y'[n+1] - y'[n]$$

Equation 2.8

An inflection point is defined as the point at which the curvature of the graph changes sign from positive to negative or *vice versa*. Only the inflection points where the curvature changes sign from positive to negative, which indicates the onset of an increase in the rate of decomposition, were clearly marked on the graphs and used to predict the mass loss for each step.

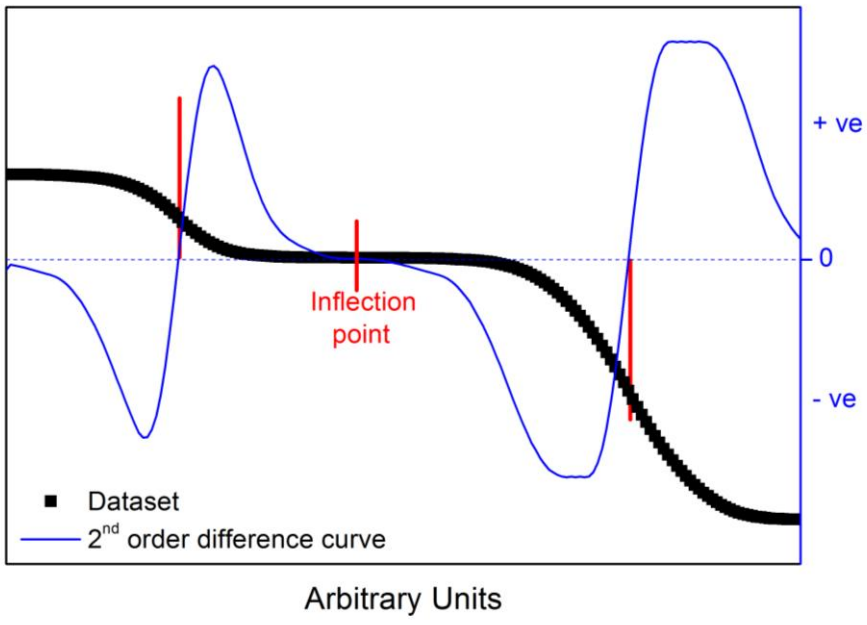

Figure 2.9: Inflection point identified using second order difference curve

For all of the TGA results where the full empirical formula was not certain, *i.e*. the identity and quantity of the guest molecules was unknown, predictions were made based on the final mass of the metal oxide after complete decomposition; the mass, and consequently the number of moles, of the metal oxide was used to calculate theoretical masses of predicted empirical formulae. These masses were converted to percentage masses by dividing by the initial mass of the experimental sample. The predicted percentage masses were clearly marked on the graphs and compared to the percentage masses that correspond to the plateaus seen in the experimental data.

2.4.3 Elemental Analysis

All elemental analysis was carried out by MEDAC Ltd. The elements that were studied include C, H, N, S, F, and various metals.

2.4.4 UV/Vis Spectroscopy

Dimethylformamide was used as the solvent for the organic molecules studied using UV/Vis spectroscopy. Spectra were recorded using a Varian Cary® 50 UV-VIS-NIR spectrophotometer from Agilent Technologies in the range of 300 - 800 nm. The scan rate was 60 nm min^{-1}.

2.4.5 Magnetic Studies

Magnetic studies were carried out using a superconducting quantum interference device known as a SQUID. The device used for these studies was a 5 T Quantum Design MPMS-5S SQUID Magnetometer capable of making measurements in the temperature range of 1.8 K to 400 K. Approximately 10 – 25 mg of sample were used for each experiment. Experiments to investigate the temperature dependence of the magnetisation were performed in a 0.01 T field in the range 2 – 400 K. The field dependence experiments were performed at four different temperatures; 5 K and 300 K

were studied for each sample whereas the other two temperatures were chosen based on the features seen in the M *vs* T experiments. Data were recorded by H. Y. Playford and L. M. Daniels.

2.5 References

1. R. M. Barrer, *Hydrothermal Chemistry of Zeolites*, Academic Press, London, 1982.

2. K. Byrappa and M. Yoshimura, *Handbook of Hydrothermal Technology*, William Andrew, 2008, vol. 1

3. C. N. R. Rao, P. J. Thomas and G. U. Kulkarni, *Nanocrystals: Synthesis, Properties and Applications*, Springer, 2007, vol. 95

4. A. Rabenau, *Angew. Chem. Int. Ed.*, 1985, **24**, 1026-1040.

5. C. S. Cundy and P. A. Cox, *Chem. Rev.*, 2003, **103**, 663-702.

6. D. R. Modeshia and R. I. Walton, *Chem. Soc. Rev.*, 2010, **39**, 4303-4325.

7. A. Gaona-Gómez and C.-H. Cheng, *Microporous Mesoporous Mater.*, 2012, **153**, 227-235.

8. X. Yang, I. D. Williams, J. Chen, J. Wang, H. Xu, H. Konishi, Y. Pan, C. Liang and M. Wu, *J. Mater. Chem.*, 2008, **18**, 3543-3546.

9. A. Michailovski, R. Kiebach, W. Bensch, J.-D. Grunwaldt, A. Baiker, S. Komarneni and G. R. Patzke, *Chem. Mater.*, 2006, **19**, 185-197.

10. H. Wu, D. Liu, H. Zhang, C. Wei, B. Zeng, J. Shi and S. Yang, *Carbon*, 2012, **50**, 4847-4855.

11. M. T. Weller, *Inorganic Materials Chemistry*, 2nd edn., Oxford University Press, 1996.

12. A. Clearfield, J. Reibenspies and N. Bhuvanesh, eds., *Principles and Applications of Powder Diffraction*, 1st edn., Wiley, 2008.

13. *JCPDS. International Center for Diffraction Data*, PA, USA, 2008.

14. A. C. Larson and R. B. Dreele, *Los Alamos National Laboratory Report LAUR*, 2000, **86**, 748.

15. B. H. Toby, *J. Appl. Crystallogr.*, 2001, **34**, 210-213.

16. A. Le Bail, H. Duroy and J. L. Fourquet, *Mater. Res. Bull.*, 1988, **23**, 447-452.

17. N. Pienack and W. Bensch, *Angew. Chem. Int. Ed.*, 2011, **50**, 2014-2034.

18. E. Antonova, B. Seidlhofer, J. Wang, M. Hinz and W. Bensch, *Chem. Eur. J.*, 2012, **18**, 15316-15322.

19. A. T. Davies, G. Sankar, C. R. A. Catlow and S. M. Clark, *J. Phys. Chem. B*, 1997, **101**, 10115-10120.

20. R. I. Walton, F. Millange, D. O'Hare, A. T. Davies, G. Sankar and C. R. A. Catlow, *J. Phys. Chem. B*, 2000, **105**, 83-90.

21. F. Millange, R. El Osta, M. E. Medina and R. I. Walton, *CrystEngComm*, 2011, **13**, 103-108.

22. F. Millange, M. I. Medina, N. Guillou, G. Férey, K. M. Golden and R. I. Walton, *Angew. Chem. Int. Ed.*, 2010, **49**, 763-766.

23. R. W. Cheary and A. A. Coelho, *Programs XFIT and FOURYA, deposited in CCP14 Powder Diffraction Library*, http://www.ccp14.ac.uk/.

24. S. J. Coles and P. A. Gale, *Chem. Sci.*, 2012, **3**, 683-689.

25. G. M. Sheldrick, *Acta Crystallogr.*, 2008, **A64**, 112-122.

26. D. C. Koningsberger and R. Prins, *X-ray Absorption: Principles, Applications, Techniques of EXAFS, SEXAFS and XANES*, John Wiley & Sons Inc., New York, NY, 1987, vol.

27. *Mantid Project*, www.mantidproject.org/.

28. A. C. Hannon, *Nucl. Instrum. Methods Phys. Res., Sect. A*, 2005, **551**, 88-107.

29. A. K. Soper, *Rutherford Appleton Laboratory Technical Report RAL-TR-2011-013*, 2011.

30. A. C. Hannon, W. S. Howells and A. K. Soper, *Inst. Phys. Conf. Ser.*, 1990, **107**, 193.

Chapter 3

Liquid Phase Studies

3 Structural Transitions of MIL-53(Fe) Studied in the Liquid Phase

This chapter details various *in situ* time-resolved energy dispersive X-ray diffraction (EDXRD) studies which have been used to investigate the adsorption properties of MIL-53(Fe). Initial studies include investigations to identify the conditions that can stabilise a transient crystalline phase which was observed in previous studies, by R. Walton and F. Millange,[1] during the expansion of the framework in response to simple alcohols. The concentration and the rate of addition of the alcohol solutions were adjusted to identify the correct conditions to induce stabilisation. The studies into alcohol adsorption were then used as *model behaviour* when considering the adsorption of other guest molecules. This model behaviour was used to help investigate the industrially relevant problem of removing N/S heterocycles from petrochemicals. A combination of EDXRD data and adsorption isotherms were used to study the effect of guest concentration and solvent choice upon the ability of the framework to be able to adsorb these guest molecules. The various interactions between the host, the guests and the solvent were considered when exploring the differences in behaviour of the framework towards the different heterocycles.

3.1 Introduction

The studies reported in this section were designed to investigate the behaviour of MIL-53(Fe) upon the adsorption of various small alcohols. Many adsorption studies have been performed on the family of MIL-53 materials, as described in Chapter 1, however, the studies presented here aim to follow the structural changes of the framework, upon guest adsorption, using *in situ* X-ray diffraction techniques. These *in situ* XRD studies

will provide valuable information about the crystalline transitions observed during the adsorption of small alcohols which will allow for the model behaviour of the framework to be established.

Liquid phase experiments were performed to study the ability of MIL-53(Fe) to act as an adsorbent. Guest molecules were dissolved in solvent and added to a suspension of MIL-53(Fe) powder in the same solvent. As MIL-53(Fe) adsorbs the guest molecules the changes to the crystalline properties of its framework were followed *in situ* using energy dispersive X-ray diffraction. *Ex situ* diffraction techniques were also used to study the framework before and after it had taken up the guest molecules. This provides reference powder diffraction data that can be used for indexing the *in situ* results.

3.2 Behaviour of MIL-53(Fe) in Response to Simple Alcohols

Energy dispersive X-ray diffraction (EDXRD) experiments, completed by R. Walton and F. Millange studying alcohol uptake in MIL-53(Fe), were performed using two instruments; Station 16.4 at the Daresbury SRS, UK (in 2006) and more recently, in 2008, Beamline F3 at the HASYLAB facility in Hamburg, Germany. Their results provided information about the breathing phenomena induced by simple alcohols. The results for hydroxylated MIL-53(Fe) show that the primary alcohols cause the framework to fully expand as expected. However, the results for the partially fluorinated MIL-53(Fe) show that the primary alcohols cause the framework to expand via a transient crystalline phase before complete expansion to the fully-open phase (1590 $Å^3$).[1]

Ex situ high-resolution PXRD experiments were performed by N. Guillou (Institut Lavoisier) to complement the *in situ* EDXRD experiments. The results for the fluorinated MIL-53(Fe)[H_2O] fully exchanged with pure alcohol solutions are shown in Table 3.1. These refined structures provide reference powder diffraction data which will be used for indexing the *in situ* EDXRD data.

Table 3.1: Unit cell parameters for the pure alcohol solutions.

Guest	MIL-53(Fe,OH,F)	
H_2O	*C2/c*	*a* = 21.1299(1) *b* = 7.64271(6) *c* = 6.83058(6) *β* = 114.9352(4) *V* = 1000.25(2)
MeOH	*Imcm*	*a* = 15.9394(3) *b* = 14.4526(3) *c* = 6.90489(8) *V* = 1590.65(5)
EtOH	*Imcm*	*a* = 16.2079(2) *b* = 14.1441(2) *c* = 6.89163(3) *V* = 1579.87(3)
^{n}PrOH	*Imcm*	*a* = 17.1382(2) *b* = 12.7876(2) *c* = 6.89262(4) *V* = 1510.56(3)
^{i}PrOH	*C2/c*	*a* = 20.2269(1) *b* = 9.9400(2) *c* = 6.87300(4) *β* = 113.0698(4) *V* = 1271.34(2)

3.2.1 Energy Dispersive X-ray Diffraction Studies

The conditions required to stabilise the transient crystalline phases of fluorinated MIL-53(Fe) were unknown, therefore the work presented here follows the same experimental procedures, using Beamline F3, to investigate the stabilisation of the transient crystalline phases.

An identical experimental setup was used for the *in situ* studies; a calibrated syringe pump controlled the addition of the aqueous guest solution to a borosilicate glass test tube containing a suspension of MIL-53(Fe)[H_2O] in water. By varying the concentration of the guest solution in the syringe and the speed of the syringe pump the conditions required to stabilise the transient phase were investigated. The concentration of the guest solutions was chosen based on previous results; therefore the same concentrations were not used for every alcohol. The syringe pump was set to three different rates of addition during the course of these experiments: 1 mL/hr, 5 mL/hr and 10 mL/hr. For each experiment performed, the data are presented as 2D contour plots to clearly show the evolution of the different crystalline phases. The individual XRD patterns for each phase identified during the experiments are also shown. Each pattern has been indexed using the crystallographic data refined from the high-resolution XRD studies. Energy was converted to *d*-spacing using Equation 2.6 (Chapter 2) and the comparison between the calculated and the experimental *d*-spacings are given in the Appendix. Some data sets that are shown were recorded by R. Walton and F. Millange using station 16.4 at the synchrotron facility in Daresbury; these results have been shown as a comparison for the new data presented here. Differences in the energy ranges between HASYLAB data sets are due to the recalibration of the instrument between visits.

Figure 3.1a shows the contour plot for the addition of a 100% (v/v) ethanol solution to hydrated MIL-53(Fe) at a rate of 1 mL/hr. The contour plot clearly shows two crystalline phases and no evidence for the presence of the transient phase. The individual XRD patterns (Figure 3.1b) were used to index the contour plot by converting the energy range to *d*-spacing. This allows a direct comparison with the lattice parameters obtained from high-resolution XRD. The *hkl* values are shown.

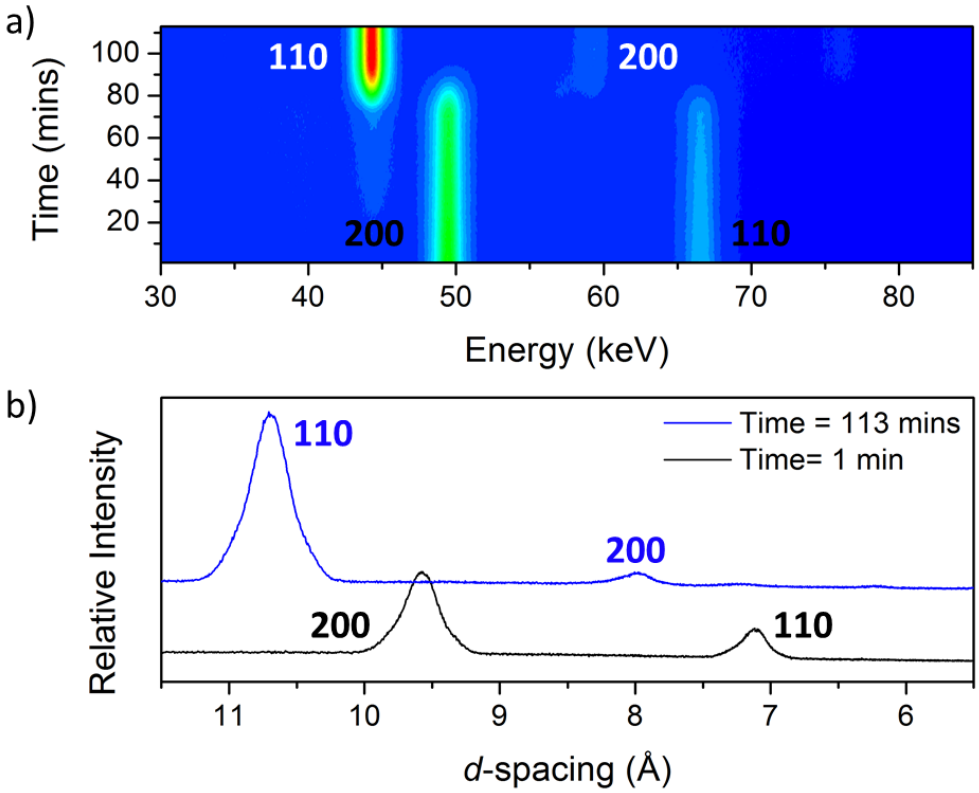

Figure 3.1: Data for the addition of 100% ethanol at a rate of 1 mL/hr presented as a) a 2D contour plot showing two crystalline phases; the hydrated phase (black hkl values) and the fully-open ethanol phase (white hkl values), and b) the individual XRD patterns for the first and last scans (black = hydrated phase and blue = fully-open ethanol phase). (Data recorded at Daresbury by R. Walton and F. Millange)

The contour plot for the addition of a 75% (v/v) aqueous solution of ethanol to hydrated MIL-53(Fe) at a rate of 1 mL/hr is shown in Figure 3.2a. These conditions also show no evidence for the transient phase. The individual XRD patterns are shown in Figure 3.2b and the patterns have been indexed as explained for the previous experiment.

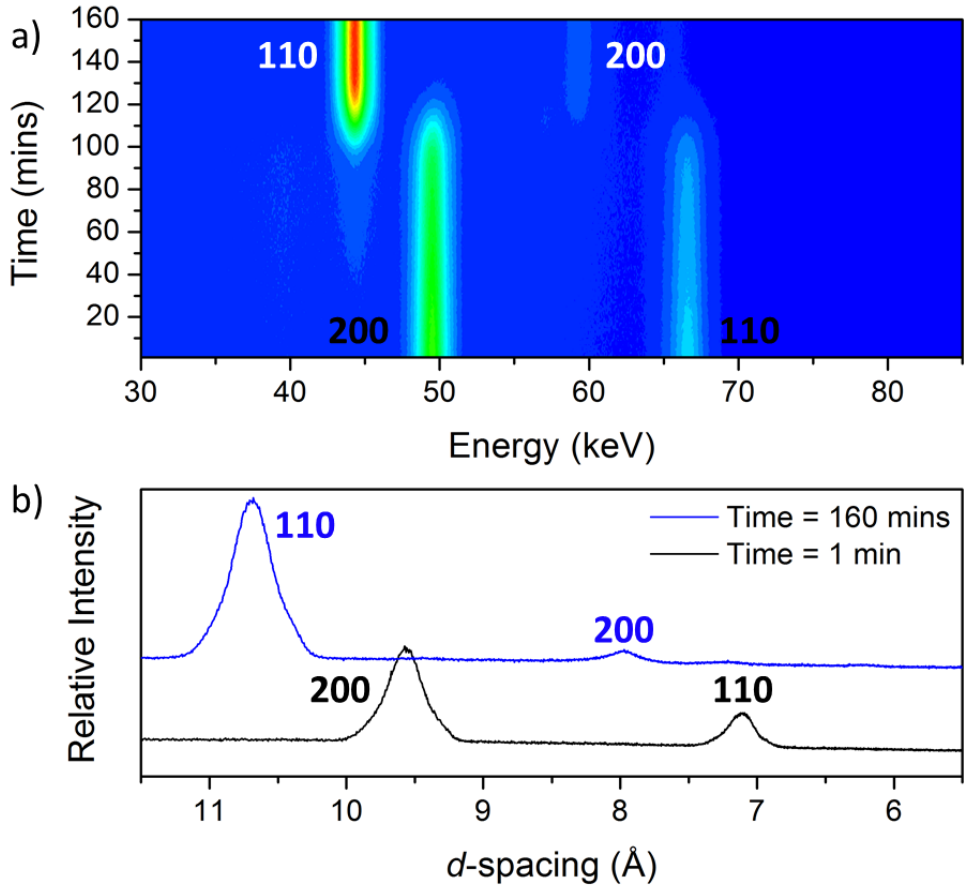

Figure 3.2: Data for the addition of 75% v/v ethanol at a rate of 1 mL/hr presented as a) a 2D contour plot showing two crystalline phases; the hydrated phase (black hkl values) and the fully-open ethanol phase (white hkl values), and b) the individual XRD patterns for the first and last scans (black = hydrated phase and blue = fully-open ethanol phase). (Data recorded at Daresbury by R. Walton and F. Millange)

Figure 3.3a shows the contour plot for the addition of a 25% (v/v) aqueous solution of ethanol to hydrated MIL-53(Fe) at a rate of 10 mL/hr. The contour plot shows evidence for the transient phase; the peaks that are unique to the transient phase never exist as an isolated phase, they are always present with either the hydrated or the fully-open phases. The individual XRD patterns show that the last scan of the contour plot is a mixture of the transient phase (red) and the fully-open ethanol phase (blue) (Figure 3.3b).

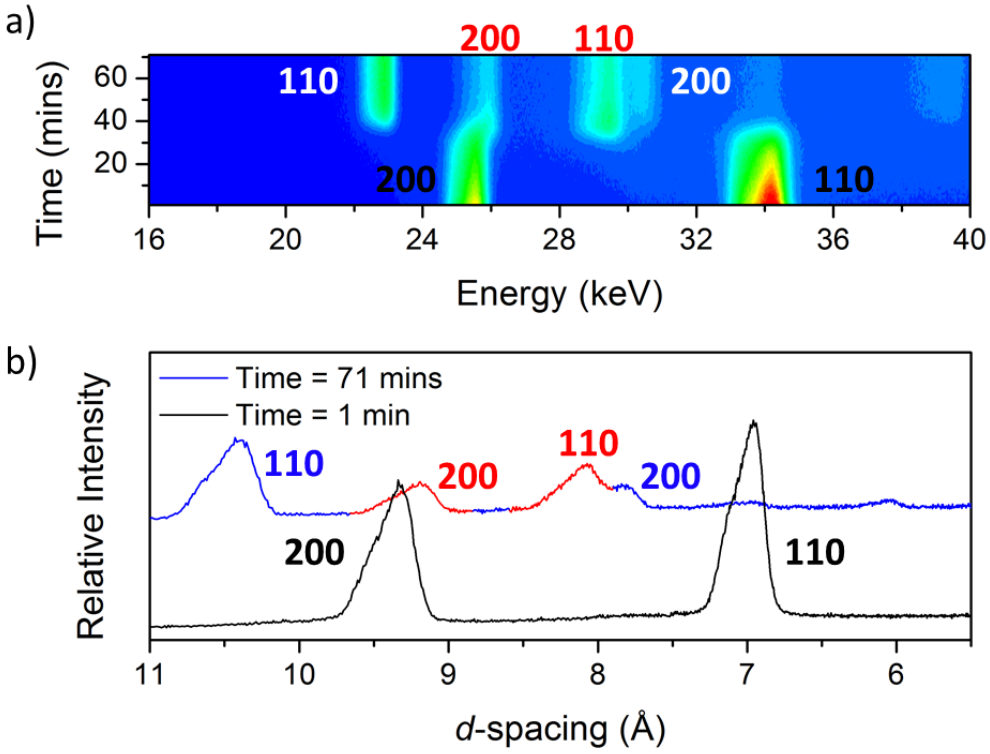

Figure 3.3: Data for the addition of 25% v/v ethanol at a rate of 10 mL/hr presented as a) a 2D contour plot showing three crystalline phases; the hydrated phase (black hkl values), the transient phase (red hkl values) and the fully-open ethanol phase (white hkl values), and b) the individual XRD patterns for the first and last scans (black = hydrated phase, red = transient phase and blue = fully-open ethanol phase). (Data recorded at HASYLAB by R. Walton and F. Millange)

The addition of a 25% (v/v) aqueous solution of ethanol to hydrated MIL-53(Fe) at a rate of 5 mL/hr is shown in Figure 3.4. This result shows that the transient phase was successfully stabilised using these conditions; the growth of the fully-open, *Imcm*, phase is not seen within the time period of this experiment.

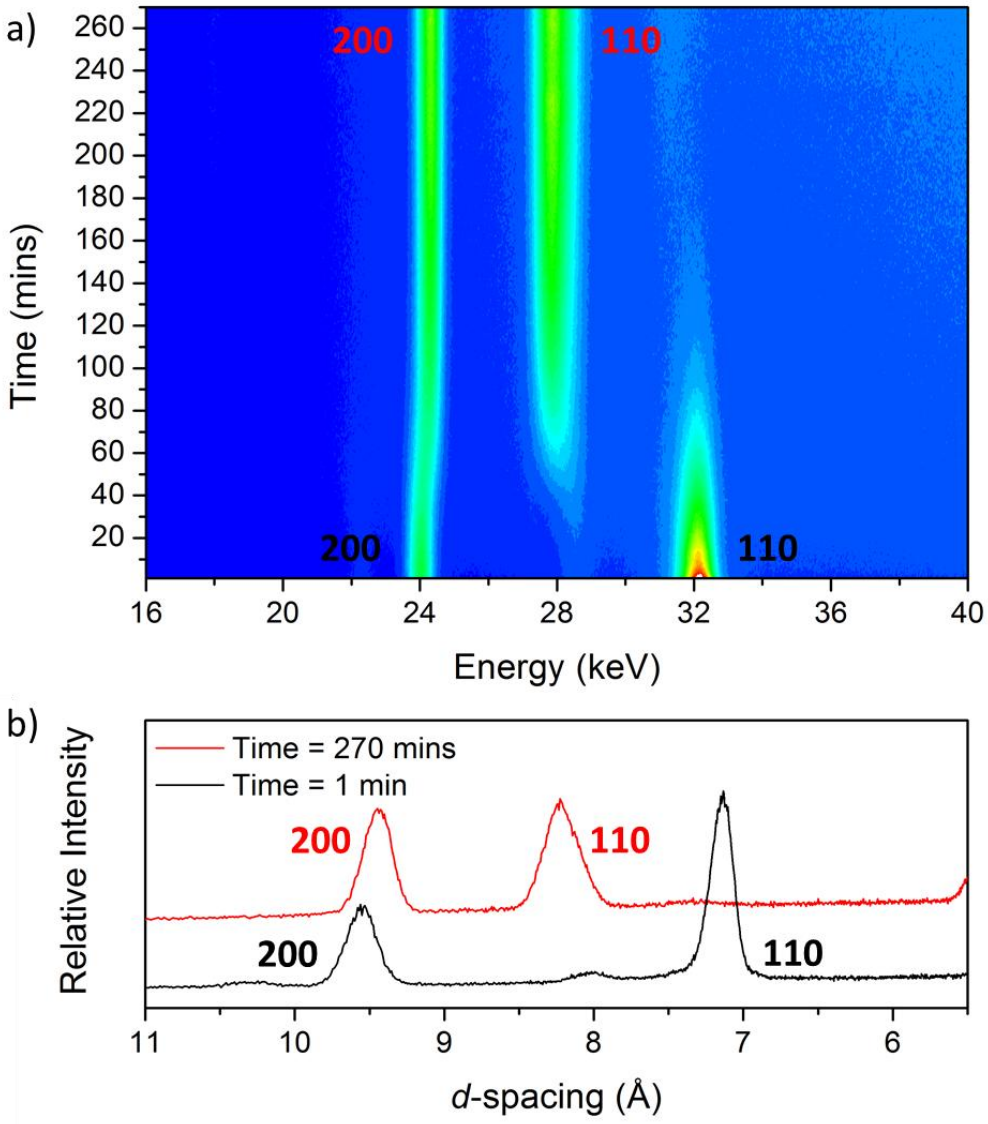

Figure 3.4: Data for the addition of 25% v/v ethanol at a rate of 5 mL/hr presented as a) a 2D contour plot showing two crystalline phases; the hydrated phase (black hkl values) and the half-open phase (red hkl values), and b) the individual XRD patterns for the first and last scans (black = hydrated phase and red = half-open phase). (Data recorded at HASYLAB)

These conditions were reproduced in capillaries to stabilise this phase *ex situ* to allow high-resolution powder X-ray diffraction data to be recorded. The data were collected by F. Millange using Beamline ID31 at the ESRF and were analysed by N. Guillou using the structural refinement software Topas. The refinement showed that this intermediate phase was similar to the half-open product seen for excess propan-2-ol, *C2/c*, V = 1199 Å^3 (Figure 3.5) and *C2/c*, V = 1271 Å^3 (Table 3.1) respectively. The

individual XRD patterns shown for each experiment were indexed using the lattice parameters determined from the high-resolution XRD data.

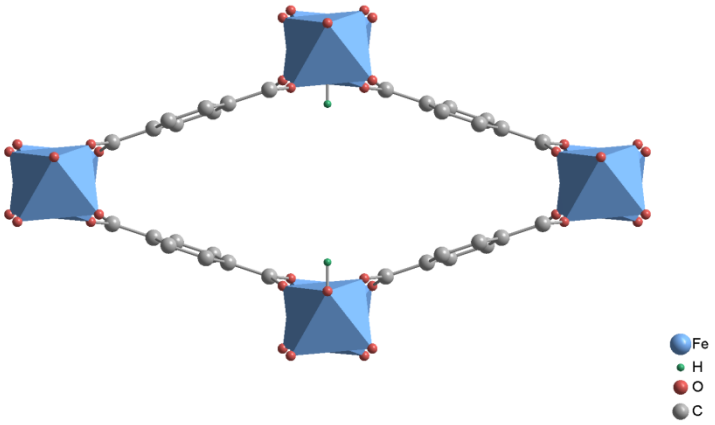

Figure 3.5: Half-open phase determined for partially fluorinated MIL-53(Fe). Guest molecules have been omitted.

The data for propan-*1*-ol shows a similar trend to ethanol; by controlling the concentration and rate of addition the transient phase can be isolated. Figure 3.6 shows the data collected for the addition of a pure propan-*1*-ol solution to hydrated MIL-53(Fe) at a rate of 1 mL/hr. The contour plot (Figure 3.6a) shows evidence for the transient phase; the peaks that are unique to the transient phase are never present as a sole phase. The individual XRD patterns show that when the transient phase appears, between 35 – 60 minutes, there is a mixture of phases present (Figure 3.6b).

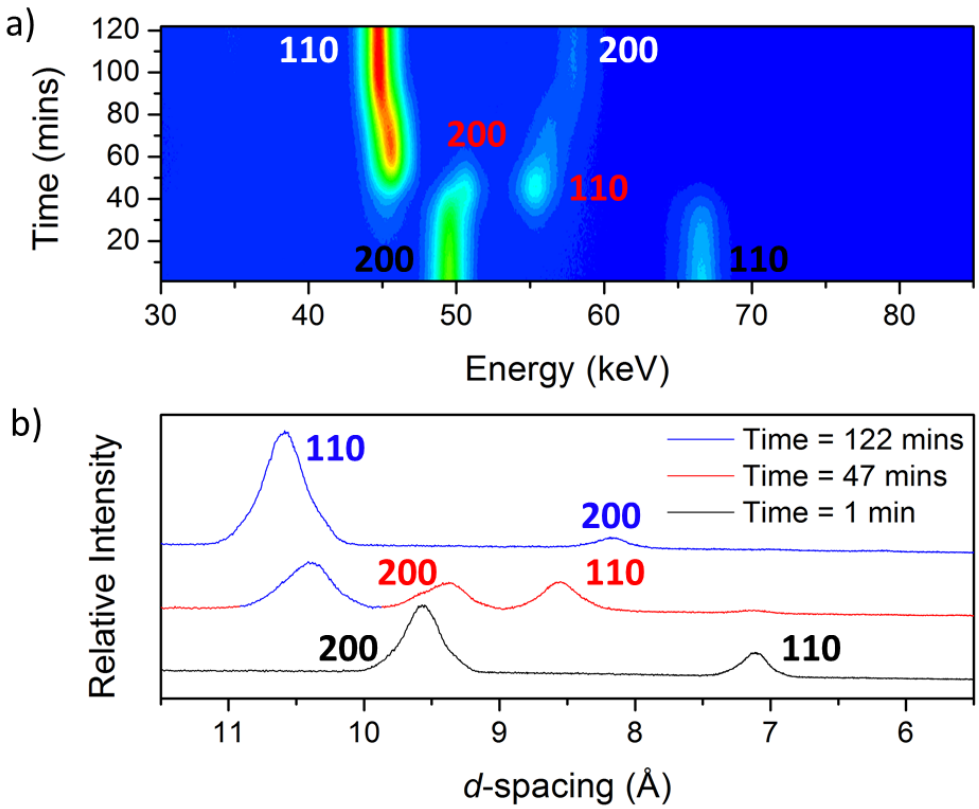

Figure 3.6: Data for the addition of 100% v/v propan-1-ol at a rate of 10 mL/hr presented as a) a 2D contour plot showing three crystalline phases; the hydrated phase (black hkl values), the transient phase (red hkl values) and the fully-open propan-1-ol phase (white hkl values), and b) the individual XRD patterns showing the three different phases (black = hydrated phase, red = transient phase and blue = fully-open propan-1-ol phase). (Data recorded at Daresbury by R. Walton and F. Millange)

The data for the addition of a 25% v/v propan-*1*-ol solution to hydrated MIL-53(Fe) at a rate of 10 mL/hr is shown in Figure 3.7. The contour plot shows evidence for the transient phase. As seen in the previous experiment the transient phase was always present as part of a mixture. The appearance of the transient phase occurs sooner and for a shorter time period as compared to the higher concentration experiment, which is due to the faster rate of addition of the alcohol solution; the concentration of guest present after 30 minutes is greater in this experiment. The individual XRD patterns show that there is a mixture of phases present in the pattern where the strongest peaks of the transient phase are seen (Figure 3.7b).

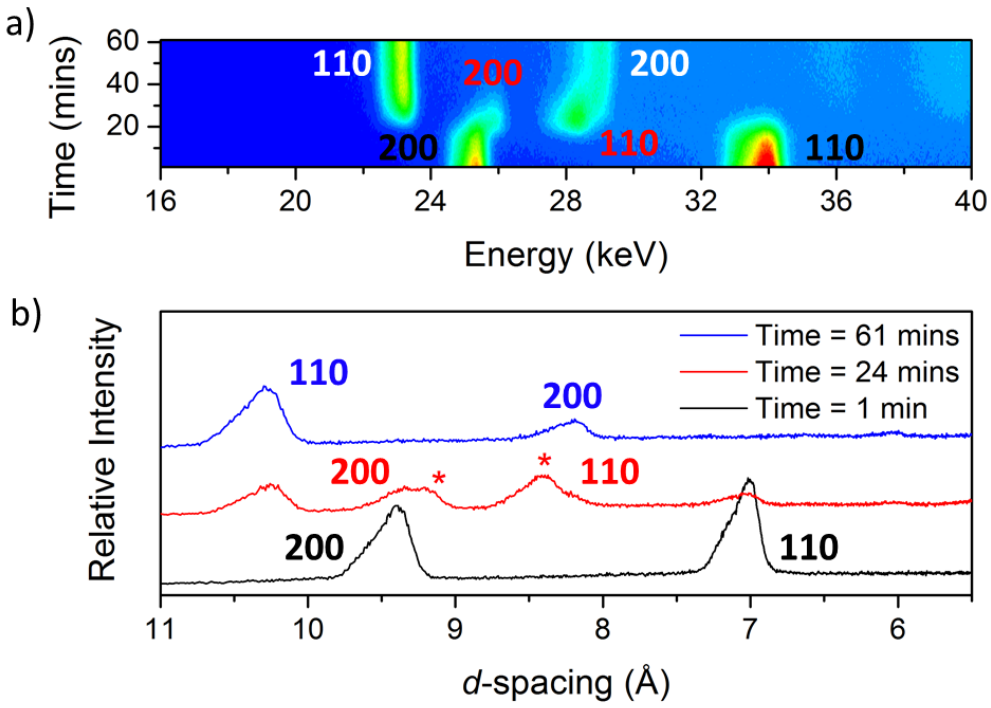

Figure 3.7: Data for the addition of 25% v/v propan-1-ol at a rate of 10 mL/hr presented as a) a 2D contour plot showing three crystalline phases; the hydrated phase (black hkl values), the transient phase (red hkl values) and the fully-open propan-1-ol phase (white hkl values), and b) the individual XRD patterns showing the three different phases (black = hydrated phase, red = transient phase and blue = fully-open propan-1-ol phase). (Data recorded at HASYLAB by R. Walton and F. Millange)

Figure 3.8a shows the contour plot for the addition of a 20% v/v propan-*1*-ol solution to hydrated MIL-53(Fe) at a rate of 5 mL/hr. This result shows that the transient phase was successfully stabilised; no growth of the fully-open, *Imcm*, phase is seen in the time period of the experiment. These conditions were used to stabilise this phase to enable high-resolution XRD data to be collected, the data were analysed by N. Guillou. These data were used to determine that this half-open phase has a monoclinic, *C2/c*, unit cell with a refined volume of 1242 $Å^3$. The individual XRD patterns were indexed using the crystallographic data obtained from high-resolution XRD studies. The individual pattern of the last scan shows that the half-open phase is the sole product (Figure 3.8b).

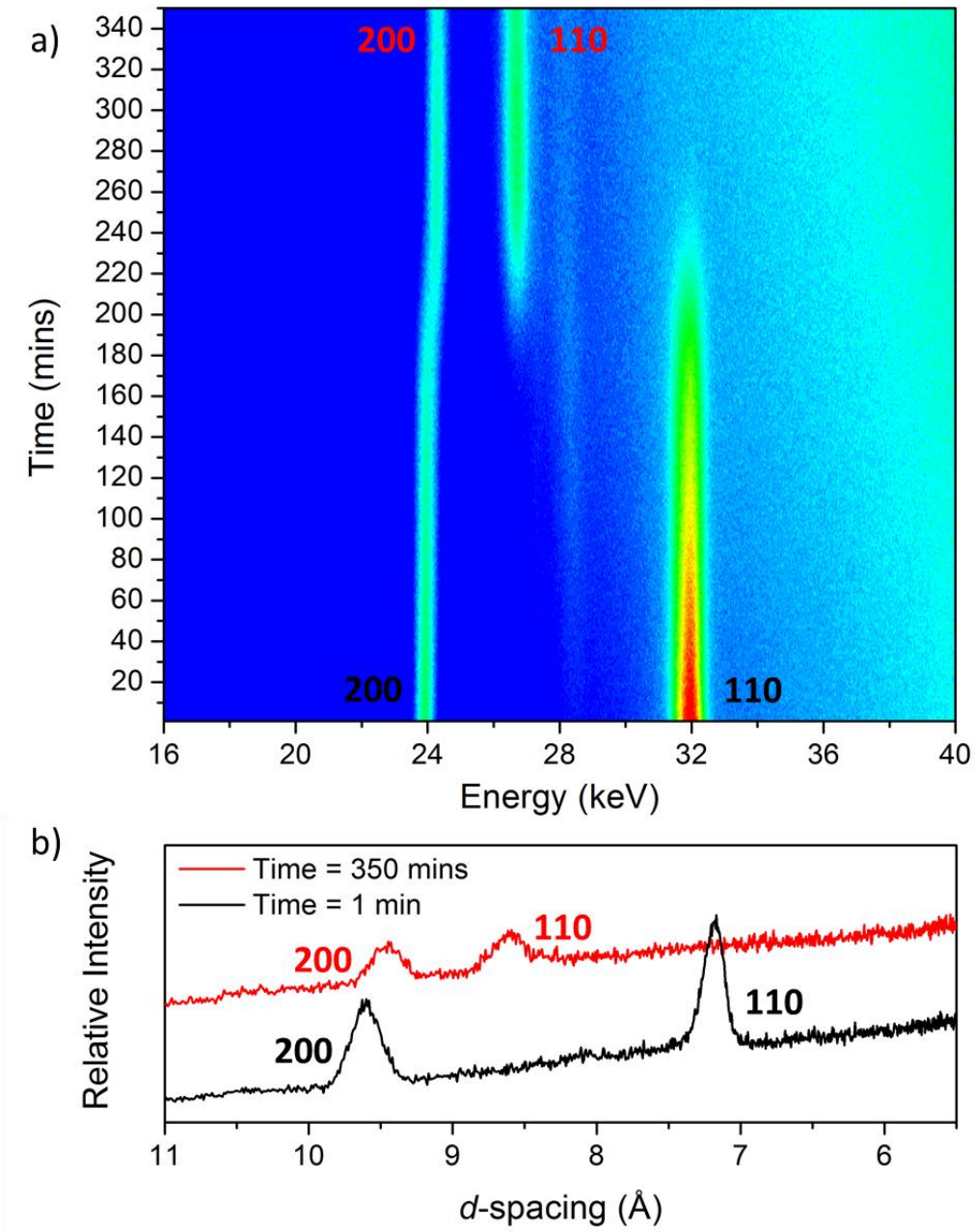

Figure 3.8: Data for the addition of 20% v/v propan-1-ol at a rate of 5 mL/hr presented as a) a 2D contour plot showing two crystalline phases; the hydrated phase (black hkl values) and the half-open phase (red hkl values), and b) the individual XRD patterns showing the first and last scans (black = hydrated phase and red = half-open phase). (Data recorded at HASYLAB)

Figure 3.9 shows the data recorded for the addition of pure propan-*2*-ol at a rate of 1 mL/hr. These data were recorded previously by R. Walton and F. Millange but have been included to show the difference in behaviour of MIL-53(Fe) towards the two propanol isomers. The contour plot shows that MIL-53(Fe) does not expand to the fully-

open phase upon the addition of a pure solution of propan-*2*-ol, it only expands as far as the half-open phase.

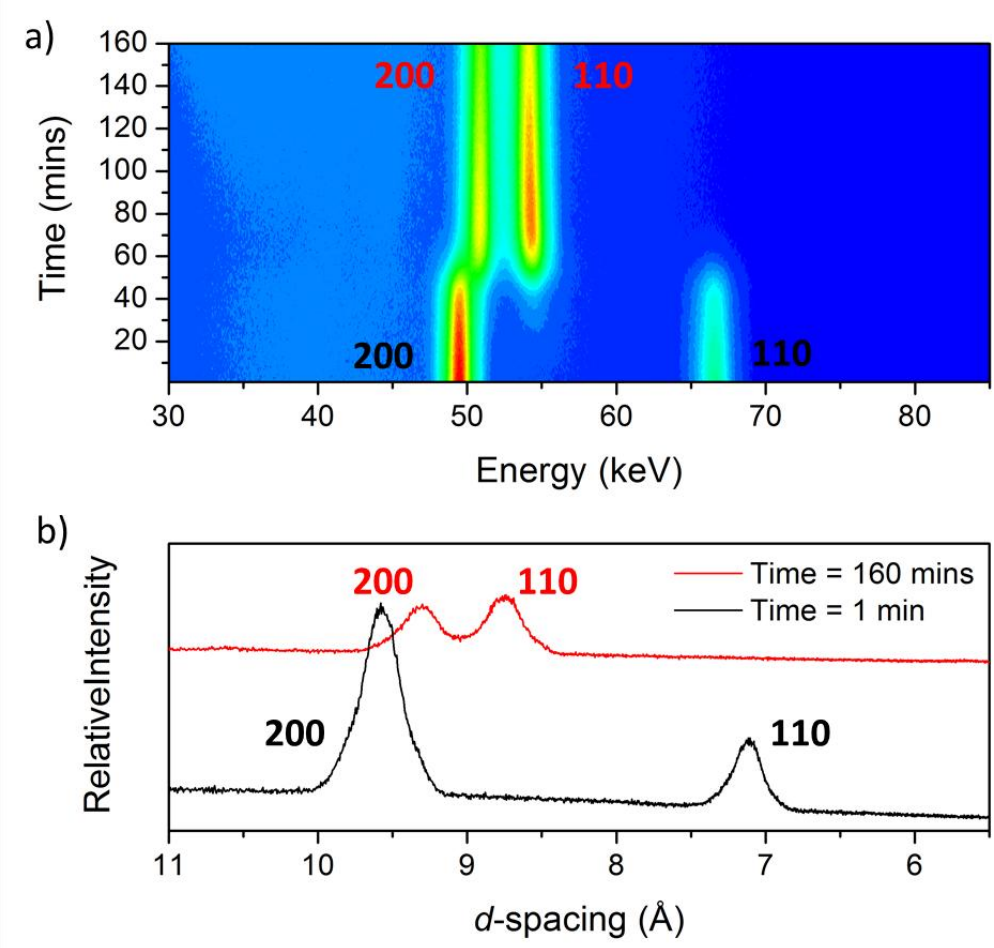

Figure 3.9: Data for the addition of 100% v/v propan-2-ol at a rate of 1 mL/hr presented as a) a 2D contour plot showing two crystalline phases; the hydrated phase (black hkl values) and the half-open phase (red hkl values), and b) the individual XRD patterns showing the first and last scans (black = hydrated phase and red = half-open phase). (Data recorded at Daresbury by R. Walton and F. Millange)

It is clear from the results above that both the concentration and the rate of addition affect the opening of the framework. The results show that under the correct conditions the transient phase can be stabilised so that it is the sole product; none of the fully-open phase is seen in the time scale of the experiment.

These results show that the expansion of the MIL-53(Fe) framework in alcohol solvents occurs in distinct steps; there is not a gradual expansion from one phase to another, the

different phases can co-exist but each phase has a unique set of Bragg peaks. Furthermore, the primary alcohols cause expansion via an intermediate phase. There are certain interactions occurring that must be responsible for the different response of the framework towards different guest molecules. Possible interactions include: a) *host-guest*, favourable interactions will result in the adsorption of guest molecules and the strength of these interactions will determine how easily the guest molecules can be displaced, b) *guest-guest*, which could prevent or encourage multiple guest molecules occupying the space within the framework, and c) *guest-solvent*, which would hinder or enhance guest uptake depending upon whether the interactions are attractive or repulsive.

It is proposed that the guest-guest interactions are the cause of the framework behaving differently in response to the primary and secondary alcohols; all of the alcohols studied here are expected to hydrogen bond to the OH groups in the host framework, as was seen for the adsorption of pyridine,[2] and the solvent-guest (water-alcohol) interactions will be similar for both the primary and secondary alcohols. Competing effects of the guest water molecules, which are present inside the pores at the start of the experiment, should be considered, however the results presented here suggest that they are easily displaced by all of the alcohol solutions studied. For the primary alcohols it is suggested that the step-wise expansion is caused by the initial uptake of one molar equivalent of alcohol per Fe atom, which gives the half-open phase. The expansion to the fully-open phase is then the response of the framework to the uptake of a second molar equivalent of alcohol. The branched nature of a secondary alcohol means that the bulk of the molecule, when hydrogen bonded to the framework –OH groups, will point directly into the pore leaving less available space for further uptake of guest molecules. For this reason, it is hypothesised that only one molar equivalent of secondary alcohol is taken

up by the framework thereby explaining why the expansion to the fully-open phase never occurs. Due to long range disorder of the occluded alcohol molecules within the pores of MIL-53(Fe) the position of these guests cannot be refined using XRD techniques.

Plotting the normalised integrated peak areas of the strongest Bragg reflections seen for each phase *i.e.* hydrated (110), gives a better understanding of the sequence of the growth and decay of each phase (Figure 3.10). When 100% and 75% ethanol solutions are added at a rate of 1 mL/hr there is a minimum concentration of ethanol that needs to be reached before any of the fully-open phase is observed. It can be seen that reducing the concentration of the guest solution increases the time taken for the fully-open phase to be reached but does not affect the exchange from the initial phase to the final phase. The initial phase exchanges directly into the final phase evident by the graphs crossing close to 50% of complete conversion; suggesting that no intermediate phase is present. When the concentration of the guest solution is reduced to 25% v/v but the syringe speed is increased to 10 mL/hr the total time for the reaction to complete decreases but the exchange from the initial phase to the final phase is not direct. This is clear from the graphs crossing at only 30% of complete conversion, which indicates that 70% of the hydrated phase has decayed and only 30% of the fully-open phase has grown suggesting that evolution occurs through an additional phase. Due to the Bragg peaks of the half-open phase overlapping with the Bragg peaks of the hydrated and fully-open phases it was not possible to integrate the peaks for this phase. When the concentration is kept at 25% v/v but the syringe speed is decreased to 5 mL/hr the transient phase is stabilised. The crossover on this graph, again, does not occur at 50%. It is proposed that the gradual decrease in the area of the initial hydrated phase, seen for all four examples, is the result of the framework rearranging through an amorphous phase before evolution to

the more open crystalline phases. This is more pronounced in the last example as the kinetics of the transition are slower.

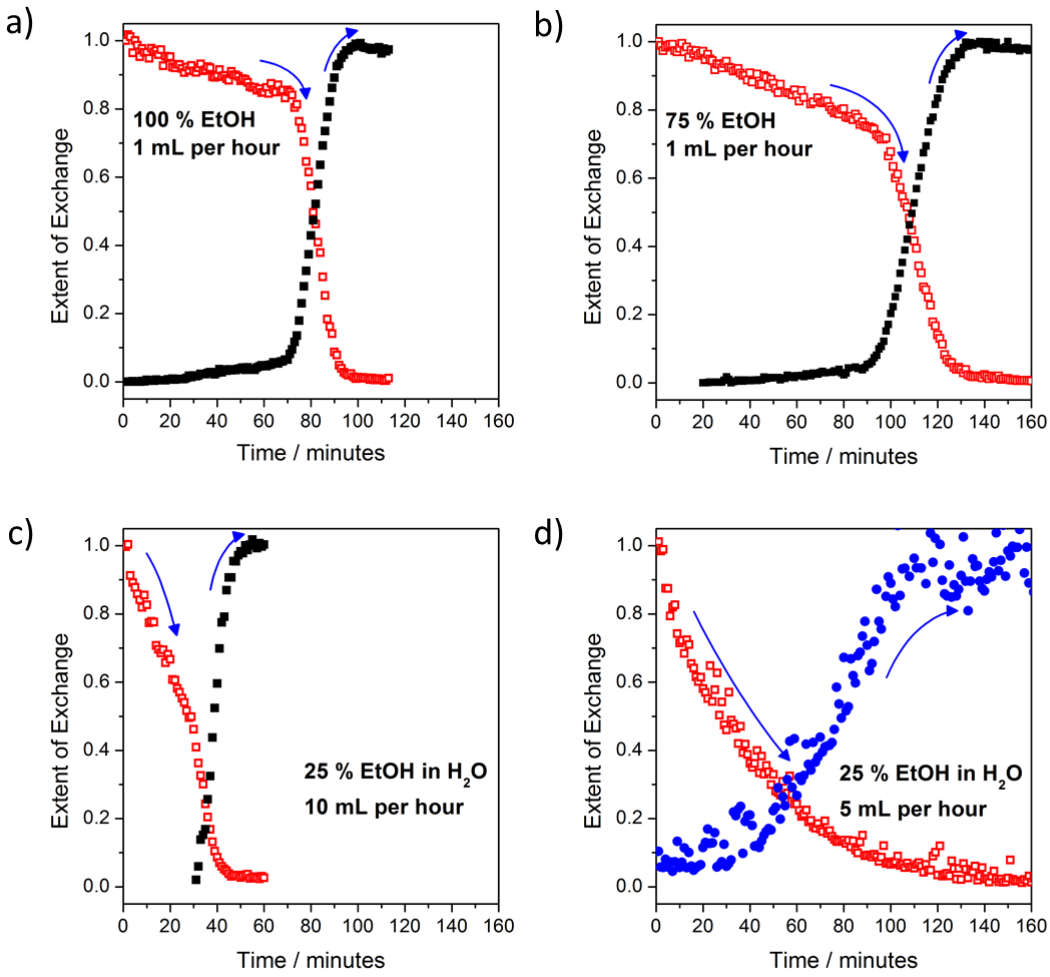

Figure 3.10: Extent of exchange graphs for MIL-53(Fe) + ethanol. Open red squares show the integrated area of the (110) peak of the hydrated phase, closed black squares show the area of the (200) peak of the fully-open phase and the closed blue circles show the area of the (110) peak of the half-open phase.

Figure 3.11 shows the extent of conversion graphs for the three conditions studied for the addition of propan-*1*-ol solutions; 100% at 1 mL/hr, 25% at 10 mL/hr and 20% at 5 mL. The data collected for the addition of a 100% v/v solution of propan-*1*-ol shows the growth of the half-open phase before the growth of the fully-open phase. When the concentration of the solution was decreased to 25% and the rate of addition increased to 10 mL/hr the time taken for the material to reach complete conversion to the fully-open

phase was reduced. The conversion was so rapid that the intermediate phase was not seen; confirmed by the graphs crossing at approximately 50%. Reducing the concentration of the solution to 20% v/v and reducing the rate of addition to 5 mL/hr resulted in the stabilisation of the half-open phase. The resolution of the XRD data collected for this experiment is poor but it can still be seen that the hydrated phase starts to decay before the growth of the half-open phase, it is suggested that this is due to the transition occurring via an amorphous phase as explained above. The decrease in the area of the final phase of each experiment can be explained as a combination of dilution; due to the continued addition of the alcohol solution, which increases the net volume therefore decreasing the average amount of sample in the beam, and the degradation of the beam; the intensity of the X-ray beam decreases with time.

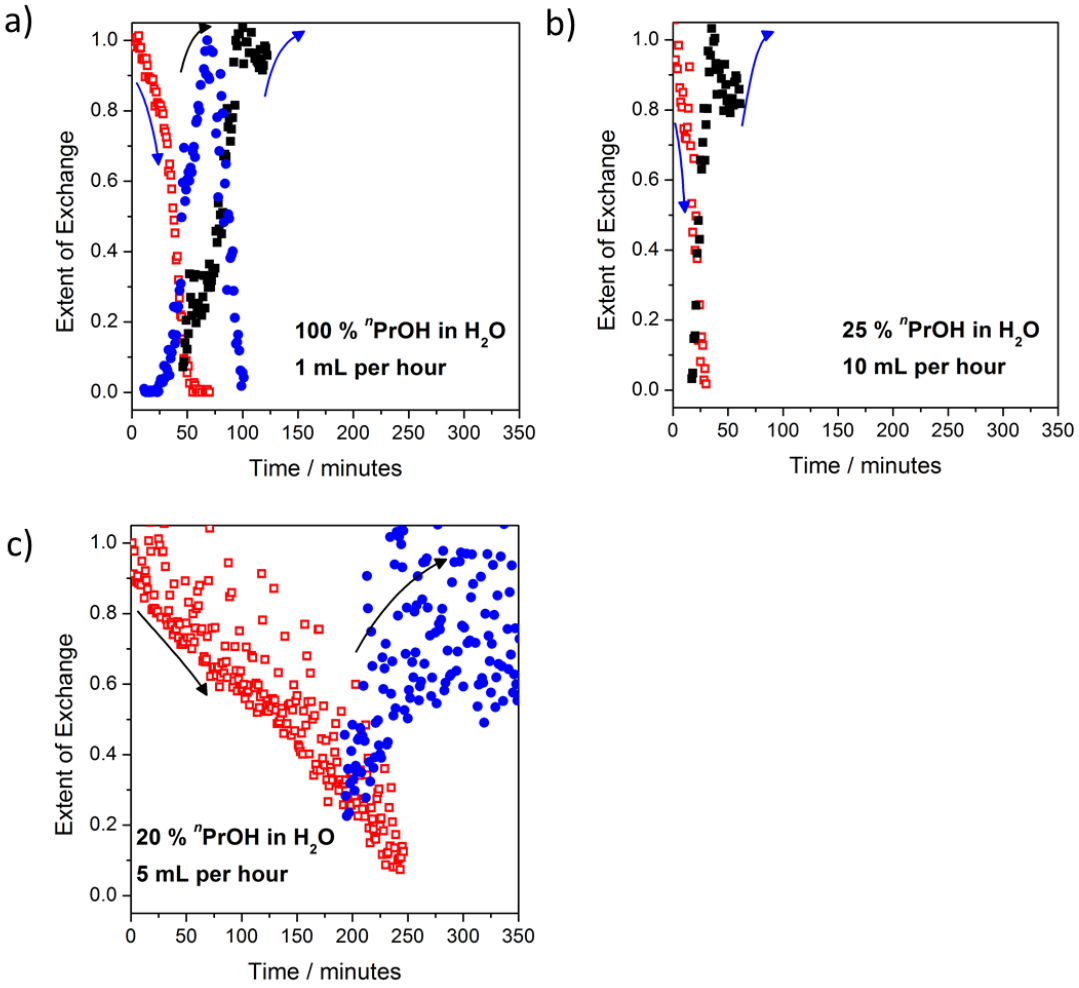

Figure 3.11: Extent of exchange graphs for propan-1-ol. Open red squares show the integrated area of the (110) peak of the hydrated phase, closed squares show the integrated area of the (200) peak of the fully-open phase and the closed blue circles show the integrated area of the (110) peak of the half-open phase.

The extent of exchange graph (Figure 3.12) for the addition of a 100% v/v solution of propan-*2*-ol shows that the decay of the hydrated phase and the growth of the half-open phase crossover at approximately 50% indicating that there is no intermediate phase seen upon expansion, as was observed from the contour plots.

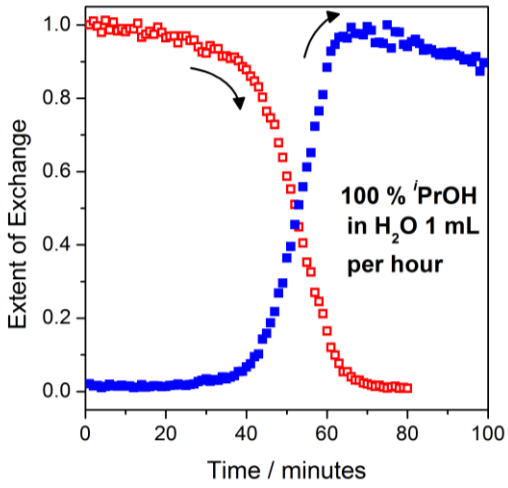

Figure 3.12: Extent of exchange graph for propan-2-ol. Open red squares show the integrated area of the (110) peak of the hydrated phase, and the closed blue squares show integrated area of the (110) peak of the half-open phase.

The results gained using simple alcohols allow *model* behaviour for the breathing of MIL-53(Fe) to be established. They show that the fluorinated framework does not immediately expand to its fullest but reacts to the size/shape of the molecules that are adsorbed. It is believed that the secondary alcohol, propan-*2*-ol, is sufficiently bulky that only one molecule can fit per pore but this molecule is not large enough to cause the framework to expand fully. However the primary alcohols show a two-step expansion via the half-open phase. It is thought that the half-open phase contains only one alcohol molecule per pore, either as the sole guest or as a mixture of alcohol and water. The fully-open phase is believed to contain two molar equivalents of alcohol which causes the framework to expand. This flexibility shows that the expansion of the framework is due to specific interactions between the host and the guest and not necessarily a general response to the removal or insertion of guests.

3.3 Studying the Uptake of S/N Containing Heterocycles

Using the model behaviour established for simple alcohols the adsorption of other molecules has been studied. The properties of MIL-53(Fe) are such that it may be possible to use the pores of the framework to remove favourably specific molecules from a given solution. One industrial application that would require this property is the removal of sulfur compounds from petrochemical fuels. The European Union mandated that the sulfur levels in commercial fuels be reduced to 10 ppm S (directive 2003/17/EC) to improve the efficiency of catalytic converters, which can be poisoned by sulphur compounds. The present method of removing S-compounds is hydrodesulfurisation (HDS), where the S-compounds are hydrogenated over a solid Co-Mo or Ni-Mo catalyst.[3] However, bulky compounds such as benzothiophene and dibenzothiophene cannot be efficiently hydrogenated using this technique[4, 5] and it has been found that nitrogen compounds, also present in fuels, can deactivate these catalysts preventing complete hydrogenation.[6, 7] Therefore, the removal of both N- and S-compounds would benefit this process. The work reported in this section proposes the use of partially fluorinated MIL-53(Fe) as a suitable material for the adsorption of N- and S-containing heterocycles. Other MOFs have been studied for the removal of these compounds. Most of the MOF structures, studied to date, have included coordinatively unsaturated sites (CUS) on metal centres,[8-15] which increases the heat of adsorption,[16] increasing the energy required for desorption.[17] Higher energy requirements for the desorption of guest molecules will hinder the usefulness of these materials for industrial applications. The uptake of dimethylsulfide by the relatively inflexible coordinatively saturated MIL-47(V)[18] has been reported. This study will investigate the uptake of bulkier S- and N- compounds such as benzothiophene using the flexible coordinatively

saturated MIL-53(Fe). This investigation aims to show the effect of the framework flexibility upon the adsorption of S- and N-compounds.

3.3.1 Energy Dispersive X-ray Diffraction Studies

It has been shown that many different molecules can be adsorbed within the pores of MIL-53(Fe) (Chapter 1) from simple alcohols to larger guests such as pyridine and lutidine.[1, 19] The results in this section show that the pores of the MIL-53(Fe) framework are capable of accommodating larger guests such as benzothiophene, benzothiazole and indole (Figure 3.13) which are the three guest molecules chosen for these experiments.

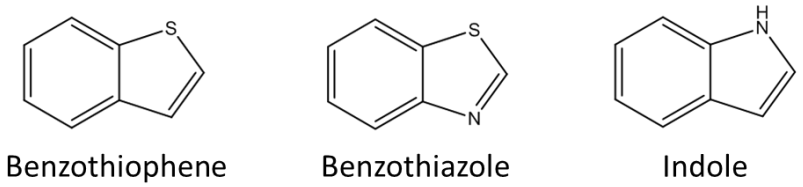

Figure 3.13: Three N/S containing heterocycles used for liquid phase adsorption studies

The uptake of these three bulky molecules was followed via energy dispersive X-ray diffraction (EDXRD). The experiments were performed in two different solvents to help study the effects of the solvent interactions. Isopropanol, a hydrophilic solvent known to be taken up by MIL-53(Fe) and heptane, a long-chain hydrophobic solvent known to interact poorly with MIL-53(Fe), were chosen as the two experimental solvents. Prior to these experiments, high-resolution X-ray diffraction (HRXRD) was used to obtain the unit cell parameters of MIL-53(Fe)[guest]. Solutions of the guest molecules in isopropanol were injected into capillaries containing MIL-53(Fe) powder. The capillaries were then centrifuged to concentrate the powder at the end of the capillary. The unit cell parameters obtained from a full Rietveld refinement (performed by N. Guillou, Institut Lavoisier) are shown below in Table 3.2.

Table 3.2: Unit cell parameters for MIL-53(Fe)[guest]. Values obtained from full Rietveld refinement of high-resolution XRD data.

Guest	**MIL-53(Fe) [benzothiophene]**	**MIL-53(Fe) [benzothiazole]**	**MIL-53(Fe) [indole]**
a/ Å	15.8023(5)	15.7727(7)	16.0647(6)
b/ Å	14.5731(4)	14.6253(6)	14.2624(5)
c/ Å	6.91279(9)	6.9026(2)	6.8769(2)
V/ Å^3	1591.93(7)	1592.3(1)	1575.6(1)
S. G.	*Imcm*	*Imcm*	*Imcm*

Isopropanol is known to only give the monoclinic half-open phase (*C2/c*, $V \approx 1200$ Å^3)[19] when adsorbed within the pores, this is in contrast to the molecules we are studying which give the fully-expanded orthorhombic phase (Table 3.2). The different symmetries of the framework induced by different guests mean that the progression of the uptake can be followed using powder X-ray diffraction. Heptane was chosen as an alternative solvent as it is more representative of the conditions for guest uptake from petrochemicals. When MIL-53(Fe) is stirred in heptane, preliminary tests show that it is not adsorbed by MIL-53(Fe) within the first 60 minutes; Bragg peaks from a secondary phase are only visible after 1.5 hours and after 10 hours adsorption is still not complete (Figure 3.14). Therefore, the framework should remain in its initial phase before addition of the guest molecules.

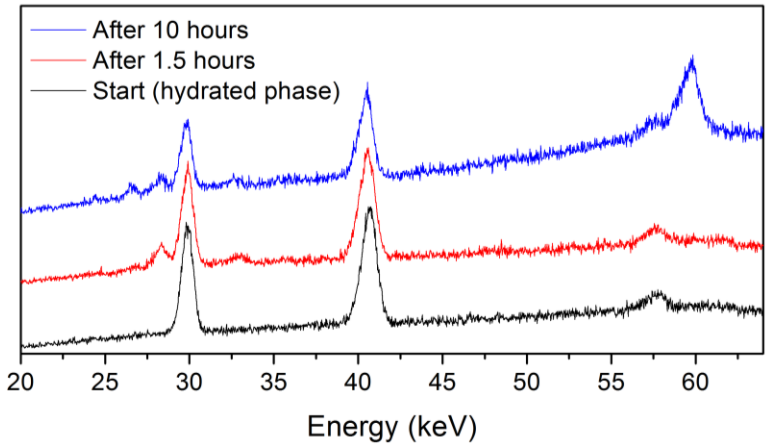

Figure 3.14: Adsorption of heptane by hydrated MIL-53(Fe)

For the initial tests two types of experimental procedure were used to follow the uptake of the guest molecules:

Static experiments- the guest solution and solvent were added straight to the test tube at the beginning of the experiment and data collection was started immediately. Final concentration = 5.2 M and the number of molar equivalents of guest present at end of the experiment = 10

Syringe pump experiments- the guest solution (10 mL) was added to a syringe and a calibrated syringe pump was used to control the addition of the solution to the test tube at a rate of 10 mL/hr. Final concentration = 0.67 M and the number of molar equivalents of guest present at end of the experiment = 5.6.

The contour maps shown below plot the energy of the Bragg peaks as a function of time. The Bragg peaks visible in the contour plots were indexed using the crystallographic data recorded using high-resolution XRD, the conversion of the EDXRD data from energy to *d*-spacing is shown in tables in the Appendix.

Figure 3.15 shows the results of the preliminary experiments performed in isopropanol, the contour plots confirm that all three guests cause the framework to expand fully. The

uptake of benzothiophene and indole was studied using the static experimental technique whereas the uptake of benzothiazole was followed using the syringe experimental technique; the expansion of the framework was too rapid to be followed using the static technique. Using the syringe technique, hydrated MIL-53(Fe) was suspended in isopropanol prior to the addition of the guest molecules with the result that the water present in the pores of hydrated MIL-53(Fe) was displaced by isopropanol; demonstrated by the presence of the Bragg peaks of the monoclinic half-open phase observed in the contour plot (Figure 3.15b). The timescale required for the completion of the benzothiophene and indole experiments provides evidence that benzothiophene is taken up more quickly by hydrated MIL-53(Fe); conversion to the fully-open benzothiophene phase is complete after 100 minutes whereas conversion to the fully-open indole phase takes more than 260 minutes.

In all three cases, the expansion from the initial phase to the fully-open phase is not gradual; the material is present in either one phase or the other. However, for benzothiazole, after expansion to the fully-open phase there is a slight shift of the Bragg peaks. The (110) peak of the fully-open phase shifts to lower energy and the (200) peak shifts to a higher energy, this is consistent with an expansion of the framework. It is suggested that this slight expansion is due to minor rearrangements of the guest molecules after adsorption. Benzothiazole contains S and N heteroatoms which are both able to interact with the host framework; this will be discussed later in more detail.

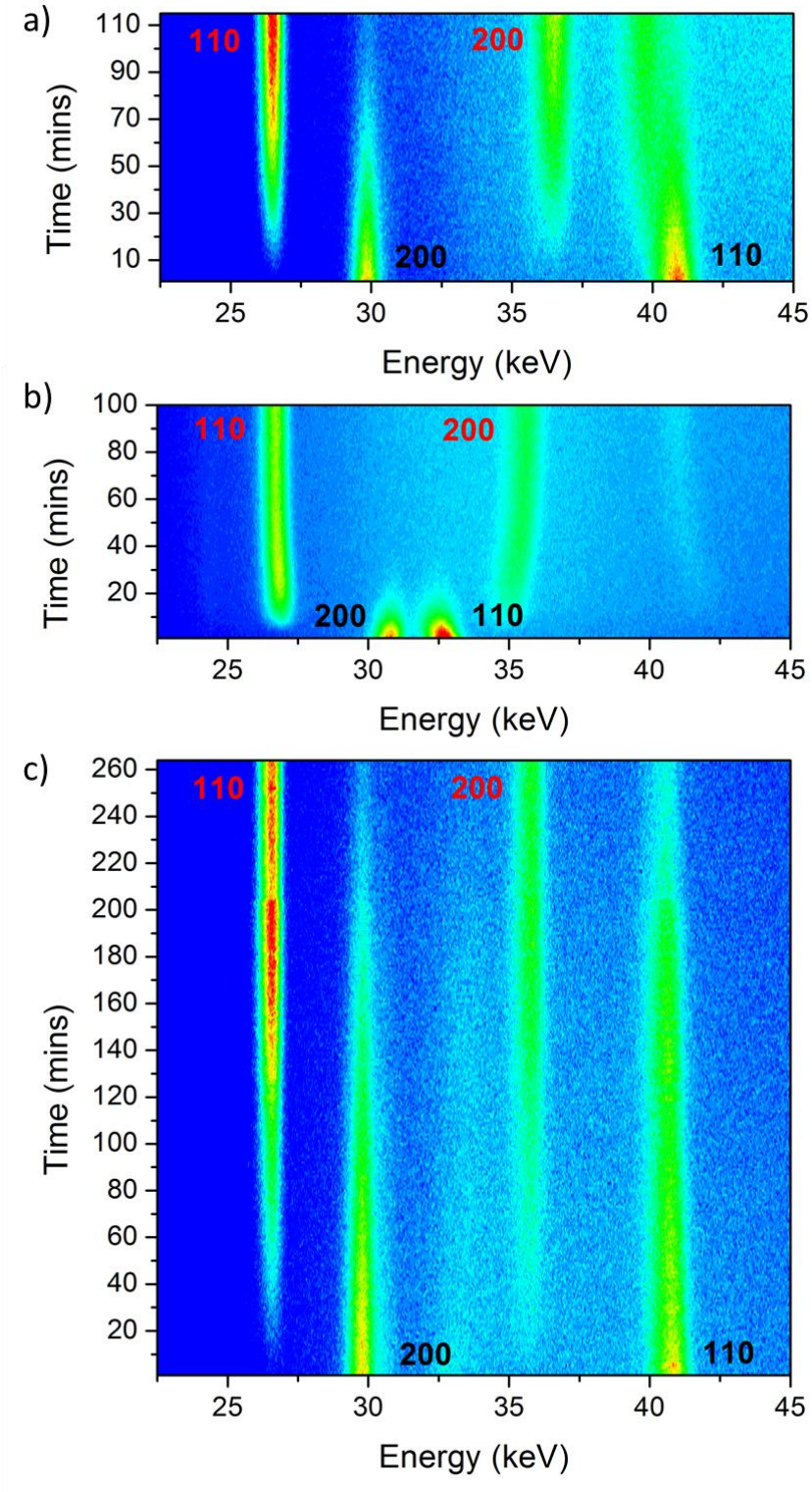

Figure 3.15: Contour plots showing the uptake of guest molecules in isopropanol a) benzothiophene (static experiment, 5.2 M) b) benzothiazole (syringe experiment, 0.67 M) and c) indole (static experiment, 5.2 M).

The static tests, where the MIL-53 remains in the hydrated phase prior to guest adsorption, gave the first evidence that the framework does not expand via the half-open

phase during the uptake of these bulky guest molecules. This is in contrast to the behaviour seen for some of the molecules that were previously studied. It is suggested that this is due purely to their bulkier size; one heterocycle molecule is too large to be able to occupy a contracted form of the framework, they require the full volume of the available pores of MIL-53(Fe).

To make these experiments more applicable to the potential industrial application, the separation of heterocycles from petroleum fuels, they were repeated, using both isopropanol and heptane, at lower concentrations of guest to see the effect, if any, on the ability of the framework to remove these molecules from solution. The concentration of the guest-solvent solution was chosen based on the maximum concentration of indole that could be dissolved in heptane. The maximum concentration was calculated to be 0.39 M, which was the concentration used in the syringe. Due to the solution being added to an additional 3 mL of solvent in the test tube the final concentration was 0.3 M. This corresponds to 2.5 molar equivalents of the guest per molar equivalent of host; the guest was always in excess at the end of each experiment.

For each guest the experiments were performed using both hydrated and dehydrated MIL-53(Fe) to investigate the effect that the water, contained in the pores of the framework, had on the uptake of these molecules. For the experiments using dehydrated MIL-53(Fe), which was dehydrated using the method described in Chapter 2.2.1.4, anhydrous isopropanol was used. The addition of the guest solutions was controlled by a syringe pump and set to a constant speed of 10 mL/hr as outlined above for this experimental technique.

The contour plots in Figure 3.16 show the uptake of the guest molecules by dehydrated MIL-53(Fe) in dry isopropanol; the initial phase at the start of each contour is the

monoclinic, *C2/c*, half-open phase, ~1200 $Å^3$. The contours show that uptake of benzothiazole by dehydrated MIL-53(Fe) in dry isopropanol is much faster than the uptake of benzothiophene. The experiment with benzothiophene never reaches completion in the time period studied (350 minutes); there is some of the initial half-open phase still present. Only the first 60 minutes of the indole experiment is shown as it was found that under these conditions, using low guest concentration and dehydrated MIL-53(Fe), the indole was not adsorbed. The test tube was re-examined in the beam periodically and after 28 hours there was still no evidence for any conversion to the fully-open phase (Figure A.1).

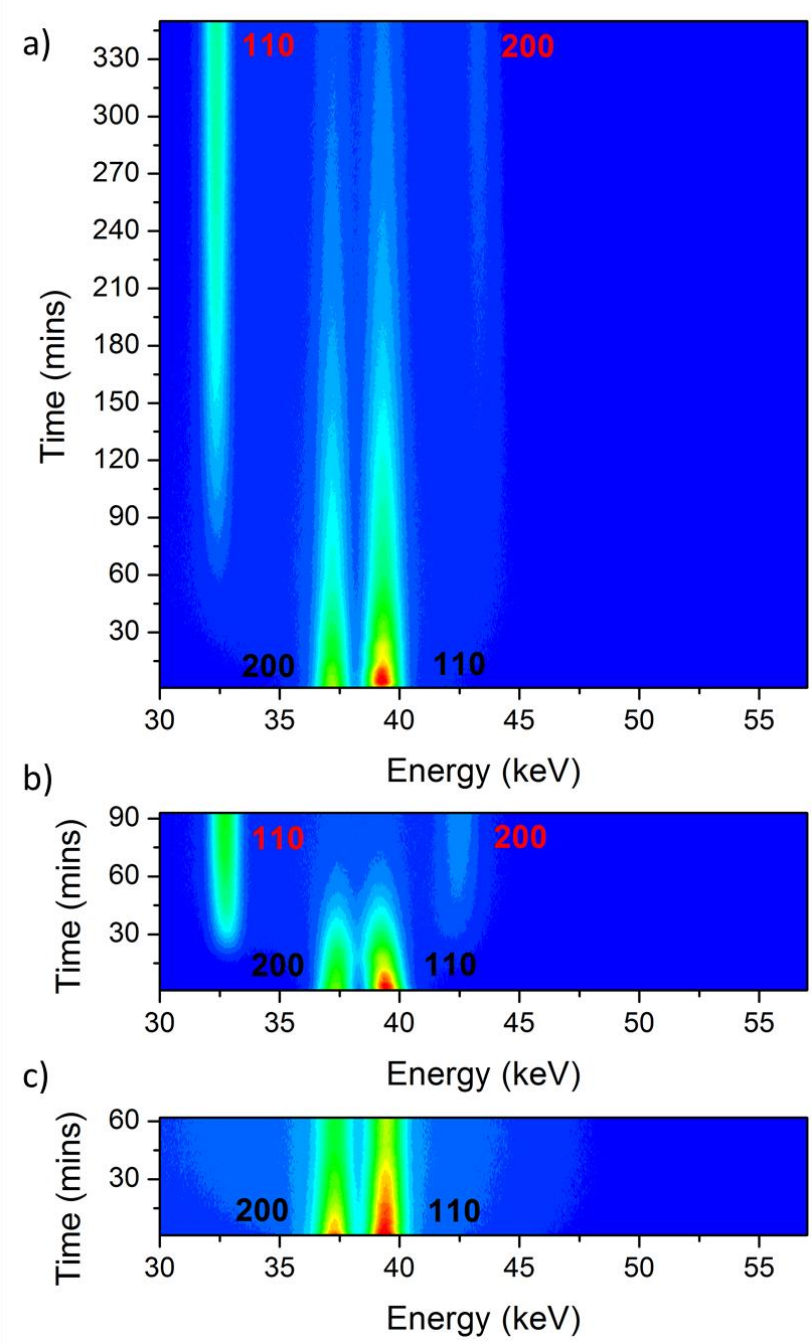

Figure 3.16: Contour plots showing the behaviour of dehydrated MIL-53(Fe) in dry isopropanol upon the addition of a) benzothiophene, b) benzothiazole and c) indole.

The contour plots for the heptane experiments performed with dehydrated MIL-53(Fe), Figure 3.17, show that the initial phase at the start of each experiment is the monoclinic, *C2/c*, dehydrated phase, ~900 $Å^3$; indicating that heptane was not adsorbed prior to guest addition. The contours show a similar trend as was seen for isopropanol; benzothiazole and benzothiophene are taken up by MIL-53(Fe) quickly while indole is

not taken up at all. However, the difference between benzothiazole and benzothiophene is less distinct than was seen in isopropanol; evidence for the fully-open phase can be seen very early-on in both experiments but benzothiazole continues to a higher conversion percentage than benzothiophene (this can be seen more clearly in the extent of conversion graphs in Figure 3.19).

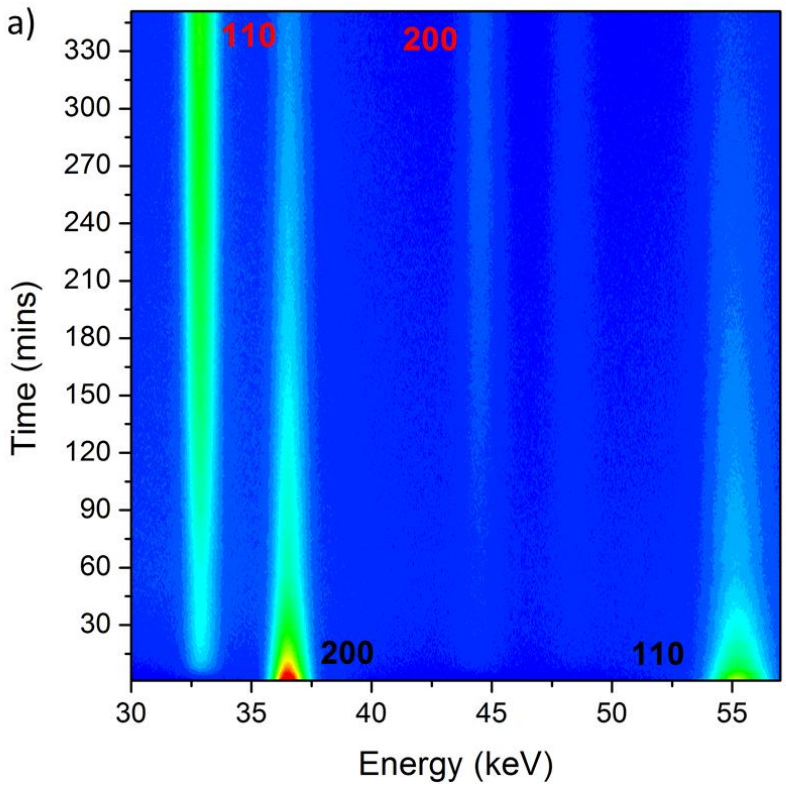

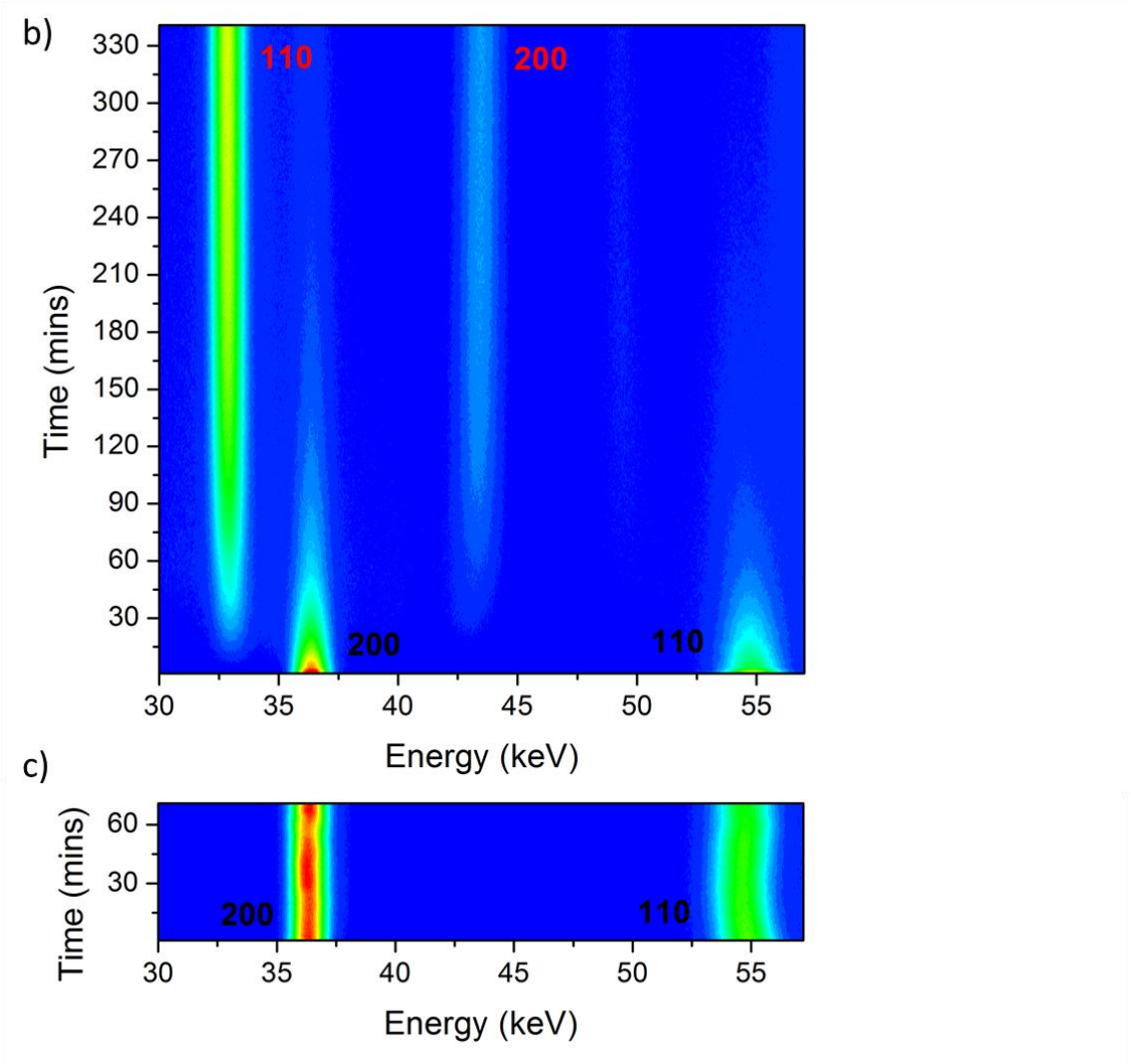

Figure 3.17: Contour plots showing the behaviour of dehydrated MIL-53(Fe) in heptane upon the addition of a) benzothiophene, b) benzothiazole and c) indole.

The results for the uptake of these heterocycles by hydrated MIL-53(Fe) in isopropanol show the same trend as was seen for dehydrated MIL-53(Fe) in isopropanol. Benzothiazole was adsorbed by the pores much more quickly than benzothiophene and indole was not taken up by the framework at all. In the contour plots for benzothiophene and indole there are Bragg peaks present that are due to the hydrated phase which was caused by the incomplete conversion of the hydrated phase to the half-open isopropanol phase before the experiment was started. This is more visible in the indole contour plot where the evolution of the hydrated (200) peak into the half-open (200) peak can be clearly seen. Experiments using hydrated MIL-53(Fe) and heptane were not possible

with the conditions used for the syringe pump experiments as efficient stirring could not be achieved due to the incompatibility of hydrophobic heptane with the hydrated solid.

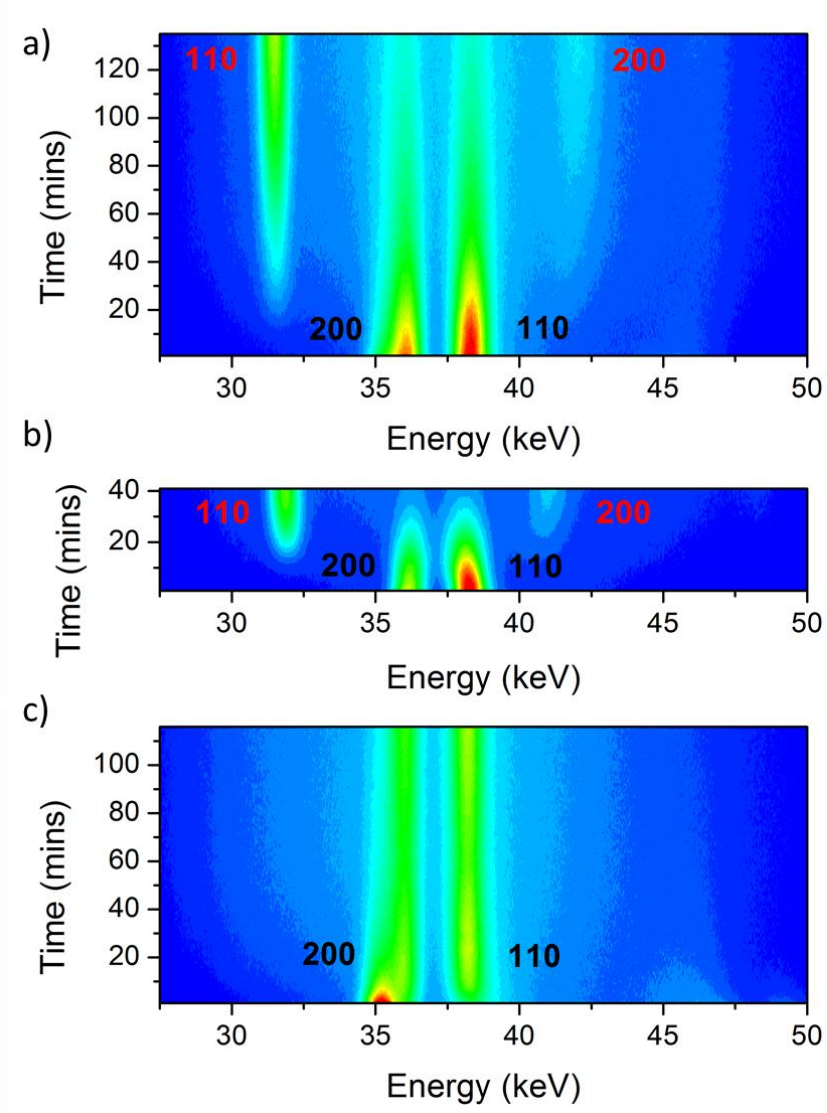

Figure 3.18: Contour plots showing the behaviour of hydrated MIL-53(Fe) in isopropanol upon the addition of a) benzothiophene, b) benzothiazole and c) indole.

It is clear from these experiments that benzothiophene and benzothiazole are still taken up by MIL-53(Fe) at these lower concentrations whereas indole is not. It can also be observed that the removal of the water molecules from the pores of MIL-53(Fe) did not affect the order of adsorption based on the rate of uptake; the order of preference seen for MIL-53(Fe) was always benzothiazole > benzothiophene > indole.

The contour plots above show that not all experiments went to completion as the peaks of the initial phase are still present in small amounts. To gain more information from these experiments the data were converted to extent of conversion curves which allows the data sets to be compared more directly.

As it was found that not all experiments reached completion, converting the data to extent of conversion graphs could not be done by normalising to the Bragg peak intensity of the final product. However, the contour plots show that evolution of pore opening does not proceed via any intermediate phases; there is only evolution from the initial to the fully-open phase. Therefore, assuming that the transition from one phase to the other is directly related, the decay of the initial phase can be used as an indication of the growth of the fully-open phase. This method also gives an indication of the percentage of completion of each experiment.

The strongest Bragg peak from the starting phase was integrated and then the complement of the normalised data (Equation 3.1) was used to create the extent of conversion graphs.

$$\boldsymbol{x_c = 1 - x_n}$$

Equation 3.1

(x_n is the normalised data and x_c is the complement of the data).

These data have been plotted as a function of time and also as a function of concentration. As the concentration of the guest solution was known and the rate of addition was controlled, the concentration at any given time can be calculated. This comparison is important as it is the behaviour of MIL-53(Fe) towards low

concentrations of guest molecules that is of interest in practical applications such as the removal of contaminant molecules.

From the graphs in Figure 3.19 it can be concluded that benzothiazole is taken up faster than benzothiophene under all conditions. Benzothiazole is taken up marginally slower from heptane than from isopropanol; it takes longer for MIL-53(Fe) to reach its maximum conversion. In contrast, the initial rate of uptake of benzothiophene is quicker in heptane compared to isopropanol but the final conversion maximum is approximately equal for both solvents when using dehydrated MIL-53(Fe). These graphs highlight that evolution of the structure continues after complete addition of the guest solution at 60 minutes. It should be noted that the experiments performed with hydrated MIL-53(Fe) were not studied for long enough so have not reached equilibration but information about the general trend of uptake can still be obtained. The results for indole have not been included as the EDXRD studies showed that indole was not adsorbed by MIL-53(Fe) under the conditions used.

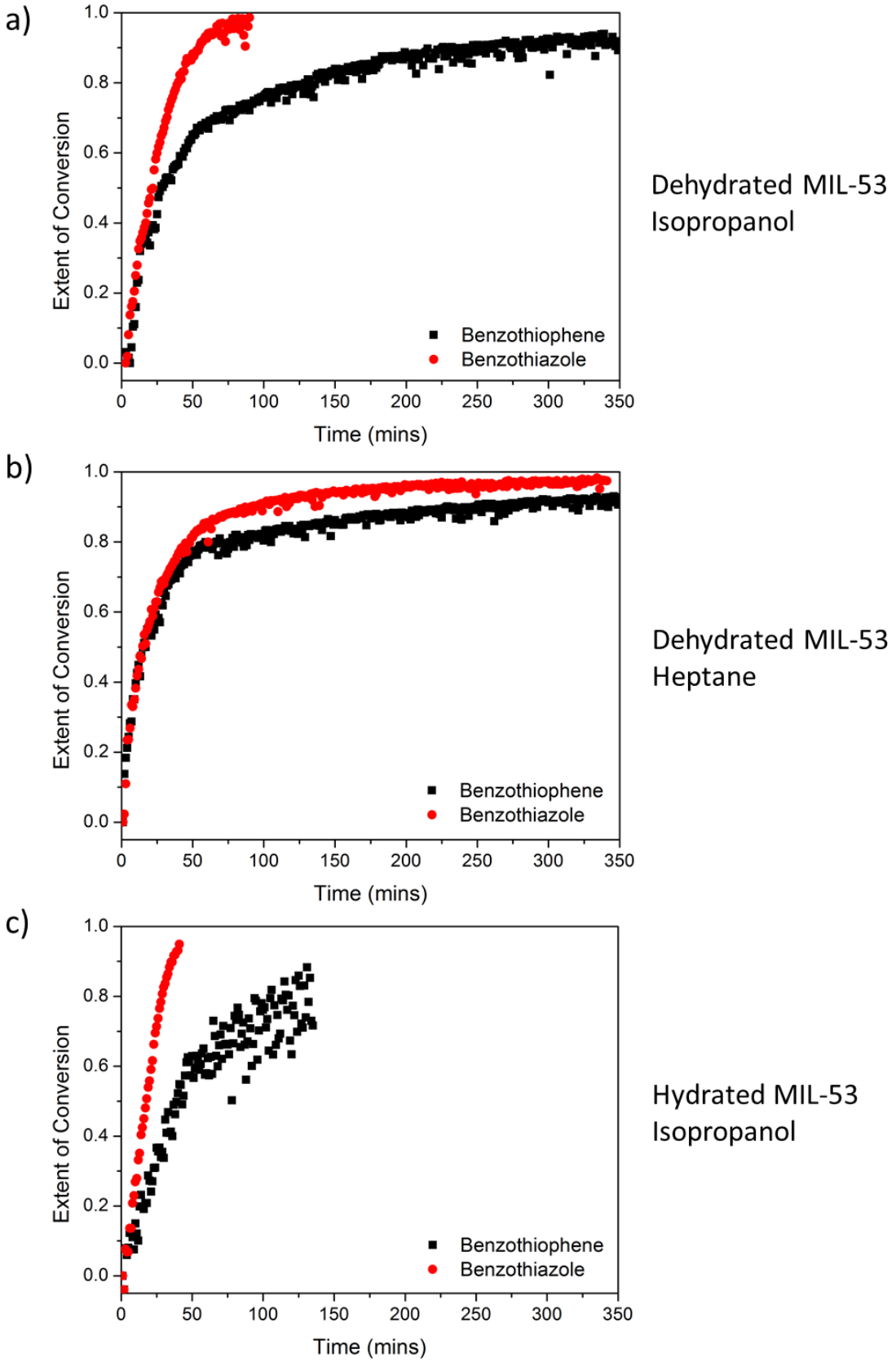

Figure 3.19: Extent of conversion as a function of time for the slow addition of benzothiophene and benzothiazole to a) dehydrated MIL-53(Fe) and isopropanol, b) dehydrated MIL-53(Fe) and heptane and c) hydrated MIL-53(Fe) and isopropanol.

From extent of conversion graphs versus guest concentration (Figure 3.20) it can be seen that at the point of complete addition (0.3 M) benzothiazole is always between 85-95% completely converted to the fully-open phase whereas benzothiophene only reaches between 65-80% of full conversion. Comparison of the lower concentrations between the heptane and isopropanol experiments shows that there is a clear solvent effect that influences the initial uptake of the guest. For both benzothiophene and benzothiazole the experiments in heptane show pore opening commences as low as 0.05 M whereas pore opening is only seen between 0.08 - 0.1 M in isopropanol.

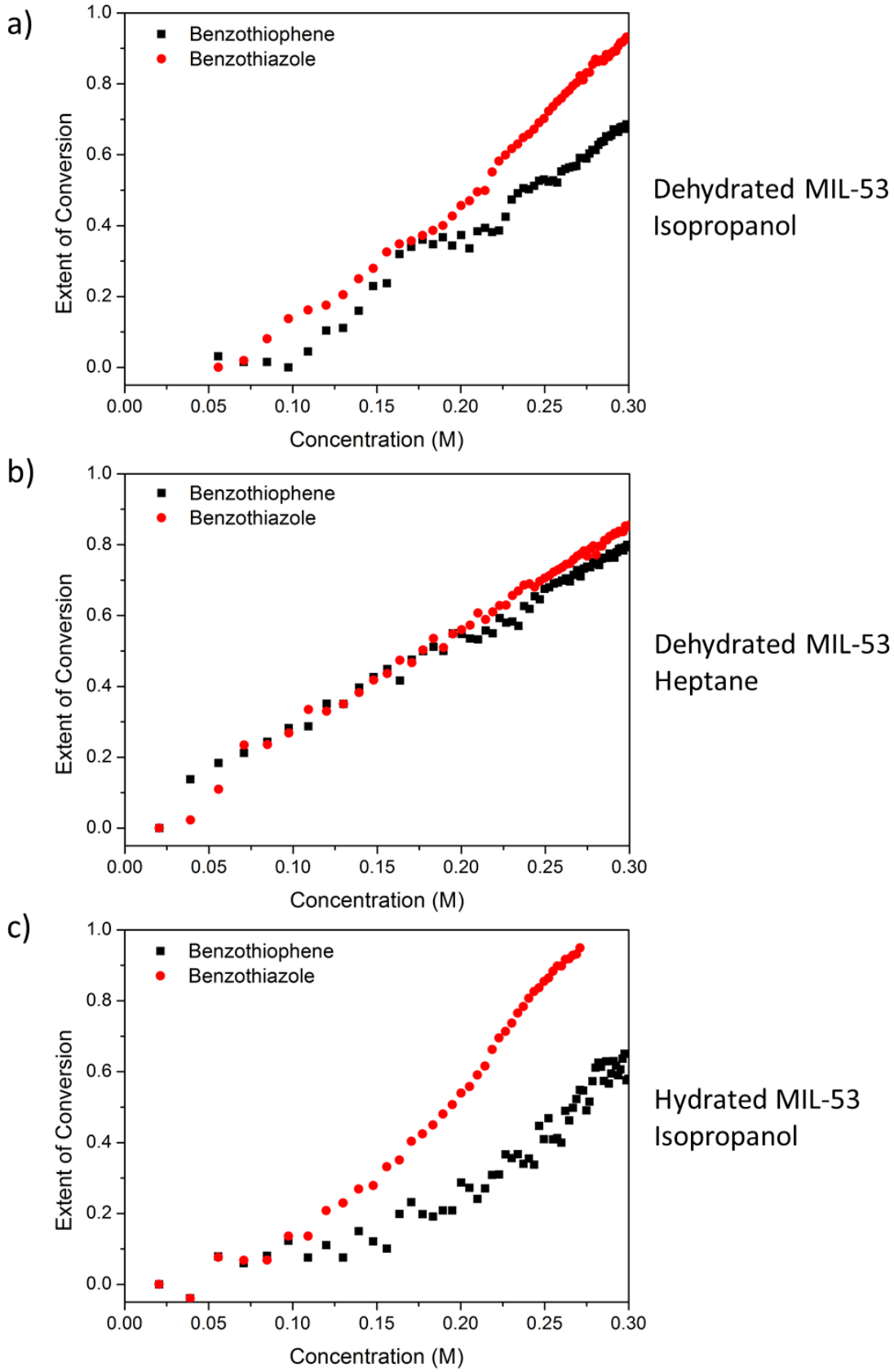

Figure 3.20: The extent of conversion as a function of time for the slow addition of benzothiophene and benzothiazole to a) dehydrated MIL-53(Fe) and isopropanol, b) dehydrated MIL-53(Fe) and heptane and c) hydrated MIL-53(Fe) and isopropanol.

Table 3.3 shows the percentage of the framework that was converted to the fully-open phase after complete addition of the guest solution; complete addition was reached after 60 minutes, the concentration at this point was 0.3 M. Also given in the table is the concentration at which the material is first observed to adsorb the guest molecules.

Table 3.3: The maximum conversion percentages immediately after complete addition at 0.3 M (60 minutes) and the concentration at which MIL-53(Fe) first takes up the guest molecule.

Guest	MIL-53(Fe)	Solvent	Conversion at 0.3 M/ %	Initial Uptake Concentration/ M
Benzothiophene	Dehydrated	Isopropanol	68	0.11
		Heptane	79	0.039
	Hydrated	Isopropanol	64	0.16
		Heptane	-	-
Benzothiazole	Dehydrated	Isopropanol	93	0.08
		Heptane	85	0.056
	Hydrated	Isopropanol	94	0.11
		Heptane	-	-

3.3.2 Studying the Adsorption using other Techniques

The time-resolved EDXRD results have been used in conjunction with adsorption isotherm measurements recorded at the Katholieke Universiteit Leuven (KUL) in Belgium to further the understanding of the different phenomena that affect the adsorption of these molecules. It should be noted that the difference between these experiments and the EDXRD studies is that for each adsorption data point the suspension of guest and host was stirred for a period of hours to allow for equilibration. Measurements taken on the supernatant solution allows the mass of guest taken up by the framework to be calculated which allows the number of equivalents of guest to be

found. The isotherm data recorded at KUL are shown in Figure 3.21. In contrast to the EDXRD results they show that a small amount of indole is adsorbed by both dehydrated and hydrated MIL-53(Fe) from heptane, however such a small amount could be accounted for by surface adsorption, which would not result in an expansion of the framework. These results show the guest concentration threshold, seen in the EDXRD studies for isopropanol, much more clearly; at very low guest concentrations, adsorption is not seen until the concentration reaches ~0.05 M, whereas guest adsorption is seen at very low concentrations in heptane. The results also show that under most conditions a higher weight percentage of benzothiazole, compared with benzothiophene, is always adsorbed by MIL-53(Fe). There is one exception; dehydrated MIL-53(Fe) in isopropanol adsorbs a higher weight percentage of benzothiophene than benzothiazole.

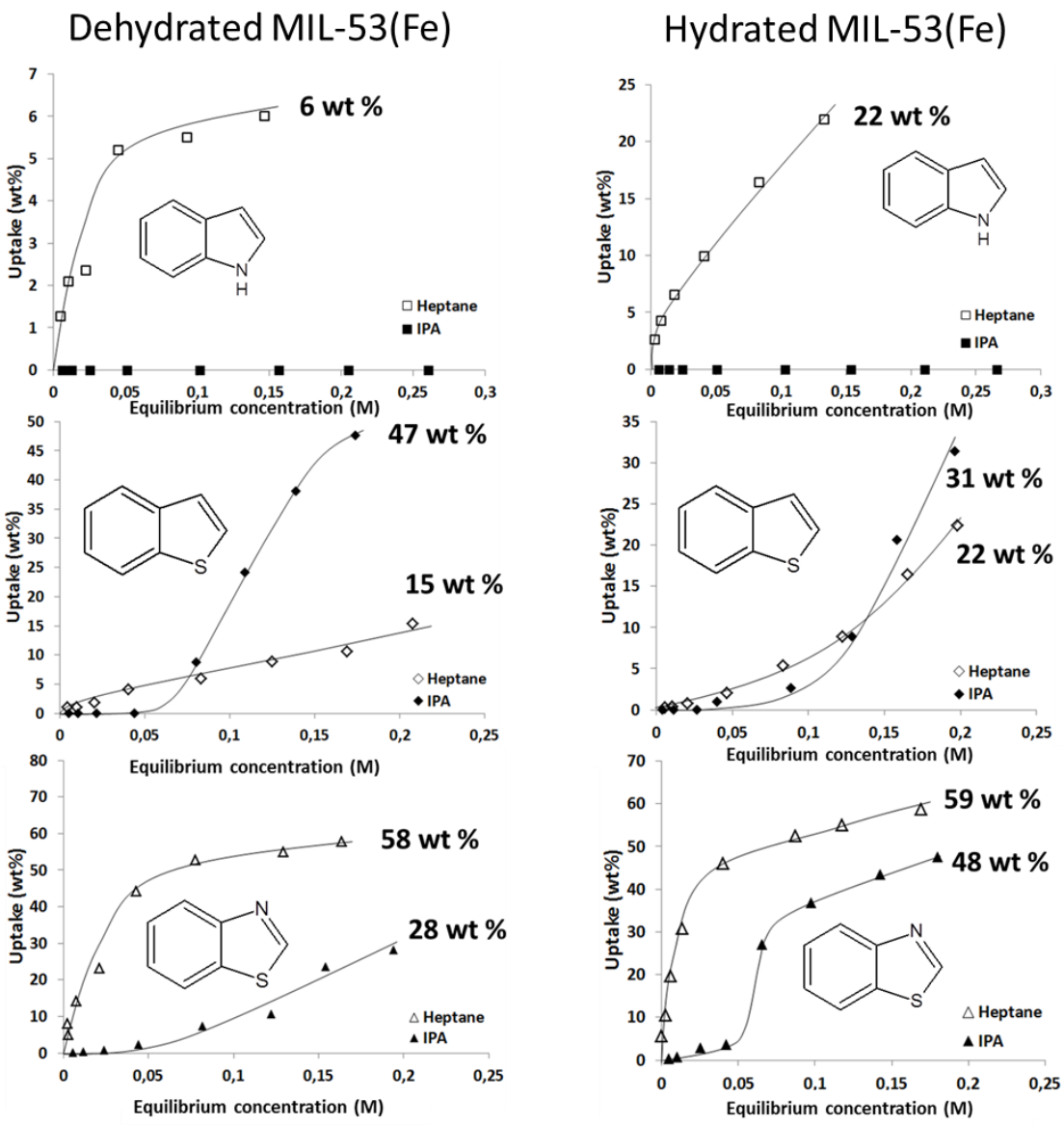

Figure 3.21: Adsorption isotherm measurements recorded at KUL. The left-hand column shows the results for dehydrated MIL-53(Fe) and the right-hand column shows the results for hydrated MIL-53(Fe)

The results of the adsorption isotherm experiments are tabulated below (Table 3.4) indicating the number of molar equivalents of guest molecules that were taken up by the framework at the maximum concentration of approximately 0.2 M.

Table 3.4: The number of molar equivalents that were taken up by MIL-53(Fe) during adsorption isotherm measurements. Recorded at KUL, Belgium.

Guest	MIL-53(Fe)	Solvent	Total Number of Molar Equivalents per Fe
Benzothiophene	Dehydrated	Isopropanol	0.83
		Heptane	0.27
	Hydrated	Isopropanol	0.59
		Heptane	0.42
Benzothiazole	Dehydrated	Isopropanol	0.39
		Heptane	1.02
	Hydrated	Isopropanol	0.91
		Heptane	1.12
Indole	Dehydrated	Isopropanol	0
		Heptane	0.12
	Hydrated	Isopropanol	0
		Heptane	0.48

IR spectroscopy was used to investigate if the solvent was present in the pores after the adsorption of the different guest molecules. Hydrated MIL-53(Fe) was stirred in solutions of solvent and guest, where the total molar equivalents of guest was always in excess compared to the molar equivalents of host. The suspensions were stirred overnight (>15 hours) to ensure equilibration was reached, the solid was collected and the spectra were recorded at room temperature. The spectra for MIL-53(Fe) stirred in the pure solvents were also recorded so that characteristic peaks due to the solvent could be identified. The graphs, shown in Figure 3.22, compare the spectra for the different guest molecules adsorbed from solutions of isopropanol and heptane; the spectrum for hydrated MIL-53(Fe) is shown for comparison. The characteristic peaks for isopropanol were identified as an OH band at 3334 cm^{-1}, an aliphatic CH stretch at 2934 cm^{-1} and a C-OH stretch at 950 cm^{-1} (these have been marked on the graph). As these three peaks

are not present in the spectra of MIL-53(Fe) fully exchanged with the guest molecules it can be concluded that the isopropanol was not taken up simultaneously with the guest molecules or that it was fully displaced by the guest molecules. The presence of heptane inside the pores was monitored by the presence of the characteristic aliphatic CH vibrations in the 2900 cm^{-1} region (marked on the graph). These characteristic peaks are not seen in the spectra for the solid containing the guest molecules therefore it is concluded that heptane is not present in the pores after the guest molecules are adsorbed.

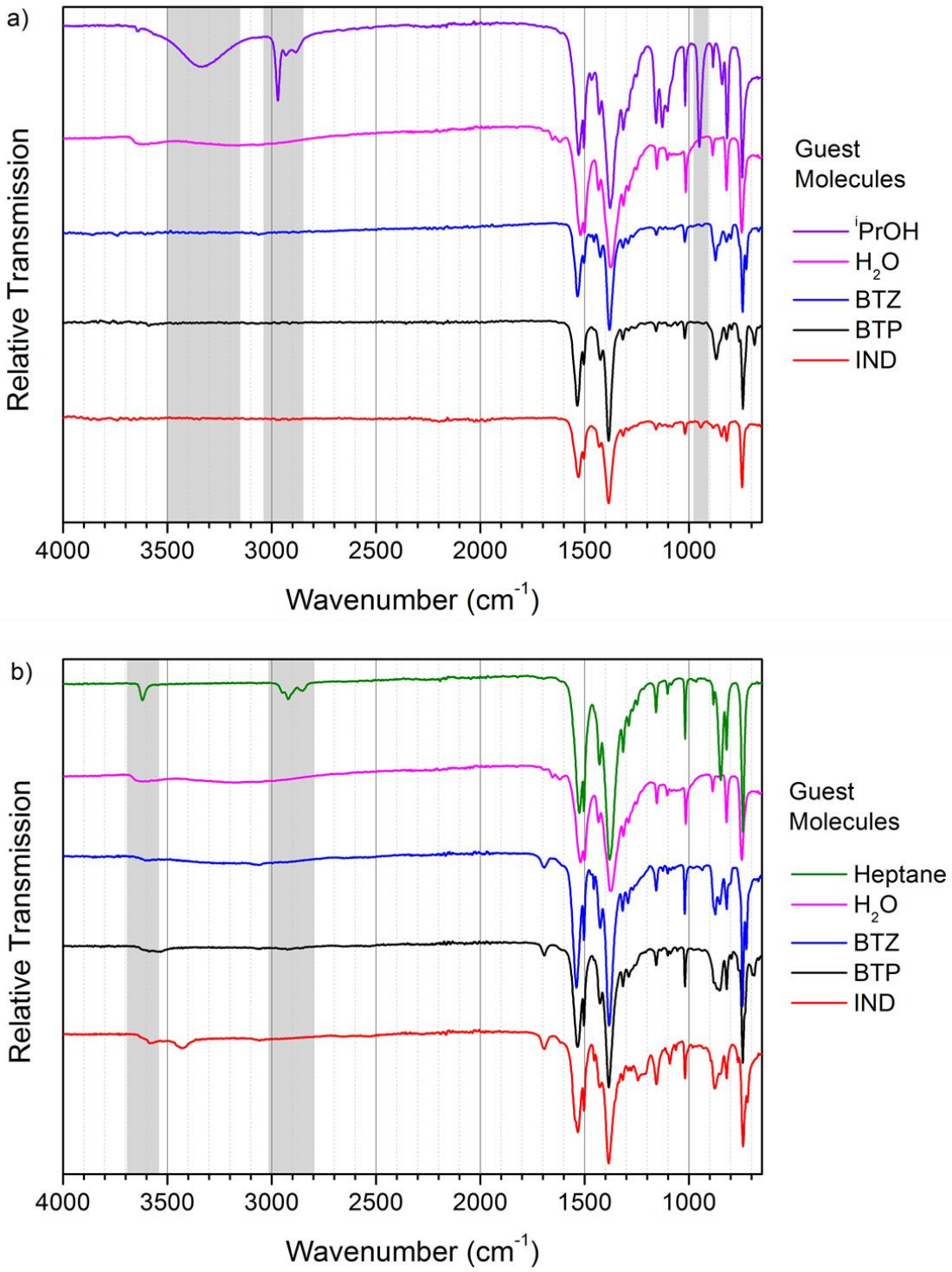

Figure 3.22: Infrared spectra of MIL-53(Fe) after the adsorption of different guest molecules

3.3.3 Discussion of Possible Interactions

The exact nature of the interactions acting on the guest and host in these experiments is not always known but there are various possible interactions that could be influencing the outcome of guest exchange, they can be grouped into five categories:

- Host-host
- Guest-guest
- Host-guest
- Host-solvent
- Guest-solvent

Host-host: interactions between framework π systems, that are thought to be responsible for the spontaneous closing of the MIL-53(Fe) framework upon removal of all occluded molecules,[20] could affect the rate of uptake of the guest molecules where the framework is in the dehydrated phase.

Guest-guest: all three of the guest molecules are aromatic and therefore have the potential for π - π interactions. This could influence their solubility in the solvent and the way they interact within the pores of the framework but at low concentrations this is unlikely to have an effect on the rate of uptake.

Host-guest: the MIL-53(Fe) structure has a high affinity for hydrogen bond acceptors as the hydrogen of the bridging –OH group points directly into the pores of the framework whereas the oxygen of this group is sterically hindered. Small aromatic molecules *e.g.* pyridine, have been shown to hydrogen bond to the framework via the nitrogen group,[2] making this a possible interaction for the larger heterocycles. Benzothiazole can act as a hydrogen bond acceptor through the sulfur and nitrogen atoms, the more electronegative

nitrogen would give the strongest interaction. Benzothiophene also acts as a hydrogen bond acceptor through the sulfur atom, whereas, in contrast, indole is a hydrogen donor via the N–H group. This interaction can explain why at low concentrations there is no uptake of indole as it is unable to form hydrogen bonds with the framework. Guest molecules without the ability to form hydrogen bonds have also been shown to be taken up by MIL-53(Fe). The isomers of xylene are reported to stack parallel to the terephthalate rings with separation distances that are indicative of π-π interactions.[21] As all three guest molecules are aromatic it is possible that they would interact in this manner rather than forming hydrogen bonds, this could explain how indole interacts with the framework when present at higher concentrations.

Host-solvent: there is the possibility of a favourable hydrogen-bonding interaction between isopropanol and the framework OH groups therefore the solvent is assumed to be in direct competition with the guest molecules. This interaction must be overcome, which explains the threshold concentration observed for guest uptake in the isopropanol experiments; a certain concentration of guest would be required to ensure that displacement of isopropanol was favourable. For heptane this is not true; a control experiment revealed that the uptake of heptane by MIL-53(Fe) is very slow (Figure 3.14). Evidence for pore opening can only be seen after 90 minutes. However, after 15 hours the resulting product is a mixed phase structure that cannot be resolved (Figure Figure A.2). This highlights that there is only a very weak interaction between heptane and the framework which in turn means that there will be no conflicting interactions for the guest molecules to overcome; this gives rise to a lower concentration threshold for guest uptake.

Guest-solvent: all three guest molecules are polar in nature therefore they interact more strongly with isopropanol than with heptane. This contributes to the observation of a threshold concentration for isopropanol; it requires a higher concentration of guest to overcome this interaction.

An additional observation made during these experiments was that the colour of MIL-53(Fe) changes upon the addition of benzothiophene from pale yellow to orange, which deepens with concentration. The colour changes of the other two guests are minimal (benzothiazole stays a pale yellow and indole changes to a pale brown). Fe^{III} is a 6-coordinated metal centre therefore has no coordinatively unsaturated sites (CUS)[22] available for metal-ligand interactions so no ligand-metal charge transfer can occur, which have been reported as a cause for brightly coloured materials.[23] To determine if the colour change is due to a specific interaction between benzothiophene and the MIL-53(Fe) structure, UV-Vis spectra for solutions of benzothiophene, terephthalic acid and a mixture of both were recorded. While the solutions for the individual compounds were transparent the solution of the mixed compounds was orange in colour due to a transition at 538 nm (Figure 3.23a). This transition is in the same spectral region as the increase in adsorption seen for the diffuse reflectance spectrum of the solid MIL-53(Fe)[benzothiophene] (Figure 3.23b), this spectrum was recorded by researchers at KUL. This suggests that the colour change is due to an interaction between benzothiophene and the linkers of MIL-53(Fe). Similar interactions were proposed for thiophene and dimethylsulphide in MIL-47(V)[18] where crystallography studies found the sulfur atoms to be orientated towards the terephthalate linkers. Computational studies show weak π-S interactions are possible for H_2S and benzene. [24-27] Although weak, the importance of these interactions in biological systems has been recognised.[28, 29]

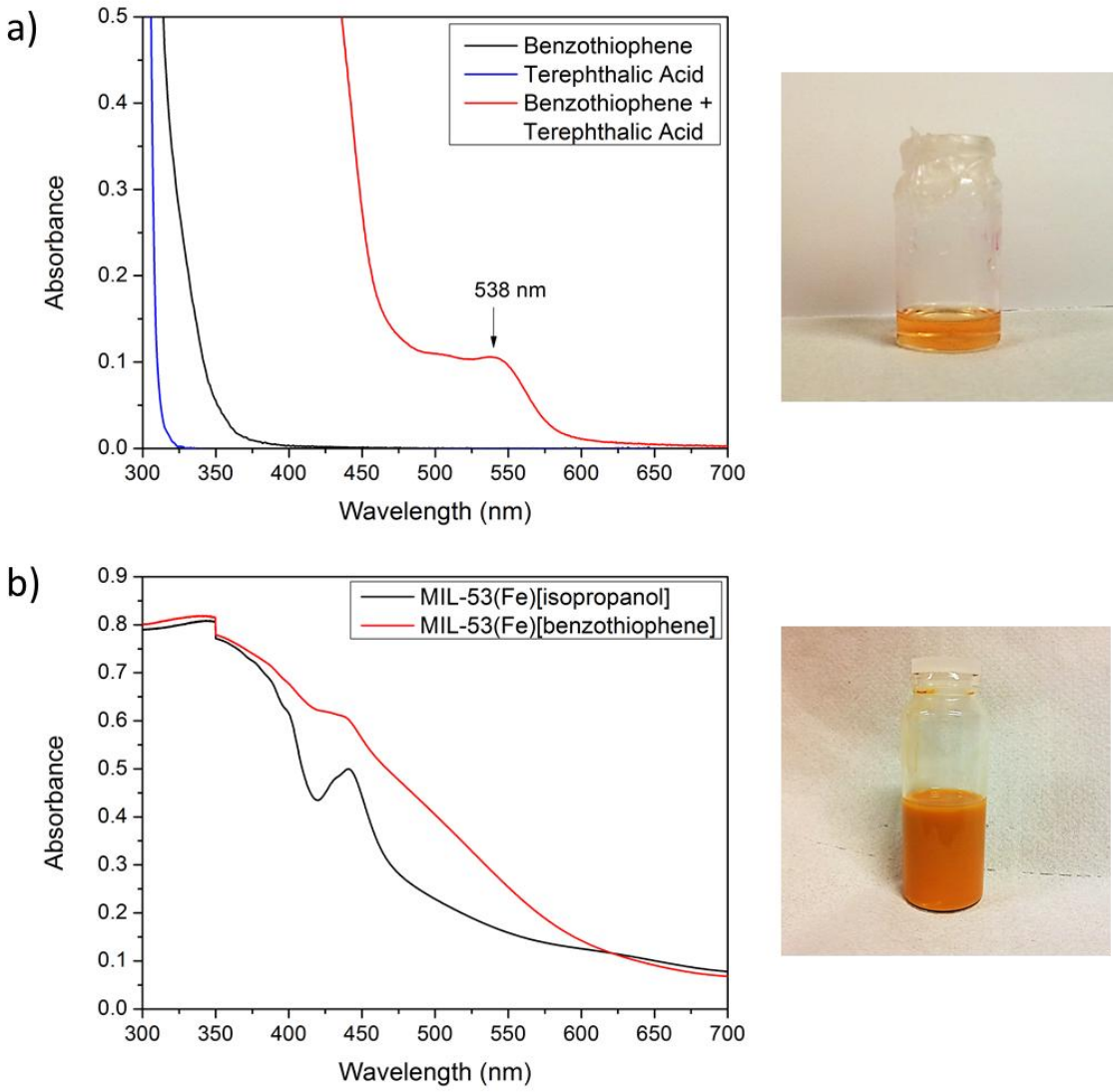

Figure 3.23: Graph a) shows the UV-Vis spectra for three different solutions, benzothiophene, terephthalic acid and a mixture of benzothiophene and terephthalic acid. The photo shows the mixture of benzothiophene and terephthalic acid in DMF. Graph b) shows the diffuse reflectance data for the two solids MIL-53(Fe)[isopropanol] and MIL-53(Fe)[benzothiophene]. The photo shows a suspension of MIL-53(Fe)[benzothiophene] in isopropanol.

The results presented in this section demonstrate the benefit of using complementary techniques to study the adsorption of guest molecules. The EDXRD results recorded using synchrotron radiation show good agreement with the adsorption isotherm data collected by the De Vos research group from KUL. The combination of the techniques allows for the exact number of adsorbed guest molecules to be calculated and the change in pore volume to be followed. The results show that the adsorption of these N/S heterocycles lead to the complete expansion of the framework to give the fully-open,

~1600 $Å^3$, *Imcm* phase. The framework was shown to have a remarkable preference for hydrogen bond acceptors such as benzothiazole and benzothiophene regarding both capacity and kinetics. The solvent was also shown to influence the adsorption of guest molecules; where the solvent was initially adsorbed by the framework, in the case of isopropanol, there was a guest concentration threshold that was required before the interaction of the solvent and the host could be overcome. Heptane was not adsorbed prior to guest adsorption therefore this guest concentration threshold was not present. This work also shows that these N/S containing pollutants can be removed from the liquid phase at ambient conditions, an important feature for the development of low energy adsorbents. Other MOF materials have been studied for the adsorption of N/S compounds however, as described in Section 3.3, these materials contain coordinatively unsaturated sites that form strong interactions with the guest molecules, making desorption more difficult. Therefore, MIL-53(Fe), a material with no coordinatively unsaturated sites, represents an attractive alternative for the development of a recyclable adsorbent.

3.4 References

1. F. Millange, C. Serre, N. Guillou, G. Férey and R. I. Walton, *Angew. Chem. Int. Ed.*, 2008, **47**, 4100-4105.

2. F. Millange, N. Guillou, M. E. Medina, G. Férey, A. Carlin-Sinclair, K. M. Golden and R. I. Walton, *Chem. Mater.*, 2010, **22**, 4237-4245.

3. R. T. Yang, *Adsorbents: Fundamentals and Applications*, John Wiley & Sons Inc., 2003, vol.

4. T. Kabe, A. Ishihara and H. Tajima, *Ind. Eng. Chem. Res.*, 1992, **31**, 1577-1580.

5. C. Song and X. Ma, *Appl. Catal., B*, 2003, **41**, 207-238.

6. W. Kaernbach, W. Kisielow, L. Warzecha, K. Miga and R. Klecan, *Fuel*, 1990, **69**, 221-224.

7. M. Macaud, M. Sévignon, A. Favre-Réguillon, M. Lemaire, E. Schulz and M. Vrinat, *Ind. Eng. Chem. Res.*, 2004, **43**, 7843-7849.

8. N. A. Khan and S. H. Jhung, *Angew. Chem. Int. Ed.*, 2012, **51**, 1198-1201.

9. N. A. Khan and S. H. Jhung, *Fuel Process. Technol.*, 2012, **100**, 49-54.

10. M. Maes, M. Trekels, M. Boulhout, S. Schouteden, F. Vermoortele, L. Alaerts, D. Heurtaux, Y.-K. Seo, Y. K. Hwang, J.-S. Chang, I. Beurroies, R. Denoyel, K. Temst, A. Vantomme, P. Horcajada, C. Serre and D. E. De Vos, *Angew. Chem. Int. Ed.*, 2011, **50**, 4210-4214.

11. D. Peralta, G. Chaplais, A. Simon-Masseron, K. Barthelet and G. D. Pirngruber, *Energy Fuels*, 2012, **26**, 4953-4960.

12. F. Shi, M. Hammoud and L. T. Thompson, *Appl. Catal., B*, 2011, **103**, 261-265.

13. H.-X. Zhang, H.-L. Huang, C.-X. Li, H. Meng, Y.-Z. Lu, C.-L. Zhong, D.-H. Liu and Q.-Y. Yang, *Ind. Eng. Chem. Res.*, 2012, **51**, 12449-12455.

14. K. A. Cychosz, A. G. Wong-Foy and A. J. Matzger, *JACS*, 2008, **130**, 6938-6939.

15. N. A. Khan, J. W. Jun, J. H. Jeong and S. H. Jhung, *Chem. Commun.*, 2011, **47**, 1306-1308.

16. H. J. Park and M. P. Suh, *Chem. Commun.*, 2012, **48**, 3400-3402.

17. E. A. Van Nierop, S. Hormoz, K. Z. House and M. J. Aziz, *Energy Procedia*, 2011, **4**, 1783-1790.

18. L. Liu, X. Wang and A. J. Jacobson, *J. Mater. Res.*, 2009, **24**, 1901-1905.

19. R. I. Walton, A. S. Munn, N. Guillou and F. Millange, *Chem. Eur. J.*, 2011, **17**, 7069-7079.

20. G. Férey and C. Serre, *Chem. Soc. Rev.*, 2009, **38**, 1380-1399.

21. R. El Osta, A. Carlin-Sinclair, N. Guillou, R. I. Walton, F. Vermoortele, M. Maes, D. de Vos and F. Millange, *Chem. Mater.*, 2012, **24**, 2781-2791.

22. F. Millange, N. Guillou, R. I. Walton, J. M. Greneche, I. Margiolaki and G. Férey, *Chem. Commun.*, 2008, 4732-4734.

23. A. Lever, *Inorganic Electronic Spectroscopy*, 2nd edn., Elsevier, Amsterdam, 1984.

24. C. A. Morgado, J. P. McNamara, I. H. Hillier, N. A. Burton and M. A. Vincent, *J. Chem. Theory Comput.*, 2007, **3**, 1656-1664.

25. R. J. Zauhar, C. L. Colbert, R. S. Morgan and W. J. Welsh, *Biopolymers*, 2000, **53**, 233-248.

26. T. P. Tauer, M. E. Derrick and C. D. Sherrill, *J. Phys. Chem. A*, 2004, **109**, 191-196.

27. J. Pranata, *Bioorg. Chem.*, 1997, **25**, 213-219.

28. G. Duan, V. H. Smith and D. F. Weaver, *Mol. Phys.*, 2001, **99**, 1689-1699.

29. G. Némethy and H. A. Scheraga, *Biochem. Biophys. Res. Commun.*, 1981, **98**, 482-487.

Chapter 4

Gas Phase Studies

4 Studies of the Gas Phase Breathing of MIL-53 Materials

This chapter describes the interactions of the various forms of the MIL-53 framework with simple guest molecules in the gas phase. This includes materials with different metal centres and modified linkers. The work in Section 3.2 with MIL-53(Fe) is extended here to include vapour phase adsorption of methanol. A detailed investigation into methanol adsorption using *in situ* X-ray diffraction to follow the expansion and contraction of the framework is described. Also included are thermogravimetric and inelastic neutron scattering experiments. The concept of modifying metal-organic frameworks to alter their properties and hence change their response to different guest molecules has been investigated by following the adsorption and desorption of guest molecules using powder X-ray diffraction. This work was completed using samples that were supplied as part of the MACADEMIA collaboration. Section 4.3.3 details the synthesis and analysis of a new modified MOF which was designed to have improved adsorption towards sulfur-containing molecules. Also reported are the results of an investigation into the local structure of the MIL-53 materials to understand better the mechanism that affects the framework flexibility.

4.1 Introduction

Many adsorption isotherm measurements have been reported on the uptake of various gases using the MIL-53 frameworks.[1-6] However, there are few that use time-resolved X-ray diffraction to follow gas phase adsorption.[7, 8] When studying flexible frameworks such as MIL-53, time-resolved X-ray diffraction allows the expanding and contracting framework to be observed *in situ* since there are large shifts in the Bragg peak positions.

The work presented here aims to expand upon the use of *in situ* powder XRD techniques to study the behaviour of MIL-53 materials in response to simple volatile organics. Studying the same guest molecules *e.g.* alcohols, which were studied previously in the liquid phase also allows conclusions to be formed over the role of the solvent during liquid phase experiments; if there are differences in the breathing behaviour between liquid and gas phase experiments then the solvent is likely to be responsible.

For all *in situ* gas phase XRD experiments described in this chapter a laboratory powder X-ray diffractometer fitted with a gas chamber was used to follow the uptake of guest molecules, as described in Chapter 2. An inert carrier gas, nitrogen, was bubbled through a Drechsel bottle containing a volatile, liquid guest creating a vapour that was then passed over the sample. Individual XRD scans were collected for a period of approximately 210 seconds.

4.2 Adsorption of Methanol Vapour by MIL-53(Fe)

To complement the studies performed in the liquid phase (Section 3.2), *in situ* XRD experiments were performed to study the breathing behaviour of MIL-53(Fe) towards vapour phase methanol. These experiments were designed to see if there was a difference in the response of MIL-53(Fe) towards liquid and vapour phase methanol guest molecules; experiments in the gas phase allow for the elimination of the competing effect of the solvent. Laboratory powder XRD was used to follow the expansion/contraction of the framework in response to the introduction/removal of methanol guest molecules. During the liquid phase experiments the half-open phase was identified therefore it is important to investigate if this phase is only seen for liquid phase guest sorption or if this phase can also be observed during these vapour phase

studies. The work in this chapter also aims to discover the amount of methanol that can be adsorbed by MIL-53(Fe) and what happens to the occluded water molecules in the hydrated phase when methanol is introduced. Due to the disorder of the guest molecules within the pores of the framework during methanol sorption it has not been possible to identify the amount of methanol/water present using XRD techniques. Therefore, other analytical techniques were used to investigate this problem. This work hopes to use thermogravimetric analysis to calculate the mass of methanol or methanol/water present within the pores for both the half-open and the fully-open phases and inelastic neutron scattering (INS) studies hope to gain insight into the host-guest and guest-guest interactions.

4.2.1 *In Situ* Powder X-ray Diffraction Studies

The contour graphs shown in this Section were produced from individual powder XRD scans recorded over a 2θ range of 6 – 30 °. This narrow range is sufficient to detect enough Bragg peaks to be able to identify each phase but short enough to observe changes in the framework symmetry in real time. Using this method of data collection allowed the response of the framework towards guest molecules to be studied *in situ*. For the experiments described in this section a flow of dry nitrogen gas was used to either remove occluded guest molecules *e.g.* water, or to act as the carrier gas to introduce guest molecules in the vapour phase.

Figure 4.1 shows the data recorded for the introduction of methanol vapour to the hydrated phase of MIL-53(Fe). The initial phase (Phase 1) seen in the contour plot is the monoclinic, hydrated phase of MIL-53(Fe).[9] Shortly after the introduction of the methanol vapour (point A) the structure expands to the half-open phase (Phase 2), which was identified during the liquid phase experiments (Section 3.2). The contour

plot highlights that there is a continuous expansion of the half-open phase until the methanol flow is increased (point B), which forces the framework into the fully-open structure (Phase 3). This phase does not gradually expand as seen by the fixed positions of the Bragg peaks.

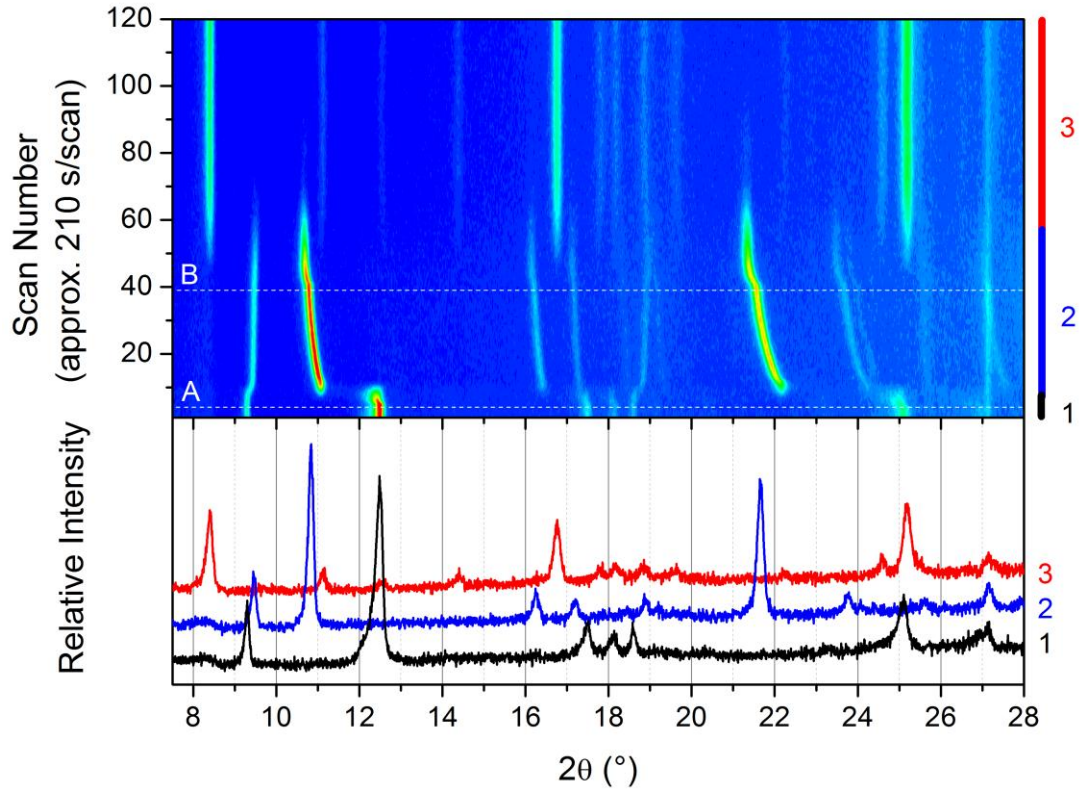

Figure 4.1: Behaviour of MIL-53(Fe)[H_2O] in response to gaseous methanol. A = start of low flow of methanol vapour, B = high flow of methanol vapour. 1 = MIL-53(Fe)[H_2O], 2 = MIL-53(Fe) half-open and 3 = MIL-53(Fe) fully-open

Dehydration of MIL-53(Fe) is known to be easily achieved by heating the material above 100 °C.[9] The loss of the occluded water molecules induces a slight contraction of the framework. This process is fully reversible; after heating and cooling back to room temperature the framework takes up water molecules from the atmosphere. Prior to this work dehydration had only been shown to occur upon the application of heat. However, this work found that a continual flow of dry nitrogen gas over the sample at 30 °C was sufficient to remove the water from the pores of MIL-53(Fe) and induce the same contraction as was seen for thermal dehydration. The contour plot in Figure 4.2 shows

that dehydration using this method is also reversible; after the flow of nitrogen gas is removed (point A) the conditions inside the sample chamber return to ambient and the sample is able to take up water from the atmosphere.

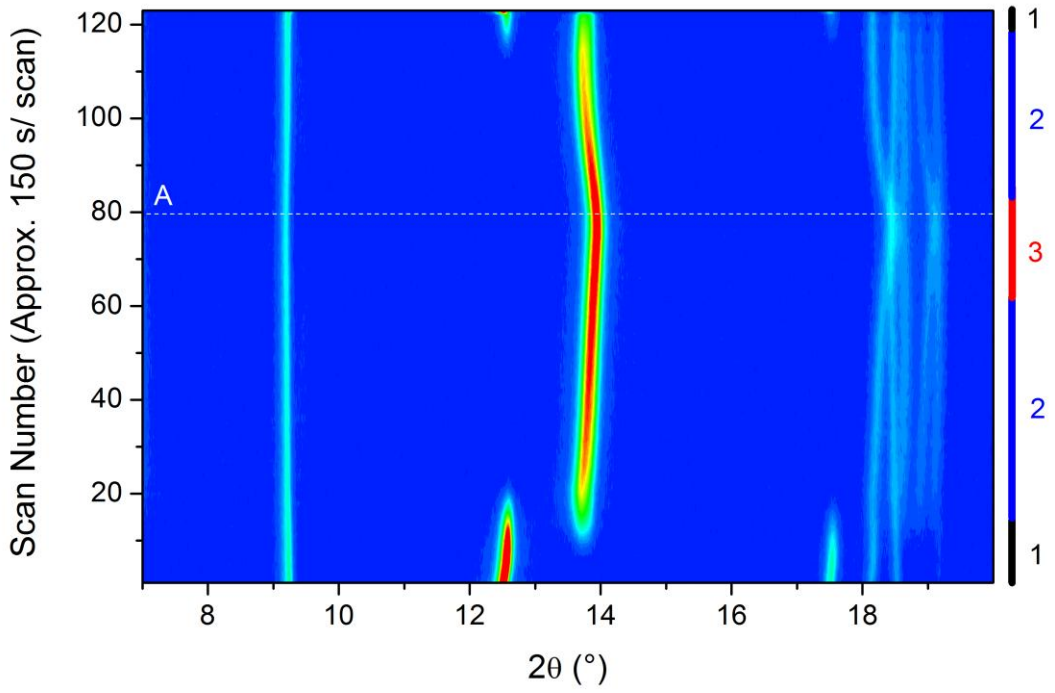

Figure 4.2: Reversible dehydration of MIL-53(Fe) using a flow of dry nitrogen gas, 1 = hydrated MIL-53(Fe), 2 = intermediate dehydrated MIL-53(Fe)[9] and 3 = dehydrated MIL-53(Fe).

The gas-phase methanol adsorption experiment was also performed using dehydrated MIL-53(Fe) to see if there were any differences in the response of the framework. Dehydration was followed *in situ* using the method outlined above. The contour plot (Figure 4.3) shows that the framework was successfully dehydrated (Phase 2) before the introduction of the methanol vapour (point B). While under a low flow of methanol vapour the sample expands to the half-open phase (Phase 3) and is stable until the flow of methanol is increased (point C); at this point the framework rapidly expands before the transition to the fully-open, *Imcm*, phase (Phase 4) is seen.

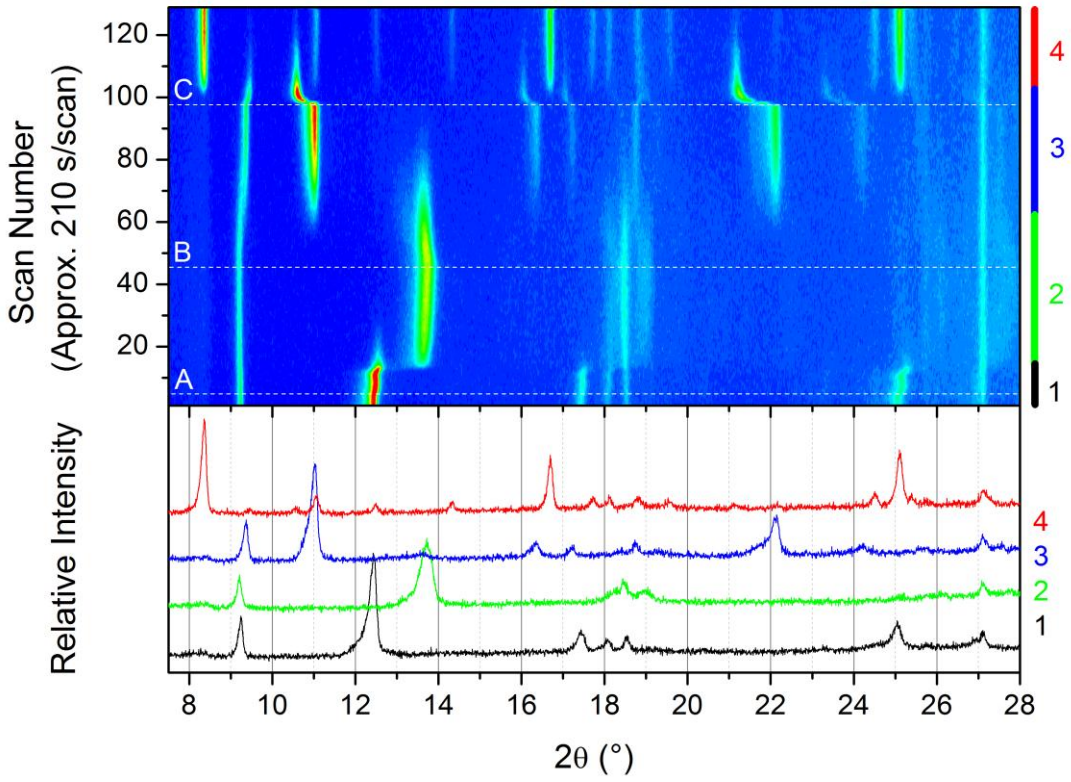

Figure 4.3: Behaviour of MIL-53(Fe) in response to different gas flows. A = introduction of pure nitrogen, B = introduction of a low flow of methanol vapour and C = high flow of methanol vapour. 1 = Hydrated MIL-53(Fe), 2 = Dehydrated MIL-53(Fe), 3 = MIL-53(Fe) half-open and 4 = MIL-53(Fe) fully-open.

As far as was possible, the external variables between experiments were kept the same, *i.e.* temperature and gas flow. The temperature of the sample chamber was set to 30 °C for all experiments. This allows for comparisons to be made between the data sets. The rate of expansion from the hydrated phase to the half-open phase (Figure 4.1) is faster than the rate of expansion from the dehydrated phase to the half-open phase (Figure 4.3); the transition is complete within 10 scans (~35 minutes) and 30 scans (~105 minutes), respectively. One possible explanation for this is guest uptake by the dehydrated phase is harder to achieve due to the smaller pore apertures of the contracted structure. Conversely, adsorption of methanol by hydrated MIL-53 may be aided by the presence of the polar water molecules inside the pores. While the samples were under a low flow of methanol, the previously hydrated sample shows a gradual expansion of the

half-open phase, evidenced by the continual shift of the Bragg peaks, whereas the previously dehydrated sample stays at a constant volume until the methanol flow rate is increased. This could indicate a difference in the kinetics of guest uptake but it is worth noting the difficulty in controlling the exact flow rate of the carrier gas and the temperature of the liquid guest, both of which would affect the amount of methanol per cubic centimetre of nitrogen. This means that accurate kinetics of guest uptake cannot be deduced from these data. It is likely that discrepancies between the flow rates used for each experiment contributed to the differences seen in the rate of expansion of the half-open phase. It is hard to deduce from these experiments if the water is fully displaced by the methanol when the experiment is started from the hydrated phase, complementary techniques are needed to investigate this problem. Other than the rate of expansion, which may be caused by the variation in the gas flow rate, there are no significant differences in the guest uptake pathway between the hydrated and dehydrated experiments. This suggests that the water has been displaced.

The four phases of MIL-53(Fe) expansion seen during the vapour phase experiments were identified by comparison of the peak positions with the simulated Bragg peaks from published crystal structures of the materials.[9, 10] It was possible to stabilise all four phases, dehydrated, hydrated, half-open and fully-open, to allow for longer data collection to improve the signal-to-noise ratio. The data for the half-open phase was more difficult to collect as this phase continually expands. To stabilise the evolution of this phase the data were measured in a stationary methanol environment rather than the continuous flow used for the other phases. A shorter data collection period was also used to reduce any peak broadening that would have been caused by the continual movement of the peaks due to expansion. A Le Bail profile fit was performed using the

structure analysis program GSAS to obtain the unit cell parameters for each phase (Figure 4.4).

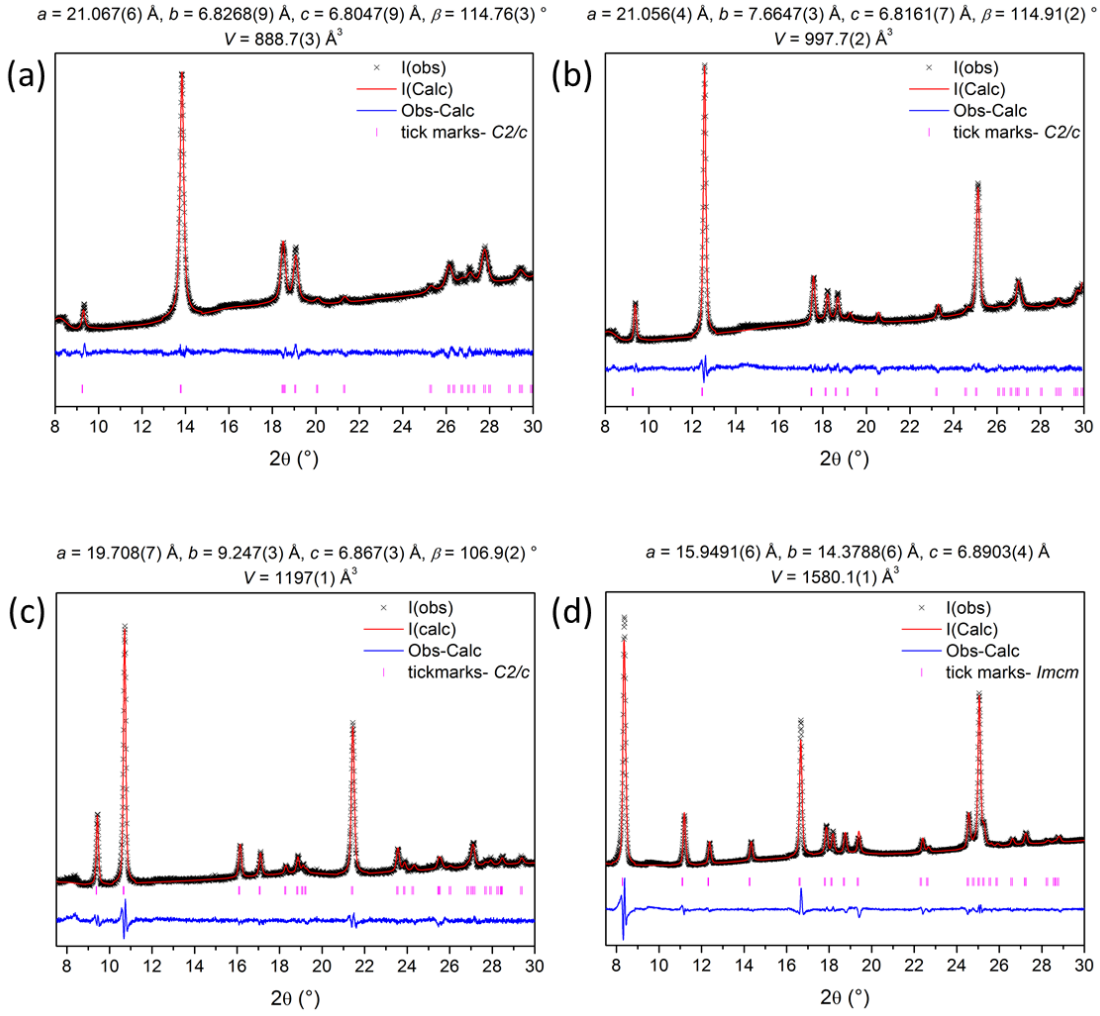

Figure 4.4: Le Bail profile fit obtained using GSAS for a) MIL-53(Fe) (dehydrated), b) MIL-53(Fe)[H_2O] (hydrated), c)MIL-53(Fe)[MeOH] (half-open) and d) MIL-53(Fe)[MeOH] (fully-open)

The unit cell volumes calculated using this method are compared with the literature values obtained from the liquid phase high-resolution XRD experiments in Table 4.1 and good agreement can be seen. The signal-to-noise ratio was lower for the half-open phase compared to the other phases and the unit cell parameters for the experimental data of this phase show the greatest discrepancy from the literature data. This is due to

the difficulties in stabilising this phase because of the variation in the volume that was observed for this phase, as described earlier.

Table 4.1 Unit cell parameters for the four different phases of MIL-53(Fe). Experimental values were obtained from a Le Bail profile fit and are compared with literature data obtained from high-resolution XRD studies in the liquid phase. The dehydrated literature data was obtained from the published crystal structure.

		a / Å	*b* / Å	*c* / Å	*β* / °	*V* / Å^3	*S.G.*
Dehydrated	**Experimental**	**21.067(6)**	**6.8268(9)**	**6.8047(9)**	**114.76(3)**	**888.7(3)**	***C2/c***
	Literature[11]	21.2525	6.8135	6.8734	114.674	904.4	*C2/c*
Hydrated	**Experimental**	**21.056(4)**	**7.6647(3)**	**6.8161(7)**	**114.91(2)**	**997.7(2)**	***C2/c***
	Literature[11]	21.1299(1)	7.64271(6)	6.83058(6)	114.9352(4)	1000.25(2)	*C2/c*
Half-open	**Experimental**	**19.708(7)**	**9.247(3)**	**6.867(3)**	**106.9(2)**	**1197(1)**	***C2/c***
	Literature[10]	20.5463(1)	9.17002(8)	6.87319(6)	112.9817(6)	1192.19(2)	*C2/c*
Fully-open	**Experimental**	**15.9491(6)**	**14.3788(6)**	**6.8903(4)**	**90**	**1580.1(1)**	***Imcm***
	Literature[10]	15.9394(3)	14.4526(3)	6.90489(8)	90	1590.65(5)	*Imcm*

4.2.2 Thermogravimetric Analysis of Methanol Uptake

The X-ray diffraction studies show that the introduction of methanol to the MIL-53(Fe) framework causes expansion to the fully-open phase via the half-open phase. This step-wise expansion could be the result of a kinetic rearrangement of guest molecules within the pores or it could be due to an increase in the amount of guest molecules taken up by the framework However, no information can be gained from these results about the amount of methanol that is taken up by the framework. The thermogravimetric studies described in this chapter were designed to investigate the mass increase due to the introduction of methanol.

Methanol is a volatile organic and it has been observed that the interaction between it and the MIL-53 framework is weak; it is easily replaced by water in the air. Consequently, to perform TGA studies methanol was introduced into the TGA apparatus using the same method used for PXRD; an inert carrier gas was used to vaporise liquid methanol allowing it to be passed over the sample. Figure 4.5 shows the results for the experiment using dehydrated MIL-53(Fe). MIL-53(Fe) was dehydrated *in situ* prior to the introduction of methanol followed by the subsequent removal of the guest and the rehydration of the framework. The sample was dehydrated by heating to 150 °C and then cooling to 30 °C under a flow of dry nitrogen to prevent the rehydration of the sample. Methanol was introduced in two steps. The first step used a flow rate of 50 cm^3 min^{-1} and in the second step the gas flow was increased to above 90 cm^3 min^{-1}. The methanol was removed by heating the sample to 150 °C. Then the sample was cooled back to 30 °C where water was introduced by flowing nitrogen gas through water at a rate of 50 cm^3 min^{-1}. Figure 4.5 shows the mass increase/decrease of MIL-53(Fe) in response to the changing external stimuli.

The mass of the dehydrated sample was chosen as the reference mass for calculating expected mass increases because the XRD data showed that 150 °C is sufficient to dehydrate the sample completely; making this point in the data the most reliable. The data shows that when this mass is used as the reference point the initial mass loss of the sample is less than expected. This is likely due to the sample being partially dehydrated as it is exposed to a continuous flow of dry nitrogen in the experiment chamber before the experiment begins. This gas flow cannot be turned off as it is a protective gas required for the efficient running of the instrument. The XRD results in Section 4.2.1 show that it is possible to dehydrate MIL-53(Fe) using a flow of dry nitrogen therefore it is reasonable to expect there to be a small mass loss due to this protective gas flow. The graph shows that the sample was dehydrated when heated to 150 °C and that there was no mass increase as the sample was cooled to 30 °C. Upon introduction of a low flow of methanol vapour the sample rapidly increases in mass. The mass change plateaus at a value close to the expected mass increase for MIL-53(Fe)[CH_3OH] when the gas flow remains constant. Upon the increase of the methanol vapour flow there is an increase in mass which corresponds with the uptake of a second equivalent of methanol guest. This step in the mass gain of the sample indicates that guest uptake is dependent upon the concentration of the guest in the experimental chamber; there is a concentration threshold that it is necessary to exceed before the sample will take up more guest molecules. The mass increase of both steps is slightly higher than predicted; this is attributed to extra surface methanol. The sample was heated to remove the occluded methanol guest molecules. At approximately 65 °C there is a slight step in the graph which corresponds to the initial loss of the second equivalent of methanol followed by the removal of the first equivalent. The methanol was completely removed when the temperature reached 150 °C and there is no mass increase as the sample is

cooled back to 30 °C. At 30 °C water is introduced to the experimental chamber using the same method that was used for methanol. The results show that there is a rapid mass increase followed by a plateau to give a mass close to the expected theoretical mass for MIL-53[H_2O]. The final mass of the hydrated sample while under a flow of water vapour is greater than the initial mass of the hydrated sample confirming the observation made earlier that the experimental conditions led to the sample being partially dehydrated at the start.

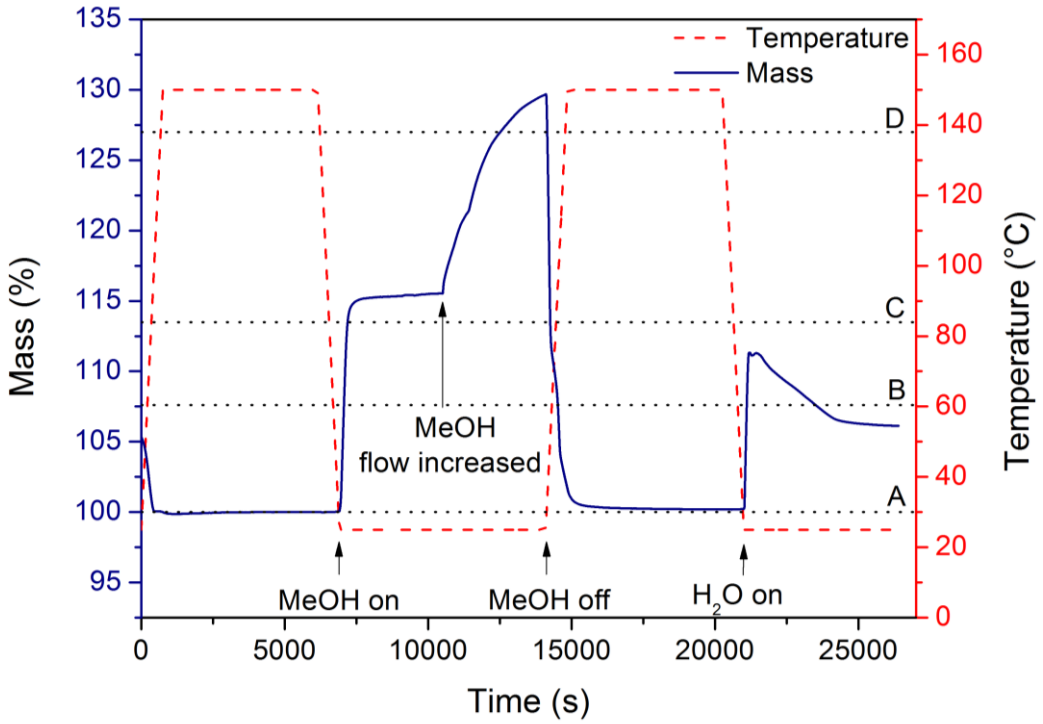

Figure 4.5: TG data showing the mass loss/gain during the removal and introduction of different guest molecules in MIL-53(Fe). The dotted lines indicate the theoretical masses of A= MIL-53(Fe), B= MIL-53(Fe)[H_2O], C = MIL-53(Fe)[CH_3OH] and D= MIL-53(Fe)[2(CH_3OH)]

This experiment was also performed without the initial dehydration of the framework. The XRD data, Section 4.2.1, show that there is little difference in the sequence of pore opening between experiments where the starting phase is hydrated or dehydrated. However, it was unknown if the half-open and fully-open materials contain both water

and methanol when the experiment is started from the hydrated phase. Although, the similarities of the XRD results suggested that the water was displaced by methanol vapour.

Figure 4.6 shows the results of methanol uptake starting from the hydrated phase. The sample was exposed to methanol vapour at the very beginning of the experiment to reduce the water loss that occurs due to the protective nitrogen gas flow. The results show that at a low flow of methanol vapour the mass increases approximately to the mass expected for MIL-53(Fe) containing one molar equivalent of methanol (C) which would suggest that the water was displaced in favour of the methanol guest. However, the mass increase seen when the gas flow was turned up was much greater than was expected for a second equivalent of methanol (E). The mass gain was much closer to the expected mass of MIL-53(Fe) containing two equivalents of methanol and one equivalent of water (F). It is unlikely that the water was lost from the framework during the low flow and then re-adsorbed when the flow rate was increased therefore it must be concluded that the sample, at the point of the initial plateau, contains a mixture of water and methanol. The sample was heated to 150 °C to remove all of the guest molecules to give the dehydrated phase and after cooling back to 30 °C water was introduced.

As before, the dehydrated phase is believed to be the most reliable value in the experimental data as heating above 150 °C has been shown previously to be more than sufficient to dehydrate the material. Therefore, this mass was used as the reference point for the theoretical calculations to predict the potential mass increases.

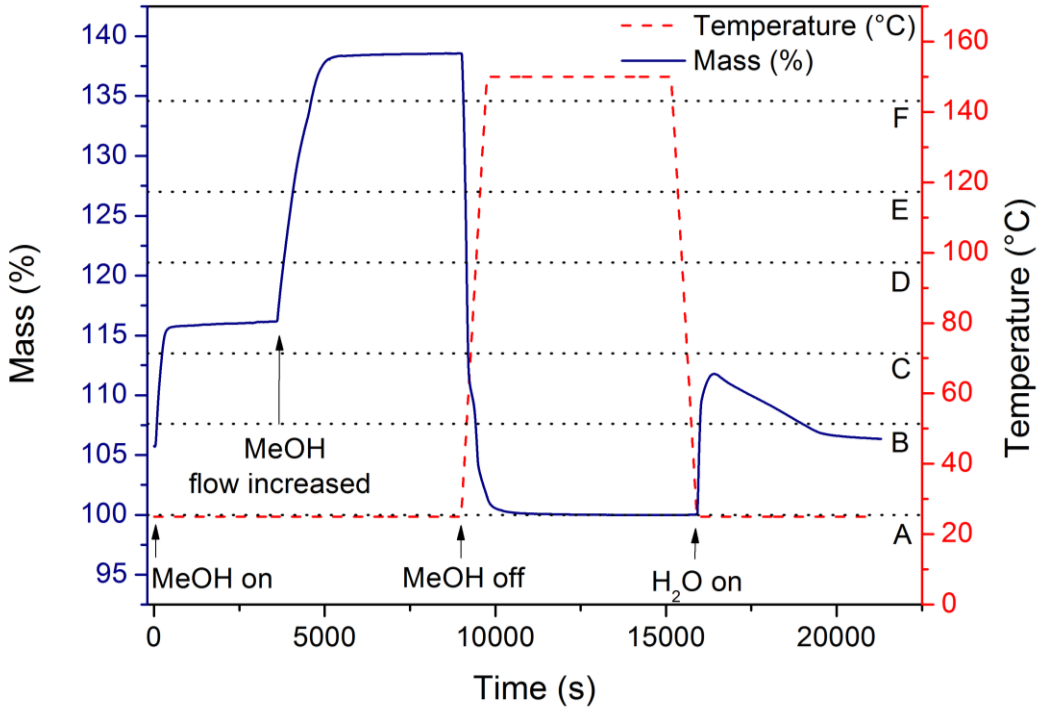

Figure 4.6: TG data showing the mass loss/gain during the removal and introduction of different guest molecules starting from hydrated MIL-53(Fe). The dotted lines indicate the theoretical masses of A= MIL-53(Fe), B= MIL-53(Fe)[H_2O], C = MIL-53(Fe)[CH_3OH] D = MIL-53(Fe)[CH_3OH + H_2O] E= MIL-53(Fe)[2(CH_3OH)] and F= MIL-53(Fe)[2(CH_3OH) + H_2O]

The TG data has provided evidence that dehydrated MIL-53(Fe) is able to accommodate two molar equivalents of methanol within the pores of the framework. By comparing this data with the XRD data a strong correlation between the different phases of breathing and the mass of methanol taken-up can be found. The step-wise mass increase is consistent with the step-wise opening of the framework. Therefore it is possible to conclude that the half-open framework contains one molar equivalent of methanol whereas the fully-open framework contains two molar equivalents of methanol.

The TG data for hydrated MIL-53(Fe) show that the final mass increase is greater than expected for two molar equivalents of methanol; this provides evidence that the sample contains a mixture of water and methanol when the experiment is started from hydrated MIL-53(Fe). By comparing this result to the result from the *in situ* XRD experiments, it

can be deduced that if the water remains inside of the pores during the adsorption of methanol from hydrated MIL-53(Fe) that the presence of water has little effect on the structural transitions of the framework; the framework always expands via the half-open phase.

4.2.3 Inelastic Neutron Scattering

Powder X-ray diffraction shows that both the hydrated and the dehydrated phases of MIL-53(Fe) take up methanol, expanding to the fully-open phase via the half-open phase. XRD provided information about the framework while the TGA provided details on the amount of guest molecules present in the pores. This means that by introducing the exact amount of methanol into the sample each distinct phase can be studied *ex situ*. The TOSCA instrument at the ISIS neutron facility in Oxfordshire was used to perform inelastic neutron scattering (INS) experiments to investigate the local interactions between guest molecules and the framework. This technique was chosen because it is sensitive to hydrogen containing molecules and it has been used previously to study H_2 adsorption in MOFs.[12] These experiments were designed to investigate the different host-guest interactions between the different phases of MIL-53(Fe) seen during methanol adsorption. Figure 4.7 shows the four different phases of MIL-53(Fe) that were investigated: dehydrated MIL-53(Fe) (V = 904.4 Å^3), hydrated MIL-53(Fe)[H_2O] (V = 1000.5 Å^3), half-open MIL-53(Fe)[MeOH] (V = 1213.2 Å^3) and fully-open MIL-53(Fe)[2MeOH] (V = 1593.2 Å^3).

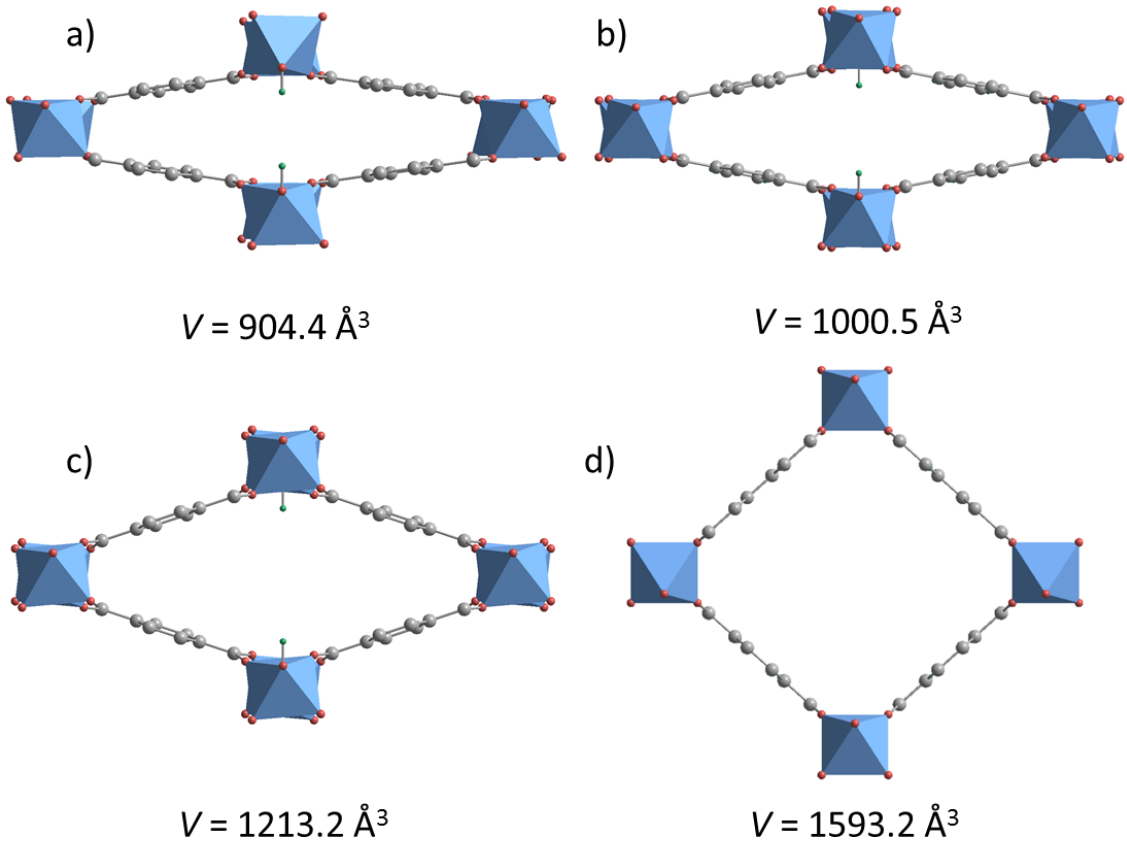

Figure 4.7: Pore volumes of the different phases seen for MIL-53(Fe) during methanol adsorption. a) dehydrated, b) hydrated, c) half-open and d) fully-open. Guest molecules have been omitted for clarity.

For all of the experiments approximately 1 g of MIL-53(Fe)[H_2O] powder was weighed accurately into the sample holder. For the experiments that required dehydrated MIL-53(Fe) the powder and holder were heated to 150 °C before sealing the holder tightly while hot. The exact volume of methanol needed for each experiment was injected into the sample holder which was then sealed tightly before being warmed gently to reach equilibrium. The samples were cooled to 15 K for data collection. The various combinations of MIL-53(Fe) and methanol that were studied allowed for observations concerning the differences in behaviour of the hydrated and dehydrated MIL-53 in response to methanol to be made. The following graphs show pairs of INS spectra and

their corresponding difference plot, which highlight the changes in the vibrations between two experiments.

The assignment of the vibrations has been achieved by considering the simulated INS spectra for the isostructural framework MIL-53(Al). This was performed by Dr A. J. Ramirez-Cuesta using the aClimax software.[13] The simulation allowed the vibrations in the region of 300 – 600 cm^{-1} to be identified as twisting libration modes of the terephthalate rings. The vibrations at higher energies, 700 – 1100 cm^{-1}, can be assigned to the vibrations of the hydrogen atoms on the terephthalate rings. The two phases that were used in the simulation were the fully-open MIL-53(Al) phase, which has a pore volume of 1412 $Å^3$, and the contracted dehydrated phase of MIL-53(Al), seen at low temperatures, which has a pore volume of approximately 900 $Å^3$.[14] Figure 4.8 shows a comparison of the difference-plots between the spectra of the two simulated phases and the comparable experimental data plotted in the region that shows the bands due to librational modes. This plot highlights that the key signature of framework opening is this difference in energy of the librational bands between the open and closed phases of MIL-53(Fe).

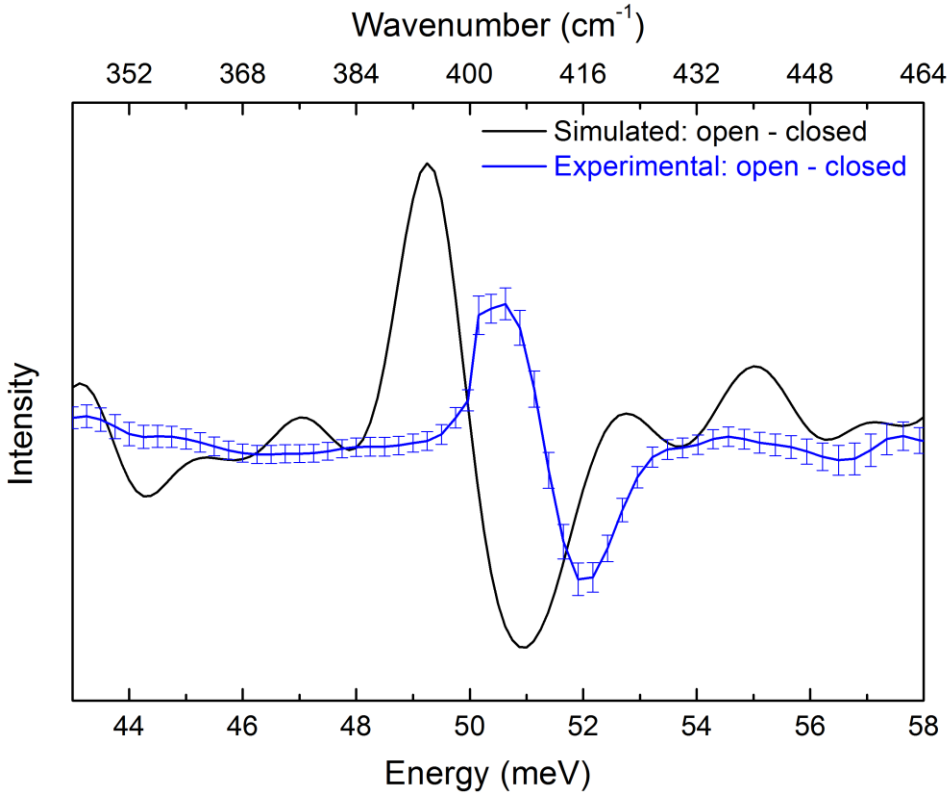

Figure 4.8: Simulated data for MIL-53(Al)[fully-open]-MIL-53(Al)[contracted] compared with experimental data for MIL-53(Fe)[2MeOH]-MIL-53(Fe)[dehydrated].

Figure 4.9 shows the INS spectra for the hydrated MIL-53(Fe) ($V \approx 1000$ Å^3) and the dehydrated MIL-53(Fe) ($V \approx 900$ Å^3) overlaid, with the difference plot shown beneath. By comparing spectra we are able to observe that there are differences in their framework vibrations. The strong signal below 200 cm^{-1} and the broad signal between 300 – 600 cm^{-1} in the spectrum of hydrated MIL-53(Fe) can be assigned as the translational and librational modes of water, respectively.[15] Other porous materials have shown similar broadened features in their INS spectra. [15] The higher background of the spectrum of the hydrated material is accounted for by the presence of water as neutron techniques are ten times more sensitive towards hydrogen than any other atom.[16] The region between 400 – 500 cm^{-1} shows a shift in the peak positions to lower energy for the hydrated phase, indicating a softening of these vibrations. A softening (*i.e.* a shift to lower energy) of the twisting librational modes is consistent with the librations of the

terephthalate rings being less constricted. The rings in the dehydrated phase are more constricted due to their closer proximity upon the contraction of the framework when water is lost. There is little change in the higher energy region due to both phases being sufficiently contracted as to equally restrict the motion of the hydrogen vibrations.

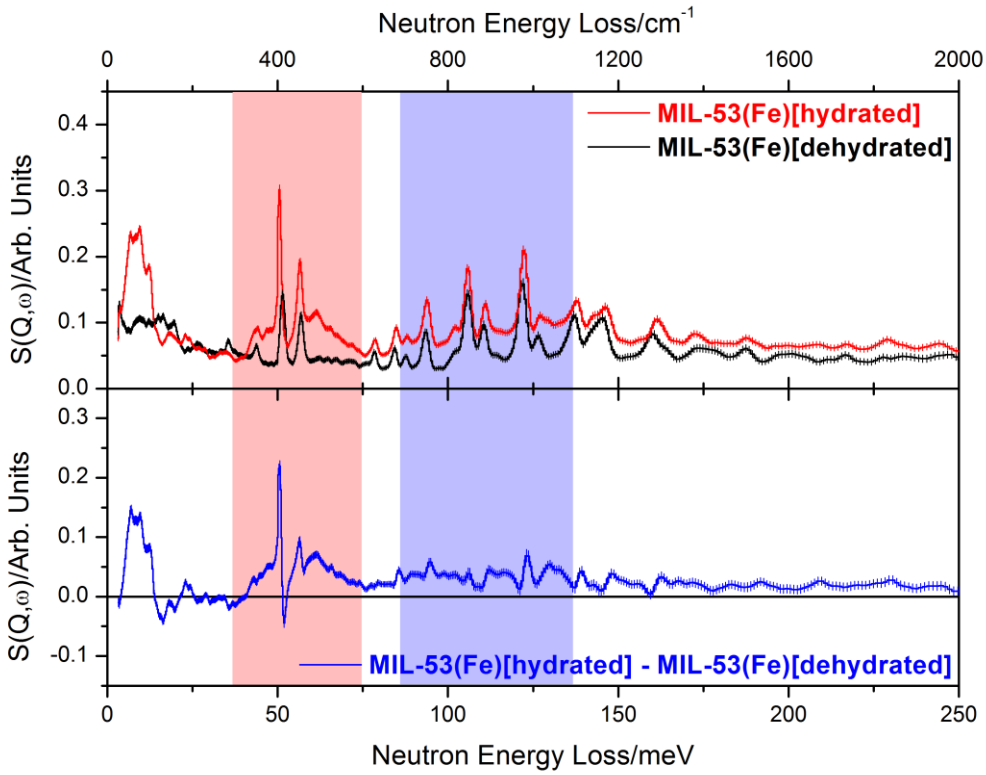

Figure 4.9 INS spectra for hydrated MIL-53(Fe) compared with the spectra for dehydrated MIL-53(Fe). The region shaded in red indicates the low energy modes which are characteristic of twisting librations of the terephthalate ring and the region shaded in blue indicates the higher energy modes which are characteristic of the vibrations of the hydrogen atoms on terephthalate rings.

Figure 4.10a shows the comparison between dehydrated MIL-53(Fe) ($V \approx 900$ Å^3) and dehydrated MIL-53(Fe) with one equivalent of d3-methanol inserted ($V \approx 1200$ Å^3). These spectra show the same softening of the terephthalate librations upon expansion of the framework, due to methanol sorption, visible between 350 – 500 cm^{-1}. The extent of the shift to lower wavenumbers seen for the methanol phase is similar to the shift seen for the hydrated phase. The opening of the framework to ~1000 Å^3 (hydrated phase) is

thought to be sufficient to remove any constraints from the librational modes of the terephthalate ring. Therefore, further opening to ~1200 $Å^3$ (half-open phase) does not result in further softening of these modes. One important difference between these two spectra is the softening of the vibrations in the 700 – 1000 cm^{-1} region that is seen upon the addition of methanol. As described above, the vibrations occurring in this energy range are due to the motion of the hydrogen atoms on the terephthalate rings. The opening of the framework to the half-open phase removes some of the constraint on these hydrogen atoms leading to a softening of these vibrations.

It is important to note that the spectrum of dehydrated MIL-53(Fe) with one equivalent of d3 methanol does not show evidence for bulk solid methanol. Figure 4.10b shows the reference spectra recorded of solid CD_3OH and CH_3OH. The intensity of the signals for solid methanol is much higher than those seen in the experimental data; the lack of these large signals suggests that the inserted methanol was taken up by the framework and that none has crystallised on the surface. Although evidence for solid methanol is not present there are additional modes in the spectrum of the methanol loaded framework; below 200 cm^{-1} there is a broad signal due to the translational modes and methyl torsions of the d3-methanol molecules that are bound within the framework.

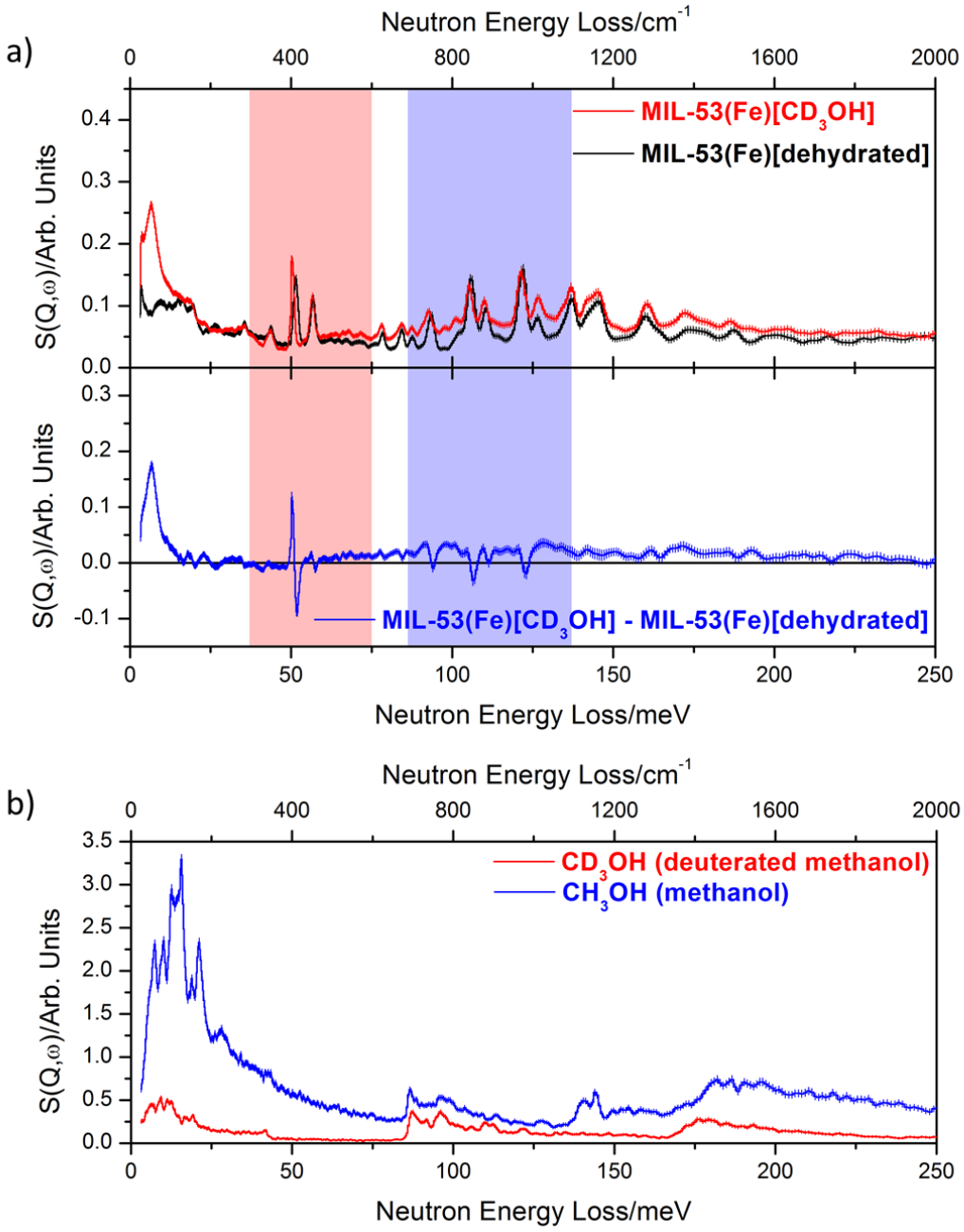

Figure 4.10 INS spectra, a) comparing dehydrated MIL-53(Fe) and one equivalent of deuterated methanol and b) of pure CH_3OH and CD_3OH.

The comparison of dehydrated MIL-53(Fe) ($V \approx 900$ Å^3) and dehydrated MIL-53(Fe) with two equivalents of d3-methanol ($V \approx 1500$ Å^3) is shown in Figure 4.11. The TGA results show that the framework is able to accommodate two molar equivalents of methanol and the INS data confirms this observation as there is no evidence for solid methanol in the spectrum (spectrum of solid methanol is shown in Figure 4.10). The

difference spectrum is very similar to the previous comparison; methyl torsions can be seen at low wavenumbers ~ 200 cm^{-1}, a softening of the librations is present between 300 – 500 cm^{-1} (indicating the opening of the framework) and a softening of the vibrations is visible in the region 700 – 1000 cm^{-1} (indicating the removal of the constraint upon the hydrogen atoms in the terephthalate ring). The softening of the hydrogen vibrations due to the presence of two equivalents of d3 methanol gives rise to a similar shift as was seen for one equivalent of d3 methanol. This suggests that expansion to the half-open phase (one d3 methanol) is sufficient to remove the majority of the constraint upon the hydrogen atoms and that further expansion to the fully-open phase (two d3 methanols) has little affect upon these vibrations.

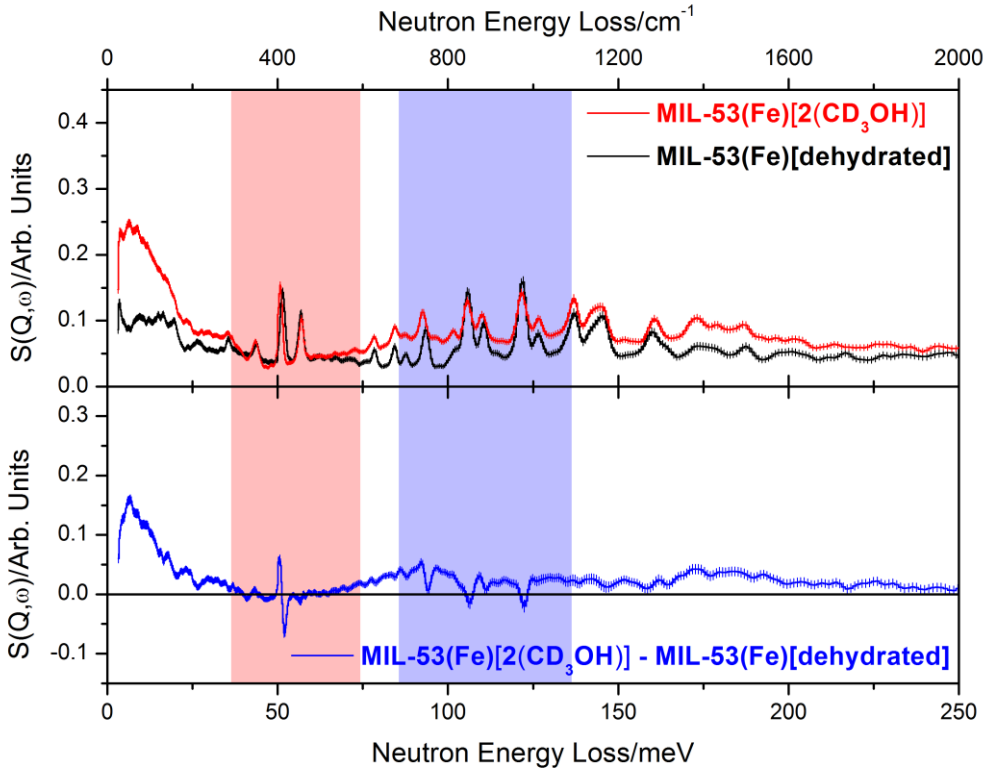

Figure 4.11: INS spectra of dehydrated MIL-53(Fe) with two equivalents of d3-methanol compared with dehydrated MIL-53(Fe)

Finally the comparison between hydrated MIL-53(Fe) ($V \approx 1000$ $Å^3$) and hydrated MIL-53(Fe) with one equivalent of d3-methanol ($V \approx 1200$ $Å^3$) is shown in Figure 4.12. This

comparison is particularly important as it shows that when methanol is added to hydrated MIL-53(Fe) the broad signal due to the librational modes of water (300 – 600 cm^{-1}) is no longer observed. Equally, there is no evidence that the water has been displaced by the methanol forcing water onto the surface of the framework which would result in solid H_2O. Therefore, it should be concluded that both the water and the methanol are present within the pores, as was indicated by the TGA data. An IR study into the adsorption of water and methanol vapour by MIL-53(Cr) reported by Bourrelly *et al.*[17] found that the water within the pores of the framework formed a hydrogen-bonded network. If it is assumed that both water and methanol are present within the pores during our experiment then it is reasonable to suggest that the methanol would disrupt any hydrogen-bonded network formed by the water molecules. As a consequence the distinct signal due to this network would no longer be present; the disappearance of the broad signal (300 – 600 cm^{-1}) is conducive to this theory. There is very little shift in the peaks in the region of 400 cm^{-1}; it was established earlier that expansion to ~1000 $Å^3$ was sufficient to give rise to the signature softening of these vibrations upon opening of the framework and that further expansion to ~1200 $Å^3$ would not result in further softening. A slight softening of the hydrogen vibrations is also seen, consistent with previous observations upon expansion of the framework.

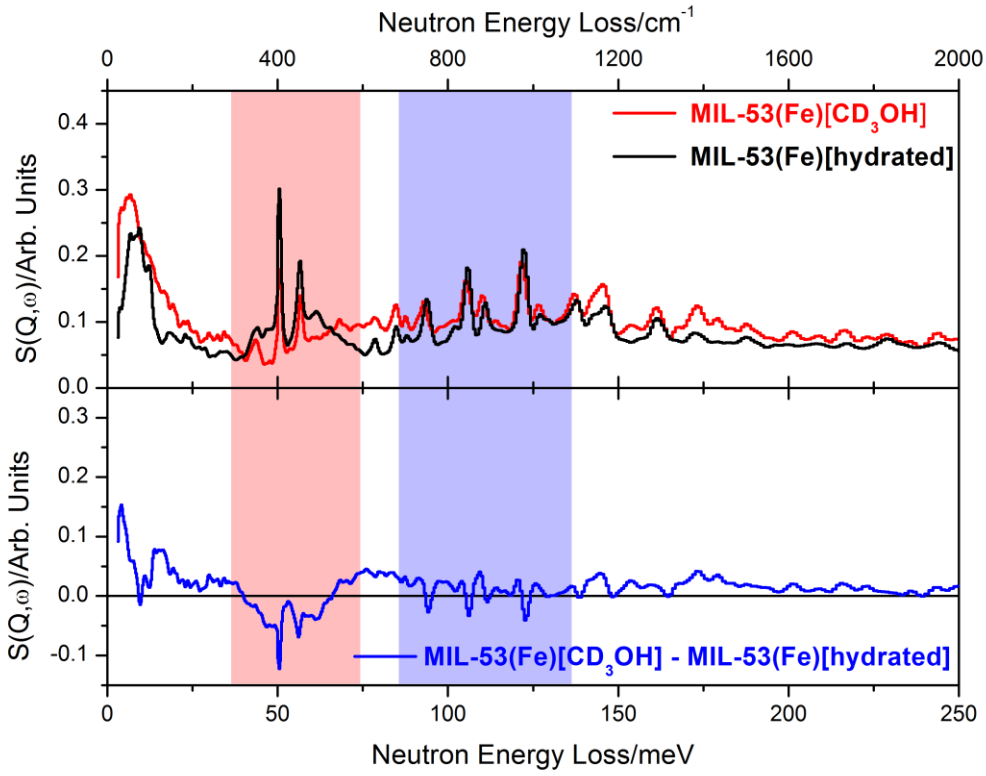

Figure 4.12: INS spectra of hydrated MIL-53(Fe) compared with hydrated MIL-53(Fe) with one equivalent of methanol.

The spectrum for dehydrated MIL-53(Fe) with one equivalent of methanol was also recorded but the data is not shown as it is very similar to the result for deuterated methanol. There was an increase in the intensity of the peaks assigned to methyl torsions ~200 cm^{-1}, which is as expected for the increased number of hydrogens.

4.3 Breathing Behaviour of Modified MIL-53(Al) Materials

Pre- and post-synthetic modification of MOFs can be used to improve or change the response of a framework towards a specific guest. The pre-synthetic modification of MIL-53(Al) has resulted in the successful synthesis of nine isostructural frameworks, whose behaviour is described in this chapter. Modifications include the functionalisation of the 1,4-benzenedicarboxylic acid linker and the substitution of this

aromatic linker for the saturated alkane, 1,4-cyclohexanedicarboxylic acid. The breathing properties of all the modified frameworks were investigated.

The breathing behaviour of the unmodified MIL-53(Al) and the isostructural MIL-53(Cr) has been published by various groups. It has been reported that both frameworks expand upon heating as a consequence of the loss of the occluded water molecules. They expand via a one-step process to give the fully-open, *Imcm*, phase.[18, 19] Bourrelly *et.al*.[2] reported that MIL-53(Cr) adsorbed methanol and ethanol in the vapour phase. Expansion via a half-open, *C2/c*, phase (1200 $Å^3$), similar to the phase seen for MIL-53(Fe)[MeOH], was observed. This study also reported that no expansion of the framework was seen for MIL-53(Cr) when exposed to water vapour. However, a subsequent study by Guillou *et.al*.[20] reported that if MIL-53(Cr) was suspended in water it could take up excess water molecules, causing the framework to expand to the fully-open, *Imcm*, phase. This phase was described as *superhydrated*.

4.3.1 Functionalised 1,4-benzenedicarboxylic acid

The MIL-53 linker was functionalised with eight different groups; nitro ($-NO_2$), amino ($-NH_2$), bromo (-Br), chloro (-Cl), methyl ($-CH_3$), carboxylic acid (-COOH) and dihydroxy ($-(OH)_2$) (Figure 4.13). MIL-53(Al) materials using these linkers were all synthesised by N. Stock's research group in Kiel, Germany, and provided as part of the MACADEMIA project. The presence of the bulkier functional groups on the linker results in the hydrated phase for all seven modified frameworks having a larger unit cell than unmodified MIL-53(Al), ~1000 $Å^3$ compared to 946 $Å^3$.[18] The unit cell volumes of the modified frameworks are closer to the volume of the hydrated MIL-53(Cr) unit cell, 994.5 $Å^3$.[20]

The breathing of these modified materials was investigated using PXRD. Three different tests were performed for each framework; thermal dehydration, superhydration and sorption of methanol vapour. Thermal dehydration and methanol sorption were followed by *in situ* PXRD using the methods that were employed to investigate MIL-53(Fe). Superhydration was investigated by creating a paste from the hydrated sample and a few drops of water. The paste was spread in the sample holder and the gradual drying of the sample at 30 °C was followed by XRD. A fourth test, the adsorption of heptane, was performed only on two of the modified frameworks. The frameworks chosen for this study were the nitro (polar) and methyl (non-polar) modified frameworks. These frameworks were chosen so that the effect of the polarity of the functional group upon the adsorption of heptane could be studied.

Powder X-ray diffraction data were recorded over a small 2θ range, 6 – 30 °, to allow for quick data collection. Quick data collection provides the best opportunity for observing any sudden changes in framework symmetry and allows the expansion and contraction of the structure to be followed *in situ*. The number of scans collected was dependent on the time it took for each experiment to reach completion.

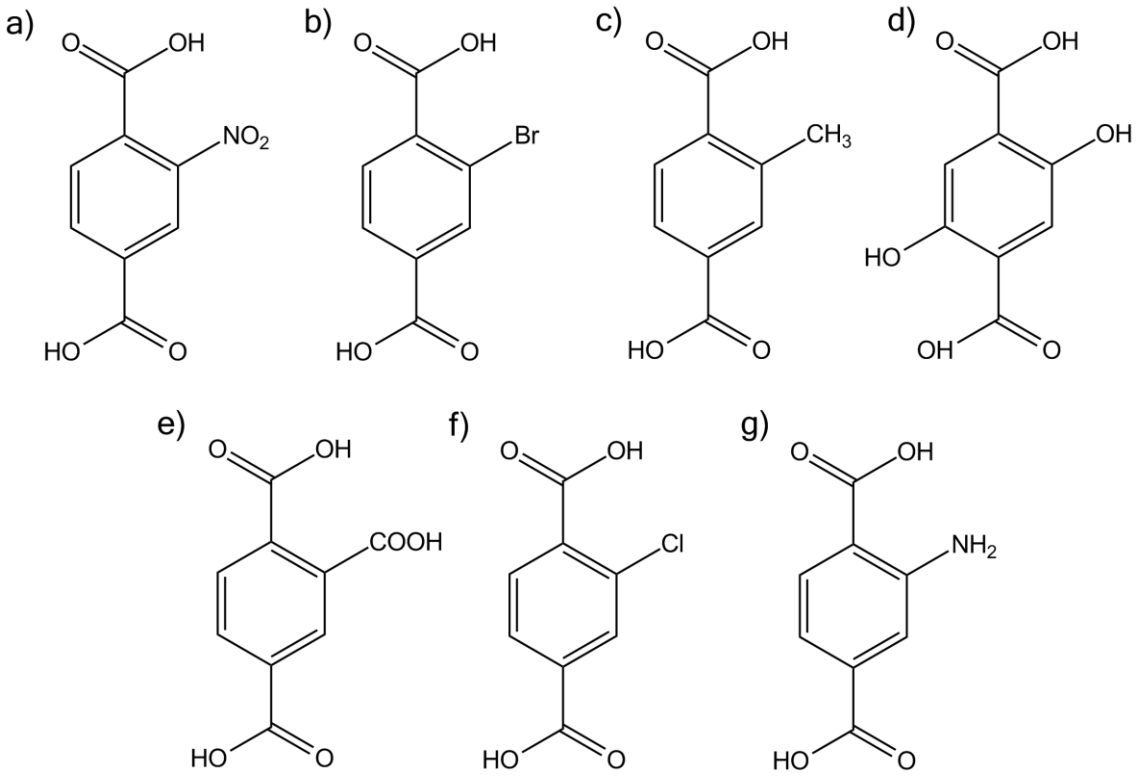

Figure 4.13 Functionalised ligands used for MIL-53(Al) synthesis, a) 2-nitro-1,4-benzendicarboxylic acid, b) 2-bromo-1,4-benzenedicarboxylic acid, c) 2-methyl-1,4-benzenedicarboxylic acid, d) 2,5-dihydroxy-1,4-benzenedicarboxylic acid, e) 1,2,4-benzenetricarboxylic acid, f) 2-chloro-1,4-benzenedicarboxylic acid and g) 2-nitro-1,4-benzenedicarboxylic acid

4.3.1.1 Nitro Modified MIL-53(Al)

The monoclinic hydrated phase of the $–NO_2$ modified framework has a unit cell volume of 1032 $Å^3$ at room temperature (Table 4.3, Section 4.3.1.8). Figure 4.14 shows the thermal dehydration of the framework. It was observed that evolution from the hydrated phase to an expanded dehydrated phase, as is seen for unmodified MIL-53(Al), was complete at a temperature of 170 °C. Similarly the cooling of the sample back to 30 °C was recorded; the results show some hysteresis in the flexibility as the framework only begins to contract below 110 °C (Figure A.3). Longer data collection was performed while the sample was held at 210 °C. These data were used to perform a Le Bail profile

fit which allows the unit cell parameters to be found. The starting point for the refinement was the unit cell of the dehydrated MIL-53(Cr), which has a unit cell volume of 1486.1 $Å^3$ and has the orthorhombic space group, *Imcm*.[21] This analysis, Figure 4.14b, confirms that the MIL-53(Al)-NO_2 expands to the fully-open structure with a unit cell volume of 1420.9 $Å^3$.

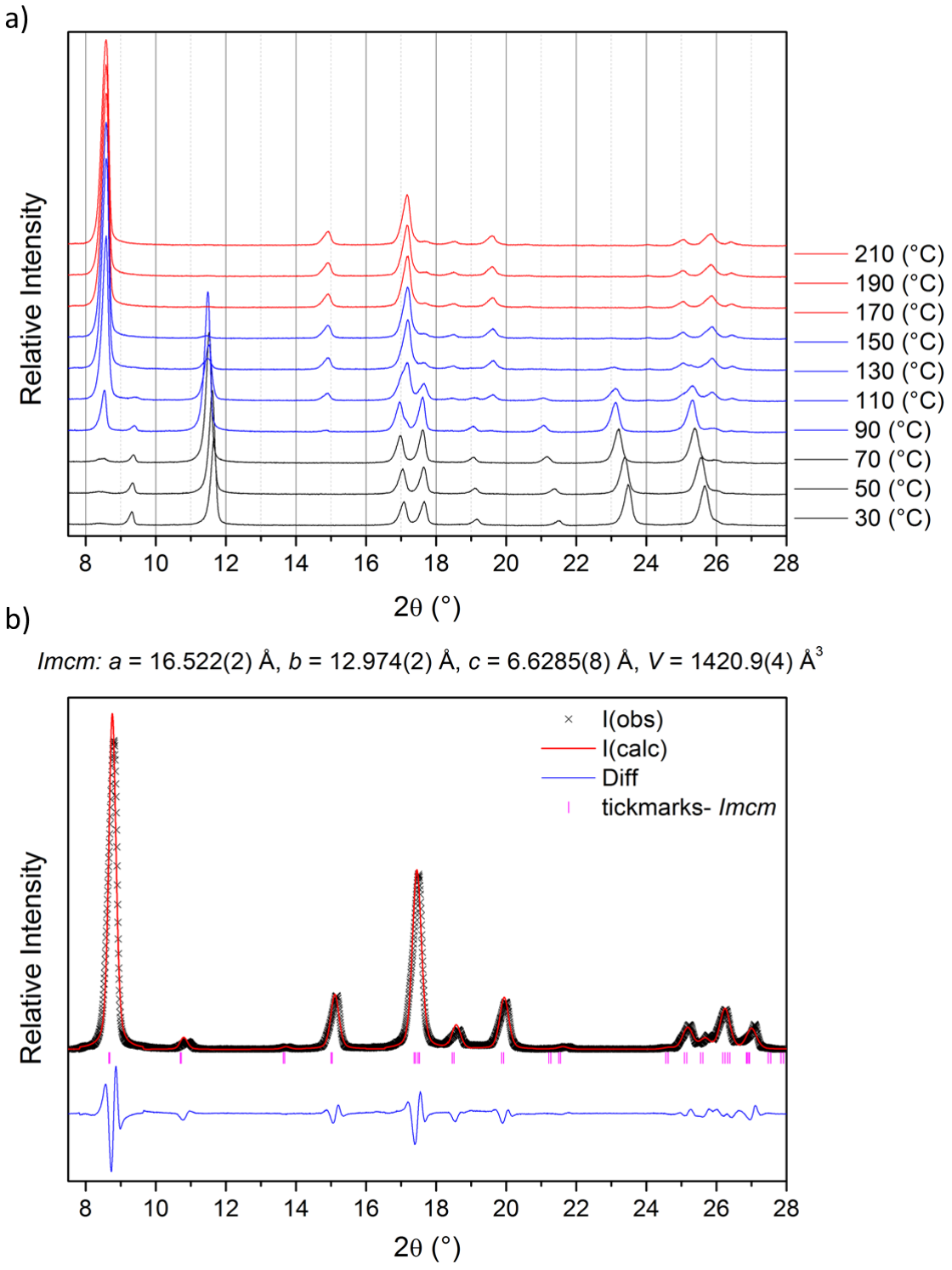

Figure 4.14: Dehydration of the -NO_2 modified MIL-53(Al) by heating to 210 °C. a) Individual XRD patterns showing the change in symmetry with increasing temperature (black = hydrated (C2/c), blue = mixed phase and red = dehydrated (Imcm)) and b) Le Bail profile fit for data recorded at 210 °C.

Figure 4.15 shows that superhydration of the framework occurs using the method described previously (*i.e.* preparing a paste with the material) and this is evidenced by

the initial pattern at 30 °C exhibiting the fully-open, *Imcm*, pattern. It was expected that the *Imcm* phase would only exist while the sample remained as a paste and that upon drying to a powder it would contract to the closed phase as was seen for MIL-53(Cr).[20] However, heat was required to remove the additional water molecules from the pores. The sample was heated to 100 °C and then returned to 30 °C, which showed that the process was fully reversible. Dehydration of the fully-open superhydrated phase occurs via the closed hydrated phase (seen at 60 °C), showing that the water is lost in two steps; the additional water being lost first. Then further heating showed that the framework started expanding to give the dehydrated phase as was seen previously for the dehydration experiment. Upon cooling to 30 °C the framework takes up water from the air and returns to the hydrated phase. Longer data collection was used to collect data at 30 °C before thermal treatment was applied. These data were used to perform a Le Bail profile fit; longer data collection was possible for this dataset as the framework retained water at 30 °C. Figure 4.15b shows that it was necessary to use a mixed-phase refinement as the expansion of the whole structure due to superhydration had not occurred; a minor amount of the hydrated phase was still present. The fully-open phase was refined using the *Imcm* space group as before, whereas the starting point of the refinement for the closed phase used hydrated MIL-53(Cr), which has a unit cell volume of 994 $Å^3$ and has the monoclinic space group, *C2/c*.[21] This analysis shows that this method was unable to superhydrate the material completely.

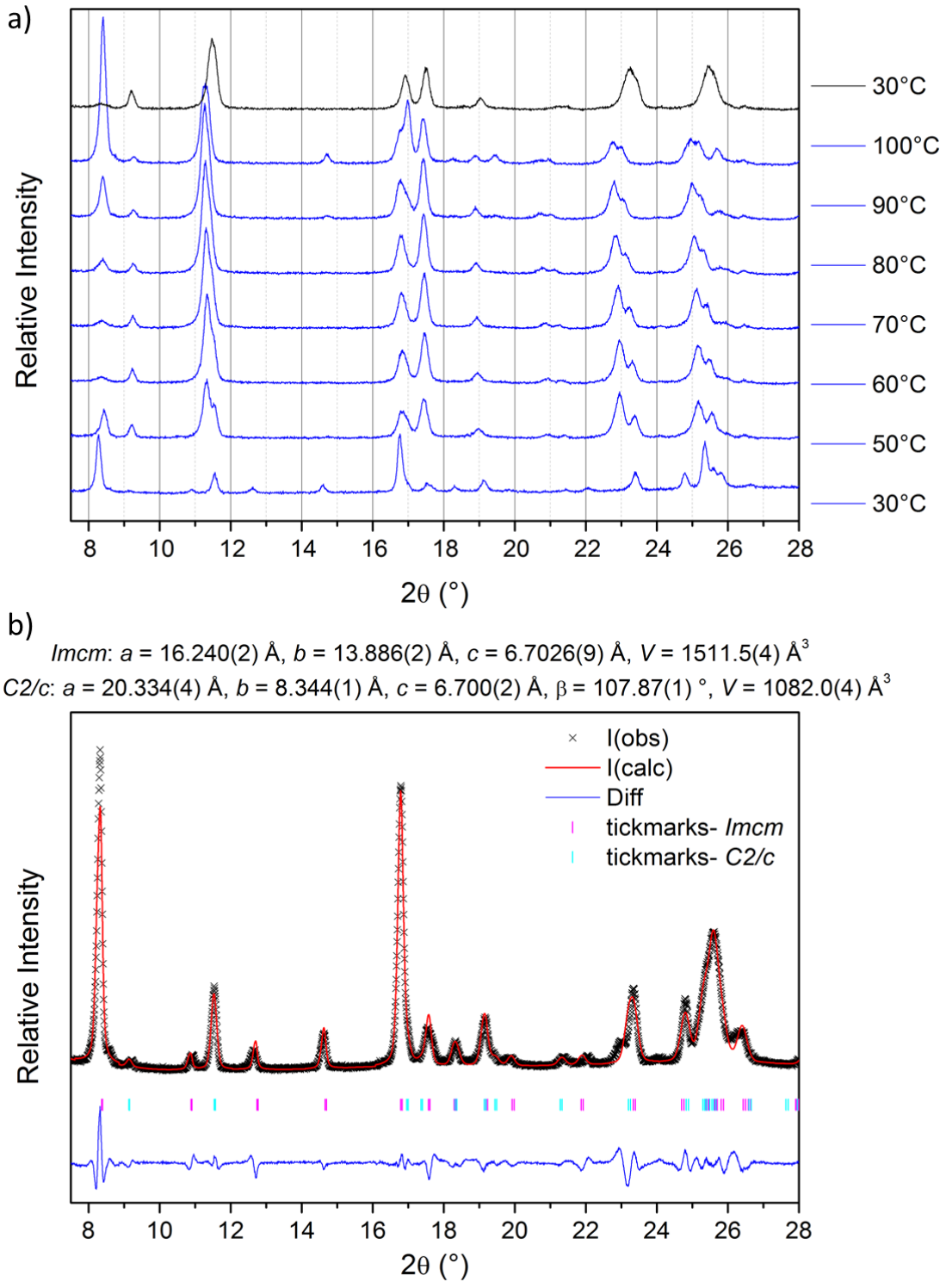

Figure 4.15: The removal of H_2O from the superhydrated phase of the -NO_2 modified MIL-53(Al). a) Individual XRD patterns show the removal of H_2O using temperature (blue = mixed phase and black = hydrated (C2/c)) and b) Le Bail profile fit for the partially superhydrated phase of NO_2 modified MIL-53(Al) recorded at room temperature.

The uptake of methanol by the –NO_2 modified MIL-53(Al) was followed using *in situ* XRD, Figure 4.16. The methanol vapour was introduced into the gas chamber on scan

number 3 (point A) and was removed and replaced with N_2 on scan number 23 (point B). The contour plot highlights the change in framework symmetry during the experiment. After the addition of methanol vapour it can be seen that the framework expands from the hydrated phase to the fully-open phase but does not expand via a transient half-open phase as was seen for fluorinated MIL-53(Fe) in the presence of methanol.[10] After the introduction of a N_2 gas flow the methanol is lost from the pores and the framework returns to a pore volume similar to the hydrated phase. Interestingly, water should not be present in the N_2 gas flow therefore it is suggested that the fully-open phase contains a mixture of methanol and water molecules as was observed for hydrated MIL-53(Fe) upon the adsorption of methanol (Section 4.2.2). Consequently, after the introduction of the pure N_2 gas flow the methanol molecules are desorbed from the framework but the water remains. This requires further investigation. To improve the signal-to-noise ratio in the pattern of the fully-open methanol phase of $–NO_2$ modified MIL-53(Al) a longer data collection was used. This dataset was used to perform a Le Bail profile fit. Figure 4.16b shows that the framework fully-opens to give the orthorhombic, *Imcm*, structure with a refined unit cell volume of 1467.6 $Å^3$. This fully-open phase is larger than the fully-open phase recorded for the dehydrated material, 1420.9 Å. Greater expansion upon the adsorption of guest molecules, when compared to the dehydrated phase, was also seen for MIL-53(Cr);[17] providing further evidence for the inclusion of the guest molecules within the $–NO_2$ modified material.

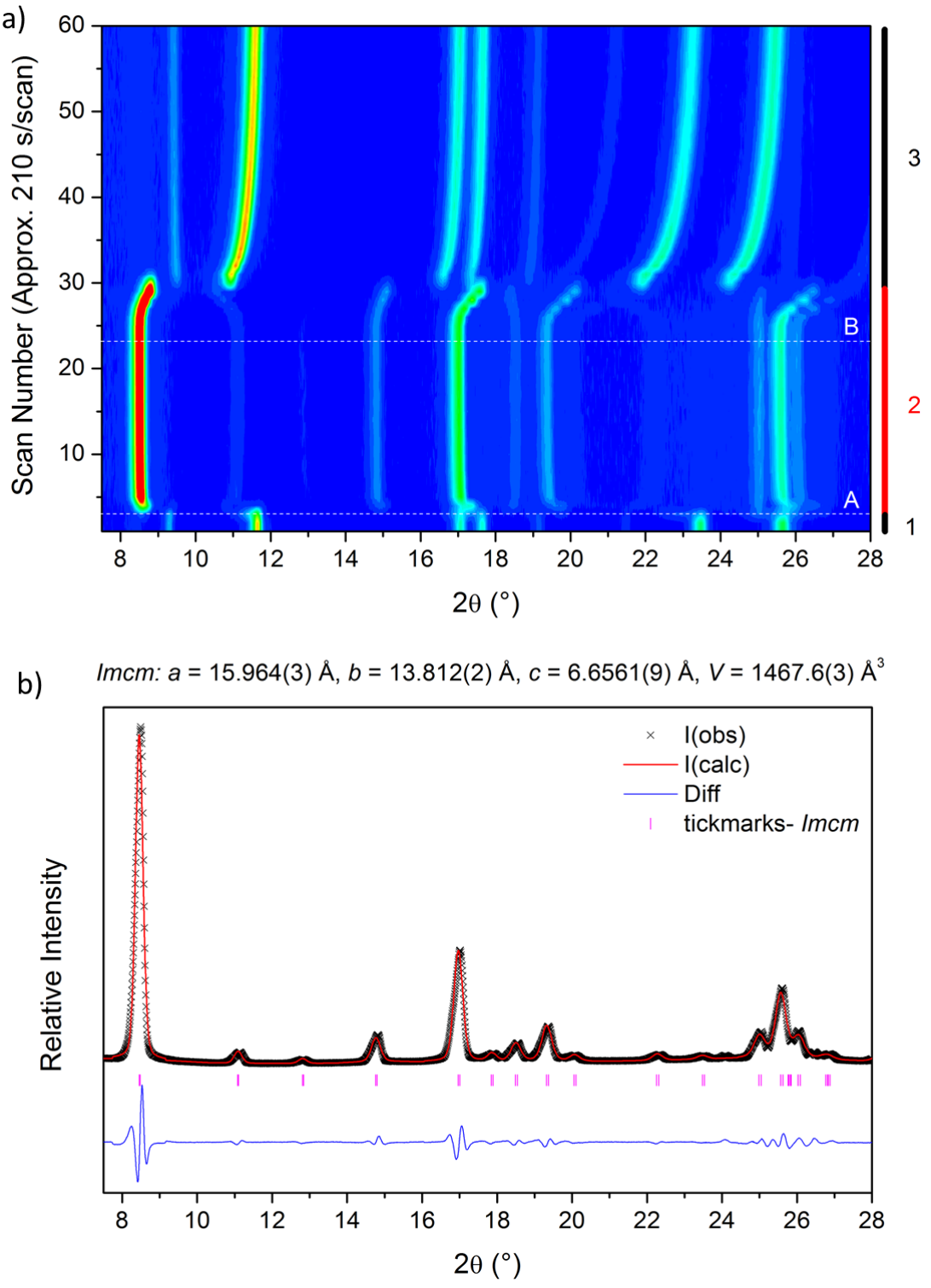

Figure 4.16: Behaviour of the -NO_2 modified MIL-53(Al) in response to methanol vapour. a) Contour plot, where A indicates the introduction of methanol vapour and B indicates when the gas flow was switched to pure N_2 (Phase 1/3 (black) = hydrated phase (C2/c), Phase 2 (red) = fully-open MeOH phase (Imcm)) and b) Le Bail profile fit for the fully-open methanol phase

Figure 4.17 shows the result of the heptane adsorption study. The contour plot shows that the hydrated phase expands in response to the heptane vapour, which was

introduced at point (A). It also shows that there is little change in the unit cell parameters after the heptane vapour is switched to a flow of pure nitrogen at point (B); only a slight contraction was observed. Using this *in situ* XRD method it is not possible to confirm if the slight contraction of the framework was due to the removal of the heptane guest molecules; complementary techniques are needed to study this behaviour. A longer data collection time was used to record the individual XRD pattern for the fully-open heptane phase. These data were used to produce a Le Bail profile fit which gave a refined unit cell volume of 1456.7 $Å^3$ (Figure 4.17b).

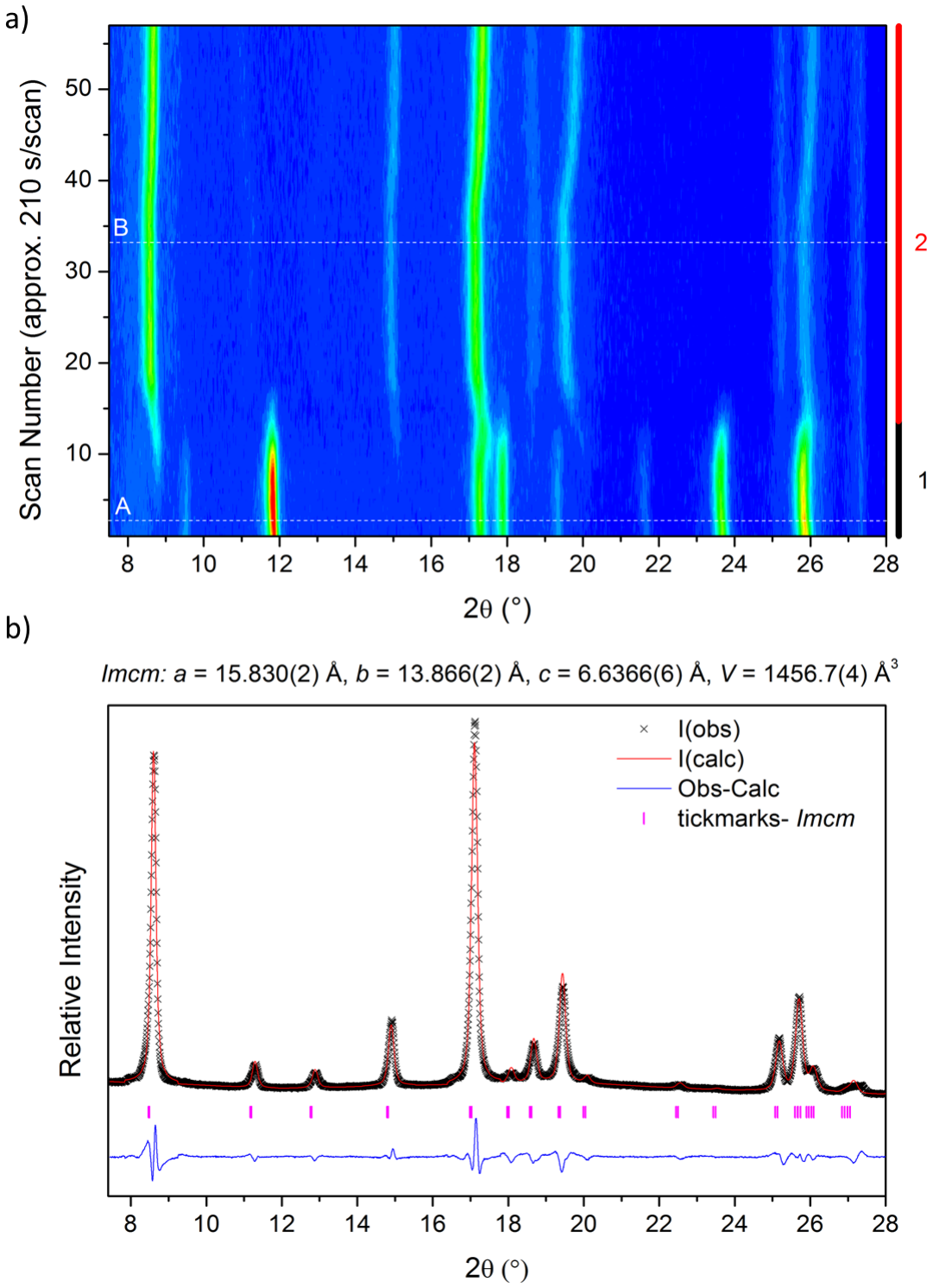

Figure 4.17: Behaviour of the -NO_2 modified MIL-53(Al) in response to heptane vapour. a) Contour plot, where A indicates the introduction of heptane vapour and B indicates when the gas flow was switched to pure N_2 (Phase 1 (black) = hydrated phase (C2/c), Phase 2 (red) = fully-open heptane phase (Imcm)) and b) Le Bail profile fit for the fully-open heptane phase

4.3.1.2 Bromo Modified MIL-53(Al)

The monoclinic hydrated phase of –Br modified MIL-53(Al) has a unit cell volume of 1055 $Å^3$ (Table 4.3). The thermal dehydration of the sample is shown in Figure 4.18. A gradual shift of the hydrated Bragg peaks towards high angle can be seen before the growth of the fully-open phase is first visible above 130 °C. However, complete evolution to the fully-open framework was not seen at 210 °C using this *in situ* method. Longer data collection was performed as the sample was held at 210 °C; as the material was held at this temperature complete evolution to the fully-open phase was achieved. The Le Bail refinement, Figure 4.18b, shows that the framework expands to the orthorhombic, *Imcm*, phase to give a unit cell volume of 1420 $Å^3$ (Table 4.3).

.

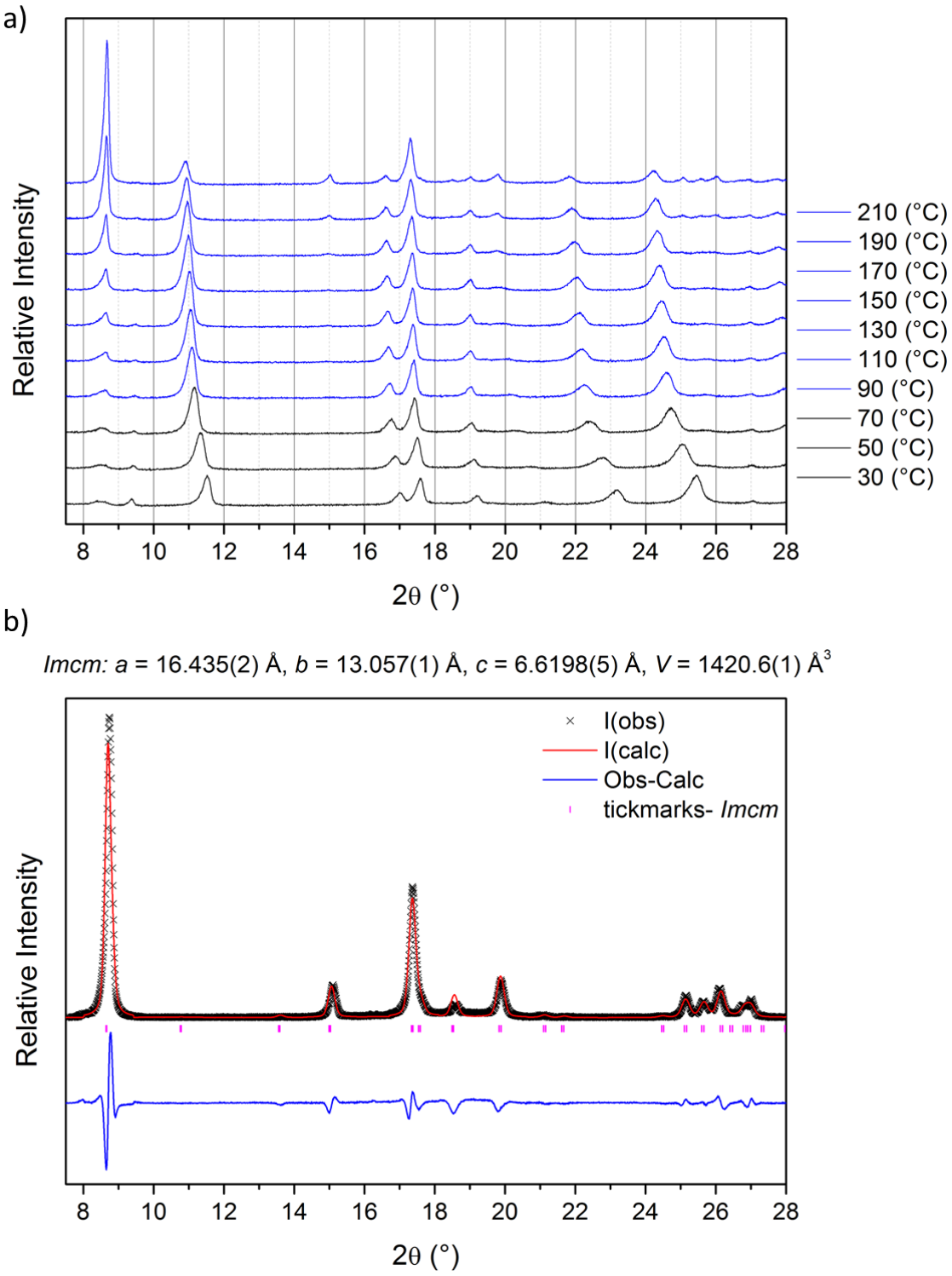

Figure 4.18: Thermal dehydration of the –Br modified MIL-53(Al) a) Individual XRD patterns showing the response of the framework to increasing temperature (black = hydrated (C2/c), blue = mixed phase and red = dehydrated (Imcm))and b) Le Bail profile fit for the phase recorded at 210 °C.

Superhydration of the framework was investigated and it was observed that although the framework initially takes up water in the powder/water suspension the interaction is not

very strong and it is easily lost from the framework. The contour plot, Figure 4.19, shows the contraction of the framework upon the loss of water without the need for any external stimuli *e.g*. heat. The sample was maintained at 30 °C throughout this experiment and no gas flow was used. Due to the difficulties experienced in making the paste remain level in the sample holder, especially after contraction upon drying, the Bragg peaks have very low intensities. Therefore the individual XRD patterns have a low signal-to-noise ratio but it is still possible to identify the strongest Bragg reflections that indicate the presence of each phase. A Le Bail profile fit was performed on the first pattern recorded for the contour plot. The low signal-to-noise ratio increased the errors of the refinement but it can be clearly seen that the superhydrated phase has the fully-open, *Imcm*, structure (Figure 4.19b).

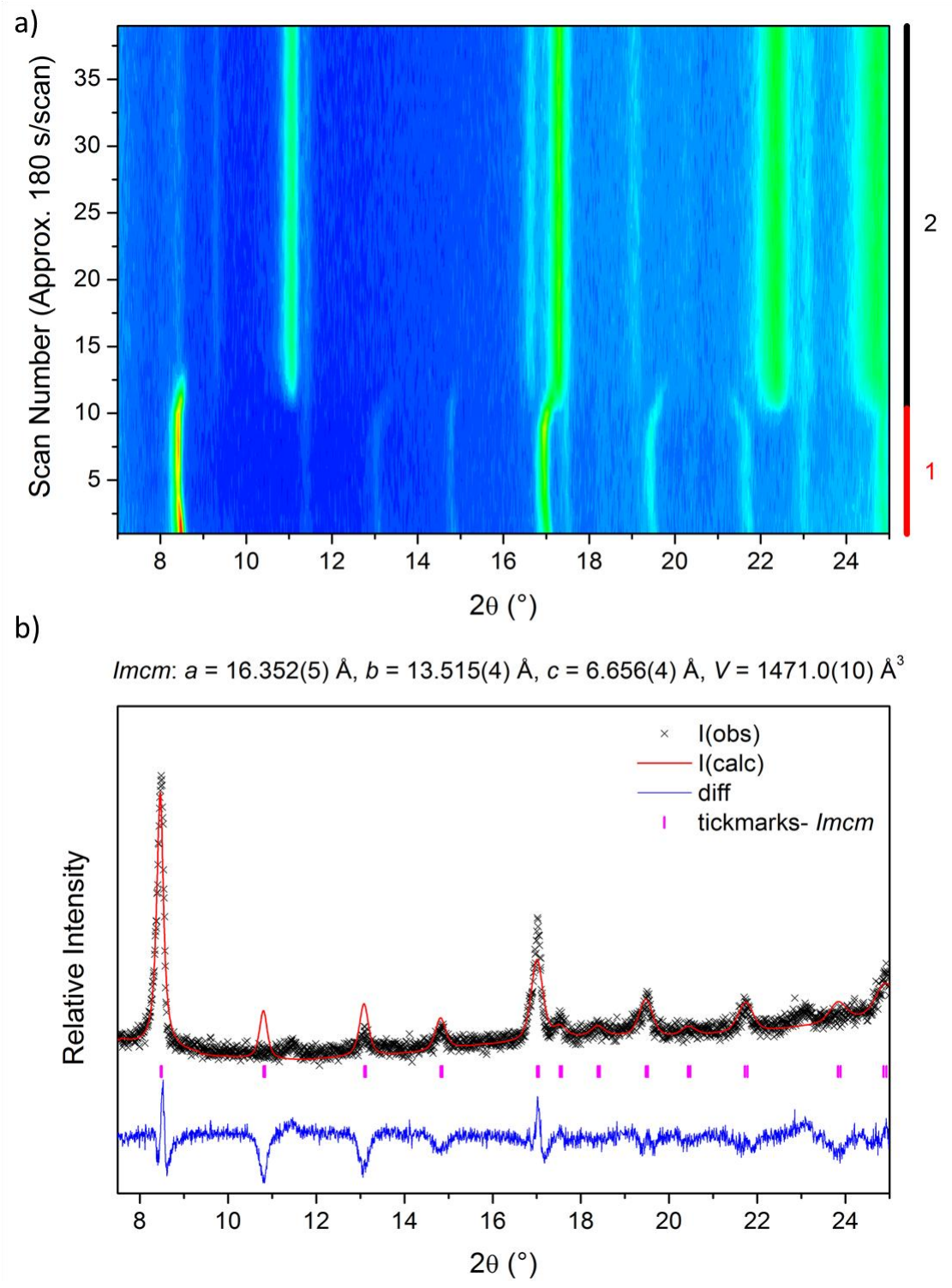

Figure 4.19: The removal of H_2O from the superhydrated phase of the -Br modified MIL-53(Al). a) Contour plot showing the gradual loss of the excess water at 30 °C (Phase 1 (red) = superhydrated phase (Imcm) and Phase 2 (black) = hydrated phase (C2/c)) and b) Le Bail profile fit of the first scan of the contour plot when the material is superhydrated.

The sample was exposed to a flow of methanol vapour and then a stationary environment was used while a long data collection was performed. This pattern, which has a good signal-to-noise ratio, was used for a Le Bail profile fit. Figure 4.20 shows that the –Br modified framework fully-opens in response to methanol vapour. The refined unit cell volume was determined to be 1476.7 $Å^3$, which is larger than the calculated volume for the dehydrated phase of this framework, 1420.6 $Å^3$.

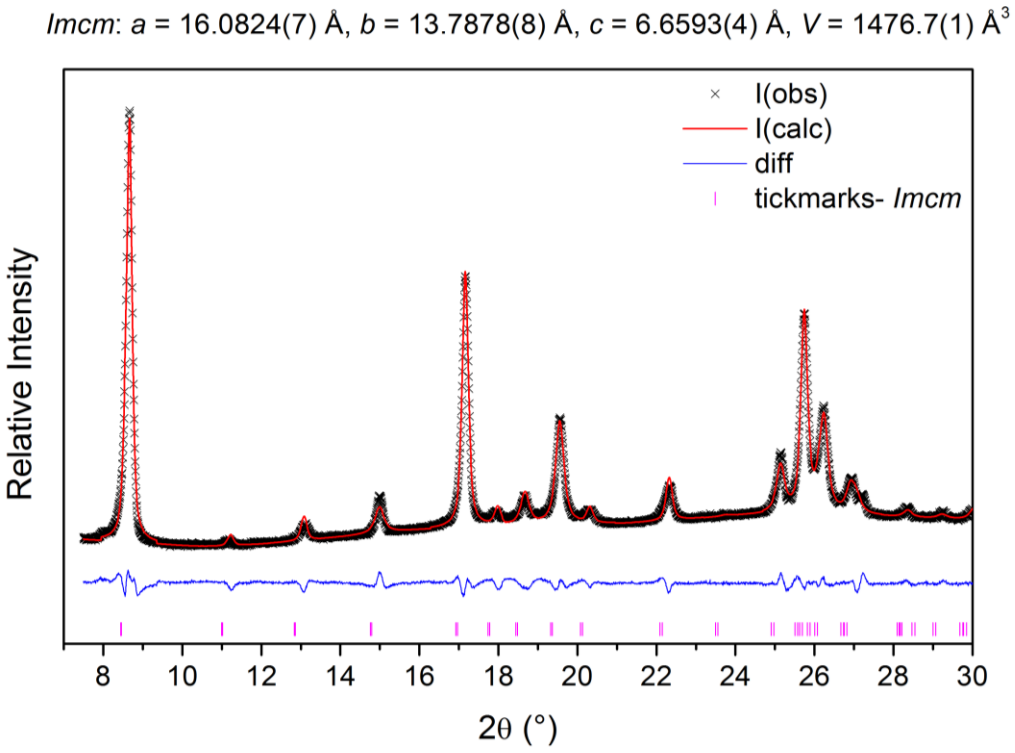

Figure 4.20: Le Bail profile fit for the fully-open methanol phase of the –Br modified MIL-53(Al)

4.3.1.3 Methyl Modified MIL-53(Al)

The monoclinic hydrated phase of the $–CH_3$ modified MIL-53(Al) framework has a unit cell volume of 998 $Å^3$. The thermal dehydration of the framework is shown in Figure 4.21, which shows that the framework reaches complete expansion at 190 °C. Upon cooling back to room temperature the framework remains fully-open until the temperature drops below 110 °C (Appendix). A long data collection was recorded while

the sample was held at 210 °C to improve the pattern used for the profile parameter refinement. The Le Bail profile parameter fit confirms that the framework is fully-expanded at high temperatures, Figure 4.21b. The refinement gives a unit cell volume of 1416.6 $Å^3$.

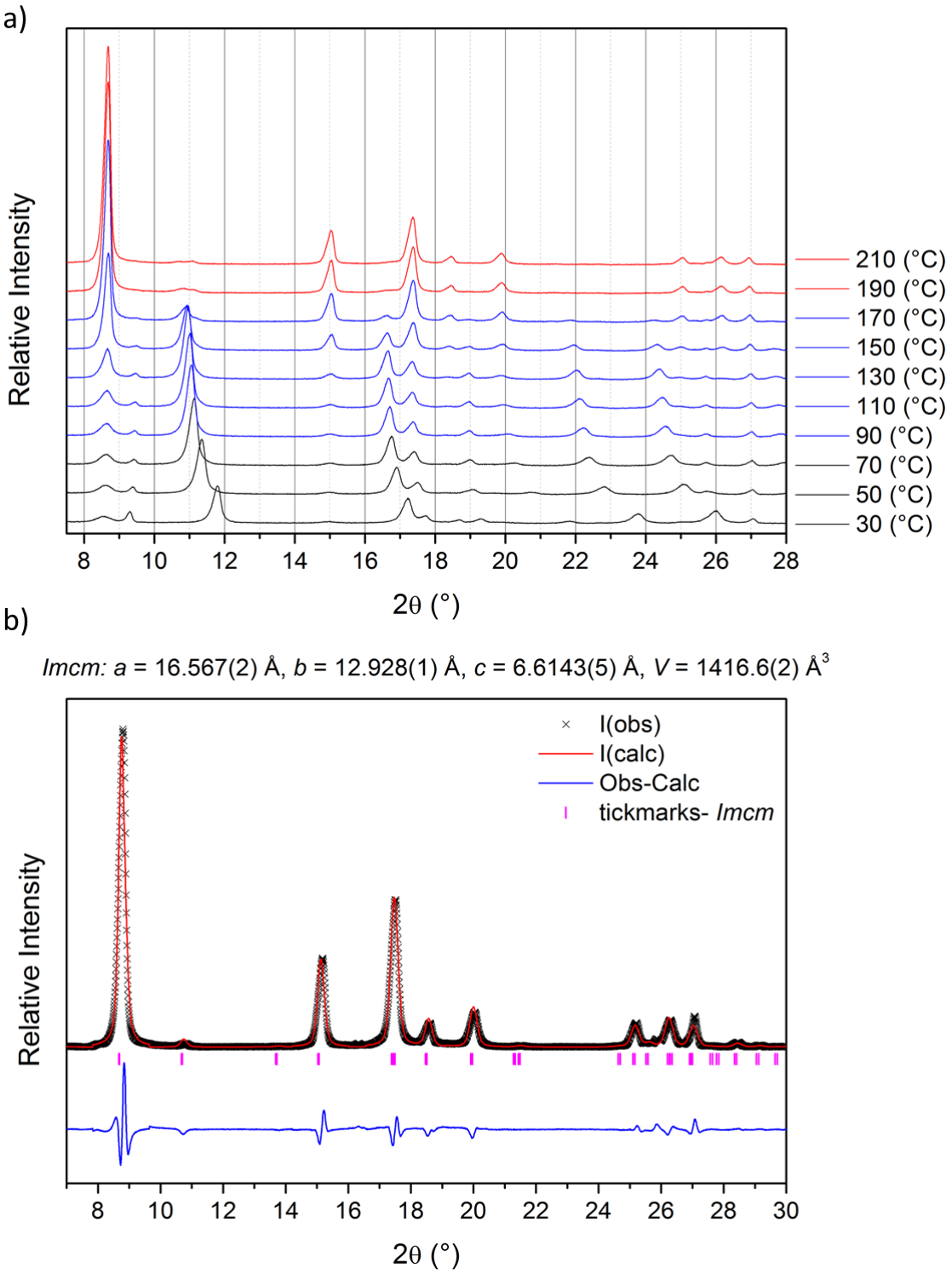

Figure 4.21: Thermal dehydration of the –CH_3 modified MIL-53(Al). a) Individual XRD patterns showing the change in symmetry with increasing temperature (black = hydrated phase (C2/c), blue = mixed phase and red = dehydrated phase (Imcm)) and b) Le Bail profile fit for data recorded at 210 °C.

Superhydration of the framework was attempted as for the previous samples. The initial individual XRD pattern shows that, under the same conditions as were used for the

other samples, this framework does not superhydrate to give the fully-open phase. The appearance of the (110) peak (~ 8°) of the fully-open phase indicates that some of the material opened, but the interaction was not sufficient to open the entire sample. A Le Bail profile fit (Figure 4.22) was performed on the first pattern recorded during this experiment, which confirms the hydrated phase has partially expanded to the, *Imcm*, structure.

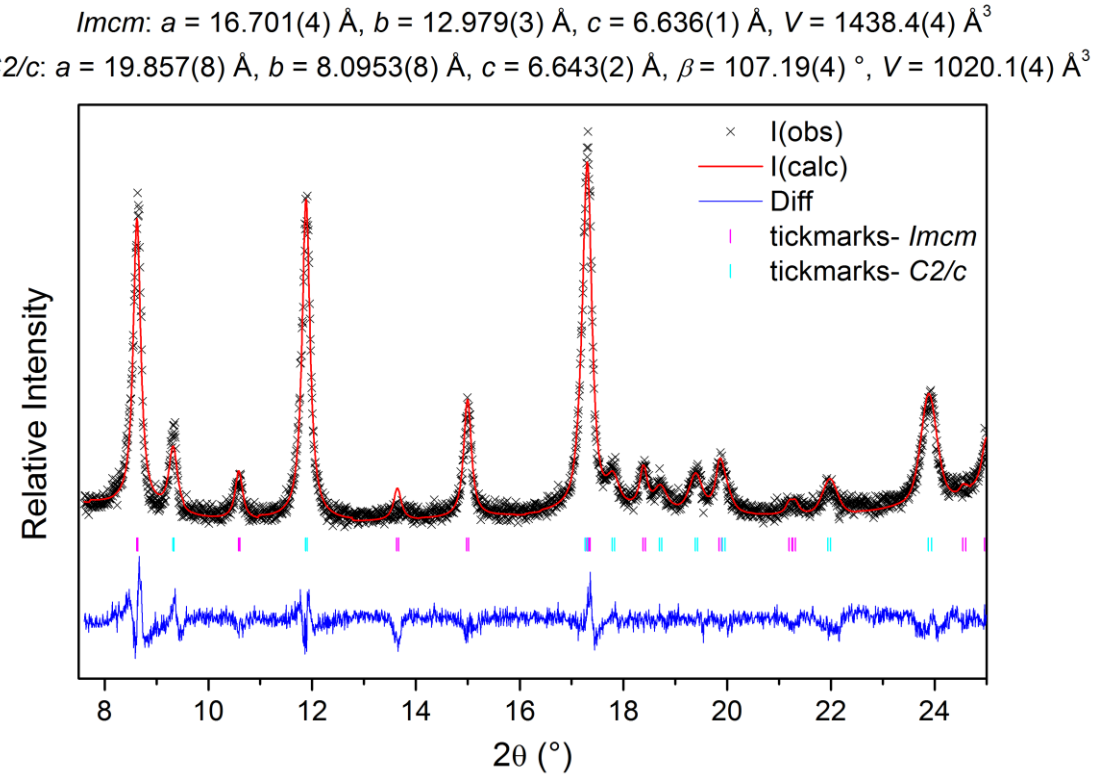

Figure 4.22: Le Bail profile fit for the partially superhydrated –CH_3 modified MIL-53(Al)

As before, the adsorption of methanol vapour was followed using *in situ* methods. The contour plot, Figure 4.23, shows that the hydrated phase undergoes a slight expansion upon the addition of methanol vapour before switching to the fully-open phase. When the methanol vapour is turned off and replaced by N_2 gas (point B) the framework exhibits a small contraction, which is indicative of the removal of the guest to give the dehydrated phase, 1416.6 Å^3. The growth of some Bragg peaks, in equivalent 2θ

positions to those seen before complete expansion, are observed suggesting that some of the material has contracted slightly upon the removal of the guest, this requires further investigation. Figure 4.23b shows the Le Bail profile parameter fit for the fully-open methanol phase; the framework expands to a unit cell volume of 1450.2 $Å^3$. Long data collection and a stationary methanol environment were used to collect these data.

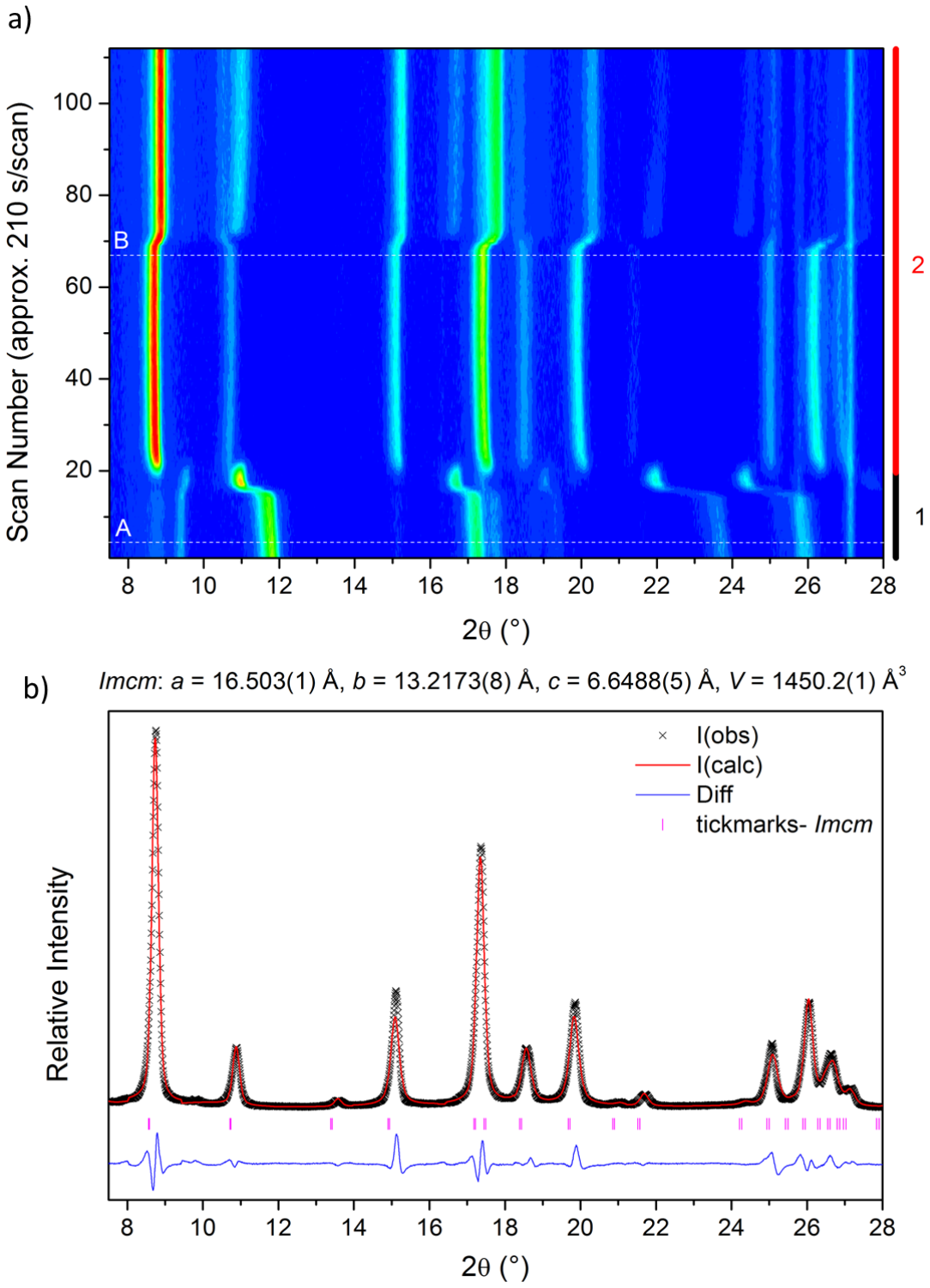

Figure 4.23: Behaviour of –CH_3 modified MIL-53(Al) in response to methanol vapour. a) Contour plot showing methanol adsorption (Phase 1 (black) = hydrated phase (Cc) and Phase 2 (red) = fully-open phase (Imcm)) and b) Le Bail profile fit for the fully-open methanol phase.

Figure 4.24 shows the result of the heptane adsorption study. The contour plot shows that the sample expands after the introduction of heptane vapour at point (A); expansion

occurs in one step. After switching the heptane vapour to a flow of pure N_2 gas at point (B) a very slight contraction of the framework is observed. To obtain the lattice parameters for the heptane phase a longer collection time was used to improve the signal-to-noise ratio of the individual XRD pattern. These data were used to produce a Le Bail profile fit with a refined unit cell volume of 1416.8 $Å^3$. This volume is the same as the unit cell volume refined for the dehydrated phase of this material, 1416.6 $Å^3$. An additional investigation found that it was not possible to dehydrate this material using a pure flow of N_2 gas, as was found for MIL-53(Fe) (Section 4.2), this implies that the expansion of the framework is due solely to the adsorption of heptane.

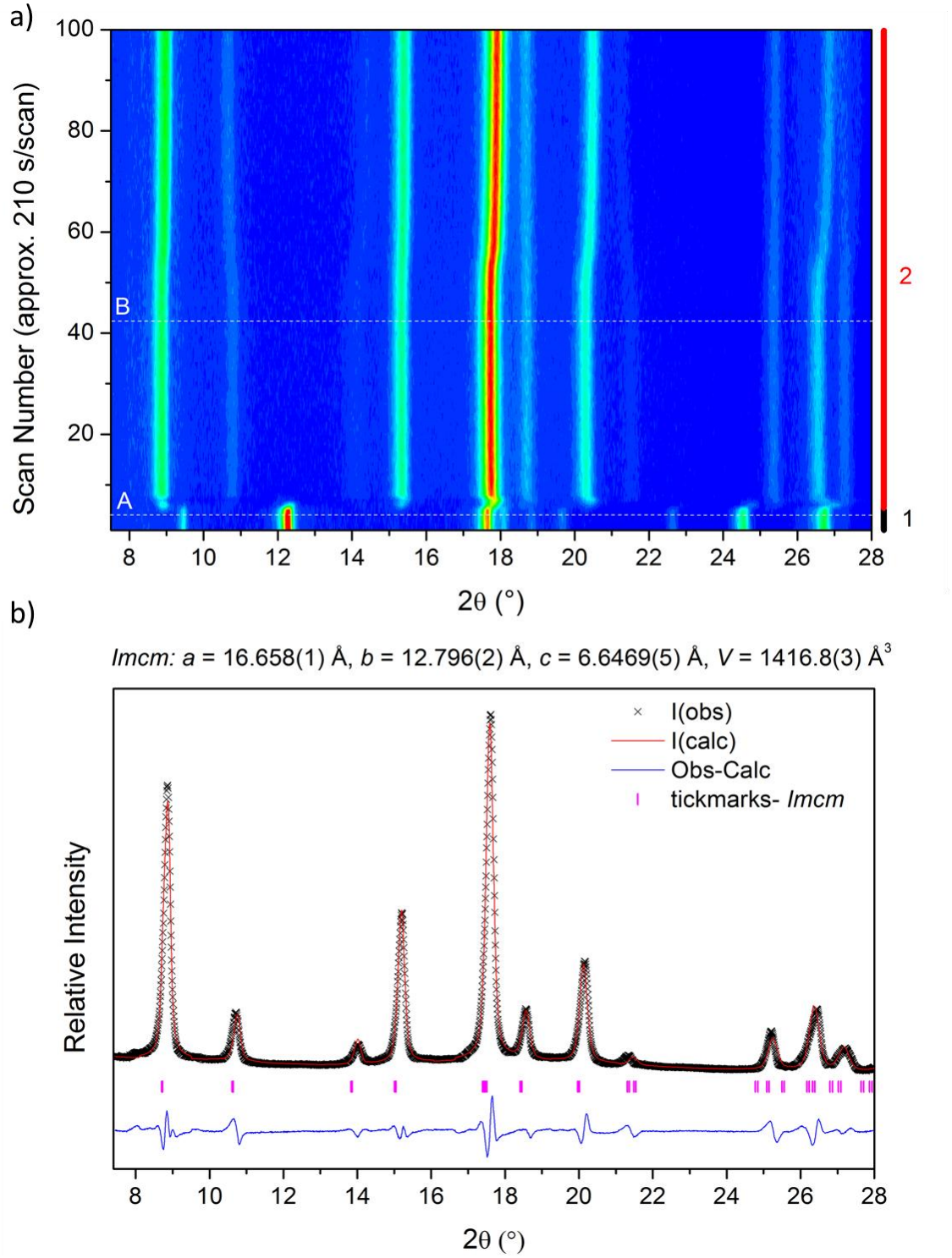

Figure 4.24: Behaviour of –$(CH)_3$ modified MIL-53(Al) in response to heptane vapour. a) Contour plot showing heptane adsorption (Phase 1 (black) = hydrated phase (Cc) and Phase 2 (red) = fully-open phase (Imcm)) and b) Le Bail profile fit for the fully-open heptane phase.

4.3.1.4 Dihydroxy Modified MIL-53(Al)

The hydrated, monoclinic phase of the -$(OH)_2$ modified MIL-53(Al) has a unit cell volume of 955 Å^3. The thermal dehydration is shown in Figure 4.25. The framework does not expand as was seen for the previous frameworks. The peaks shift to a higher value of 2θ indicating that the structure has contracted. A possible reason for this contrast in behaviour is that the –OH functional groups which have been added to the terephthalate rings are able to hydrogen bond with neighbouring groups resulting in the framework being "locked" in a contracted phase. These interactions would be strengthened as a result of the removal of water as the functional groups could come closer together. Figure 4.25b shows the Le Bail profile fit for the data recorded *in situ* at 210 °C. The monoclinic, *C2/c*, dehydrated phase of MIL-53(Fe), 904.4 Å^3, was used as a starting point for the refinement as a contraction upon dehydration is also seen for this material.[9] This analysis confirms that the framework contracts upon dehydration and shows the assumption that it contracts in a similar way to MIL-53(Fe) to be reasonable. The unit cell volume was refined to be 903.6 Å^3.

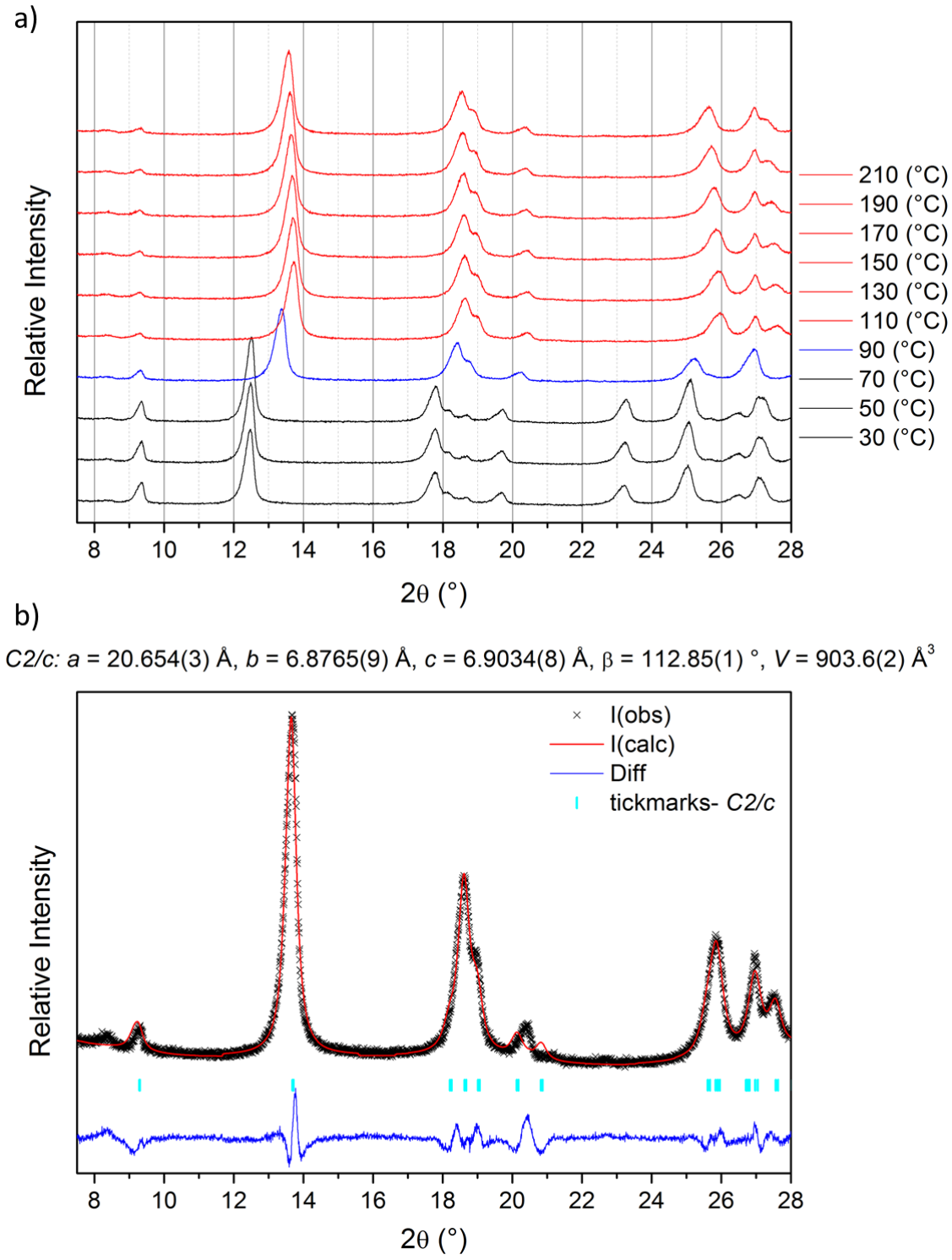

Figure 4.25: Thermal dehydration of the –$(OH)_2$ modified MIL-53(Al). a) Individual XRD patterns showing the change in unit cell parameters with increasing temperature (Black = hydrated phase (C2/c), blue = mixed phase and red = dehydrated phase (C2/c)) and b) Le Bail profile fit for data recorded at 210 °C.

The superhydration experiment for the –$(OH)_2$ modified MIL-53(Al) shows that the pores of the framework are able to accommodate extra water at room temperature as the

framework expands to the fully-open phase (Figure 4.26). It was also found that the interaction between the excess water and the framework was stronger than the interaction seen between the –Br modified MIL-53(Al) and excess water. After leaving at 30 °C for several hours, which was enough to remove the excess water from the –Br modified framework, only a minor contraction of the dihydroxy modified framework was seen. The sample was left overnight under the same conditions but no further contraction was seen when the sample was tested the following day. The in situ data collection was resumed with a flow of dry nitrogen which forced the excess water molecules out of the framework to give the hydrated phase. As the sample was not removed from the diffractometer between experiments it was possible to join the two datasets together; labelled as point (A) in the contour plot. The first scan from the contour plot was used to perform a Le Bail profile fit for this dataset, Figure 4.26b. This analysis confirms that the framework fully-opens in the presence of excess water to give the orthorhombic structure with a refined unit cell volume of 1397.6 $Å^3$. This is smaller than the unit cell volume found for the other superhydrated modified materials (Table 4.3, Section 4.3.1.8). One possible explanation for the smaller unit cell volume is that hydrogen bonding between the additional –OH groups on the linkers and the H_2O guest molecules can occur; resulting in a smaller unit cell volume.

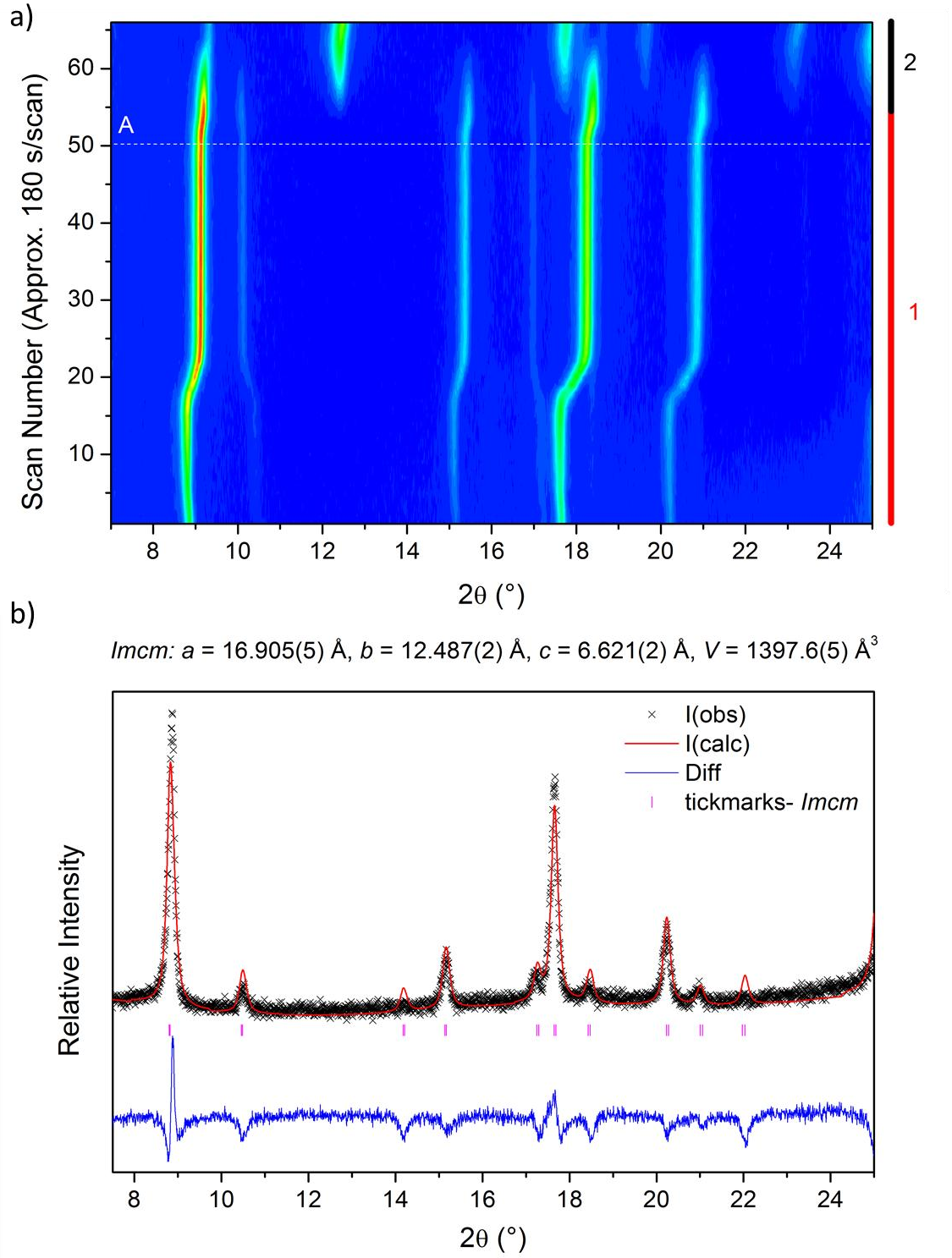

Figure 4.26: Removal of excess H_2O from the superhydrated –$(OH)_2$ modified MIL-53(Al) a) contour plot showing the removal of the excess water using a flow of dry nitrogen gas (Phase 1 (red) = superhydrated phase (Imcm) and Phase 2 (black) = hydrated phase(C2/c)) and b) Le Bail profile fit for the superhydrated phase; data were recorded at room temperature.

The methanol sorption experiment shows that the framework also expands in response to methanol vapour. The interaction between methanol and this framework is strong

enough that residual methanol vapour inside the sample chamber was sufficient to open the framework fully before data collection had begun. A flow of methanol vapour was passed over the sample to ensure it had opened fully before being replaced by a flow of pure N_2 gas (point B). The contour plot in Figure 4.27a shows that there is a gradual contraction of the fully-open phase before it exhibits a change in symmetry upon closing to a unit cell volume similar to the half-open phase seen for MIL-53(Fe).[10] After more than three hours under a flow of N_2 gas, contraction to the dehydrated phase was not seen. A Le Bail profile fit (Figure 4.27b) was performed for both phases seen in the contour plot. A longer data collection, in a stationary methanol environment, was used to record the data used for the refinement of the fully-open phase whereas the data collected *in situ* was used for the half-open phase refinement. The unit cell parameters of the half-open MIL-53(Fe)[lutidine][22] phase were used as the starting point for the refinement of the half-open phase. These analyses show that the framework expands to the fully-open, *Imcm*, phase with a unit cell volume of 1444.5 $Å^3$ and contracts via a half-open, *C2/c*, phase with a unit cell volume of 1110.5 $Å^3$.

The methanol adsorption experiments for MIL-53(Fe) showed that the framework could contain two equivalents of methanol in the fully-open phase and one equivalent of methanol in the half-open phase (Section 4.2). The contraction of the MIL-53(Al)-$(OH)_2$ framework to a volume similar to this half-open phase could be a consequence of the methanol being removed from the framework in two steps.

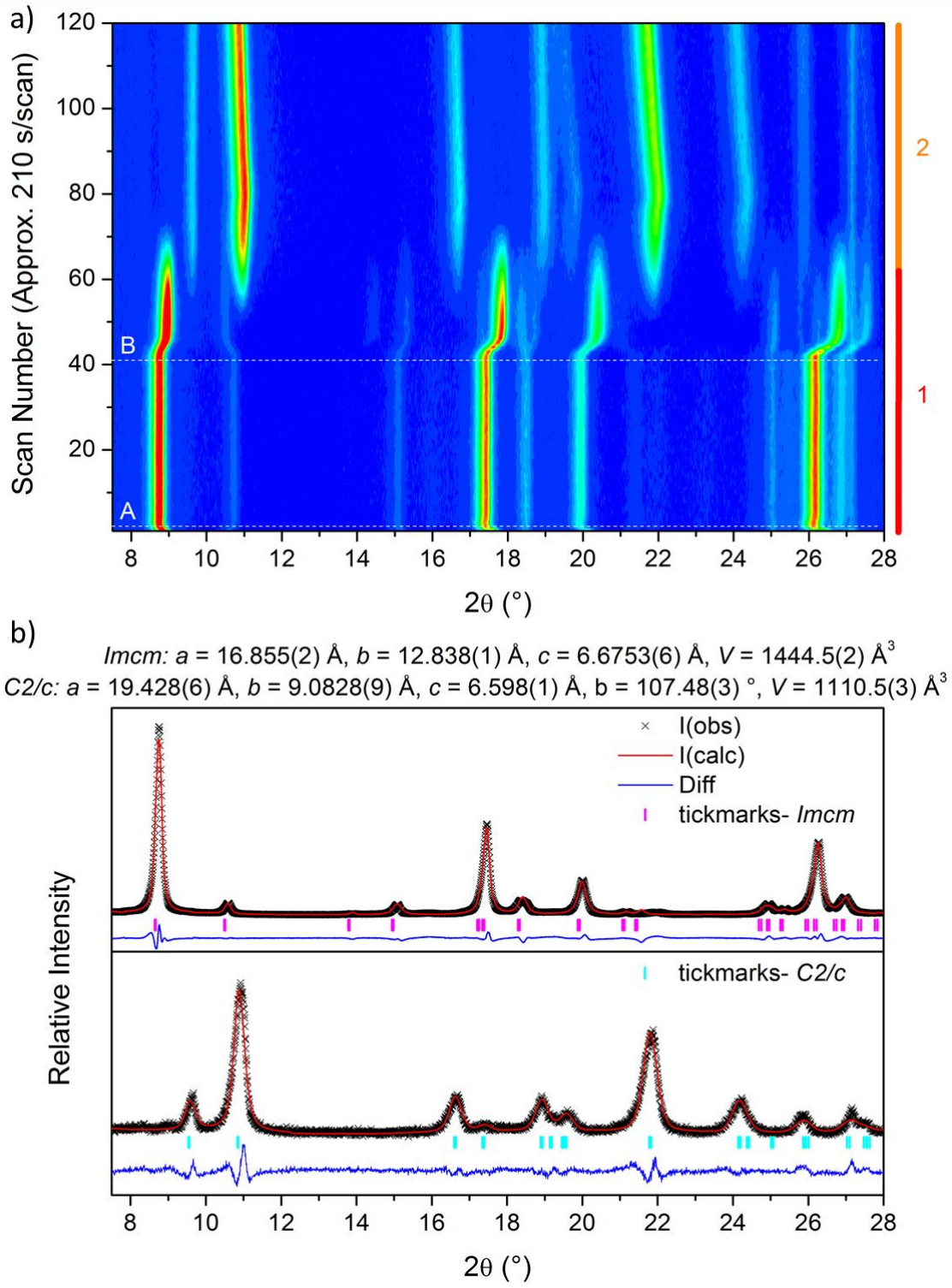

Figure 4.27: Behaviour of –$(OH)_2$ modified MIL-53(Al) in response to methanol vapour. a) Contour plot showing methanol desorption (Phase 1 (red) = fully-open methanol phase (Imcm) and Phase 2 (orange) = half-open methanol phase (C2/c)) and b) Le Bail profile fit for the fully-open methanol phase (top) and the half-open phase (bottom).

4.3.1.5 Breathing of the Carboxy Modified MIL-53(Al)

The hydrated, monoclinic phase for the –COOH modified MIL-53(Al) has a unit cell volume of 1055 $Å^3$. The thermal dehydration experiments show that the framework expands to the fully-open phase. Complete conversion to this phase does not occur until it is heated above 300 °C (Figure 4.28). The Le Bail profile fit for dehydrated –COOH modified MIL-53(Al) is shown in Figure 4.28b; the data collected *in situ* was used for this refinement. This analysis shows that the framework fully-opens to give the *Imcm* structure upon removal of the guest water molecules. The refined unit cell volume was found to be 1434.2 $Å^3$.

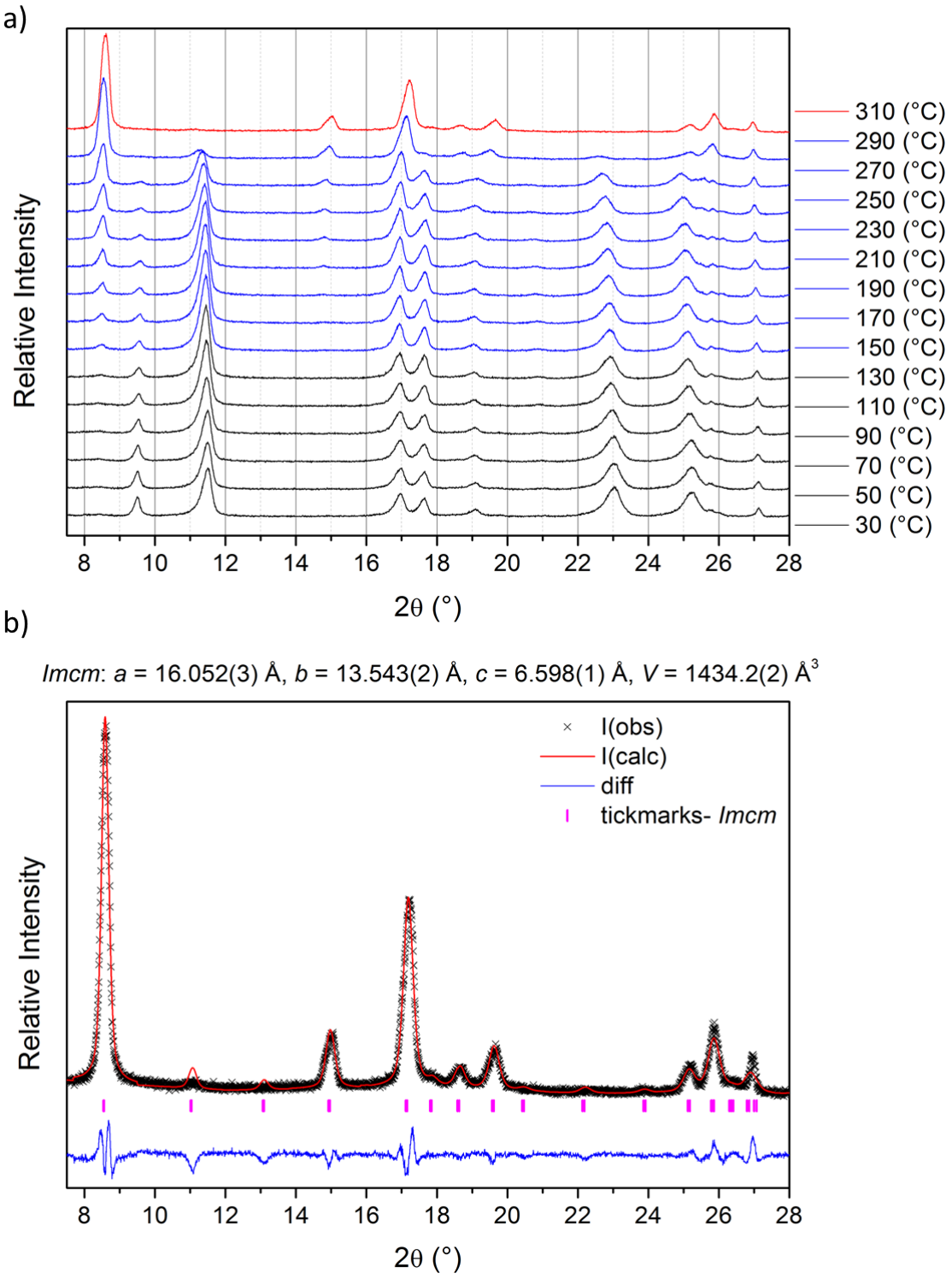

Figure 4.28: Thermal dehydration of the-COOH modified MIL-53(Al). a) Individual XRD patterns showing a change in symmetry with increasing temperature (black = hydrated (C2/c), blue = mixed phase and red = dehydrated (Imcm)) and b) Le Bail profile fit for data recorded at 310 °C.

The superhydration experiment shows that the framework partially expands in the presence of excess water, however there is still evidence in the individual XRD pattern

(Figure 4.29b) for some residual hydrated phase (peak at ~ 11.5 °). The contour plot gives evidence that the excess water is not bound strongly within the framework as it is lost after approximately 30 minutes when held at 30 °C. Upon losing the excess water molecules the fully-open phase shows a gradual contraction before contracting fully to give the hydrated phase (Figure 4.29a). Figure 4.29b shows the Le Bail profile fit for the superhydrated –COOH modified MIL-53(Al). Data with a better signal-to-noise ratio could not be collected due to the rapid nature with which the framework loses the excess water. A mixed phase refinement was performed, as the whole framework had not expanded to give the fully-open *Imcm* structure; part of the framework still had the hydrated structure.

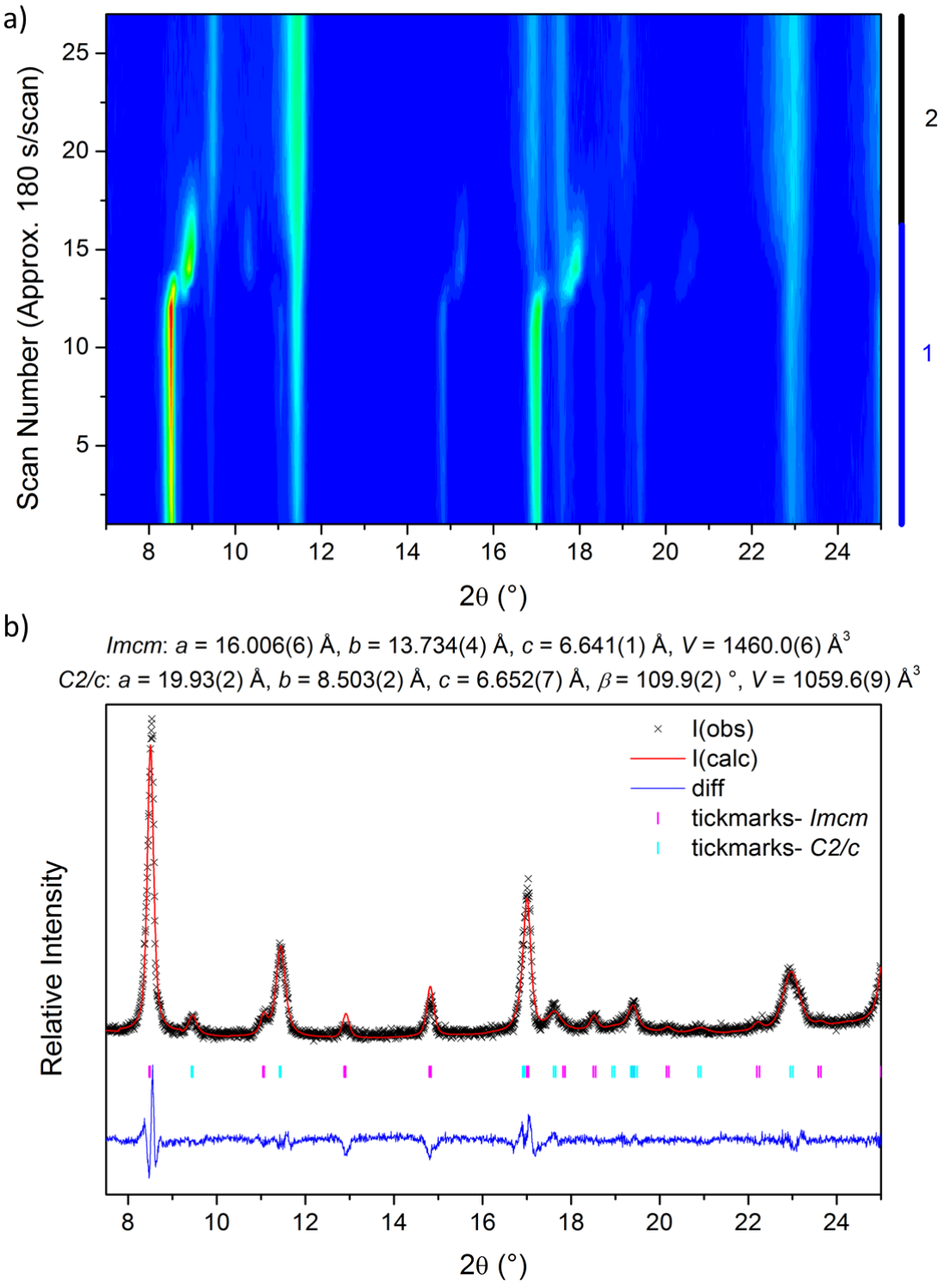

Figure 4.29: Removal of excess water from the Superhydrated –COOH modified MIL-53(Al). a) Contour plot showing the contraction of the framework upon removal of water (Phase 1 (blue) = mixed phase and Phase 2 (black) = hydrated phase (C2/c)) and b) Le Bail profile fit for the partially superhydrated phase.

The methanol sorption experiment shows that the framework expands in response to methanol vapour (Figure 4.30). The methanol vapour was added to the sample chamber

on scan 4 (point A) causing a one-step expansion of the framework to the fully-open phase. On scan 56 (point B) the methanol vapour was exchanged for pure nitrogen, after which the fully-open phase shows a gradual contraction before closing to a phase with a similar XRD pattern to the half-open methanol phase identified for the $-(OH)_2$ modified framework. The Le Bail profile fit for the fully-open methanol phase is shown in Figure 4.30b; the data collected *in situ* was used for this refinement. This analysis shows that the framework expands to the fully-open *Imcm* structure upon addition of methanol vapour. The refined unit cell volume was determined to be 1440 $Å^3$. A Le Bail profile fit of the half-open phase was not possible as it does not exist as a pure phase and the *in situ* data has a very low signal-to-noise ratio.

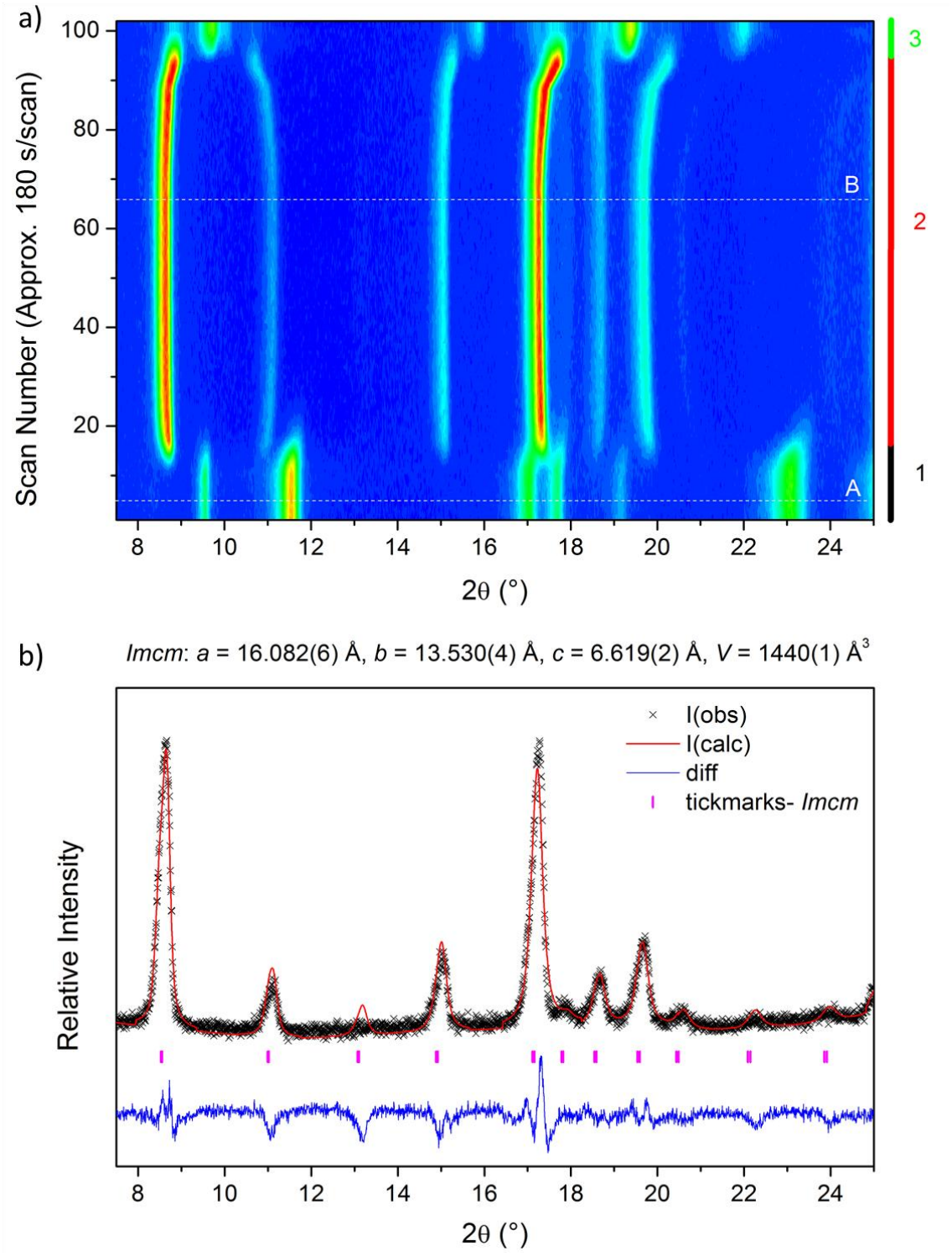

Figure 4.30: Behaviour of the –COOH modified framework in response to methanol vapour. a) Contour plot showing the change in framework symmetry (Phase 1 (black) = hydrated phase (C2/c),Phase 2 (red) = fully-open methanol phase (Imcm) and Phase 3 (green) = mixed phase (fully-open and half-open)) and b) Le Bail profile fit for the fully-open methanol phase.

4.3.1.6 Breathing of the Chloro Modified MIL-53(Al)

The hydrated, monoclinic phase of the –Cl modified MIL-53(Al) framework has a unit cell volume of 993 $Å^3$ (Table 4.3). The thermal dehydration experiment (Figure 4.31) shows that the framework expands to the fully-open phase when heated above 190 °C. Subsequent cooling back to 30 °C shows that the framework remains open below 110 °C (Figure A.8). Figure 4.31b shows the Le Bail profile fit for the dehydrated phase; a longer data collection was used while the sample was held at 210 °C. This analysis confirms that the dehydrated material has the orthorhombic, *Imcm*, structure with a unit cell volume of 1431.3 $Å^3$.

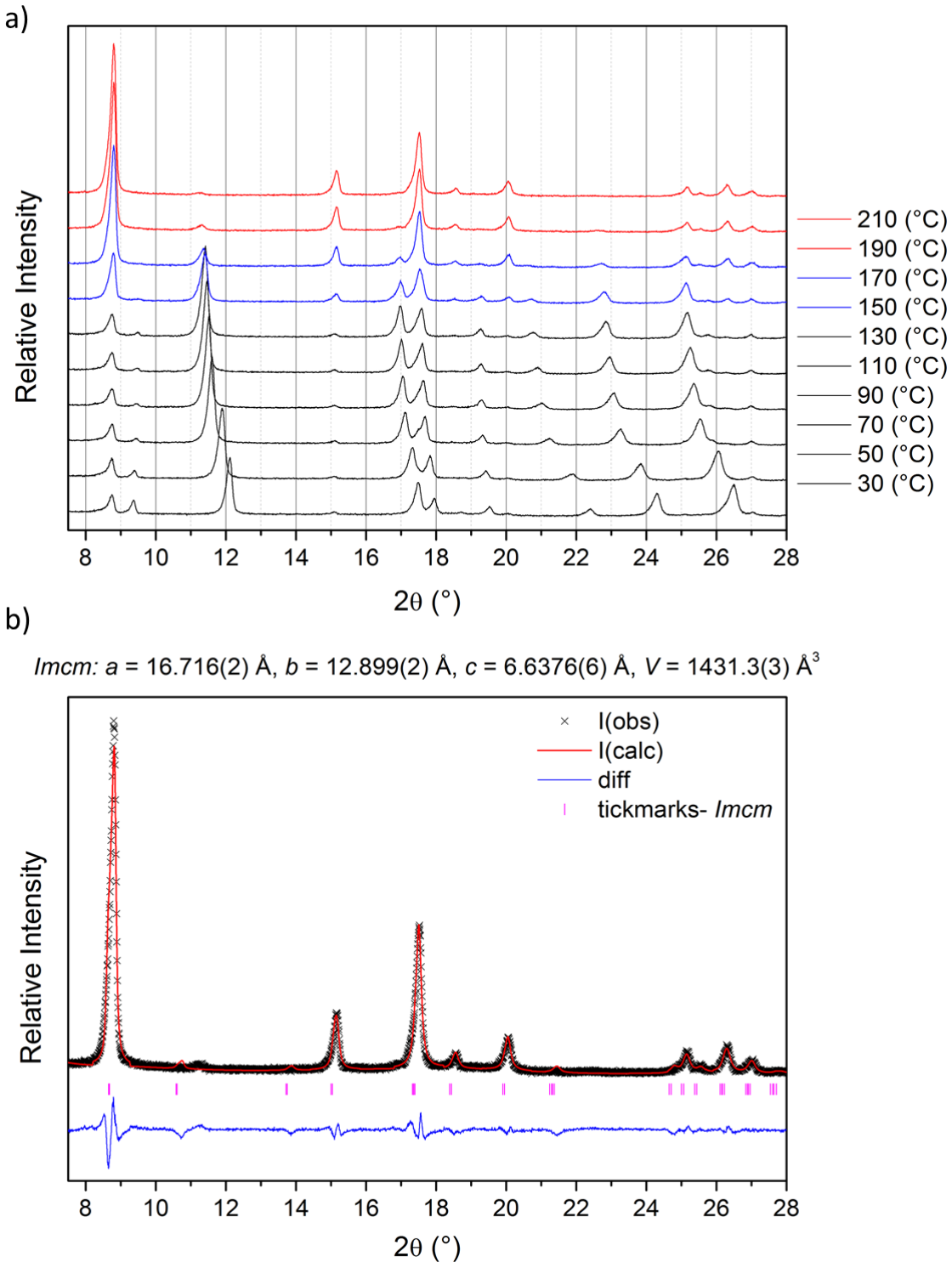

Figure 4.31: Thermal dehydration of –Cl modified MIL-53(Al). a) Individual XRD patterns showing a change in symmetry with increasing temperature (Black = hydrated phase (C2/c), blue = mixed phase and red = dehydrated phase(Imcm)) and b) Le Bail profile fit for data recorded at 210 °C.

The superhydration experiment shows that the –Cl modified framework only partially expands in the presence of excess water; the majority of the framework remains closed. A mixed phase Le Bail profile fit was performed, using the data collected *in situ*, and the result is shown in Figure 4.32. The refinement confirms that the majority of the sample remains unchanged with the *C2/c* structure and only a small amount of the sample expands to the *Imcm* structure.

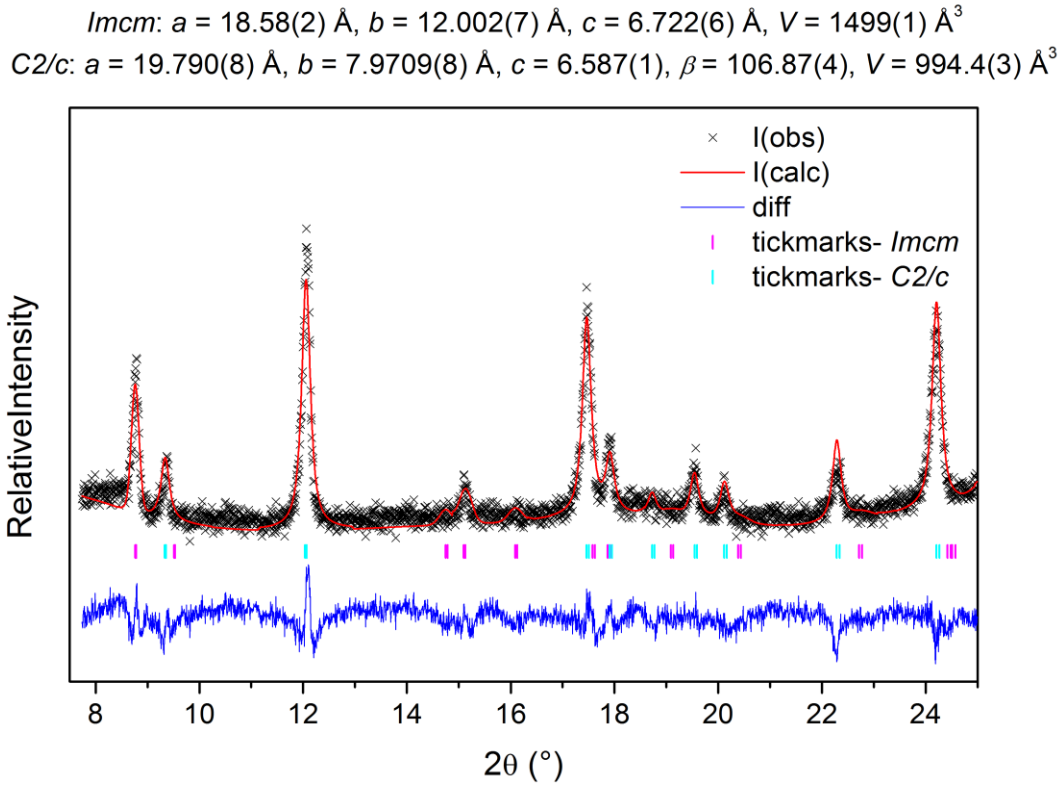

Figure 4.32: Le Bail profile fit for the superhydrated –Cl modified MIL-53(Al). The Imcm space group was used to model the fully-open structure and the space group C2/c was used to model the closed structure.

The contour plot in Figure 4.33 shows the behaviour of the framework in response to methanol vapour which was added on scan 4 (point A). The hydrated phase shows some gradual expansion before expanding completely to the fully-open phase. The methanol vapour was replaced by a pure flow of nitrogen gas on scan 85 (point B), it can be seen that the flow of nitrogen was not sufficient to remove the methanol from the pores even

after more than four hours. A Le Bail profile fit was performed on an individual pattern from the *in situ* data (Figure 4.33b). Although this pattern has a low signal-to-noise ratio it was possible to obtain unit cell parameters which confirm that the sample has the fully-open *Imcm* structure upon addition of methanol vapour. This refinement gave a unit cell volume of 1411 $Å^3$, which, in contrast to the other modified materials (Table 4.3, Section 4.3.1.8), is smaller than its corresponding dehydrated phase (1431 $Å^3$). No strong interactions are expected between the additional –Cl groups and the MeOH guest molecules that would result in a contraction of the framework. Higher resolution studies are needed to confirm this result as the data used for this refinement are of insufficient quality to give a high degree of confidence in the refined parameters.

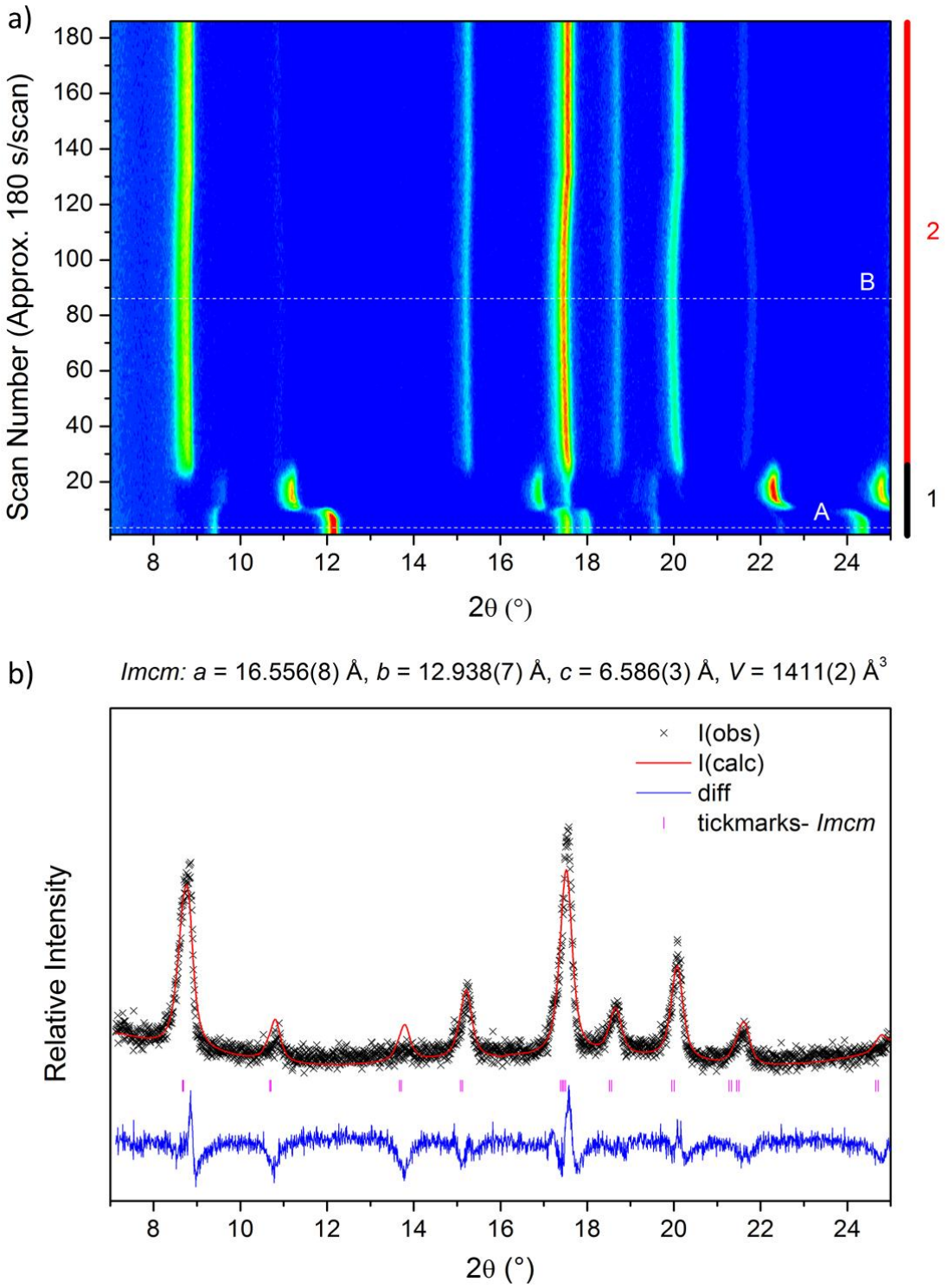

Figure 4.33: Behaviour of the –Cl modified MIL-53(Al) towards methanol vapour. a) Contour plot showing the change in symmetry of the framework as methanol is taken up (Phase 1 (black) = hydrated phase (C2/c) and Phase 2 (red) = fully-open phase (Imcm)) and b) Le Bail profile fit for the fully-open phase.

4.3.1.7 Breathing of Amino Modified MIL-53(Al)

The hydrated phase of $-NH_2$ modified MIL-53(Al) has a unit cell volume of 961 $Å^3$. The thermal dehydration of this material, shown in Figure 4.34, does not cause any significant changes in the framework unit cell parameters; there is no evidence that the structure breathes. This is in agreement with previously published XRD results.[23] Density functional theory (DFT) simulations were performed by Stavitski *et al.*,[24] which calculated that the closed form of MIL-53(Al)-NH_2 is more stable than the fully-open form when there are no occluded molecules in the framework pores. They showed that hydrogen bonding interactions can occur between the NH_2 group and the μ^2-OH groups of the AlO_6 octahedra. The superhydration of the framework was also studied using the method outlined above but the experiment resulted in the conclusion that this framework was unable to breathe in response to these conditions. However, experimental and theoretical work predicts that this framework is able to breathe under certain conditions such as in response to CO_2 gas.[25]

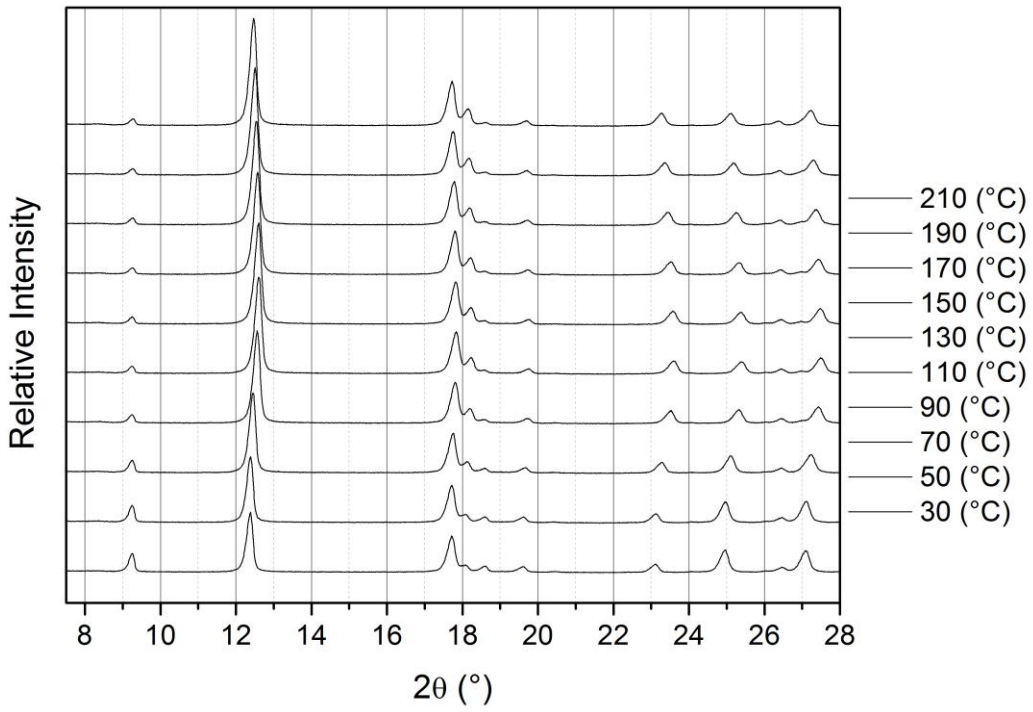

Figure 4.34: Thermal dehydration of the –NH_2 modified MIL-53(Al)

4.3.1.8 Comparisons of Modified MIL-53(Al) Materials

The results of the *in situ* XRD breathing experiments for each of the functionalised frameworks detailed above have been summarised in Table 4.2. The Le Bail profile fits for the individual phases observed during these experiments are shown in Table 4.3. These data are compared with the literature data for the hydrated phase and the dehydrated phase of unmodified MIL-53(Al).

The amino framework has been excluded from the following discussion of the results as it was not shown to exhibit any breathing behaviour under the conditions studied.

The dehydration experiments using thermal treatment showed that all of the modified frameworks, except the –$(OH)_2$ modified framework, fully-opened upon dehydration.

The $–NO_2$ modified framework was dehydrated most easily, showing complete conversion at 170 °C. The -COOH modified framework was shown to be the most difficult to dehydrate, where complete conversion to the fully-open phase was not seen until 310 °C. In contrast to the other frameworks, the $–(OH)_2$ modified framework contracts during thermal treatment, this contraction is complete by 110 °C. All of the frameworks showed some hysteresis upon cooling to room temperature; the frameworks remained in their respective dehydrated phases to temperatures lower than those required to dehydrate them.

The superhydration experiments showed that only three of the modified frameworks, $–NO_2$, –Br and $–(OH)_2$, could be fully superhydrated using this method. The $–CH_3$ and –COOH modified frameworks showed that the majority of the sample was superhydrated, whereas only a small amount of the –Cl modified sample was superhydrated using this method. There was a weak interaction between most of the frameworks and the excess water molecules, which could be removed either at 30 °C with no gas flow or at 30 °C with a flow of N_2 gas. However, the $–NO_2$ modified framework required heat to remove the excess water from the pores indicating a stronger interaction.

The methanol vapour experiments show that all of the modified frameworks could be opened fully in the presence of methanol vapour. The refined unit cells show that the fully-open methanol phases are, in general, larger than the fully-open dehydrated phases. The exception to this rule is the –Cl modified framework, however the refinement for this methanol phase was performed with data with a low signal-to-noise ratio, and thus may not be accurate. *In situ* data for the adsorption and desorption of methanol vapour was recorded for all samples except the –Br modified framework. The

desorption was only investigated using N_2 gas, where pure N_2 gas is passed over the sample to remove the methanol from the pores. The $–NO_2$ and $–CH_3$ modified frameworks show a slight contraction upon the introduction of the N_2 gas which is consistent with a contraction to the slightly smaller pore volume of the fully-open dehydrated phase. The –Cl modified framework shows very little change. It is hard to deduce if this is due to the framework having a strong interaction with the methanol guest or if the unit cell parameters of the two fully-open phases are too similar to see a contraction upon dehydration. The $–(OH)_2$ and –COOH modified frameworks both exhibit a change in framework symmetry upon the introduction of N_2 gas; they both contract to a pore volume similar to the half-open phase seen for MIL-53(Fe). MIL-53(Fe) was shown to contain two equivalents of methanol when the framework was fully-open and one equivalent of methanol when the framework was half-open. The half-open phase seen for these two frameworks could be the result of the methanol guest being lost in two stages. This would suggest that the removal of both equivalents of methanol from these frameworks was not possible using just a flow of N_2 gas.

The heptane adsorption experiments were performed to investigate if the polarity of the additional functional groups in the modified materials had an impact on the adsorption of a non-polar guest molecule. The $–NO_2$ and $–CH_3$ modified frameworks were used in this study and they both expanded to the fully-open phase upon adsorption of heptane vapour. No differences were seen in the behaviour of the two materials, they both expanded via a one-step process. It was not possible to determine if the heptane was removed from the framework using a flow of N_2 gas due to the similar pore volumes of the fully-open heptane and dehydrated phases. These results highlight that these two frameworks do not show selectivity towards the guest molecules investigate in this study. However, little information can be gained regarding the retention of the different

molecules within the materials. Complementary techniques would be required to take this investigation further.

This work highlights that the modification of the linker did change the breathing behaviour of the framework upon dehydration. However, selectivity towards specific guest molecules was not seen during these studies. Further studies are required to investigate the properties of these frameworks. The adsorption studies showed few differences between the properties of the frameworks but these experiments are not able to determine the strength of the interaction between guest and host, further studies such as break-through experiments and calorimetry measurements are needed to investigate this further The added functional groups change the size and shape of the pore apertures, therefore these frameworks could have potential for molecular separation studies.

Table 4.2: Summary of the in situ XRD results detailed in Section 4.3.1

	Adsorbates							
	Dehydration		H_2O (Superhydration)		MeOH			Heptane
Modification	Fully-open 	Complete dehydration (°C)	Fully-open 	Removal Conditions (°C/ gas flow)	Fully-open 	Half-open 	Removal Conditions (°C/ gas flow)	Fully-open 
-NO_2	✓	170	✓	60	✓	✗	30 /N_2	✓
-Br	✓	210	✓	30	✓	✗	30 /N_2	-
- CH_3	✓	190	✓✗	-	✓	✗	30 /N_2	✓
-$(OH)_2$	✗	110	✓	30 /N_2	✓	✓	30 /N_2	-
-COOH	✓	310	✓✗	-	✓	✓	30 /N_2	-
-Cl	✓	190	✓✗	-	✓	✗	30 /N_2	-
-NH_2	✗	N/A	✗	N/A	-	-	-	-

✓ Present as a single phase, ✓✗ Present as a mixture of phases, ✗ Phase indicated was not seen for this sample

Table 4.3: Unit cell parameters of various modified MIL-53(Al) frameworks compared with the unmodified framework. Experimental data was obtained using a Le Bail profile fit. Indication of the space group is given where a Le Bail fit was not performed. Fully-open, orthorhombic phases are shown in red; hydrated, monoclinic phases are shown in black; closed, monoclinic phases are shown in green and mixed phases are shown in blue.

Functional Group	Hydrated	Dehydrated	Superhydrated	Methanol
-H	a = 19.513(2) Å b = 7.612(1) Å c = 6.576(1) Å **_Cc[18]_** β = 104.24(1) ° V = 946.8 Å^3	a = 6.6085(9) Å b = 16.675(3) Å c = 12.813(2) Å **_Imma[18]_** V = 1412.0 Å^3	- -	- -
-NO_2	a = 19.687(10) Å b = 8.257(5) Å c = 6.635(3) Å **_Cc[23]_** β = 106.87(4) ° V = 1032.1(12) Å^3	a = 16.522(2) Å b = 12.974(2) Å c = 6.6285(8) Å **_Imcm (170 °C)_** V = 1420.9(4) Å^3	a = 16.240(2) Å b = 13.886(2) Å c = 6.7026(9) Å V = 1511.5(4) Å^3 **_Imcm (major phase)/ C2/c_** a = 20.334(4) Å b = 8.344(1) Å c = 6.700(2) Å β = 107.87(1) ° V = 1082.0(4) Å^3	a = 15.964(3) Å b = 13.812(2) Å c = 6.6561(9) Å **_Imcm_** V = 1467.6(3) Å^3

-Br	*a* = 19.567(14) Å *b* = 8.532(12) Å *c* = 6.616(5) Å *β* = 107.22(6) ° *V* = 1055.1(23) Å^3	***Cc*^{23}**	*a* = 16.435(2) Å *b* = 13.057(1) Å *c* = 6.6198(5)Å *V* = 1420.6(1) Å^3	***Imcm (210 °C)***	*a* = 16.082(6) Å *b* = 13.530(4) Å *c* = 6.619(2) Å *V* = 1471.0 (10) Å^3	***Imcm***	*a* = 16.0824(7) Å *b* = 13.7878(8)Å *c* = 6.6593(4) Å *V* = 1476.7(1) Å^3	***Imcm***
-CH_3	*a* = 19.700(17) Å *b* = 7.999(7) Å *c* = 6.603(5) Å *β* = 106.40(5) ° *V* = 998.1(19) Å^3	***Cc*^{23}**	*a* = 16.567(2) Å *b* = 12.928(1) Å *c* = 6.6143(5) Å *V* = 1416.6(2) Å^3	***Imcm (190 °C)***	*a* = 16.701(4) Å *b* = 12.979(3) Å *c* = 6.636(1) Å *V* = 1438.4(4) Å^3 *a* = 19.857(8) Å *b* = 8.0953(8) Å *c* = 6.643(2) Å *β* = 107.19(4) ° *V* = 1020.1(4) Å^3	***Imcm*** *(major phase)/* ***C2/c***	*a* = 16.503(1) Å *b* = 13.2173(8) Å *c* = 6.6488(5) Å *V* = 1450.2(1) Å^3	***Imcm***
-$(OH)_2$	*a* = 19.762(4) Å *b* = 7.6320(16) Å *c* = 6.5786(14) Å *β* = 105.768(13) ° *V* = 954.9(5) Å^3	***Cc*^{23}**	*a* = 20.654(3) Å *b* = 6.8765(9) Å *c* = 6.9034(8) Å *β* = 112.85(1) ° *V* = 903.6(2) Å^3	***C2/c***	*a* = 16.905(5) Å *b* = 12.487(2) Å *c* = 6.621(2) Å *V* = 1397.6(5) Å^3	***Imcm***	*a* = 16.855(2) Å *b* = 12.838(1) Å *c* = 6.6753(6) Å *V* = 1444.5(2) Å^3	***Imcm***

-COOH	*a* = 19.6055(17) Å *b* = 8.4476(22) Å *c* = 6.6520(6) Å *β* = 106.8(6) ° *V* = 1054.7(4) Å^3	***Cc*^{26}**	*a* = 16.052(3) Å *b* = 13.543(2) Å *c* = 6.598(1) Å *V* = 1434.2(2) Å^3	***Imcm* *(310 °C)***	*a* = 16.006(6) Å *b* = 13.734(4) Å *c* = 6.641(1) Å *V* = 1460.0(6) Å^3 *a* = 19.93(2) Å *b* = 8.503(2) Å *c* = 6.652(7) Å *β* = 109.9(2) ° *V* = 1059.6(9) Å^3	***Imcm* *(major phase)/* *C2/c***	*a* = 16.082(6)Å *b* = 13.530(4) Å *c* = 6.619(2) Å *V* = 1440(1) Å^3	***Imcm***
-Cl	*a* = 19.776(4) Å *b* = 7.9371(16) Å *c* = 6.6010(17) Å *β* = 106.589(13) ° *V* = 993.0(5) Å^3	***Cc*^{23}**	*a* = 16.716(2) Å *b* = 12.899(2) Å *c* = 6.6376(6) Å *V* = 1431.3(3) Å^3	***Imcm* *(190 °C)***	*a* = 18.58(2) Å *b* = 12.002(7) Å *c* = 6.722(6) Å *V* = 1499(1) Å^3 *a* = 19.790(8) Å *b* = 7.9709(8) Å *c* = 6.587(1) Å *β* = 106.87(4) ° *V* = 994.4(3) Å^3	***C2/c* *(major phase)/* *Imcm***	*a* = 16.556(8)Å *b* = 12.938(7) Å *c* = 6.586(3) Å *V* = 1411(2) Å^3	***Imcm***

-NH_2	a = 19.722(7) Å^3 b = 7.692(3) Å^3 c = 6.578(4) Å^3 β = 105.1(3) ° V = 961.5(10) Å^3	***C2/c*[23]**	-	***C2/c***	-	***C2/c***	-	-

Table 4.4: Extension of the table above, includes the unit cell parameters for the adsorption of heptane

Functional Group	Heptane	
-NO_2	a = 15.830(2) Å b = 13.866(2) Å c = 6.6366(6) Å V = 1456.7(4) Å^3	***Imcm***
-CH_3	a = 16.658(1) Å b = 12.796(2) Å c = 6.6469(5) Å V = 1416.8(2) Å^3	***Imcm***

4.3.2 Breathing of the Metal-Organic Framework CAU-13

CAU-13 was synthesised by N. Stock's research group in Kiel, Germany. This MOF is isostructural to MIL-53(Al); the 1,4-benzenedicarboxylic acid (bdc) linker of MIL-53 was substituted for 1,4-cyclohexanedicarboxylic acid (cdc). The cdc linker used in the synthesis of this MOF is less rigid than the bdc linker; conformational isomers of the cyclohexane ring exist which gives rise to some inherent flexibility within the framework. High-resolution powder XRD data were recorded and analysed by F. Niekiel from the University of Kiel, Germany. The data were refined using the TOPAS software,[27] which allowed for the structural information to be obtained. Hydrated CAU-13 is triclinic, $P\bar{1}$, and has a unit cell volume of 526.84 $Å^3$. The dehydrated form of CAU-13 retains the same symmetry but the unit cell volume increases slightly to 534.7 $Å^3$. The data for the dehydrated sample were recorded at room temperature after the sample had been heated to 200 °C under vacuum before being sealed in a capillary. Figure 4.35 shows the partially refined crystal structures for both the hydrated and dehydrated phases of CAU-13 and their corresponding cyclohexanedicarboxylate linkers in the two conformations that exist within each phase.

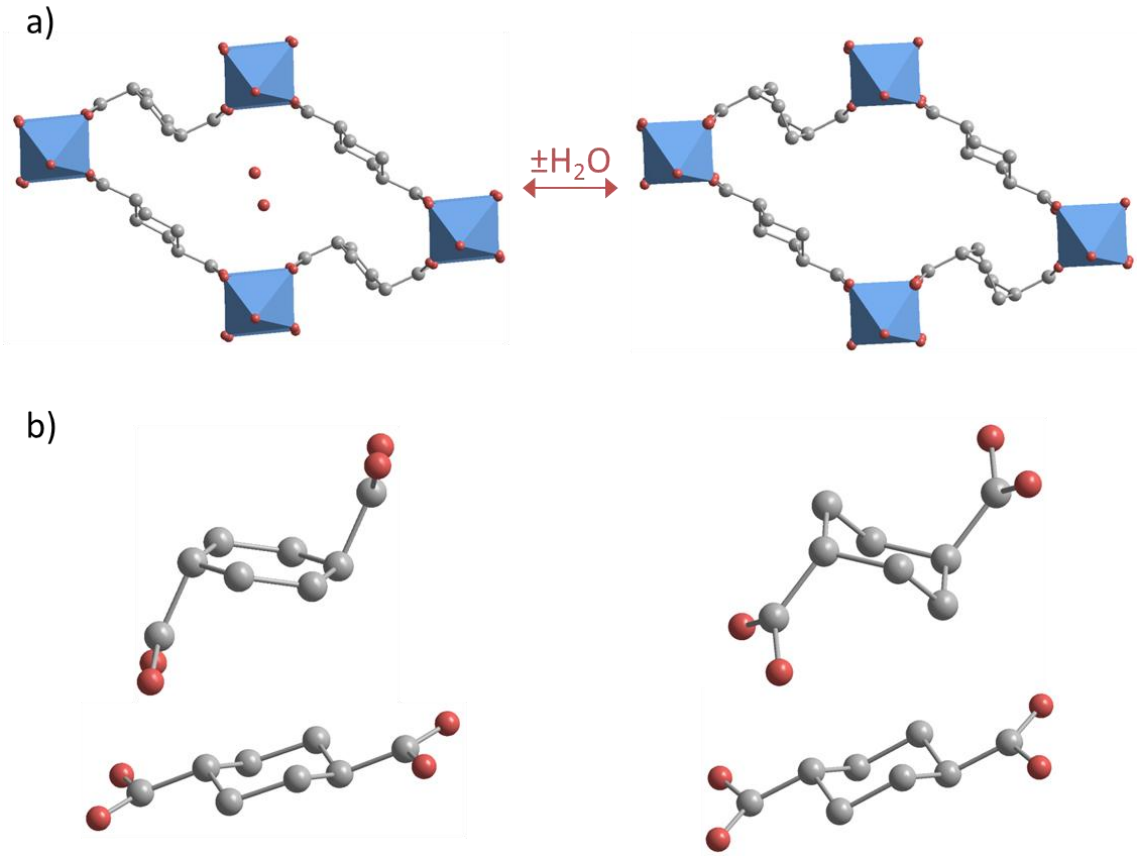

Figure 4.35: Behaviour of CAU-13 upon dehydration. a) Slight change in pore volume upon dehydration (viewed along the a-axis) and b) the different conformations of the cdc linker in both phases.

To compare the breathing properties of this MOF with the other modified MIL-53(Al) frameworks the same experiments were performed; thermal dehydration, superhydration and sorption of methanol vapour. In addition, studies of xylene adsorption were investigated.

The results for the *in situ* thermal dehydration experiment are shown in Figure 4.36, they show that the framework does not expand or contract in the same way as MIL-53(Al) when the material is heated above 200 °C. Some Bragg peaks show a slight shift to a higher 2θ value, indicating an expansion in *d*-spacing, there is also the loss of a peak at ~10.5 °. These small shifts are consistent with minor changes in the spatial arrangement of the cdc linker seen for the high-resolution XRD experiments. There is

no evidence for the framework expanding in volume to approximately 1500 Å^3 as is seen for unmodified MIL-53(Al).[18]

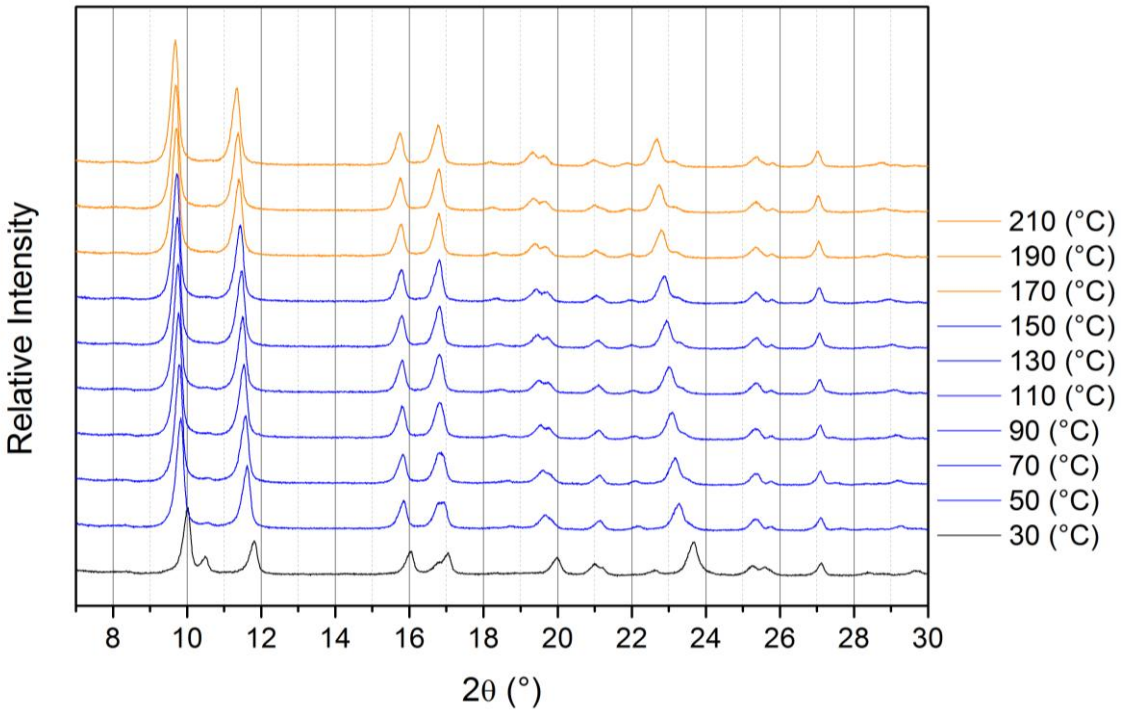

Figure 4.36: Thermal dehydration of 1,4-cyclohexanedicarboxylic acid MIL-53(Al). The black pattern shows the hydrated phase, the blue patterns show a mixture of phases and the orange patterns indicate that the material has been fully dehydrated.

The individual XRD patterns recorded at 30, 50 and 210 °C are compared with the simulated XRD patterns, obtained from the high-resolution XRD studies, in Figure 4.37. The experimental data for hydrated CAU-13 agrees well with the simulated pattern. The simulated pattern for dehydrated CAU-13 agrees well with the experimental data for the pattern recorded at 50 °C. However, it can be seen that the data recorded at 210 °C shows a greater degree of expansion; the (010) and (00-1) peaks have shifted to lower 2θ values.

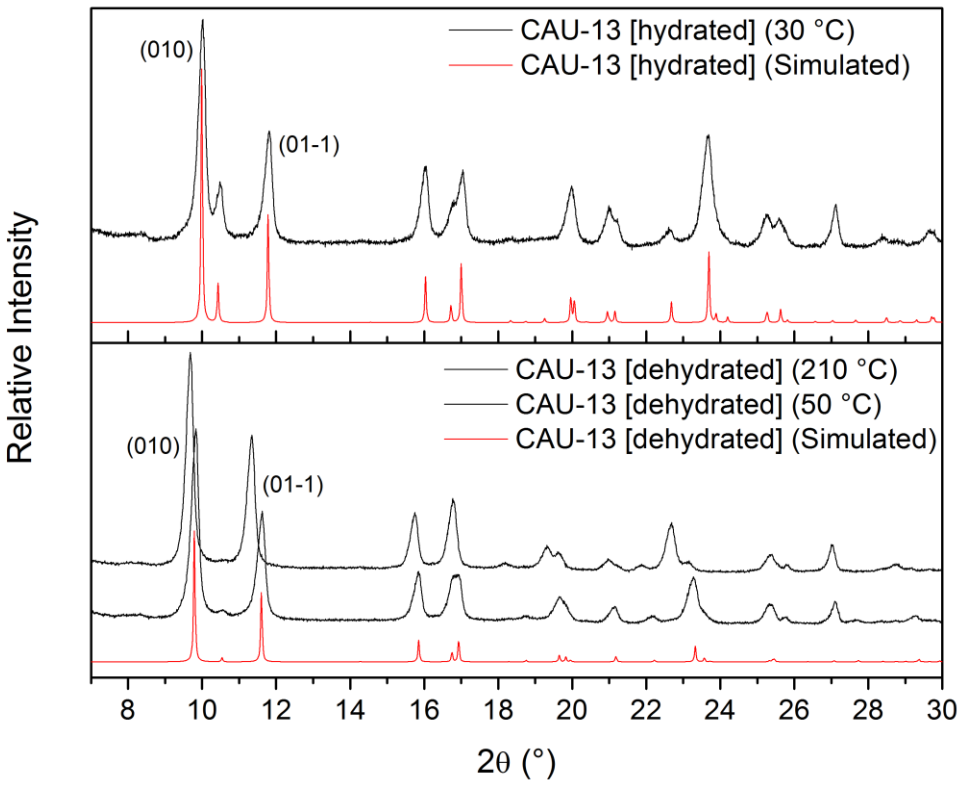

Figure 4.37: Individual XRD patterns recorded during the thermal dehydration experiment compared with the simulated patterns for hydrated and dehydrated CAU-13.

The experiments for superhydration and the sorption of methanol were attempted but they also did not result in a large expansion of the framework. There was no change seen in the unit cell parameters, suggesting that no extra water or exchange of water for methanol occurred during these experiments. The first and last individual XRD patterns for each experiment are shown in Figure 4.38.

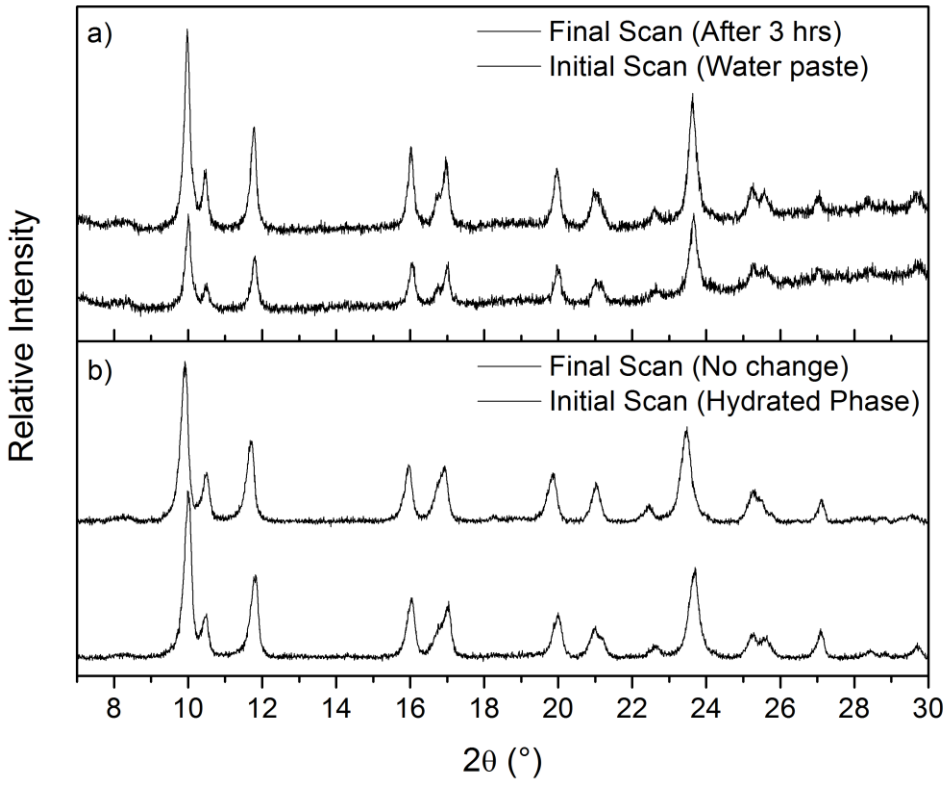

Figure 4.38: Behaviour of CAU-13) in response to a) superhydration and b) methanol vapour

The different behaviour observed between CAU-13 and the other modified MIL-53(Al) frameworks can be explained by the different chemistry of the C6 rings in the linkers. The cyclohexyl ring is more hydrophobic than phenyl; the delocalised electrons in the phenyl ring are able to interact with polar molecules.[28] The interaction between the cdc modified framework and the polar guest molecules, water and methanol, is not strong enough to result in the adsorption of these molecules. Therefore sorption experiments were tried using the non-polar xylene (dimethylbenzene) isomers. The sorption of vapour phase xylene was studied using the method that was used to study methanol vapour phase adsorption; a nitrogen gas flow was bubbled through liquid xylene creating the vapour phase guest that was passed over the sample. The contour plot, Figure 4.39, shows the behaviour of the cdc modified framework towards the introduction of *m*-xylene. The gas flow was turned on at point (A). The contour plot

clearly shows that there is a change in the unit cell parameters of the framework as some Bragg reflections shift to a lower 2θ value, indicating a larger *d*-spacing. This suggests that there was an expansion of the framework in response to the guest. Due to the expected unit cell parameters of this phase being unknown it is not possible to perform a Le Bail profile fit. The individual XRD patterns of the initial hydrated phase and the final phase containing the xylene guest are also shown in Figure 4.39.

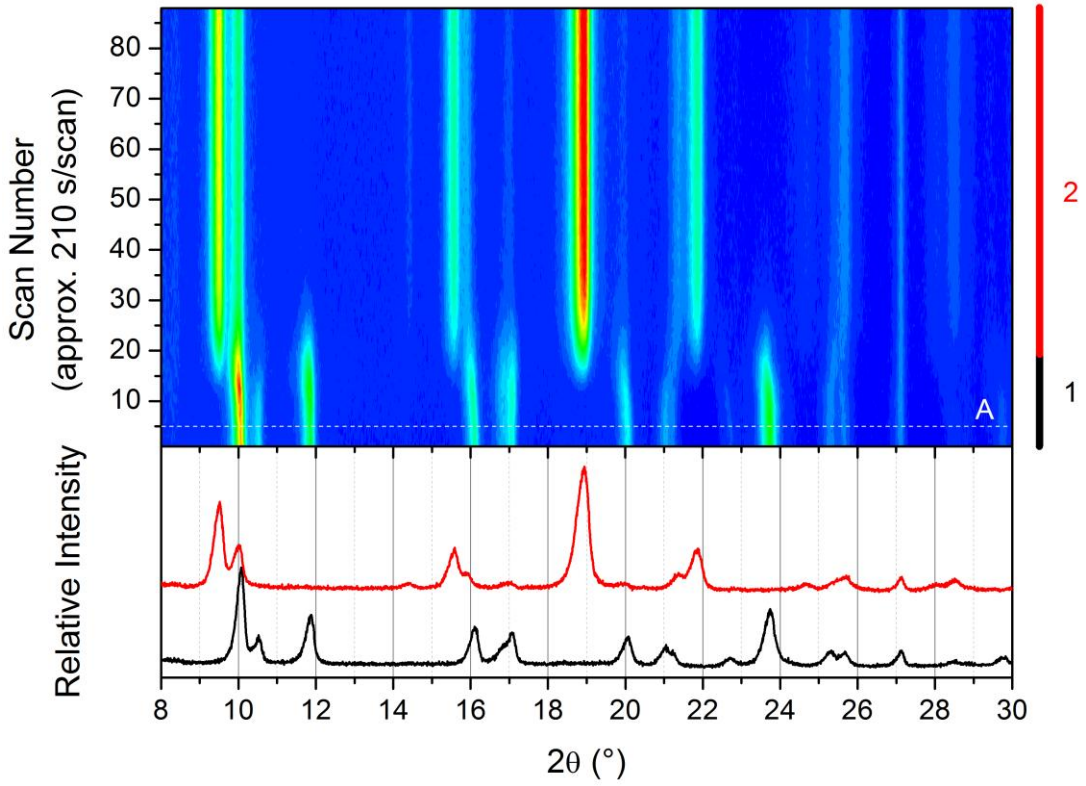

Figure 4.39: Sorption of m-xylene by CAU-13. Contour plot shows the introduction of m-xylene (top) and the individual XRD patterns show the two phases identified in the contour plot (bottom). Black = CAU-13 [hydrated], red = CAU-13 [m-xylene].

The removal of the guest from CAU-13 was also studied. The guest could not be removed at 30 °C even with a flow of dry nitrogen passing over the sample. Heat was required to remove *m*-xylene from the pores of the framework. For all of the contour plots showing guest removal in this section the individual scans were recorded in 1 °C intervals in the range 60 –150 °C. Figure 4.40 shows the contour plot for the removal of

m-xylene. It can be deduced from this plot that *m*-xylene starts to be lost from the framework at ~105 °C and that the removal is complete at ~115 °C. Figure 4.40b shows the individual XRD patterns for the two phases seen during the experiment. The first phase is the expanded phase containing *m*-xylene and the second phase is the dehydrated phase present after the removal of the guest at high temperatures. The framework returns to the hydrated phase when cooled back to 30 °C.

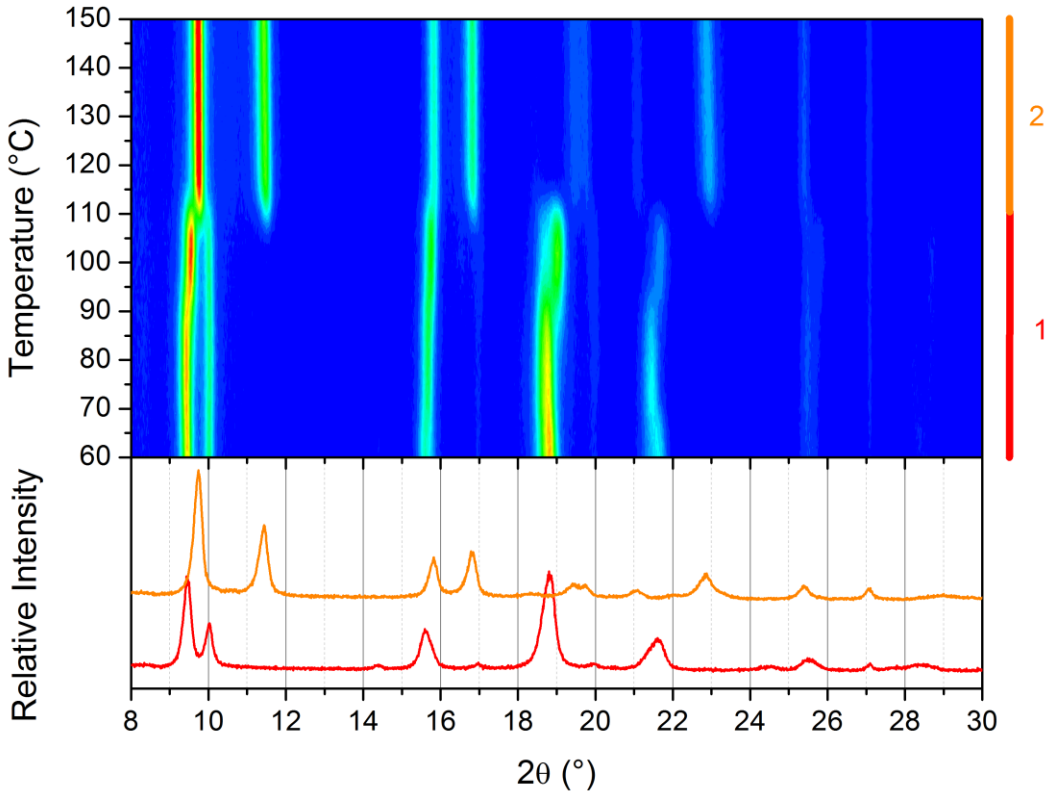

Figure 4.40: Removal of m-xylene from CAU-13 using thermal treatment. The contour plot shows the removal of m-xylene as a function of temperature (top) and the individual XRD patterns show the two phases identified in the contour plot (bottom). Red = CAU-13 [m-xylene] and Orange = CAU-13 [dehydrated].

The same sorption experiments were performed with *o*-xylene and the results show a similar behaviour to that seen for *m*-xylene (Figure 4.41). Due to the difficulties in regulating the flow of nitrogen gas between experiments a comparison between the rates of expansion of the frameworks upon introduction of the xylenes is not possible.

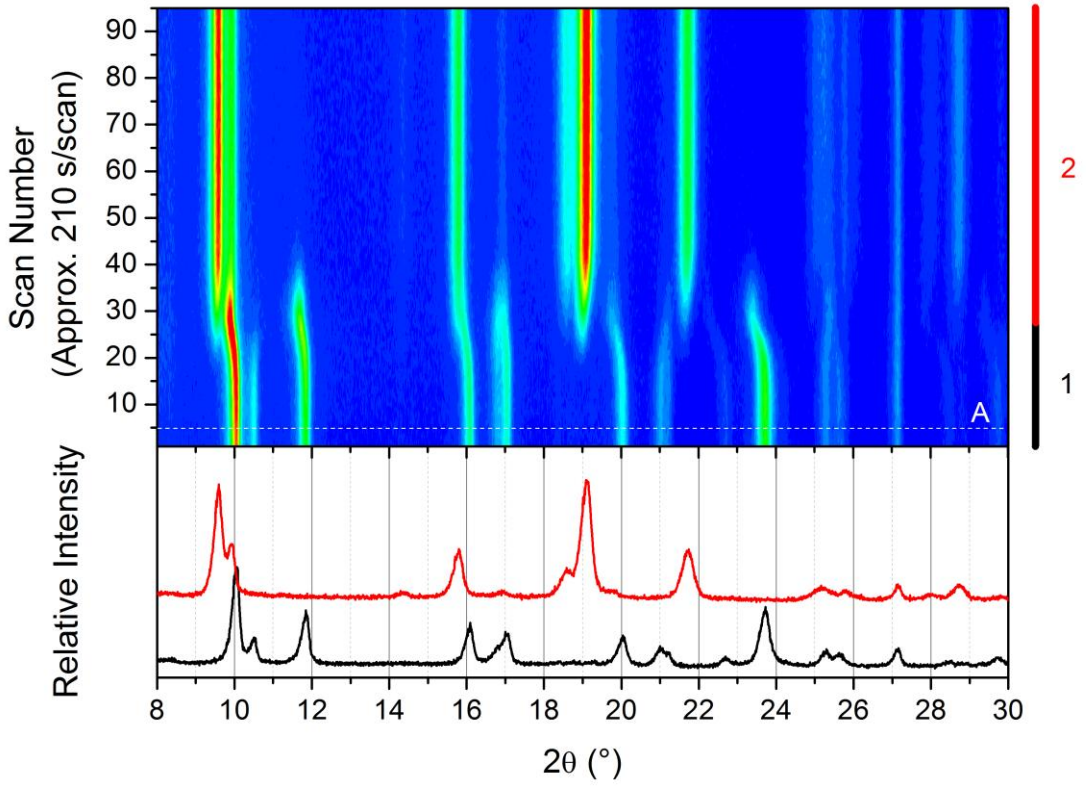

Figure 4.41: Sorption of o-xylene by CAU-13. The contour plot shows the introduction of o-xylene (top) and the individual XRD patterns show the two phases identified in the contour plot (bottom). Black = CAU-13 [hydrated], red = CAU-13 [o-xylene].

The removal of the guest was performed under controlled conditions, and therefore the temperature at which the guest is removed can give an indication of the strength of the interaction between the guest and the framework. Figure 4.42a shows that the framework starts to lose the *o*-xylene at ~115 °C and complete conversion to the dehydrated phase is achieved above 125 °C. This is approximately 10 °C higher than was observed for *m*-xylene showing that the framework has a stronger interaction with the ortho isomer.

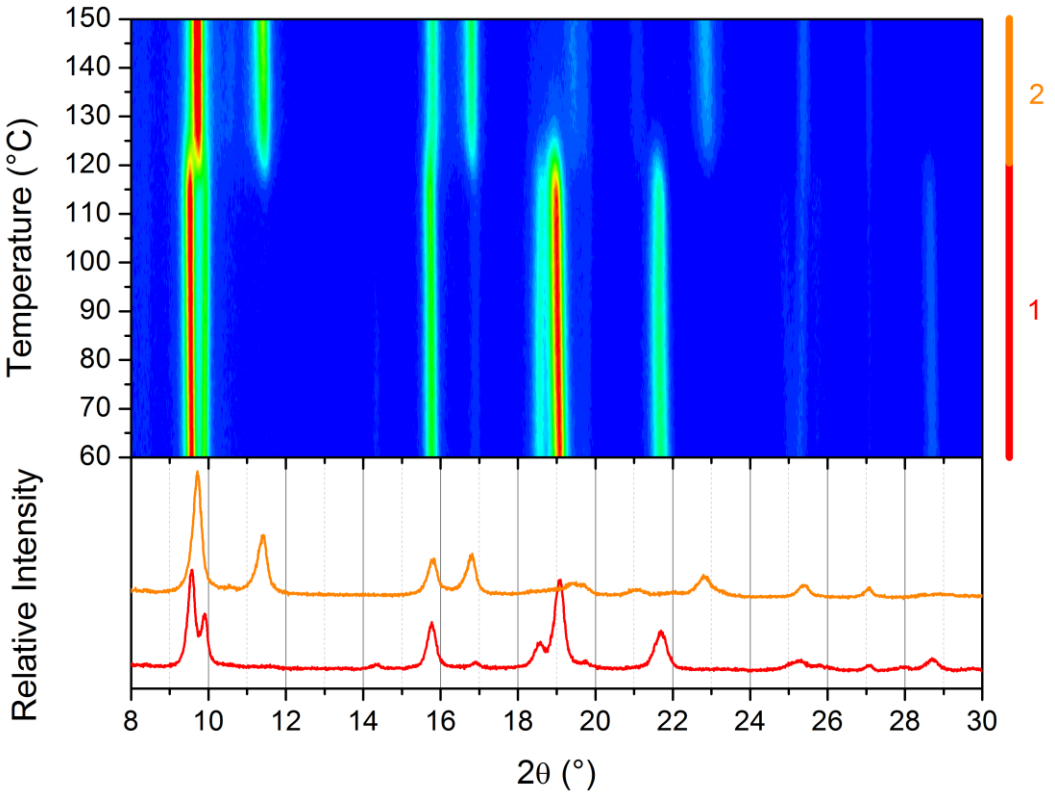

Figure 4.42: Removal of o-xylene from CAU-13 using thermal treatment. The contour plot shows the removal of o-xylene as a function of temperature (top) and the individual XRD patterns show the two phases identified in the contour plot (bottom). Red = CAU-13 [o-xylene] and orange = CAU-13 [o-xylene].

Sorption experiments for *p*-xylene were also performed. Figure 4.43 shows that *p*-xylene is taken up by the CAU-13 just as easily as the other two isomers and it can be seen that the same change in unit cell parameters is also observed.

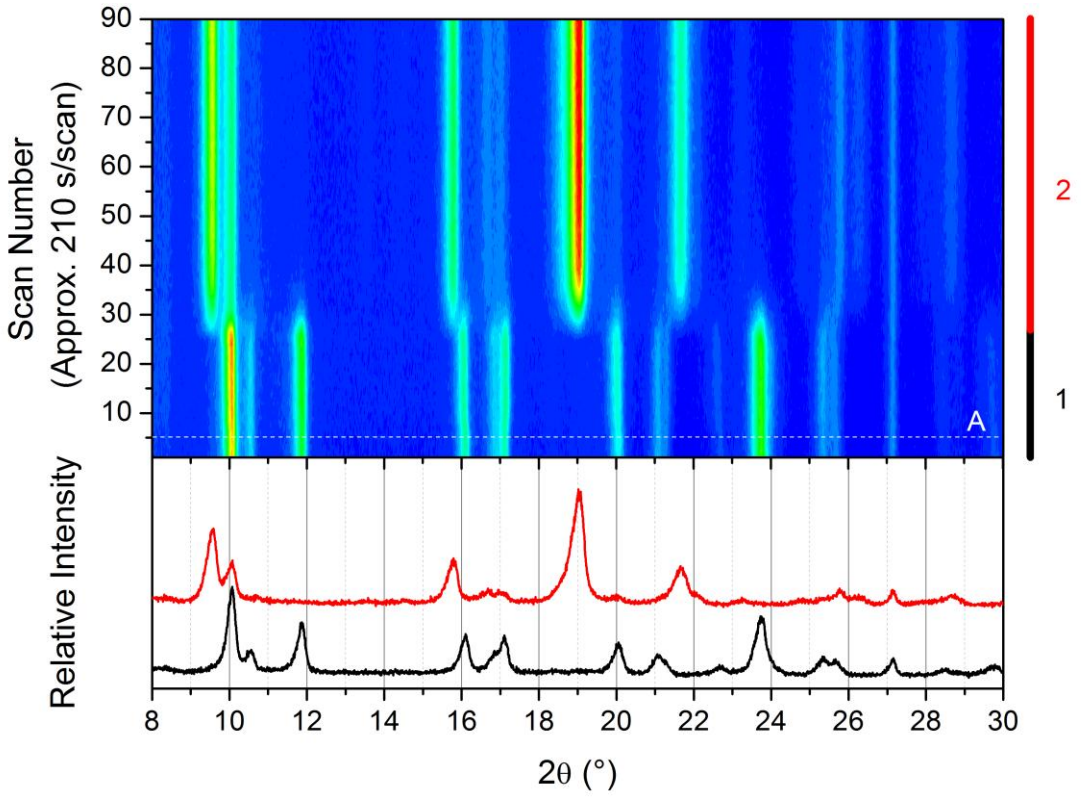

Figure 4.43: Sorption of p-xylene by CAU-13. The contour plot shows the introduction of p-xylene (top) and the individual XRD patterns show the two phases identified in the contour plot. Black = CAU-13 [hydrated], red = CAU-13 [p-xylene].

The contour plot displaying the removal of *p*-xylene shows that conversion to the dehydrated phase occurs at the higher, and narrower, temperature range of 130 – 135 °C. This indicates that CAU-13 shows a greater affinity towards the para isomer compared to either the ortho or meta isomers.

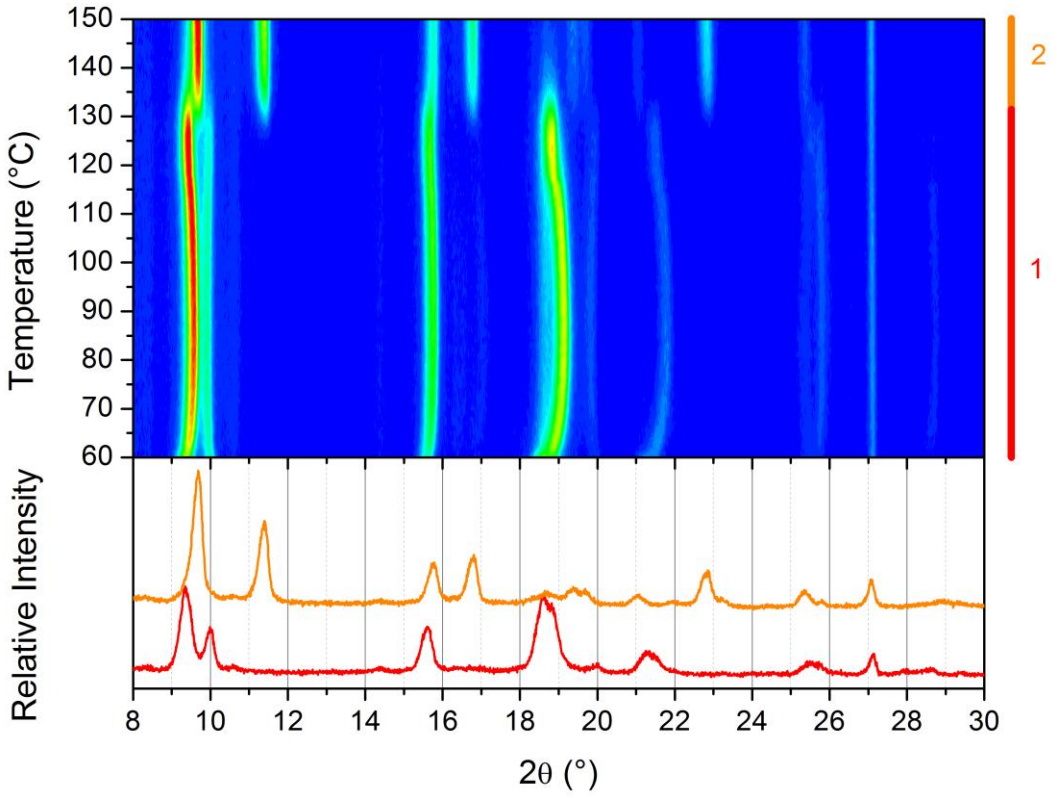

Figure 4.44: Removal of p-xylene from CAU-13 using thermal treatment. The contour plot shows the removal of p-xylene as a function of temperature (top) and the individual XRD patterns show the two phases identified in the contour plot (bottom). Red = CAU-13 [p-xylene] and orange = CAU-13 [dehydrated].

These experiments show that there is a difference in the behaviour of CAU-13 and its response to the three xylene isomers. The boiling points of the pure isomers are 138 °C (*p*-xylene), 139 °C (*m*-xylene) and 144 °C (*o*-xylene). The isomers were expelled from the framework at 130 °C (*p*-xylene), 105 °C (*m*-xylene) and 115 °C (*o*-xylene). These results clearly show that the framework interacts differently with each isomer. If the interactions between the framework and the different isomers were of a similar strength then the temperature at which each isomer is expelled would be expected to follow the order of increasing boiling point. It is clear from these experiments that the CAU-13 has a higher affinity for the para isomer with the order of preference being *p*-xylene > *o*-xylene > *m*-xylene, based on the temperatures required to remove the guest molecules.

Finsy *et al.*[29] performed gas phase adsorption isotherms for the three xylene isomers using MIL-53(Al). Their results revealed that MIL-53(Al) showed a higher capacity for *o*-xylene over the other two isomers. These experiments could only identify the amount of isomer taken up by the framework; there is no indication of the strength of the interaction of each isomer with the framework. However, complementary studies in the liquid phase were performed by Moreira *et al.*[30] which showed that in various eluents the ortho isomer always gave the highest retention time. The order of retention, irrespective of eluent, was always *o*-xylene > *p*-xylene ≈ *m*-xylene. Similar studies into xylene separation have been performed by El Osta *et al*.[31] who reported that the order of preference of MIL-53(Fe), based on eluent times, was *o*-xylene > *m*-xylene > *p*-xylene. Alaerts *et al.*[32] also reported that MIL-47(V) showed a greater preference for *p*-xylene over *m*-xylene, *o*-xylene was not included in this study. Although a direct comparison between these studies and the *in situ* PXRD studies reported here cannot be made, it is clear that varying the ligand and the metal cation changes the properties of the framework. These changes alter the affinity towards specific guest molecules. Current methods for separating these isomers rely on distillation techniques which makes the separation of *p*- and *m*-xylene the most difficult. Therefore, the results reported in this section are important as they show CAU-13 has the highest preference for *p*-xylene and the lowest preference for *m*-xylene which could be advantageous for the process of separating these two isomers. It is probable that the preference for *p*-xylene at high temperatures would lead to longer eluent times if this material was used for a column separation as was reported previously for MIL-53(Al). Separation studies using *in situ* laboratory PXRD are not possible due to all three xylene isomers causing the framework to expand to the same unit cell volume. Therefore identification of the isomer/s present in the pores would not be possible.

Since the completion of this thesis a partial refinement of the xylene phases of CAU-13 was completed by F. Niekiel from Christian-Albrechts-Universitaet Kiel, the results are tabulated below.

Table 4.5: Unit cell parameters for the three xylene phases of CAU-13

	CAU-13		
Guest	o-xylene	m-xylene	p-xylene
a/ Å	6.672(2)	6.6717(9)	13.168(6)
b/ Å	18.219(4)	18.069(2)	18.013(6)
c/ Å	10.959(1)	11.206(1)	11.166(4)
β/ °	89.60(3)	91.270(9)	91.18(3)
V/ Å^3	1332.0(6)	1350.5(3)	2647(2)
Space group	$P2_1/m$	$P2_1/m$	$P2_1/m$

4.3.3 Synthesis of Thiol-Modified MIL-53(Al)

MOFs have been studied for their use in the adsorption of a range of guest molecules. The adsorption of sulfur-containing molecules has become an important application for the petrochemical industry as European and U.S. governments are encouraging the production of low sulfur fuels (directive 2003/17/EC). Various MOFs have been investigated for their ability to adsorb different sulphur-containing molecules *i.e.* thiophene, benzothiophene.[33-35]

Presented here is the synthesis of a thiol-modified MOF which was investigated as an adsorbent for S-containing compounds. A new thiol-containing MOF was produced using the synthesis conditions of the published dihydroxy modified framework, MIL-53(Al)-$(OH)_2$. This synthetic procedure was chosen as it used some of the mildest conditions for synthesising the MIL-53-type framework. The synthesis conditions and reagent ratios were used unchanged.

All reagents were obtained from chemical vendors and used without further purification with the exception of the 2,5-dithiolterephthalic acid (2,5- dimercaptoterephthalic acid) which was synthesised by F. Millange, Versailles, France using a published synthesis.[36]

$Al(ClO_4)_3 \cdot 9H_2O$ (1.96 g, 4.02 mmol), 2,5-dithiolterephthalic acid (0.47 g, 4.02 mmol) and 10 mL *N*,*N*-diethylformamide were combined in a 20 mL Teflon-lined autoclave, stirred for 15 minutes and then heated to 125 °C for 5hrs. The resulting yellow powder was stirred in a large amount of methanol for 1-5 days and the suspension was then centrifuged to collect. The sample was separated as product **A** and **B** after a minor colour change was observed; product **B** is a slightly darker shade of pale yellow. Product **A** was stirred for 1-3 days in methanol and product **B** was stirred for 4-5 days. Both samples were dried in air at approximately 70 °C. The results of the elemental analysis of product **A** and **B** are shown in Table 4.6; they are compared with theoretical values for the elemental percentage content of different empirical formulae. Both products agree most closely with the predicted composition of the empirical formula $Al(C_8H_4O_4S_2)(OH) \cdot [H_2O]$. However, the carbon and sulphur content of product **A** do not agree strongly with this prediction; the lower percentage content of these two elements suggests that there are other elements present. Other occluded molecules could be present within the pores of the framework. The small percentage of nitrogen present in each sample can be accounted for as residual DEF on the surface of the sample.

*Table 4.6: Experimental and theoretical elemental analysis results for MIL-53(Al)-$(SH)_2$ **A** and **B***

		C %	H %	N %	S %
Experimental	**A**	28.82	2.63	<0.10	18.30
	B	31.78	2.28	0.24	20.05
Theoretical	$Al(C_8H_4O_4S_2)(OH)$	35.30	1.85	-	23.56
	$Al(C_8H_4O_4S_2)(OH)\cdot[H_2O]$	33.10	2.08	-	22.09
	$Al(C_8H_4O_4S_2)(OH)\cdot[MeOH]$	35.53	2.98	-	21.07
	$Al(C_8H_4O_4S_2)(OH)\cdot[DEF]$	41.82	4.32	3.75	17.18

The samples obtained by this method were poorly crystalline but it was possible to obtain a PXRD pattern for the two phases that were isolated. The powder X-ray diffraction patterns for both products are shown in Figure 4.45. Product **A** is compared with the XRD pattern recorded for the dehydrated, fully-open, phase of the –Cl modified MIL-53(Al). The graph shows that there is a reasonable comparison between the two patterns suggesting that the thiol product **A** has the MIL-53 framework and that this sample has a unit cell volume similar to the fully-open phase, 1431 $Å^3$. Product **B**, which was obtained after washing in methanol for a longer period of time, is compared with the hydrated phase of the –Br modified MIL-53(Al). There is reasonable agreement between the patterns suggesting this product has the MIL-53 structure and a unit cell volume similar to the hydrated phase of the bromo modified MIL-53(Al), 1055 $Å^3$.

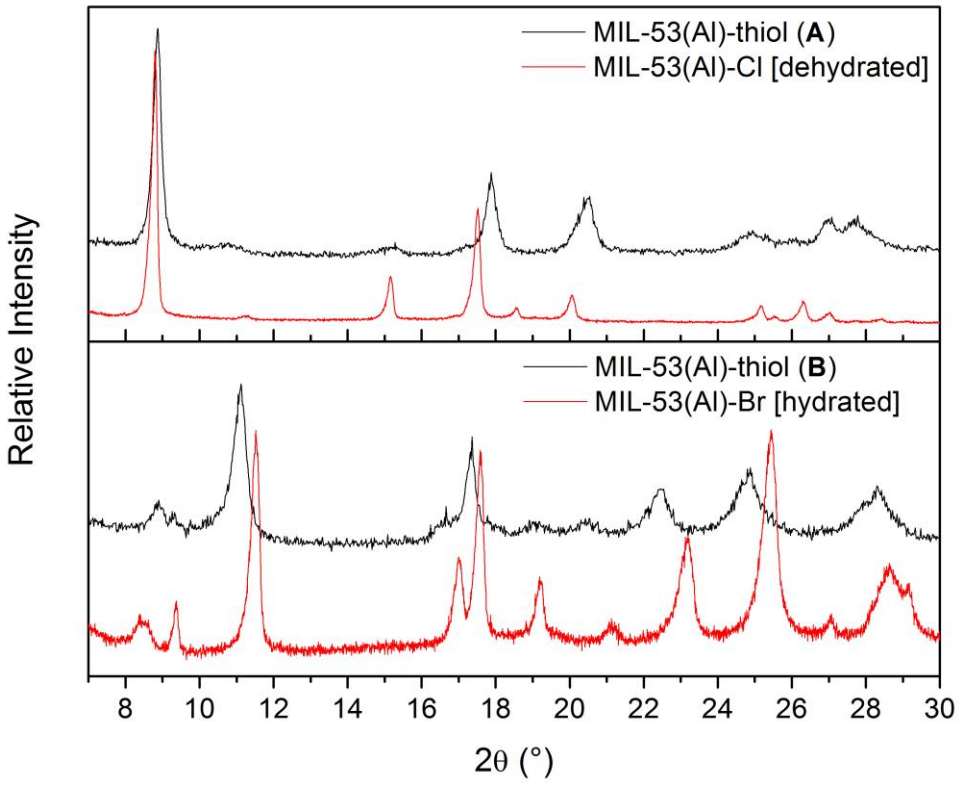

*Figure 4.45: XRD of MIL-53(Al)-thiol **A** compared with MIL-53(Al)-Cl [dehydrated] and MIL-53(Al)-thiol **B** compared with MIL-53(Al)-Br [hydrated]*

Thermogravimetric analysis was performed on both products and the results are shown in Figure 4.46. The TG data were analysed by using the final mass of Al_2O_3, after complete decomposition of the material, to predict the possible empirical formulae for these products. For product **A**, which XRD shows to have a more open framework, the TG data shows that there is a small immediate mass loss which is assumed to be due to the loss of occluded solvent molecules. Using the results gained from elemental analysis the empirical formula was assumed to contain one molar equivalent of water. The predicted percentage masses of $Al(C_8H_4O_4S_2)(OH)\cdot[H_2O]$ (1) and the empty framework, $Al(C_8H_4O_4S_2)(OH)$ (2) are shown on the graph in Figure 4.46a. It is observed that the predicted percentage mass losses (indicated by the dashed lines) agree well with the plateaus seen in the experimental data. The first mass loss is complete below 100 °C which is consistent with the loss of water molecules. The percentage

masses corresponding to the positions of the plateaus observed in the experimental data for both **A** and **B** are tabulated in Table A.8. The TG data for product **B** is shown in Figure 4.46b. Only the predicted percentage mass of the empirical formula of the empty framework, $Al(C_8H_4O_4S_2)(OH)$ (1), is shown on the graph. This predicted percentage mass is equal to 99.6% suggesting that there should be no occluded molecules. However, there is a small mass loss observed at low temperatures in the experimental data which could be due to surface or occluded molecules. It is also possible that the assumed empirical formula of the empty framework is not correct. It is not possible to identify which of these conclusions is correct using the data that were collected.

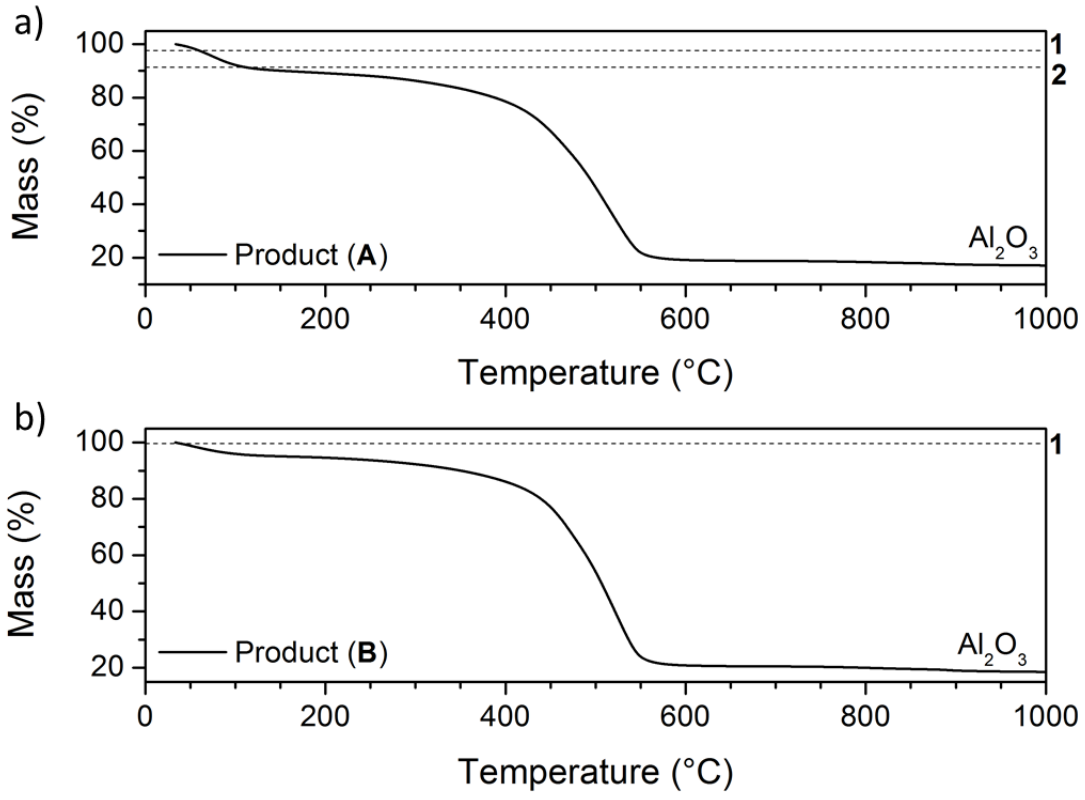

Figure 4.46: TGA of MIL-53(Al)-thiol framework. The predicted masses are shown (dashed lines).

To study the affinity of the thiol-modified framework for sulphur-containing molecules, H_2S adsorption isotherms were performed by G. De Weireld from the Faculté Polytechnique Mons, Belgium. A sample of product **A** was activated under vacuum

(10^{-5} bar) at 150 °C. Measurements were taken at 150 °C at various pressures up to and including 10 bar. Product **A** was found to have an adsorption capacity of 2.2 mmol g^{-1} at 1 bar and 4.8 mmol g^{-1} at 10 bar. The unmodified MIL-53(Al) material was studied for comparison. The data show that the unmodified material has a greater capacity for H_2S; 3.6 mmol g^{-1} and 12.0 mmol g^{-1} at 1 and 10 bar respectively. However, at very low pressures the Henry's constant for product **A** was found to be 16 mmol g^{-1} bar^{-1} which is three times higher than the value calculated for MIL-53(Al), 5.14 mmol g^{-1} bar^{-1}. This is indicative of a strong interaction between H_2S and the thiol linker. The reduced adsorption capacity of product **A** is thought to be due to the bulky thiol groups blocking entry to the framework pores. Adsorption studies have not been performed on product **B**. For a complete comparison these studies should be completed in the future.

To understand the effect of the thiol linker more conclusively a more crystalline sample of the MOF needs to be obtained so that the structure can be solved. The correct activation process also needs to be established so that it is certain that the pores are empty at the start of future adsorption studies.

4.4 Studying the Local Structure of MIL-53(Cr) Using Total Neutron Scattering

This thesis has concentrated on investigating one important property of the MIL-53 framework, its flexibility. Various versions of MIL-53 exist and they all exhibit this flexibility in varying degrees. Most notably, the Al and Cr versions both expand by approximately 50% in volume upon complete removal of any occluded molecules whereas the Fe version contracts by approximately 10% in volume upon removal of occluded molecules. Only minor geometric differences exist between the different frameworks and none are considered great enough to account for such different

behaviour.[9] The crystal structures for these materials were obtained using Rietveld refinement of powder X-ray diffraction patterns therefore the structural data represents an average of the bulk sample. The work presented here aims to investigate the local structure of the MIL-53 framework. Only one of the MIL-53 frameworks will be used in this investigation: MIL-53(Cr). Recent work on the similar framework, MIL-53(Al),[14] using inelastic neutron scattering (INS) studies showed that the dehydrated phase spontaneously closed when cooled below 150 K. This work by Liu *et al*. showed that not only was contraction possible without the presence of guest molecules but also that the flexibility of the framework experienced hysteresis when cooled to low temperatures; the framework did not begin to contract until the temperature was below 150 K but after cooling to 77 K the framework did not start to expand until heated above 325 K. The work presented here which investigates MIL-53(Cr) hopes to expand upon the work reported by Liu *et al*.; total neutron scattering experiments will be used to investigate the local structure using pair distribution function (PDF) analysis in an attempt to understand better the mechanism that governs framework expansion/contraction. MIL-53(Cr) was chosen as it shows the same breathing properties, at high and ambient temperatures, as MIL-53(Al) but benefits from a simpler synthesis.

The instrument GEM at the ISIS facility was used to perform neutron diffraction studies. The closed cycle refrigerator (CCR) sample holder was used for the entire experiment to allow the sample to be studied in the range of 5-300 K. Before data collection began the sample was equilibrated at 5 K to allow for contraction of the framework. During heating to 300 K data were collected every 50 K. Three temperatures were chosen for long data collection during the heating run: 5 K, 150 K and 300 K. After reaching 300 K it was necessary to remove the sample from the CCR

and heat the sample in an oven (still sealed in the can) to approximately 400 K to ensure that the framework had fully expanded. The can was returned to the CCR and data were collected every 25 K as the sample was cooled to 50 K. Two temperatures were chosen for long data collection during cooling: 300 K and 150 K.

The results show that dehydrated MIL-53(Cr) displays the same contraction at low temperatures as MIL-53(Al). However, the diffraction data (Figure 4.47) reveals that when cooled to 5 K the framework does not completely close; the pattern shows the co-existence of the open and the closed phases. It was also observed that MIL-53(Cr), like MIL-53(Al), displays hysteresis of framework opening and closing. Upon heating from 5 K to room temperature the framework remained in the mixed phase where most of the sample was closed, re-opening only when heated above 300 K. Conversely, after starting with the fully-open phase at 300 K the framework only starts to close when it is cooled below 175 K.

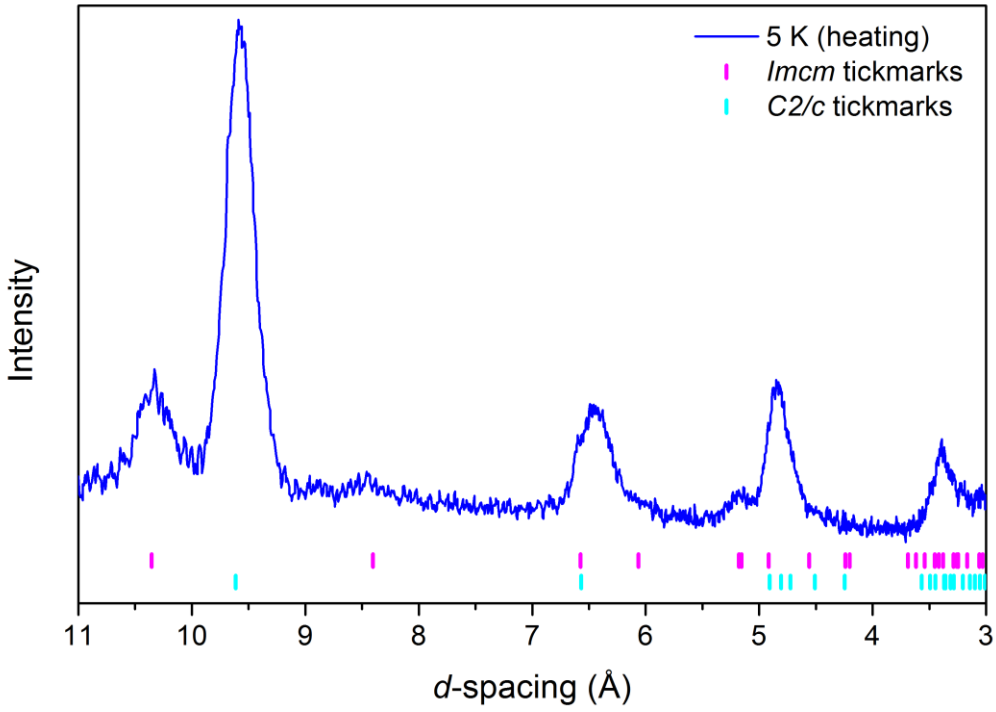

Figure 4.47: Diffraction pattern for dehydrated MIL-53(Cr) recorded at 5 K.

The reasons for the framework never contracting completely are not yet fully understood but it is possible that this is due only to kinetics and that a longer time held at 5 K would have resulted in the full closing of the framework. Also conceivable is that the whole sample can never fully close due to structural defects that restrict the flexibility of some regions or individual crystallites; resulting in the co-existence of the two phases. It is not clear whether the two pore sizes, fully-open (~1500 $Å^3$) and closed (~900 $Å^3$), can co-exist within the same crystal or whether the mixture of pore sizes is only possible as a result of different domains. Figure 4.48 shows two-dimensional representations of these two alternatives. Figure 4.48b shows a suggestion for how the two pore sizes could co-exist within the same crystal; it is necessary for areas of the structure to exist with intermediate pore sizes, however, these small disordered domains would not be visible in a diffraction experiment when surrounded by ordered domains of the open and closed structures.

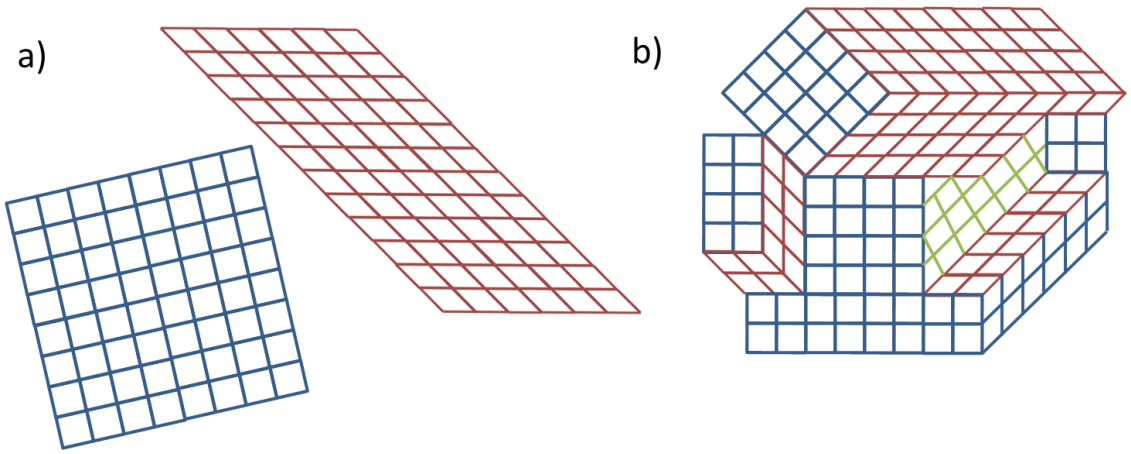

Figure 4.48: Schematic of the co-existence of different pore sizes a) different pore sizes existing in different domains and b) different pore sizes tessellated in the same crystal, the green area indicates a section containing various pore sizes.

Figure 4.49 shows the diffraction data recorded upon cooling MIL-53(Cr) from 175 K to 50 K. The data from 300 K to 200 K have been omitted as there is no change in the patterns at these temperatures. At 175 K it can be seen that the framework still exists as a single phase, the fully-open phase, but upon cooling to 150 K evidence for the monoclinic closed phase can be seen. Upon further cooling it can be seen that the closed phase continues to increase in intensity as the fully-open phase decreases. The pattern recorded at 50 K shows that the framework still contains some fully-open pores. It is important to note that the contraction and expansion of the pores does not occur gradually; the pores either exist as fully-open or closed. The diffraction data highlights this as the peaks for the monoclinic phase can be seen to grow alongside the peaks of the orthorhombic phase; there is no gradual expansion from one phase to the other.

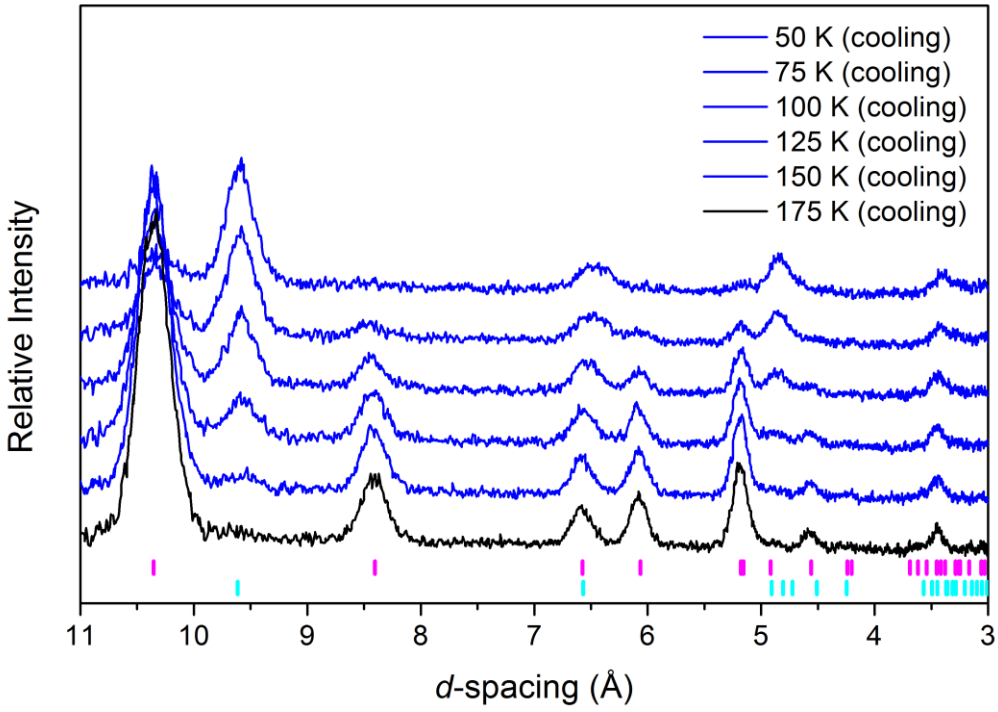

Figure 4.49: Diffraction data showing the behaviour of MIL-53(Cr) upon cooling from 175 K to 50 K. Tickmarks for the different phases are shown: Imcm (pink), C2/c (blue)

Using the General Structure Analysis System (GSAS) software, unit cell parameters were determined using the Le Bail profile refinement technique at each temperature studied during the experiment. Mixed-phase refinements were necessary for the majority of the datasets. The fully-open phase was modelled using the dehydrated MIL-53(Cr) structure (*Imcm*, 1496 $Å^3$) recorded at high temperatures,[20] and the closed structure was modelled using the dehydrated MIL-53(Fe) structure (*C2/c*, 904.4 $Å^3$)[10] This structure was chosen as it was considered likely that when the MIL-53(Cr) framework closed in the absence of guest molecules it would contract further than the smallest pore volume previously reported for the Cr analogue which contains H_2O molecules (*C2/c*, 994.5 $Å^3$). Liu *et al.* had previously observed that at low temperatures dehydrated MIL-53(Al) contracted further (~846 $Å^3$) than is seen upon hydration (~947 $Å^3$) and this was also found to be the case for MIL-53(Cr). The refined unit cell

volumes for each phase at each temperature are shown in Figure 4.50 and also shown are the standard deviations associated with each data point. The graph shows that each phase is subject to thermal expansion as the temperature is increased. However, the volume of the *Imcm* phase remains constant during the cooling run, even after some of the sample has contracted to the *C2/c* phase, until the sample is cooled below 125 K. Using this type of analysis it is not possible to determine the amount of each phase present at each temperature.

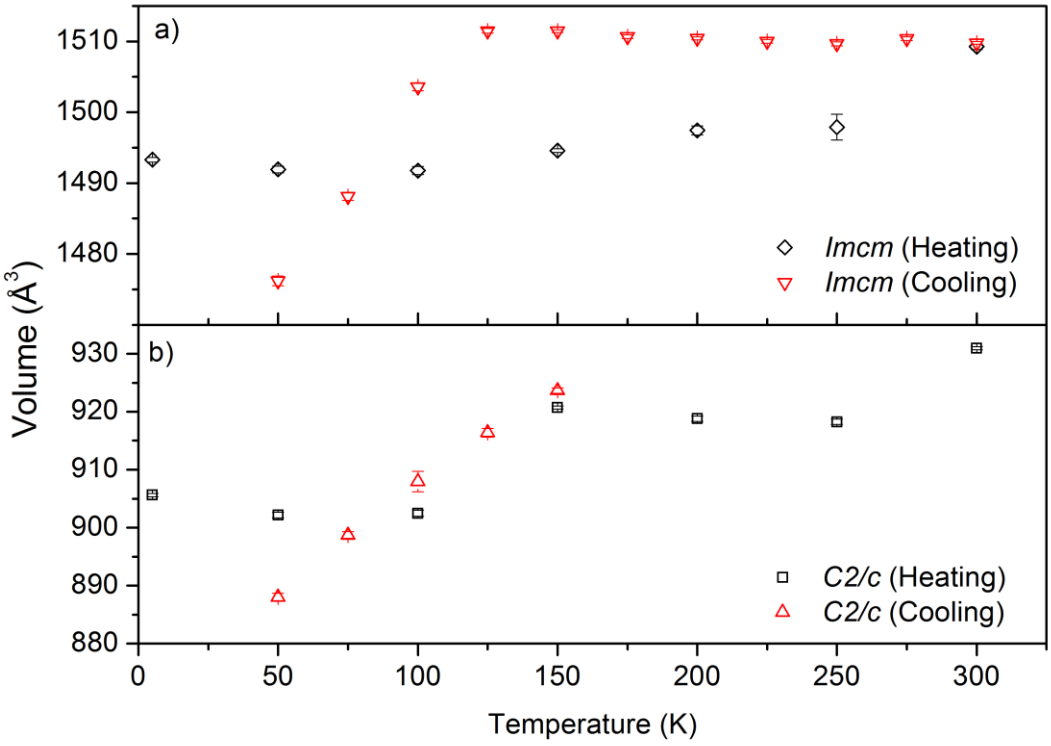

Figure 4.50: Le Bail unit cell volumes for a) the fully-open Imcm phase and b) the closed C2/c phase. Error bars are shown, but are generally smaller than the data points.

To estimate the weight fraction for each phase at each temperature, a partial Rietveld refinement was performed; the coordinates, occupancies and thermal parameters of the atoms were left unchanged from the published crystal structures and only the lattice parameters and the scaling of each phase were refined. Figure 4.51 shows the change in weight fraction of the *Imcm* phase as a function of temperature. This graph clearly

shows the hysteresis of framework breathing with temperature; the percentage of the sample that has the *Imcm* structure during the heating run remains approximately constant at 20 %, whereas upon cooling from 175 K to 50 K the percentage of the *Imcm* phase drops from 100% to < 30%.

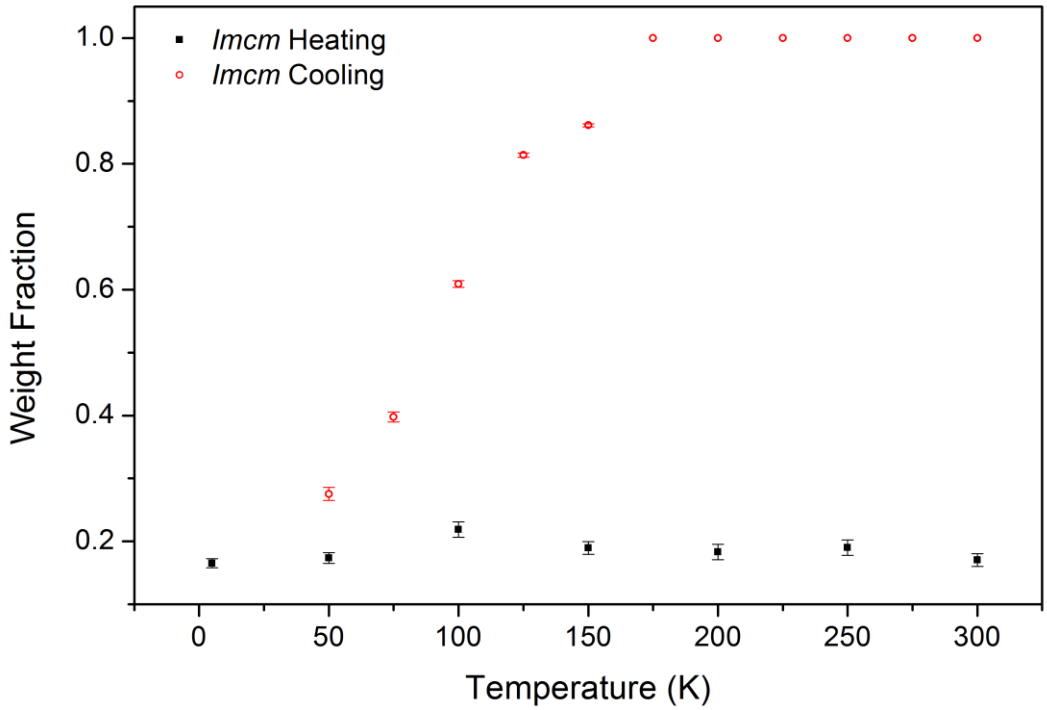

Figure 4.51: Weight Fraction of the Imcm phase of MIL-53(Cr) present at each temperature.

To investigate the local structure, and therefore the possible cause for framework breathing, atomic pair correlation functions were produced for the data recorded at 5 K, 150 K and 300 K during the heating run and at 300 K and 150 K during the cooling run. Data were collected in one hour accumulations to allow the breathing of the framework to stabilise at each temperature (Figure A.9). The one hour accumulations, which showed no change in their diffraction patterns, were combined to produce the correlation functions. The functions are plotted in Figure 4.52 in the range 0.5 – 30 Å. Key areas have been highlighted; they show the regions of *r* where there are large

differences between the datasets. It can also be seen that the major differences only exist between the different runs *i.e.* heating and cooling; the three datasets collected during the heating run (>80% closed, *C2/c*) show very few differences, the same trend is seen for the two datasets collected during the cooling run (300 K = 100% *Imcm*, 150 K >85% *Imcm*). It is important to note that there are no distinct differences between all five datasets in the low *r* region (0.5 – 6 Å). It can also be observed that the peaks for both datasets collected at 300 K are broader than the other datasets, which is caused by the increased thermal motion in the framework at higher temperatures.

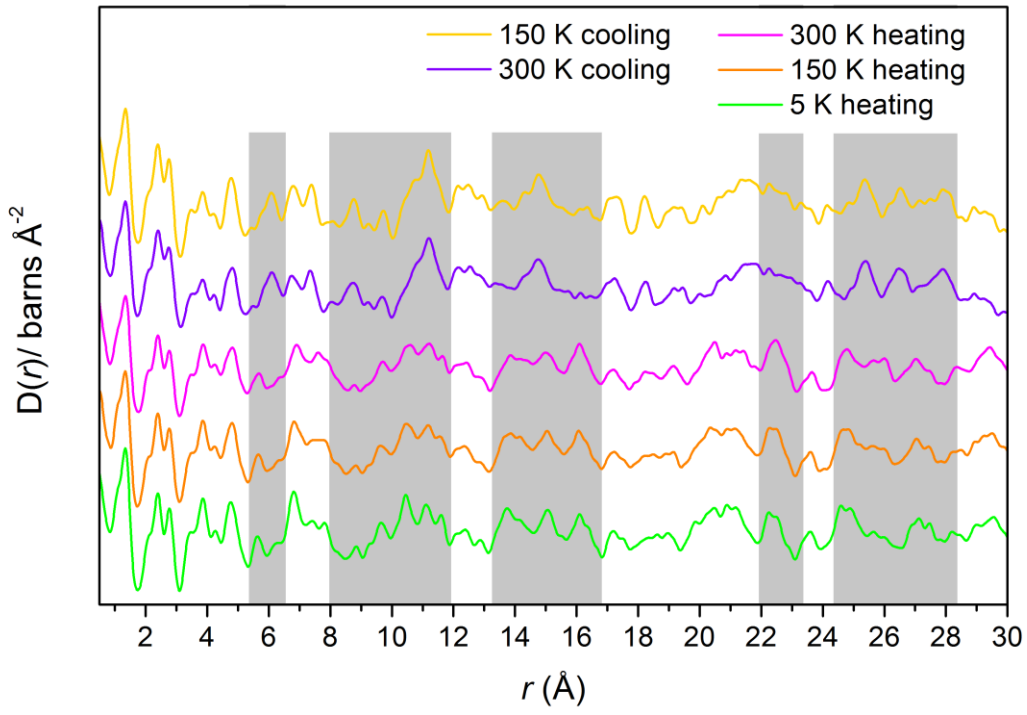

Figure 4.52: Atomic pair correlation functions for all experimental datasets.

Simulated atomic pair correlation functions were produced using the crystal data from the two phases of MIL-53 that were used for the analysis of the diffraction data, MIL-53(Cr) [dehydrated] (the *open* phase) and MIL-53(Fe) [dehydrated] (the *closed* phase). The results from the Bragg diffraction data showed that during the heating run the

framework never fully contracted to the closed phase, it was only approximately 80% closed, while the remaining 20% stayed in the open phase. Therefore a simulated correlation function was created that contained 80% of the closed phase simulation and 20% of the open phase simulation. A simulated correlation function was also produced for a single, isolated terephthalate molecule. This simulation is shown in Figure 4.53 compared with the simulated data for the two extreme situations found for MIL-53(Cr). Also shown are the ranges of *r* that correspond to specific intramolecular atomic pairs found within the terephthalate molecule. This simulation illustrates that most of the PDF of MIL-53 at low *r* is accounted for by the PDF of terephthalate. However, there are some distinct peaks at 2-3 Å and 4-5 Å which change upon expansion. The simulation for the terephthalate molecule has been compared with both the mixed (closed + open) phase simulation and the open phase simulation. It is expected that the intramolecular distances of the terephthalate linker will remain constant throughout the expansion and contraction of the framework.

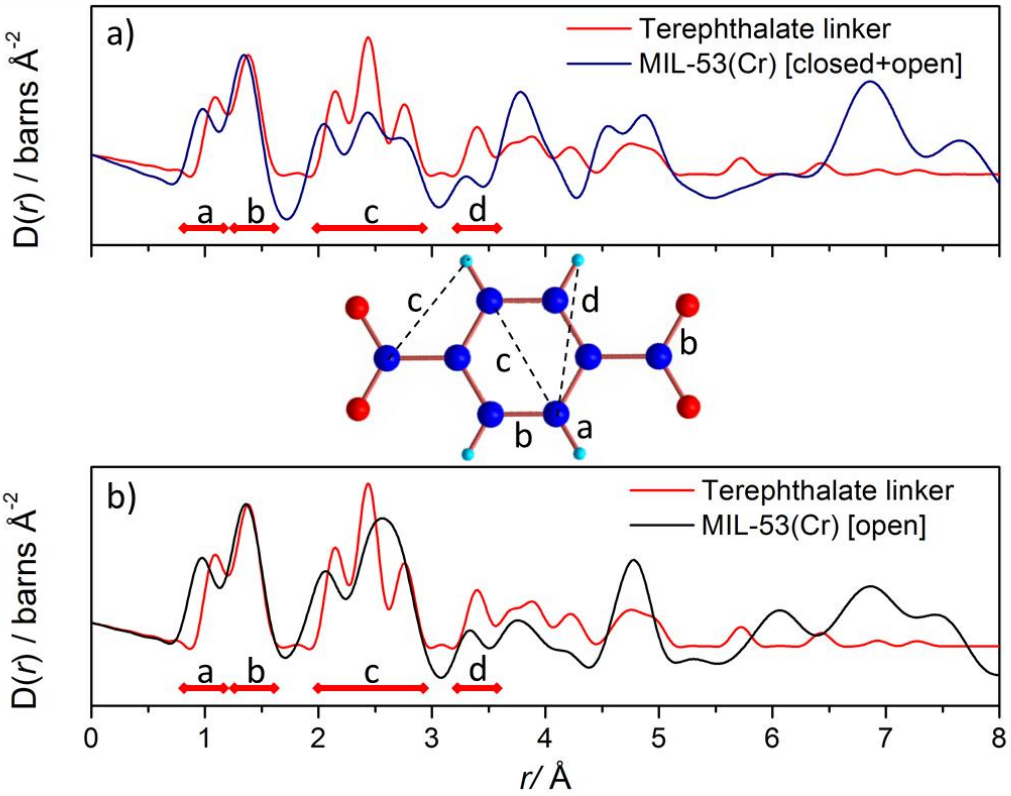

Figure 4.53: Simulated correlation function of the terephthalate linker compared with the simulated functions for a) MIL-53 80% closed + 20% open and b) MIL-53 open. Atomic pair distances found in the terephthalate molecule are indicated.

Figure 4.54 shows the simulated correlation functions alongside views of the crystal structure that highlight the atomic correlations involved. Comparable C-C atomic pairs have been highlighted on the framework pictures and the corresponding *r* values are indicated on the graphs. The range of intramolecular distances due to the terephthalate linker is also shown. The purpose of this figure is to draw attention to the large changes in *r* observed between the equivalent intermolecular atomic pairs, before and after opening, and also the overlap in the ranges of *r* between the intra- and intermolecular atomic pairs. The large changes in *r* and the overlap between intra- and intermolecular distances make analysis of the data difficult.

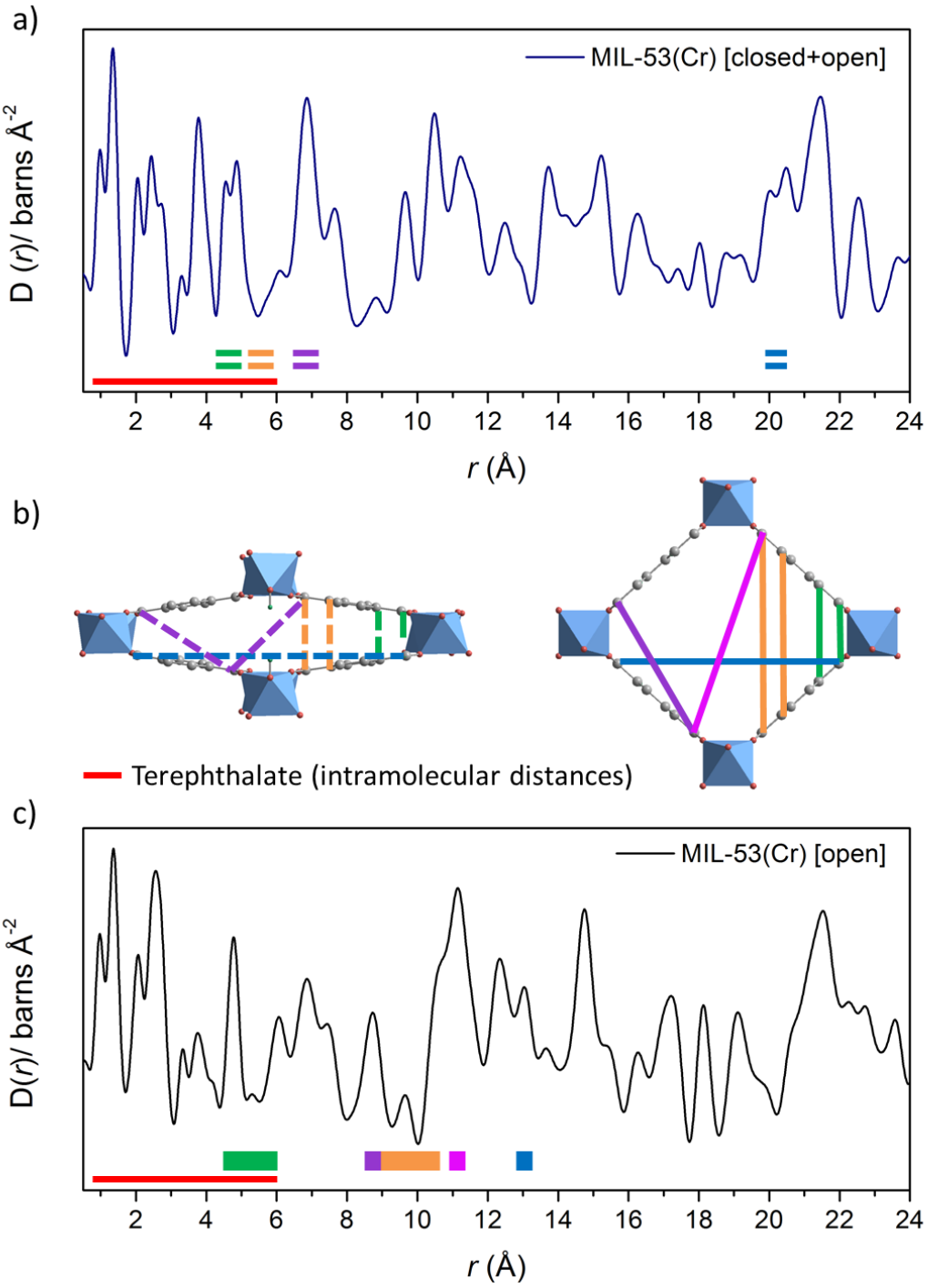

Figure 4.54: Simulated atomic pair correlation functions for a) MIL-53(Cr) [closed+open] and c) MIL-53(Cr) [open].Comparable C-C atomic pairs between the two phases have been highlighted on the crystal structure views shown in b).

Partial atomic correlation functions were also produced so that the atomic pairs which contribute the most intensity to the final PDF could be identified. The most prominent differences, at low *r*, between the total correlation functions shown in Figure 4.54 are

two intense peaks in the mixed phase simulation at ~4 Å and ~7 Å and one intense peak in the open phase simulation at ~8.5 Å. The partial correlation functions (Figure 4.55) were used to identify the atomic pairs that contribute to these intense peaks as C-D and C-C, respectively, for the mixed phase and a combination of C-C and C-D contributions for the open phase. As highlighted in Figure 4.54, both of these C-C contributions were identified as intermolecular C-C pairs where the atoms are positioned across the pore from each other. The C-D contributions were identified as the interactions between these atoms which are positioned similarly *i.e.* across the pore, to the C-C pairs.

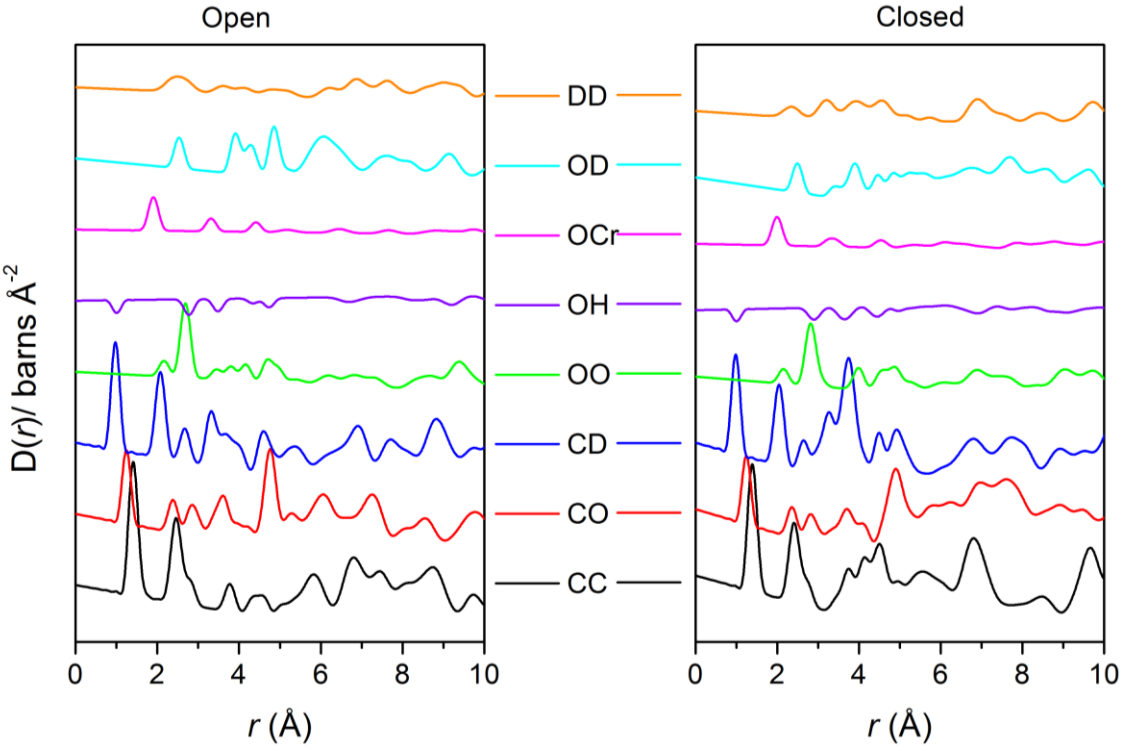

Figure 4.55: Partial atomic pair correlation functions for the simulated data for MIL-53(Cr) [open] (left) and MIL-53(Cr) [closed] (right). Only the partials that contribute the most intensity are shown.

The experimental data recorded at 300 K during the heating run, which was found to contain approximately 80% of the closed phase and 20% of the open phase, is compared with the appropriate simulated function in Figure 4.56. It can be seen that the simulation agrees reasonably well with the experimental data. There are a few discrepancies at low

r; it was shown previously that this region is dominated by the contribution from the terephthalate linker. The intramolecular distances used in the simulation are not a perfect reflection of the experimental data; the first peak in the simulation appears at a lower value of *r* than the first peak in the experimental data. This peak corresponds to the directly bonded C–D pair in the terephthalate ring therefore it is clear that the model used for the simulation needs adjusting. There are also some peaks in the 2 – 3 Å region of the simulation which are offset from the experimental data; this region was identified as having most contributions from the C–C and C–O pairs of the terephthalate linker. Discrepancies between these distances could be due to a greater degree of twisting of the rings as the framework contracts than has been accounted for in the simulation.

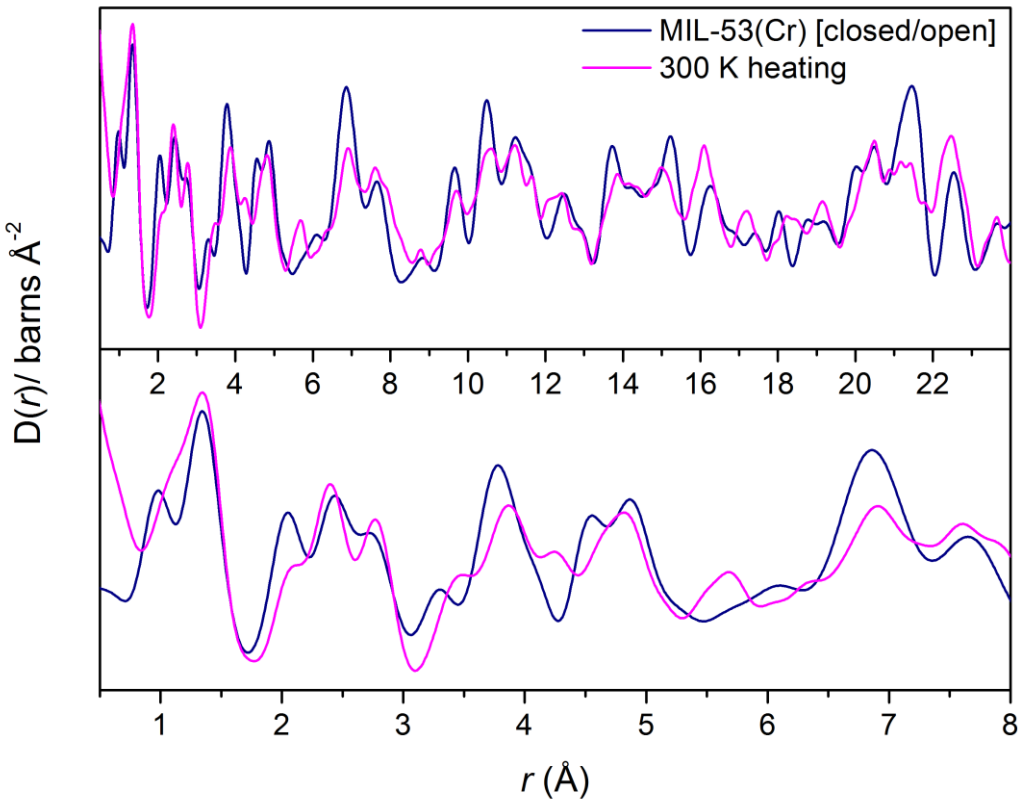

Figure 4.56: Atomic pair correlation function for the 300 K heating run compared with the simulated correlation function for MIL-53(Cr) [closed/open]

The experimental data recorded at 300 K during the cooling run was compared with the simulated data for the open phase and is shown in Figure 4.57. There is good agreement between the two functions. However, similar discrepancies as those seen in the previous comparison can be seen in the low *r* region.

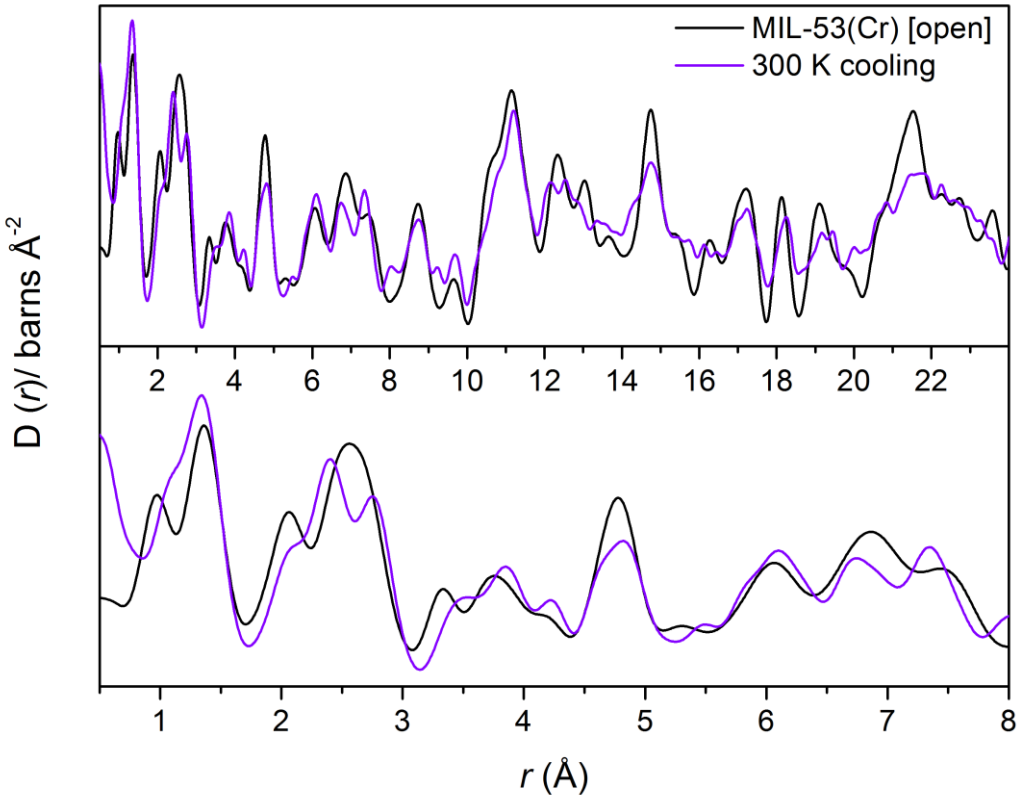

Figure 4.57: Atomic pair correlation function for the 300 K cooling run compared with the simulated correlation function for MIL-53(Cr) [open]

The simulated correlated functions were improved by modelling the thermal motion of the framework but further improvements could be made by also modelling the particle size. The effect of modelling a smaller particle size would be the increased dampening of the intensity of the peaks with *r*, which would give a better comparison with the experimental data. The minor discrepancies seen in the comparisons between simulated and experimental data indicate that the models used for the simulations are not completely correct. The potential problems with the models are: 1) not all the bond

distances are correct; the C-D atom positions were estimated not refined from XRD data, 2) the twisting of the terephthalates is not modelled correctly; the degree of twisting can be affected by the degree of expansion/contraction of the framework, and 3) the degree of expansion/contraction is not modelled correctly; the structural models used for the simulations and the experimental data were recorded at different temperatures which could lead to differences in the unit cell volumes.

To improve the comparison between the simulation and experimental data several techniques could be applied. Longer data collection at each temperature would facilitate a full rigid-body Rietveld refinement allowing the crystal structure at each temperature to be obtained. This information could then be used to improve the model for the simulation. Conversely, the PDFgui software can be used to fit structure models directly to PDF data; benefitting from refinements performed in real space. Reverse Monte Carlo (RMC) modelling techniques could also be used to establish a more comprehensive model. However, this technique cannot be used at present for this work as multi-phase modelling is not yet possible. Complementary X-ray PDF studies could also be performed which would provide additional information for the heavier elements in the framework. However, instruments capable of producing X-rays with sufficiently high energies for this type of analysis are still in the development stage at synchrotron X-ray sources. Comparable studies on the analogous MIL-53 frameworks, which display a contraction upon the removal of guest molecules (*e.g.* the Fe and Sc frameworks), could potentially provide the necessary evidence to explain why these frameworks behave differently in the absence of occluded guest molecules.

4.5 References

1. G. Férey, M. Latroche, C. Serre, F. Millange, T. Loiseau and A. Percheron-Guegan, *Chem. Commun.*, 2003, 2976-2977.

2. S. Bourrelly, P. L. Llewellyn, C. Serre, F. Millange, T. Loiseau and G. Ferey, *JACS*, 2005, **127**, 13519-13521.

3. V. Finsy, L. Ma, L. Alaerts, D. E. De Vos, G. V. Baron and J. F. M. Denayer, *Microporous Mesoporous Mater.*, 2009, **120**, 221-227.

4. L. Hamon, P. L. Llewellyn, T. Devic, A. Ghoufi, G. Clet, V. Guillerm, G. D. Pirngruber, G. Maurin, C. Serre, G. Driver, W. Van Beek, E. Jolimaître, A. Vimont, M. Daturi and G. Férey, *JACS*, 2009, **131**, 17490-17499.

5. L. Hamon, C. Serre, T. Devic, T. Loiseau, F. Millange, G. Férey and G. D. Weireld, *JACS*, 2009, **131**, 8775-8777.

6. A. Boutin, M.-A. Springuel-Huet, A. Nossov, A. Gédéon, T. Loiseau, C. Volkringer, G. Férey, F.-X. Coudert and Alain H. Fuchs, *Angew. Chem. Int. Ed.*, 2009, **48**, 8314-8317.

7. C. Serre, S. Bourrelly, A. Vimont, N. A. Ramsahye, G. Maurin, P. L. Llewellyn, M. Daturi, Y. Filinchuk, O. Leynaud, P. Barnes and G. Férey, *Adv. Mater.*, 2007, **19**, 2246-2251.

8. P. L. Llewellyn, P. Horcajada, G. Maurin, T. Devic, N. Rosenbach, S. Bourrelly, C. Serre, D. Vincent, S. Loera-Serna, Y. Filinchuk and G. Férey, *JACS*, 2009, **131**, 13002-13008.

9. F. Millange, N. Guillou, R. I. Walton, J. M. Greneche, I. Margiolaki and G. Férey, *Chem. Commun.*, 2008, 4732-4734.

10. R. I. Walton, A. S. Munn, N. Guillou and F. Millange, *Chem. Eur. J.*, 2011, **17**, 7069-7079.

11. N. Guillou, R. I. Walton and F. Millange, *Z. Kristallogr. - Cryst. Mater.*, 2010, **225**, 552-556.

12. F. M. Mulder, T. J. Dingemans, H. G. Schimmel, A. J. Ramirez-Cuesta and G. J. Kearley, *Chem. Phys.*, 2008, **351**, 72-76.

13. A. J. Ramirez-Cuesta, *Comput. Phys. Commun.*, 2004, **157**, 226-238.

14. Y. Liu, J.-H. Her, A. Dailly, A. J. Ramirez-Cuesta, D. A. Neumann and C. M. Brown, *JACS*, 2008, **130**, 11813-11818.

15. H. Yang, R. I. Walton, S. Biedasek, S. Antonijevic, S. Wimperis, A. J. Ramirez-Cuesta, J. Li and A. I. Kolesnikov, *J. Phys. Chem. B*, 2005, **109**, 4464-4469.

16. P. C. H. Mitchell, S. F. Parker, A. J. Ramirez-Cuesta and J. Tomkinson, *Vibrational Spectroscopy With Neutrons With Applications in Chemistry, Biology, Materials Science and Catalysis*, World Scientific Publishing Co. Ptc. Ltd., 2005.

17. S. Bourrelly, B. a. Moulin, A. Rivera, G. Maurin, S. Devautour-Vinot, C. Serre, T. Devic, P. Horcajada, A. Vimont, G. Clet, M. Daturi, J.-C. Lavalley, S. Loera-Serna, R. Denoyel, P. L. Llewellyn and G. r. Férey, *JACS*, 2010, **132**, 9488-9498.

18. T. Loiseau, C. Serre, C. Huguenard, G. Fink, F. Taulelle, M. Henry, T. Bataille and G. Férey, *Chem. Eur. J.*, 2004, **10**, 1373-1382.

19. F. Millange, C. Serre and G. Férey, *Chem. Commun.*, 2002, 822-823.

20. N. Guillou, F. Millange and R. I. Walton, *Chem. Commun.*, 2011, **47**, 713-715.

21. C. Serre, F. Millange, C. Thouvenot, M. Nogues, G. Marsolier, D. Louer and G. Férey, *JACS*, 2002, **124**, 13519-13526.

22. F. Millange, N. Guillou, M. E. Medina, G. Férey, A. Carlin-Sinclair, K. M. Golden and R. I. Walton, *Chem. Mater.*, 2010, **22**, 4237-4245.

23. S. Biswas, T. Ahnfeldt and N. Stock, *Inorg. Chem.*, 2011, **50**, 9518-9526.

24. E. Stavitski, E. A. Pidko, S. Couck, T. Remy, E. J. M. Hensen, B. M. Weckhuysen, J. Denayer, J. Gascon and F. Kapteijn, *Langmuir*, 2011, **27**, 3970-3976.

25. A. Boutin, S. Couck, F.-X. Coudert, P. Serra-Crespo, J. Gascon, F. Kapteijn, A. H. Fuchs and J. F. M. Denayer, *Microporous Mesoporous Mater.*, 2011, **140**, 108-113.

26. N. Reimer, B. Gil, B. Marszalek and N. Stock, *CrystEngComm*, 2012, **14**, 4119-4125.

27. A. Coelho, *Topas Academic Version 4.1. Computer Software, Topas Academic, Coelho Software,* , Brisbane, 2007.

28. J. P. Garcia Villaluenga and A. Tabe-Mohammadi, *Journal of Membrane Science*, 2000, **169**, 159-174.

29. V. Finsy, C. E. A. Kirschhock, G. Vedts, M. Maes, L. Alaerts, D. E. De Vos, G. V. Baron and J. F. M. Denayer, *Chem. Eur. J.*, 2009, **15**, 7724-7731.

30. M. A. Moreira, J. C. Santos, A. F. P. Ferreira, J. M. Loureiro and A. E. Rodrigues, *Ind. Eng. Chem. Res.*, 2011, **50**, 7688-7695.

31. R. El Osta, A. Carlin-Sinclair, N. Guillou, R. I. Walton, F. Vermoortele, M. Maes, D. de Vos and F. Millange, *Chem. Mater.*, 2012, **24**, 2781-2791.

32. L. Alaerts, M. Maes, P. A. Jacobs, J. F. M. Denayer and D. E. De Vos, *PCCP*, 2008, **10**, 2979-2985.

33. S. Achmann, G. Hagen, M. Hämmerle, I. M. Malkowsky, C. Kiener and R. Moos, *Chem. Eng. Technol.*, 2010, **33**, 275-280.

34. S. Biswas, M. Maes, A. Dhakshinamoorthy, M. Feyand, D. E. De Vos, H. Garcia and N. Stock, *J. Mater. Chem.*, 2012, **22**, 10200-10209.

35. L. Liu, X. Wang and A. J. Jacobson, *J. Mater. Res.*, 2009, **24**, 1901-1905.

36. L. Vial, R. F. Ludlow, J. Leclaire, R. Pérez-Fernández and S. Otto, *JACS*, 2006, **128**, 10253-10257.

Chapter 5

Synthesis of carboxylate MOFs

5 Synthesis of New Metal-Organic Frameworks

This chapter includes the synthesis and characterisation of various new metal-organic frameworks. Different characterisation techniques such as single-crystal X-ray diffraction, thermogravimetry, magnetometry and X-ray absorption spectroscopy have been used to analyse these materials.

A Mn(II) metal-organic framework published in 2010 was used as inspiration for new cobalt-containing materials. The published work was expanded upon with the aim of synthesising a new flexible MOF. The flexibility of the new cobalt materials was explored using methods such as thermal treatment and framework modifications. The use of pre-synthetic modifications resulted in a series of mixed-metal MOFs and a series of isoreticular MOFs with expanded unit cell volumes. This work also led to the discovery of two new porous MOFs, the properties of which have been explored through collaborations with MACADEMIA partners.

5.1 Introduction

In 2010, Xu *et al.*[1] published the structure of a Mn^{II} three-dimensional framework with the same topology as MIL-53 where the $-\mu^2(OH)$ groups along the backbone of the MIL-53 framework were replaced with neutral, pendant, pyridine-*N*-oxide (PNO) groups bound through the oxygen. The empirical formula of this material is Mn^{II}(bdc)(PNO) (bdc = 1,4-benzenedicarboxylic acid and PNO = pyridine-*N*-oxide). Like MIL-53, the 3-dimensional connectivity can be described as $I^1O^2.^2$ Due to the similarities between the structures it was hypothesised that this framework may display a similar flexibility to MIL-53, therefore it was chosen for further investigations. To

investigate the effect of the metal centre on the framework properties other metal cations were also investigated. The aim was to synthesise isostructural frameworks therefore metal cations with similar ionic radii, which give regular octahedral geometries and are stable in the +2 oxidation state were chosen for investigation. From the first row transition metals, Sc, Ti, V, Fe, and Cr were disregarded due to the high probability that any +2 salts would readily oxidise to +3 (Sc, Fe, Cr) and +4 (Ti, V) under the synthesis conditions that would be used.[3] Cu^{II} and Zn^{II} were also not chosen as the d^9 and d^{10} configurations, respectively, are not expected to give regular octahedra. The d^9 configuration of Cu^{II} is expected to exhibit Jahn-Teller distortions and the small radius of Zn^{II}, due to its high nuclear charge, means that tetrahedral coordination is almost exclusively preferred.[3] These metal cations have also been shown in the literature to form metal clusters when coordinated with carboxylate ligands,[4, 5] which are not present in the MIL-53 frameworks. Therefore, only Co and Ni were investigated for the purpose of synthesising isostructural frameworks as they are known to form stable +2 complexes with regular octahedral geometries.[3]

5.2 M^{II}(1,4-benzenedicarboxylate)(pyridine-*N*-oxide)

The published synthesis for the Mn^{II} framework was followed to produce an analogous Co^{II} framework.[1] The published synthesis uses an aqueous solution of manganese nitrate whereas the Co^{II} framework was successfully synthesised using the hydrated nitrate salt. $Co(NO_3)_2.6H_2O$ (150 mg), 1,4-benzenedicarboxylic acid (128 mg), pyridine-*N*-oxide (74 mg), *N*,*N*-dimethylformamide (8 mL) (molar ratio, 1:1.5:1.5:200) were added to a 18 mL Teflon-lined autoclave and heated to 120 °C for 18 hrs. Single-crystal analysis was performed (Section 5.2.1) and the empirical formula was determined to be $Co(C_8H_4O_4)(C_5H_5NO)$ which agrees with elemental analysis results:

experimental- C: 47.4%, H: 2.58%, N: 4.7%, calculated- C: 49.1%, H: 2.85%, N: 4.4%. The interest in this particular framework was due to the possibility that the framework may be flexible, due to the structural similarities with the flexible MIL-53, or that the framework could be modified, resulting in a flexible framework. One method that was experimented with was substituting the PNO groups with fluoride groups as is seen for MIL-53(Fe) where some of the bridging OH^- groups are replaced by F^-. The fluoride groups were introduced at the synthesis stage using aqueous hydrofluoric acid. $Co(NO_3)_2.6H_2O$ (140 mg), 1,4-benzenedicarboxylic acid (240 mg), pyridine-*N*-oxide (32 mg), $HF(H_2O)$ 40% (0.05 mL) and *N*,*N*-dimethylformamide (6 mL) (molar ratio, 1:3:0.7:2.2:184) were added to a 18 mL Teflon-lined autoclave and were heated to 120 °C for 18 hours. The molar ratio of PNO was reduced to encourage the coordination of F^- and the increased ratio for bdc was found necessary for the formation of single crystals. Single-crystal X-ray diffraction data confirmed that the framework was analogous to the pure PNO framework however this type of analysis was unable to determine the degree to which F^- had replaced PNO. The elemental analysis results agree with the predicted empirical formula, $Co(C_8H_4O_4)(C_5H_5NO)_{0.65}(F)_{0.35}$, which assumes 35% of the PNO groups have been replaced with F^-. Experimental results: C: 43.2%, H: 2.72%, N: 3.56%, F: 2.25%. Calculated: C: 46.35%, H: 2.51%, N: 3.12%, F: 2.28%.

It was seen for the MIL-53 materials that the metal centre can affect the properties of the framework,[6] therefore to investigate this, the pure PNO framework was also synthesised with nickel. $Ni(NO_3)_2.6H_2O$ (5 mg), 1,4-benzenedicarboxylic acid (2 mg), pyridine-*N*-oxide (2 mg) and *N*,*N*-dimethylformamide (10 mL) were added to a 18 mL Teflon-lined autoclave and were heated to 120 °C for 18 hours. Single-crystal analysis was not possible for this material, however, high-resolution X-ray diffraction was used

to confirm that this material had the same structure as the Mn and Co materials, as shown in Figure 5.1. Elemental analysis shows reasonable agreement with the empirical formula $Ni(C_8H_4O_4)(C_5H_5NO)$. Experimental results: C: 47.57%, H 2.83%, N 4.77%, calculated results: C: 49.11%, H 2.85%, N 4.41%

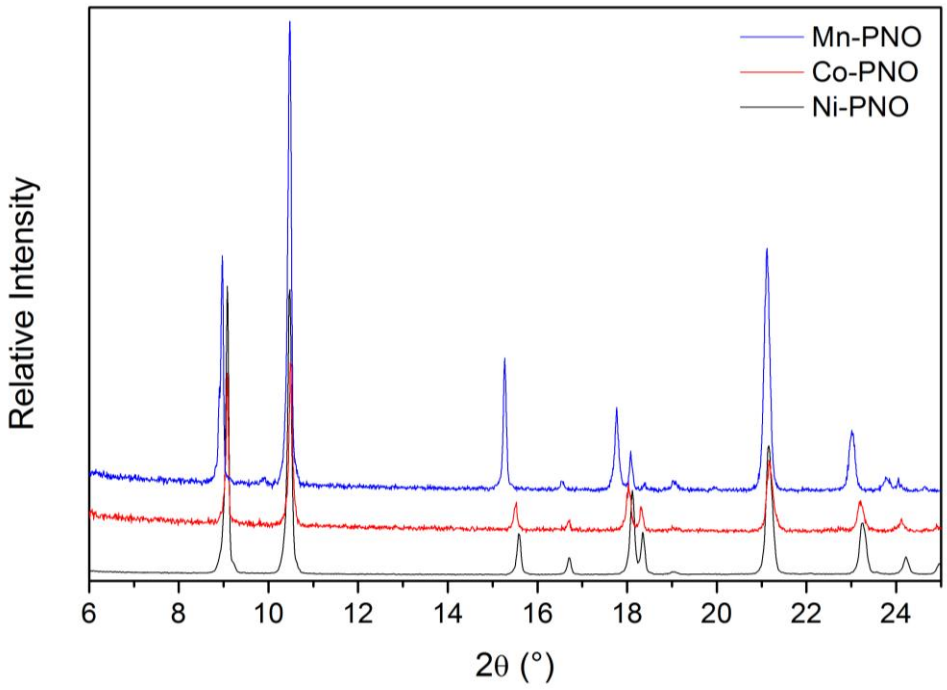

Figure 5.1: Experimental XRD patterns for the three pure pyridine-N-oxide materials.

5.2.1 X-ray Diffraction Studies

Single-crystal and high-resolution X-ray diffraction were used to investigate the structures of the PNO materials. Single-crystal analysis was possible for both of the Co^{II} samples (*i.e.* fluorinated and non-fluorinated). The pure PNO sample crystallised with a monoclinic unit cell, *C2/c*, with a unit cell volume of 1250 $Å^3$ when studied at 120 K. Some discrepancies between this result and the data obtained from powder XRD at room temperature were noticed so the single-crystal measurement was re-recorded at room temperature. The material was shown to have an orthorhombic, *Imma*, unit cell

with a cell volume of 1286.1 $Å^3$. This result confirms that the framework has retained some of the flexibility seen for MIL-53. The structure recorded at room temperature is shown in Figure 5.2 viewed along the *c*-axis, alternative views of the structure along the *a*-axis are also shown. The four metal oxide chains that form the corners of one diamond-shaped pore have been labelled as *1* and *2* in accordance with their relative positions in the pore (Figure 5.2a). In Figure 5.2b the chains labelled as *2* and the terephthalate linkers have been omitted so that the bonding and spacing of the PNO groups can be shown. It can be seen that there is no twisting of the PNO groups; they all lie parallel to each other along the pores. Similarly, in Figure 5.2c the PNO groups have been omitted to show the bridging between metal centres and the cross-links between chains formed by the terephthalate linkers. This view shows that the terephthalate linkers lie perpendicular to the metal oxide chains. The low temperature structure is very similar. It has the same topology but exhibits some twisting of the terephthalate rings, associated with a slight contraction of the pores (Figure 5.3).

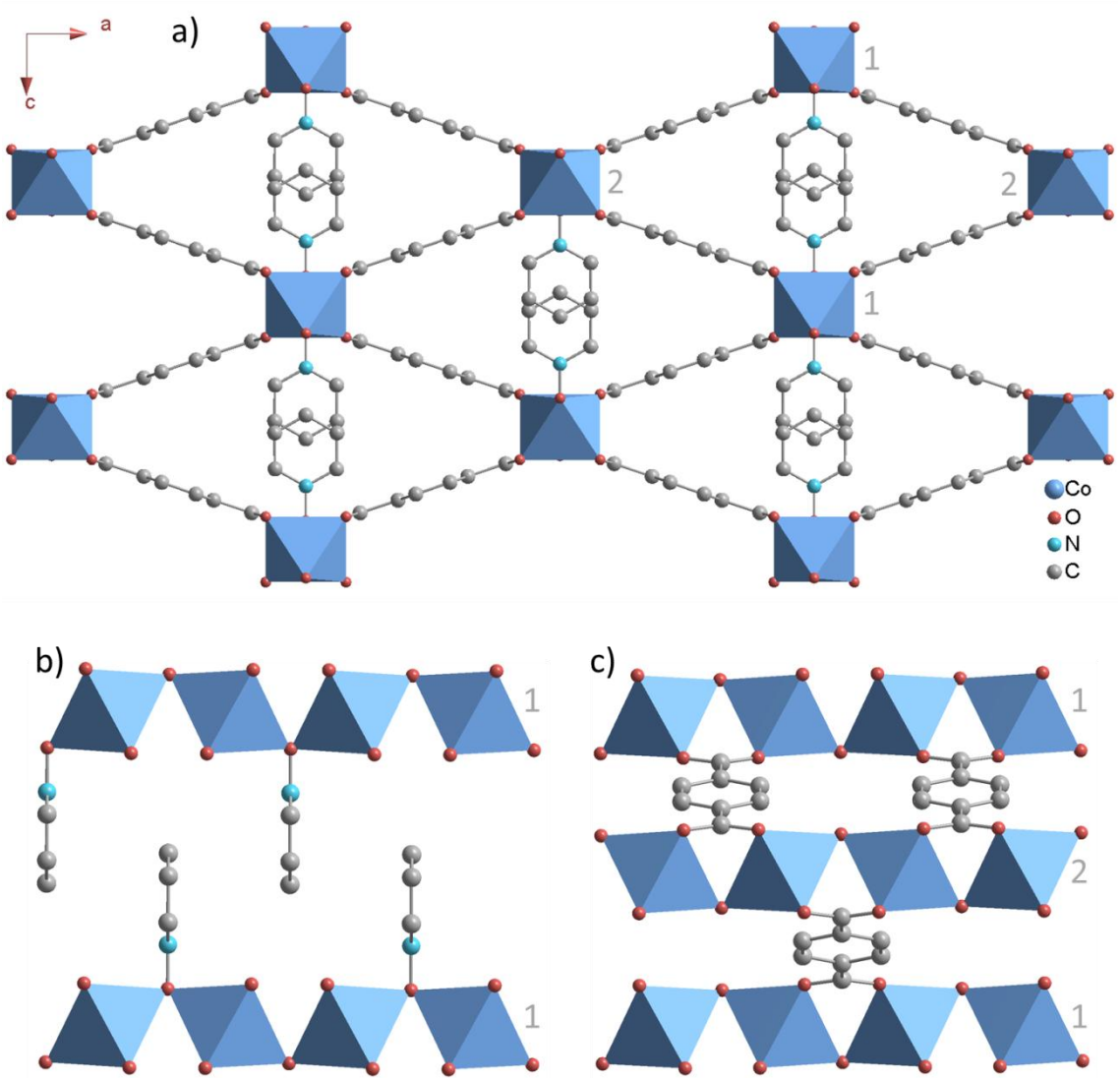

Figure 5.2: Crystal structure for Co(bdc)(PNO) determined at 293 K. a) viewed along the c-axis, b) PNO groups viewed along the a-axis and c) terephthalate groups viewed along the a-axis.

Single-crystal analysis was also performed on the partially fluorinated sample. However, the refinement was unable to identify any partial occupancy of the pyridine-*N*-oxide ligand. The unit cell volume was determined to be 1277.6(2) $Å^3$ at 120 K with monoclinic symmetry (*C2/c*). It was not possible to record single-crystal data at room temperature, therefore the unit cell volume was refined from powder XRD data recorded at room temperature; the *Imma* structure of the room temperature Co(bdc)(PNO) material was used as the starting point for the refinement, the refined unit cell volume was 1284.7(5) $Å^3$ (Figure 5.4a). Both unit cell volumes are larger than

those recorded for the corresponding pure PNO material (Table 5.1). The same trend is seen when MIL-53(Fe) is fluorinated; the fluorinated framework (1000 $Å^3$) has a slightly expanded structure compared to the hydroxylated framework (986.8 $Å^3$).[7]The distance between PNO groups can be seen in Figure 5.2a (spacing in the Co-PNO/F framework is very similar to the pure framework), the distance between rings is approximately 3.6 Å. At these distances it may be deduced that there are π-π interactions between the pyridine rings.[8] These interactions influence the pore size by "locking" the chains closer together. Therefore, the removal of some of these rings, by substitution with F^-, would disrupt these π-π interactions resulting in a slight expansion of the framework.

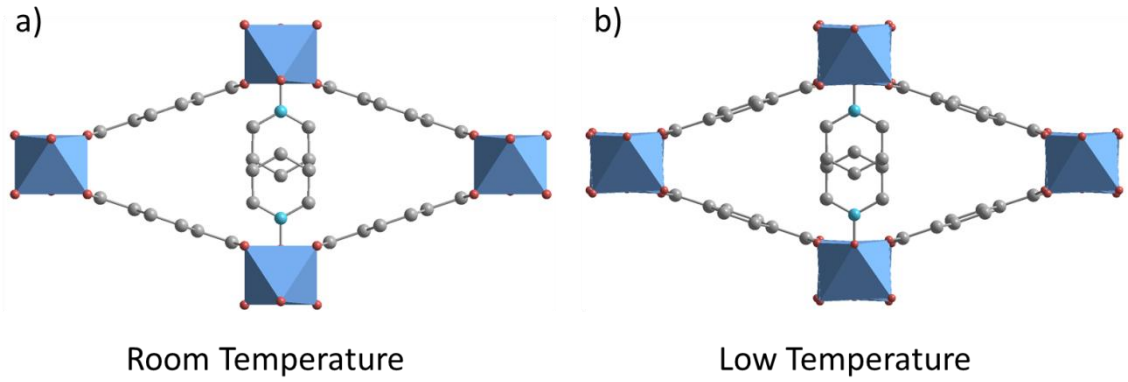

Figure 5.3: Single diamond-shaped pores showing the small differences in the room temperature and low temperature structures of Co(bdc)(PNO).

High-resolution X-ray diffraction data collected at room temperature using beamline ID31 at the ESRF were used to perform a Le Bail profile fit which confirmed that the Ni^{II} material also has a framework with orthorhombic symmetry and a unit cell volume of 1261 $Å^3$, at room temperature. The Le Bail profile fits for the fluorinated Co material and the Ni material are shown in Figure 5.4. The data for the partially fluorinated sample was collected using the laboratory D8 diffractometer.

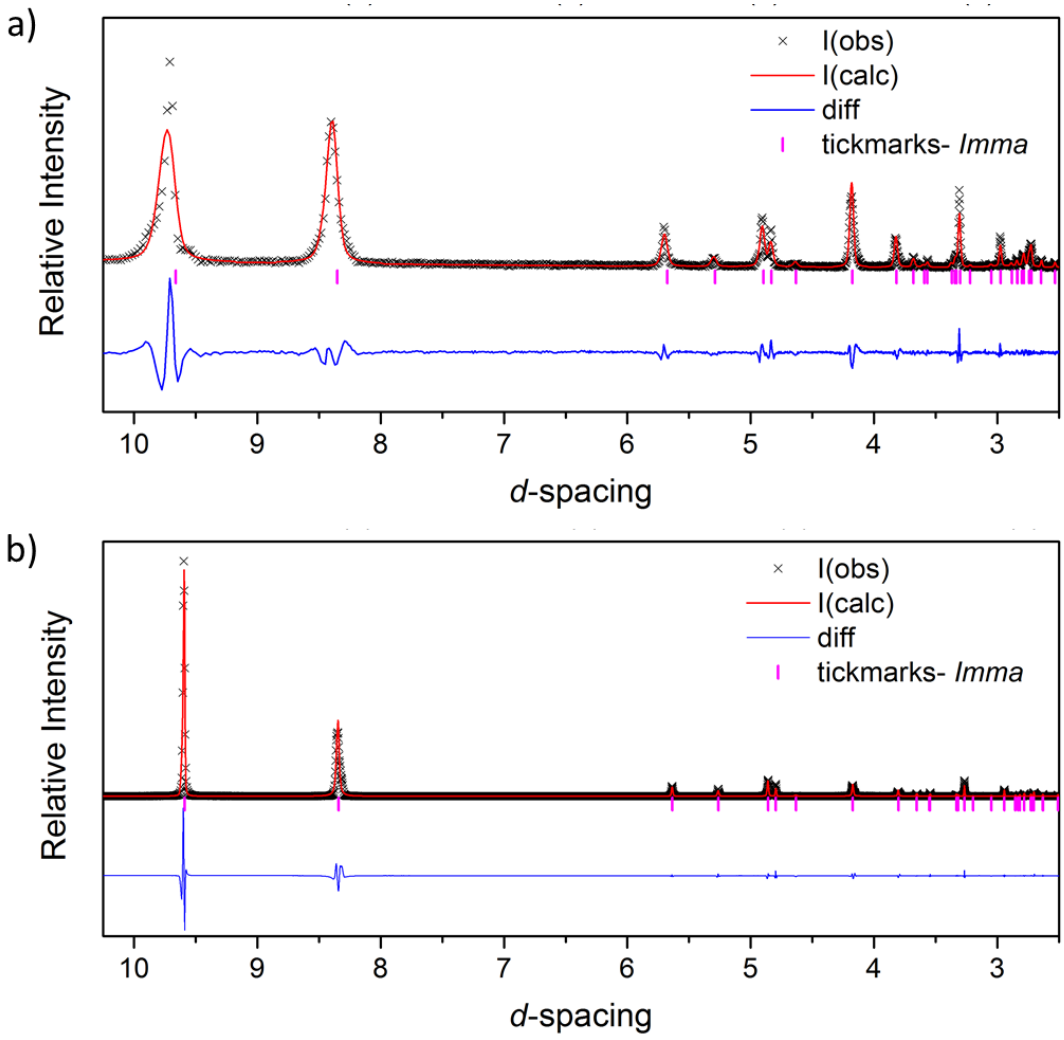

Figure 5.4: Le Bail profile fits for a) Co(bdc)(PNO/F) and b) Ni(bdc)(PNO). All data were recorded at room temperature. The wavelengths used were 1.5418 (Cu Kα1/2) and 0.7998 Å respectively.

The unit cell parameters obtained from single-crystal analysis and Le Bail profile fits for all materials detailed in this section are shown in Table 5.1.

*Table 5.1: Unit cell parameters for all new M^{II}-pyridine-N-oxide MOFs. Unit cell parameters were refined from single-crystal analysis or a Le Bail profile fit performed using powder X-ray diffraction data (**bold**).*

MOF	Space group	*a* / Å	*b* / Å	*c* / Å	β / °	*V* / Å^3
$^1Mn^{II}$	*Imma*	19.509(5)	7.376(2)	9.320(3)	90	1341.1(6)
Co^{II}	*Imma*	19.2841(15)	7.1837(7)	9.2835(9)	90	1286.1(2)
Co^{II}	*C2/c*	20.4094(13)	9.1206(5)	7.1342(4)	109.377(5)	1252.78(1
Co^{II} (F)	*C2/c*	20.4413(15)	9.2327(7)	7.1660(5)	109.147(4)	1277.6(2)
Co^{II}	***Imma***	**19.317(4)**	**7.1824(9)**	**9.260(1)**	**90**	**1284.7(5)**
Ni^{II}	***Imma***	**19.18051(9)**	**7.09935(9)**	**9.2643(1)**	**90**	**1261.51(2)**

The interest in these frameworks lay in the possibility that they may display some flexibility due to their similarities with MIL-53. To investigate if these frameworks did show any breathing behaviour, *in situ* XRD data were collected while the samples were heated to 330 °C. The graphs below show that these frameworks do not show evidence for breathing (Figure 5.5); no changes in the Bragg peak positions are seen. Above 300 °C the Bragg peaks visible in the patterns for the Co, Co/F and Mn materials decrease in intensity, this is consistent with the onset of decomposition of these materials at this temperature. The Ni material was shown to be stable up to the higher temperature of 350 °C (TG results are shown in Section 5.2.2).

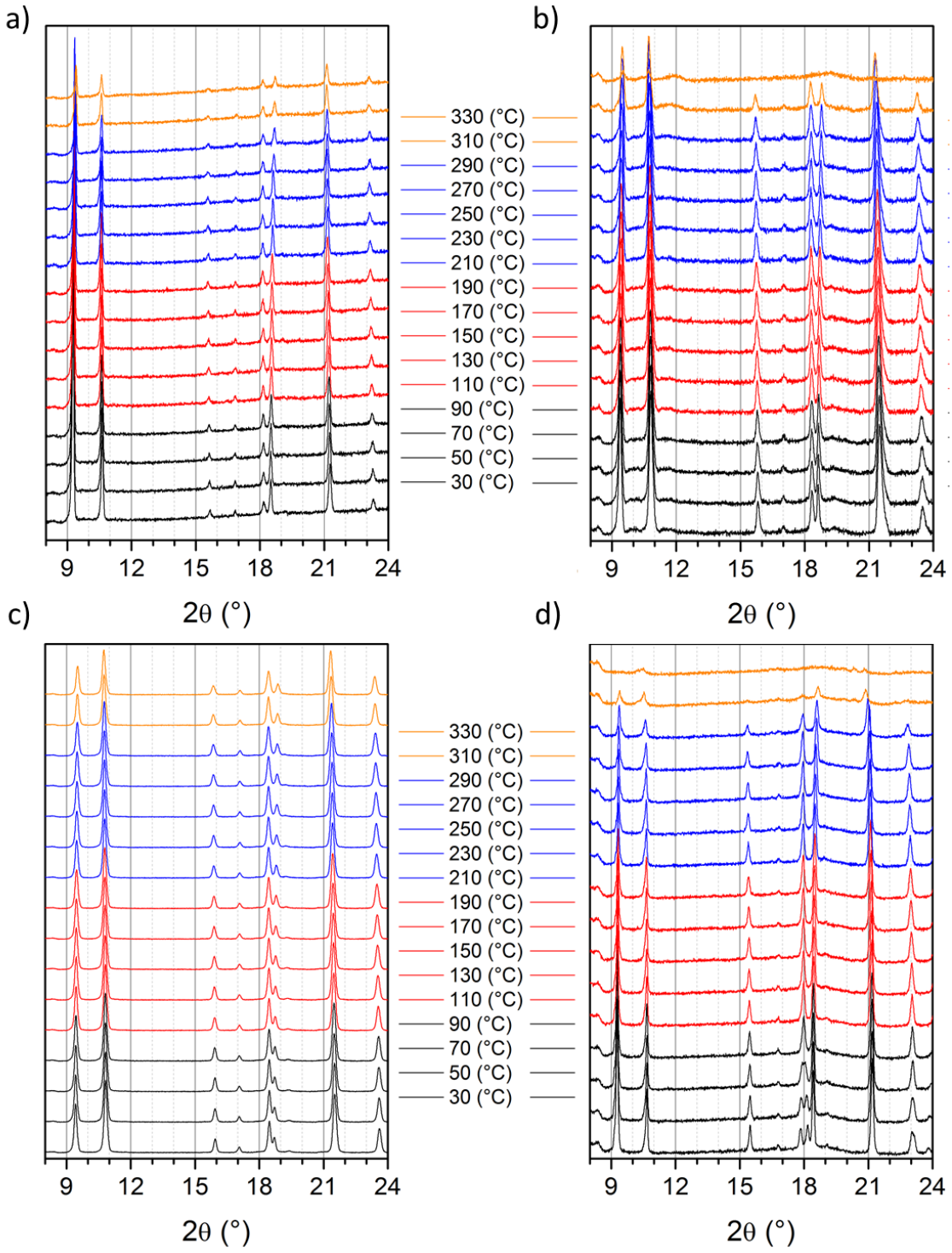

Figure 5.5: In situ XRD heating experiments for a) Co(bdc)(PNO), b) Co(bdc)(PNO)$_{0.65}$F$_{0.35}$, c) Ni(bdc)(PNO) and d) Mn(bdc)(PNO)

5.2.2 Investigations using Thermogravimetric Analysis

The original work on Mn^{II}(bdc)(PNO) reported that the framework had "no appreciable pores"[1] which is assumed to be due to the pendant PNO groups blocking any available

pore volume. Therefore, an attempt was made to remove these groups from the framework using thermal treatment. Thermogravimetry was used to investigate if there was a step in the decomposition profile that corresponded to the loss of the PNO groups. If successful then isolation of this phase would be explored.

Thermogravimetry (TG) data were collected for the PNO materials (Figure 5.6). These experiments were used to identify if the decomposition occurred in two stages. A two-stage decomposition might allow for the isolation of an intermediate phase. Inflection points in the data were used to identify if the decomposition occurred in two steps.

Figure 5.6a shows the TG data recorded for Co(bdc)(PNO). There is no evidence for occluded solvent molecules; mass loss is only seen above 200 °C. The inflection point was calculated to occur at 412 °C which corresponds to an initial percentage mass loss of 28.2%, this agrees well with the theoretical percentage mass loss of pyridine (C_5H_5N), 24.9%. The initial mass loss is assumed to be due to the loss of pyridine and not pyridine-*N*-oxide as the removal of the oxygen atom would result in the complete decomposition of the framework. The experimental percentage mass loss for the complete decomposition to Co_3O_4, 74.4%, agrees well with the theoretical percentage mass loss of 74.8%. The theoretical percentage mass losses were calculated using the empirical formula $Co(C_8H_4O_4)(C_5H_5NO)$.

TG data for Co(bdc)(PNO/F) is shown in Figure 5.6b. Similar to the Co(bdc)(PNO) framework there is no evidence for occluded guest molecules as mass loss does not occur until above 200 °C. The inflection point occurs at 403 °C, which is lower than the temperature recorded for the pure PNO material. The theoretical percentage mass losses were calculated using the molecular formula, $Co(C_8H_4O_4)(C_5H_5NO)_{0.65}(F)_{0.35}$, which was predicted from the elemental analysis results. The theoretical percentage mass loss

of C_5H_5N is 17.6% which was lower than the experimental percentage mass loss of 21.2%. This implies that there are more pyridine groups in the framework than were calculated using the elemental analysis data. The theoretical percentage mass loss expected upon complete decomposition to Co_3O_4 is 71.6% which is greater than the recorded value of 68.1%. These discrepancies indicate that the empirical formula of the fluorinated framework is not yet completely understood as the TG results provide conflicting evidence with the elemental analysis.

The data recorded for the Ni(bdc)(PNO) framework does not show evidence for occluded molecules (Figure 5.6c) neither does it show a step-wise decomposition. Mass loss begins above 300 °C where complete decomposition to NiO occurs. The percentage mass loss of 76.7% agrees well with the predicted value of 76.5%, calculated using the empirical formula $Ni(C_8H_4O_4)(C_5H_5NO)$

The TG data for the Mn(bdc)(PNO) framework were collected for comparison and is shown in Figure 5.6d. The graph shows no evidence for occluded molecules; mass loss only begins above 250 °C. The second difference graph shows that the inflection point occurs at 395 °C which corresponds to a percentage mass loss of 26.0%, which agrees well with the theoretical mass loss of pyridine, 25.2%. The step in the decomposition profile is more pronounced for this material suggesting that the second phase is temporarily stable. The theoretical percentage mass loss expected upon complete decomposition to MnO_2 is 72.3% which agrees well with the recorded value of 74.1%.

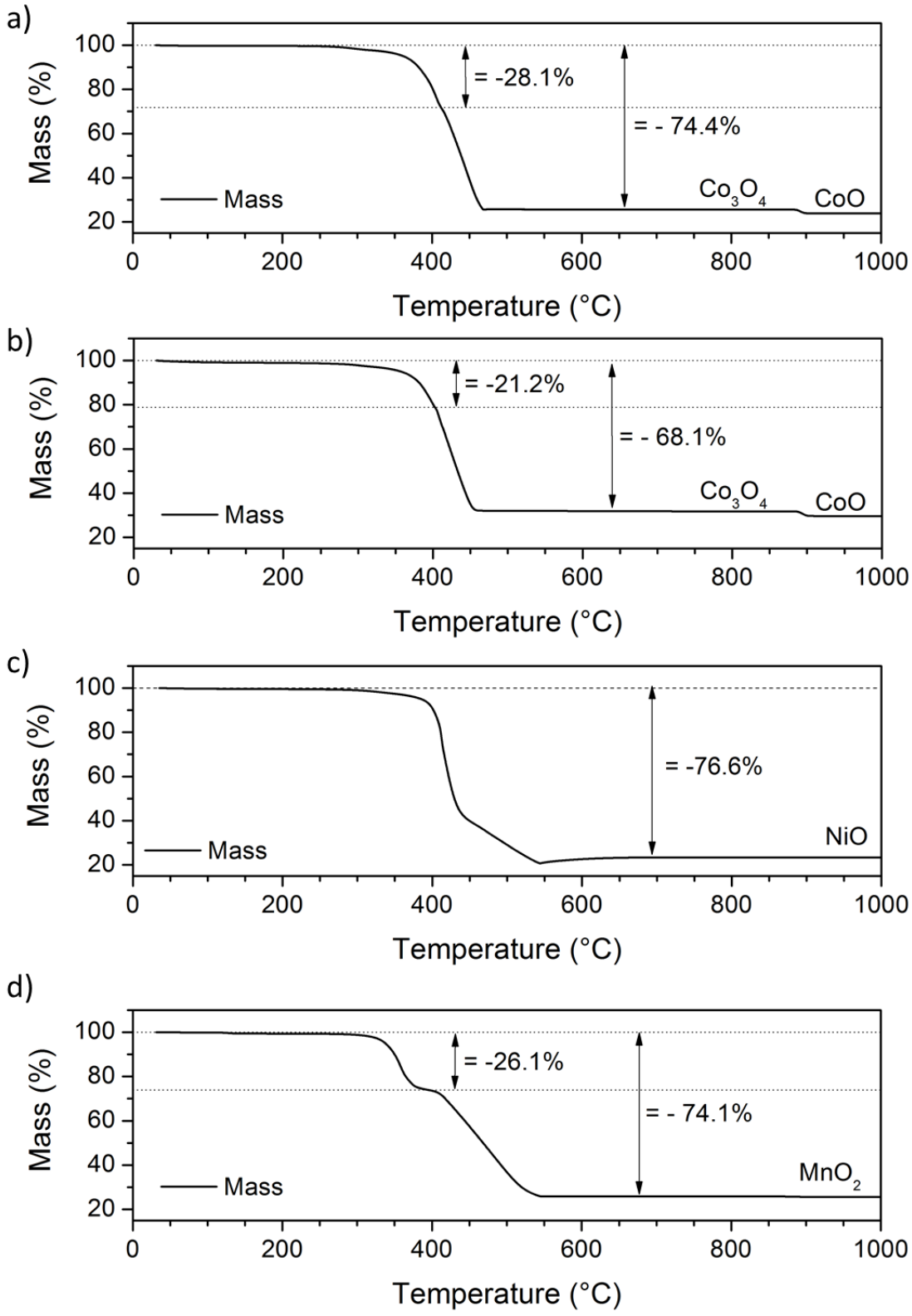

Figure 5.6: Thermogravimetry results for a) Co(bdc)(PNO), b) Co(bdc)(PNO)$_{0.65}$F$_{0.35}$, c) Ni(bdc)(PNO) and d) Mn(bdc)(PNO).

The information gained from the TGA was used to heat the Co(bdc)(PNO) and Co(bdc)(PNO/F) materials as close to the temperature that the first step occurred but without decomposing the material to Co_3O_4. Upon heating the materials *ex situ*, which are pink in colour at room temperature, they turn purple indicating a change in the environment around the Co cation. If heated below ~300 °C then the colour change was reversible, however if the material was heated for an extended period of time at this temperature then the colour change became permanent at room temperature. The colour change indicates that there was some physical or chemical change in the material. If the colour change was due to the removal of occluded/surface water molecules then we would not expect this change to become permanent at room temperature. If heating caused a change in the framework's structure then we would expect to see this using XRD and this was not the case, as was shown in the *in situ* heating experiments (Section 5.2.1). Therefore it is thought that the colour change was due to a modification in the environment of the Co octahedral which in this case could be caused by an alteration in the bonding of the pendant ligands that bridge between Co cations. Other characterisation techniques have been used to investigate this theory and the properties of these modified frameworks.

5.2.3 X-ray Absorption Near Edge Spectroscopy (XANES)

An absorption edge is defined as the characteristic wavelength at which the X-ray absorption of an element changes dramatically. Spectra recorded near this edge (XANES) can contain electronic and geometrical information about the absorbing element allowing for details such as an element's oxidation state to be elucidated.

For the samples studied in this section the spectra were recorded around the Co K-edge. Four samples were chosen to be studied using this technique: Co(bdc)(PNO) as-made,

Co(bdc)(PNO) preheated to 300 °C, Co(bdc)(PNO/F) as-made and Co(bdc)(PNO/F) preheated to 300 °C. It is important that the reference materials are chosen carefully to aid the assignment of oxidation states. The Co^{II} centres in all four samples were expected to have octahedral coordination. The Co(bdc)(PNO) *as-made* material is expected to have Co^{II} centres coordinated to six oxygen groups. The oxidation state of the *preheated to 300 °C* sample is unknown. The Co(bdc)(PNO/F) *as-made* material is expected to have a mixture of Co^{II} and Co^{III} centres where the Co^{III} centres are expected to be coordinated to four/five oxygen groups and one/two fluorine groups. The oxidation state of the *preheated to 300 °C* sample is unknown. Three reference samples were chosen: $Co(NO_3)_2 \cdot 6H_2O$, $Co(acac)_3$ and Co_3O_4. Cobalt nitrate hexahydrate has Co^{II} centres octahedrally coordinated to six oxygen atoms, making it a good comparison for the Co(bdc)(PNO)materials. Cobalt acetylacetonate has Co^{III} centres octahedrally coordinated to six oxygen groups which will provide a good comparison if oxidation of the metal centres occurs when the materials are heated to 300 °C. Cobalt oxide contains Co centres with two oxidation states; Co^{II} which are tetrahedrally coordinated to four oxygens and Co^{III} which are octahedrally coordinated to six oxygens. This material will provide a comparison for the Co(bdc)(PNO/F) material which is expected to contain Co centres with a mixture of oxidation states.

The results from the XANES data show that all four of the studied materials give very similar spectra (Figure 5.7) and agree well with the reference spectra of $Co(NO_3)_2 \cdot 6H_2O$. This would infer that all four materials only have Co^{II} centres in octahedrally coordinated environments. These results imply that the colour change of the preheated materials is not due to a change in the oxidation state of cobalt but is more likely due to minor changes in this environment such as ligand reorientation. These data also show that the expected change in oxidation state due to the presence of F^- is not

seen. There are two possible reasons for this: 1) that F^- is not bridging between Co centres as assumed, although this would disagree with the TGA and elemental analysis data and 2) that the bridging ligand is not F^- but a neutral fluorine containing species, such as HF.[9]

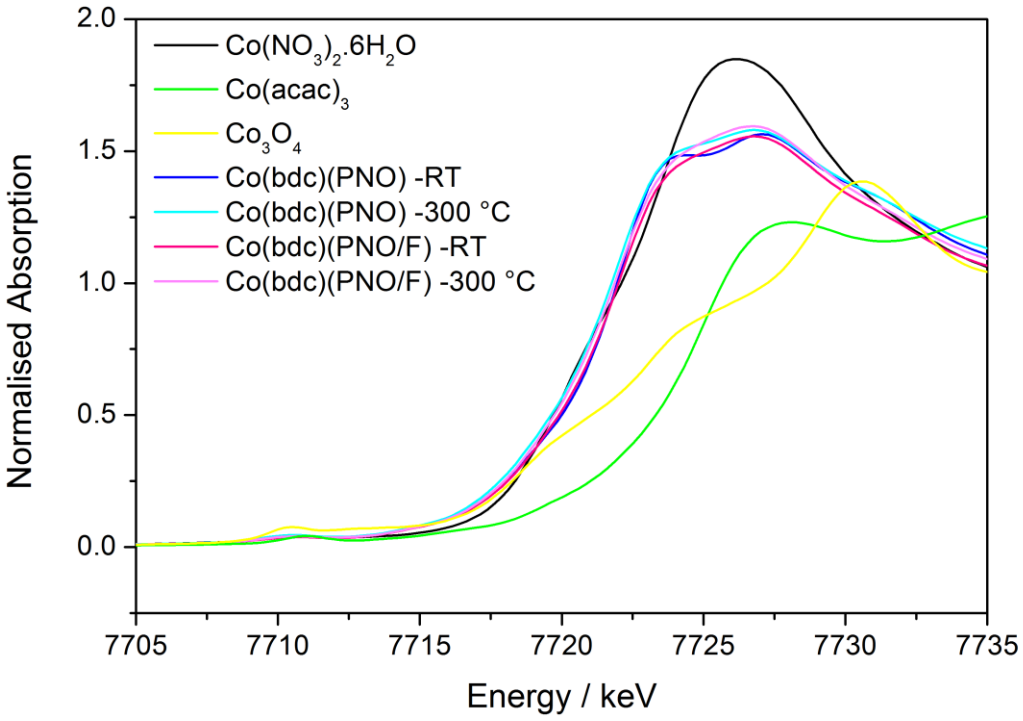

Figure 5.7: XANES data for the cobalt PNO (as-made and preheated) and cobalt PNO/F (as-made and preheated) compared with three reference materials: $Co(NO_3)_2$, $Co(acac)_3$ and Co_3O_4

5.2.4 Magnetic Studies

A Superconducting Quantum Interference Device (SQUID) magnetometer was used to investigate the magnetic properties of the M^{II}(bdc)(PNO) materials (M = Co, Mn, Ni) and the partially fluorinated cobalt material. The magnetic properties of the samples were studied as a function of temperature and under magnetic field up to 5 Tesla. Figure 5.8 shows the temperature dependence of these four materials under an applied magnetic field of 0.01 T. As the temperature decreases the susceptibilities increase; this is typical of a paramagnetic material. However the Mn, Ni and fluorinated Co materials

all show a maximum in the susceptibility, which is a signature of the onset of antiferromagnetic order. The distinct maximum visible at low temperature for the fluorinated Co material was seen at approximately 15 K in both the zero field cooled and the field cooled data therefore this unusual feature is assumed to be real and not just an artefact from the instrument.

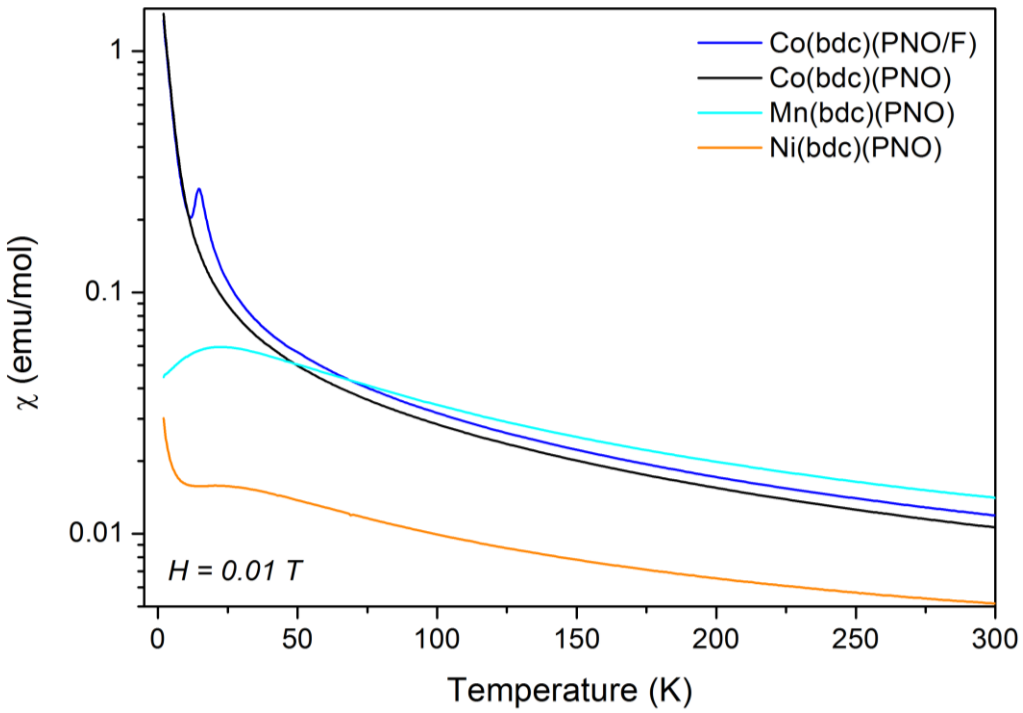

Figure 5.8: Magnetic susceptibility as a function of temperature for the M^{II}(bdc)(PNO) materials. Applied field = 0.01 Tesla.

Analysis was performed using Equation 5.1 which gave the Curie constant, C, and the Curie-Weiss temperature, θ_w, for each material (Table 5.2). The mean effective moment, μ_{eff}, can also be deduced from these data; these values are shown to be in good agreement with those quoted by Kittel for octahedral metal centres.[10] The mean effective moment indicates the number of unpaired electrons per metal centre therefore these values show that the Mn- and Co-containing materials have a high-spin electron configuration. The Curie-Weiss temperature gives an idea of the strength of the

exchange interaction between magnetic ions in the paramagnetic state, the weakest interaction seen in these data is for the pure Co material.

$$\chi(T) = \chi_0 + \frac{C}{(T - \theta_w)}$$

Equation 5.1

Table 5.2: Analysis of magnetic data: Curie-Weiss temperature (K), Curie constants (in CGS units) deduced from $\chi(T) = \chi_0 + C/(T - \theta w)$ fits. The deduced effective moments (in μ_B) are compared with typical values.[10]

Metal (M^{II}) ions	θ_w/ K	C	μ_{eff}/ μ_B	μ_{eff}/ μ_B
	Curie-Weiss Temperature	Curie Constant	Effective moment per M (deduced)	Typical values from Kittel
Co	-20.00	3.41	5.23	4.80
Co (with F^-)	-20.97	3.82	5.53	4.80
Ni	-100.00	1.98	3.98	3.20
Mn	-40.06	4.78	6.18	5.90

Figure 5.9 shows the magnetism of the M^{II}(bdc)(PNO) materials as a function of applied field at two temperatures: 300 K and 5K. At 300 K all four materials are paramagnetic (Figure 5.9a); the plots are linear with positive gradients. However, at 5 K the two cobalt materials show some ferromagnetic behaviour where magnetic saturation is almost reached at 5 T and a small coercivity is present. In contrast, the Mn and Ni materials show much lower magnetisation with a linear relationship.

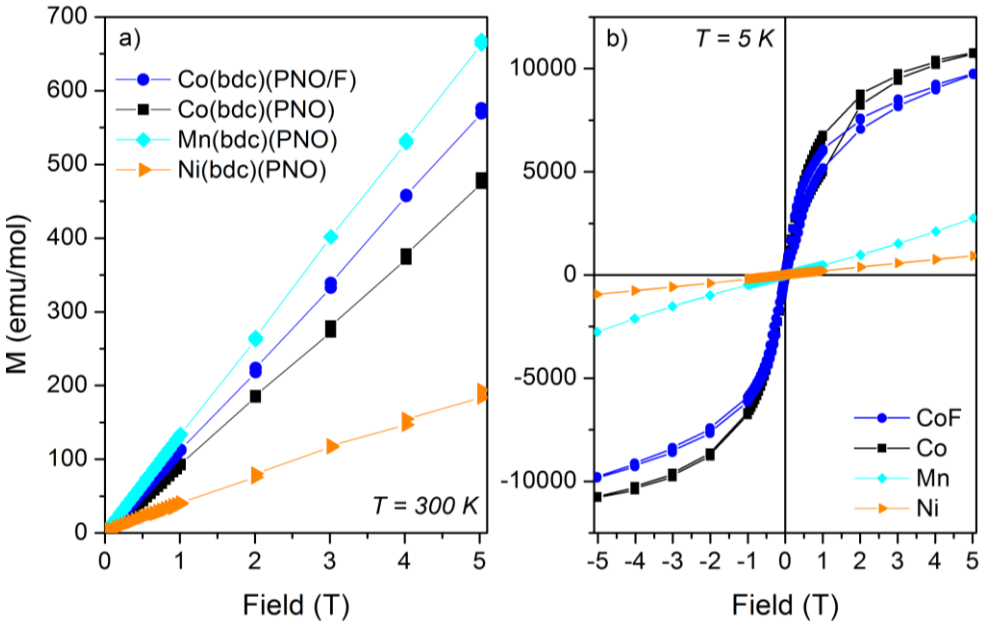

Figure 5.9: Magnetism versus magnetic field recorded at two temperatures a) 300 K and b) 5 K.

The low field region of the data recorded at 5 K is shown in Figure 5.10 for the two cobalt materials. This graph shows that the partially fluorinated cobalt material has some remanent magnetisation at zero field. This behaviour is more typical of a ferromagnetic material.

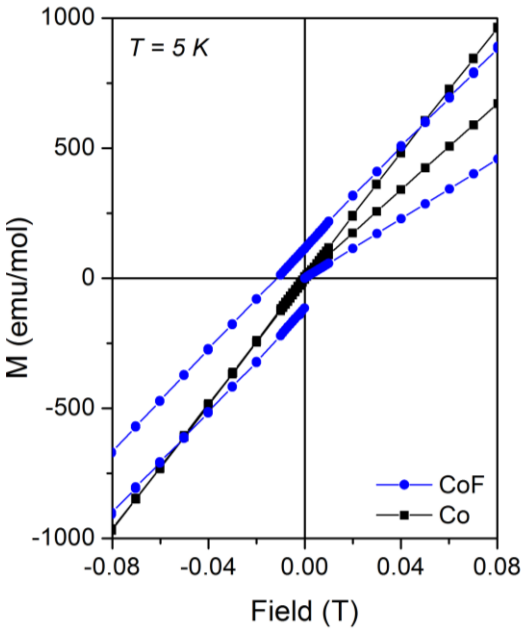

Figure 5.10: Low field region of the magnetic field dependence data recorded at 5 K for Co(bdc)(PNO) and Co(bdc)(PNO/F)

Further investigation of the behaviour of the cobalt materials is needed as the response of Co^{II} at 5 K in the field dependence studies is not typical of a Langevin Co^{II} paramagnetic response.[11] One possible explanation for the ferromagnetic behaviour seen at low temperatures is interchain interactions.

The characterisation of these new materials shows that the Co and Ni analogues of the Mn^{II}(bdc)(PNO) have been successfully synthesised. Powder X-ray diffraction studies were used to determine the unit cell parameters in the absence of singe-crystal data and thermodiffraction data were used to show that the frameworks did not show evidence for structural flexibility upon heating. The oxidation state of the cobalt centres in the non-fluorinated and fluorinated materials were shown to be the same: +2. The magnetic studies revealed a difference in the magnetic behaviour of the fluorinated material however the cause of this is unknown. Further investigations of this material are needed to understand fully the effect of incorporating fluorine into the framework.

5.3 Mixed-Metal-Organic Frameworks

The pyridine *N*-oxide frameworks described in Section 5.2 were synthesised using three different metal cations: Mn,[1] Co and Ni. All three cations gave the same structure but with decreasing unit cell volumes, as expected based on the decrease in M^{II} radii going across the 1^{st} row of the transition metals. Due to the similarities in the synthesis conditions and the structures of the M^{II}(bdc)(PNO) materials it was theorised that the synthesis of mixed-metal frameworks may be possible. Mixed-metal frameworks are important for real industrial applications as they would provide sites with different reactivities within the same material. This type of modification has been shown to be advantageous for adsorption or catalytic processes, as described in Chapter 1. Different ratios of Co and Mn/Ni were experimented with: Co:Mn- 25:75, 50:50 and 75:25 and

Co:Ni- 50:50 (the ratio shown is the molar ratio of metal salts at the start of the reaction).

5.3.1 X-ray Diffraction Studies

If a true mixed-metal framework can be synthesised without changing the topology of the structure then the unit cell volumes of each framework should follow a trend which corresponds to the ionic radii of the individual cations. XRD data provides an indication of the average structure therefore as the average of the ionic radii decreases the unit cell volume is also expected to decrease.

The combinations 25:75 and 75:25 (Co:Mn) gave products that were suitable for single-crystal analysis. The data showed that the material had the same topology as the pure metal frameworks, and showed the same change in symmetry at low temperatures, but with a slightly altered unit cell volume. Due to the similarity of the electron density of Co and Mn X-ray diffraction cannot distinguish easily between the two metal centres. Therefore, distribution of the metal centres in the final product is unknown. The other mixed-metal materials gave crystalline powders which had similar PXRD patterns, indicating that they have formed frameworks with the same topology. PXRD patterns were either recorded with a laboratory X-ray diffractometer using long data collection or with the high-resolution beamlines, I11 at the DIAMOND light source in Oxfordshire or ID31 at the ESRF in Grenoble. For all powder patterns, the Le Bail profile fit was performed (Figure 5.11) and the lattice parameters of the unit cell were refined (Table 5.3). The orthorhombic space group, *Imma*, was used for all materials. The XRD patterns have been plotted in *d*-spacing so that the graphs are comparable as each instrument that was used for this characterisation operates with a different wavelength.

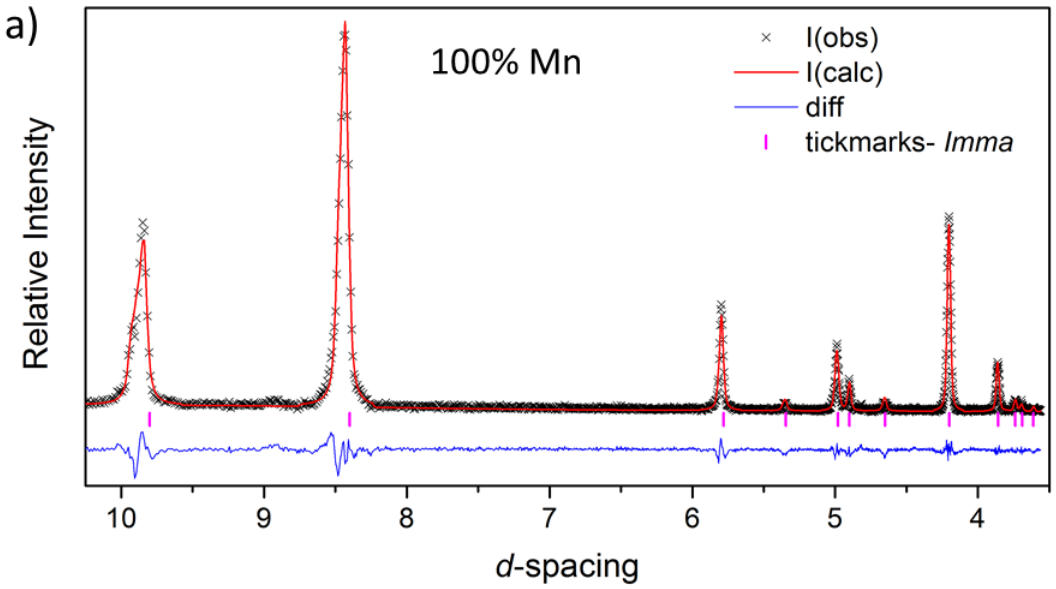
a)
100% Mn
I(obs)
I(calc)
diff
tickmarks- Imma
Relative Intensity
10
9
8
7
6
5
4
d-spacing

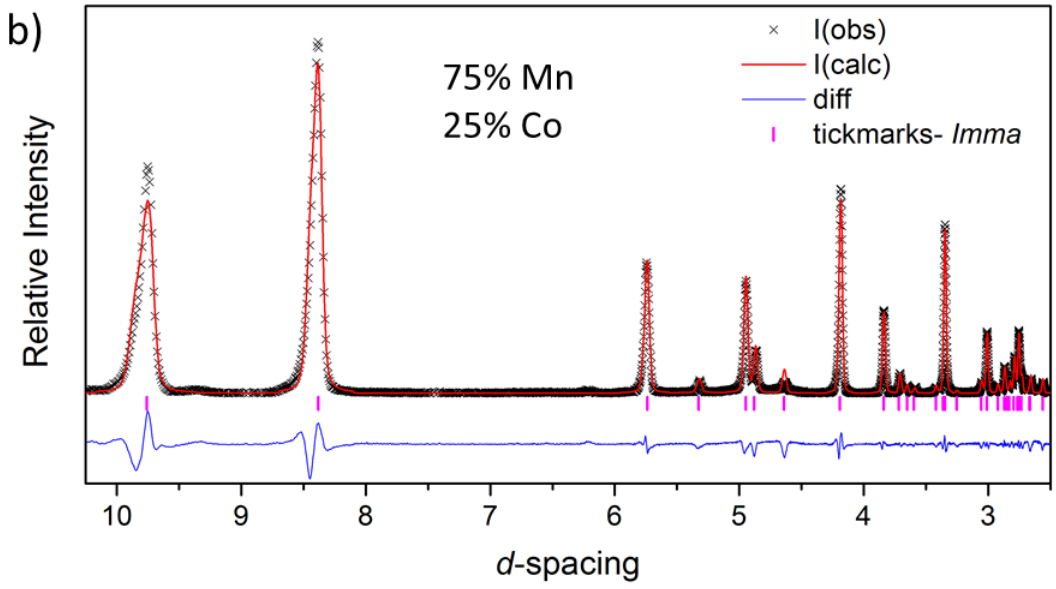
b)
75% Mn
25% Co
I(obs)
I(calc)
diff
tickmarks- Imma
Relative Intensity
10
9
8
7
6
5
4
3
d-spacing

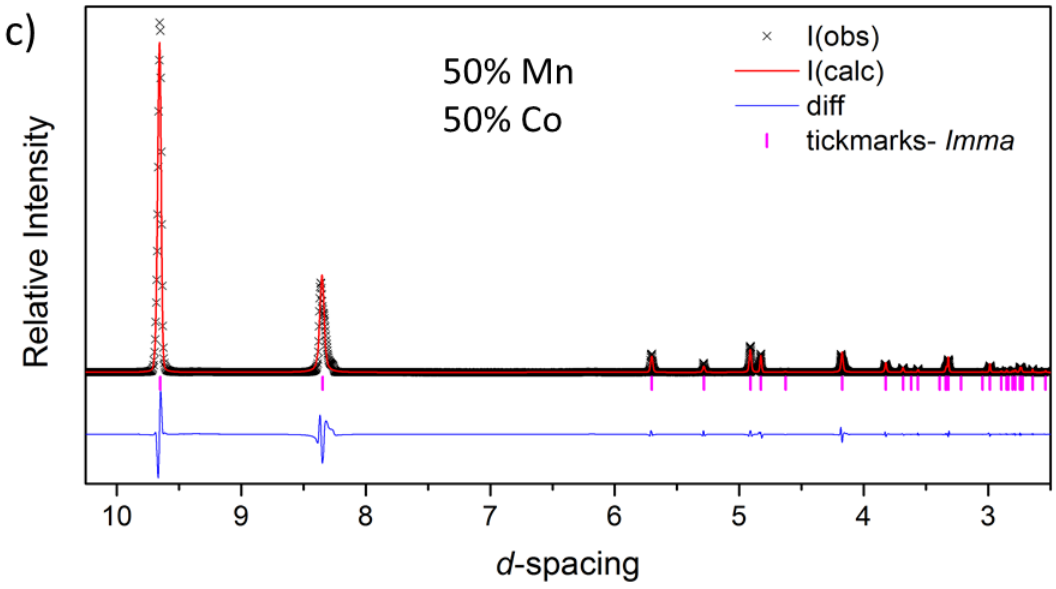
c)
50% Mn
50% Co
I(obs)
I(calc)
diff
tickmarks- Imma
Relative Intensity
10
9
8
7
6
5
4
3
d-spacing

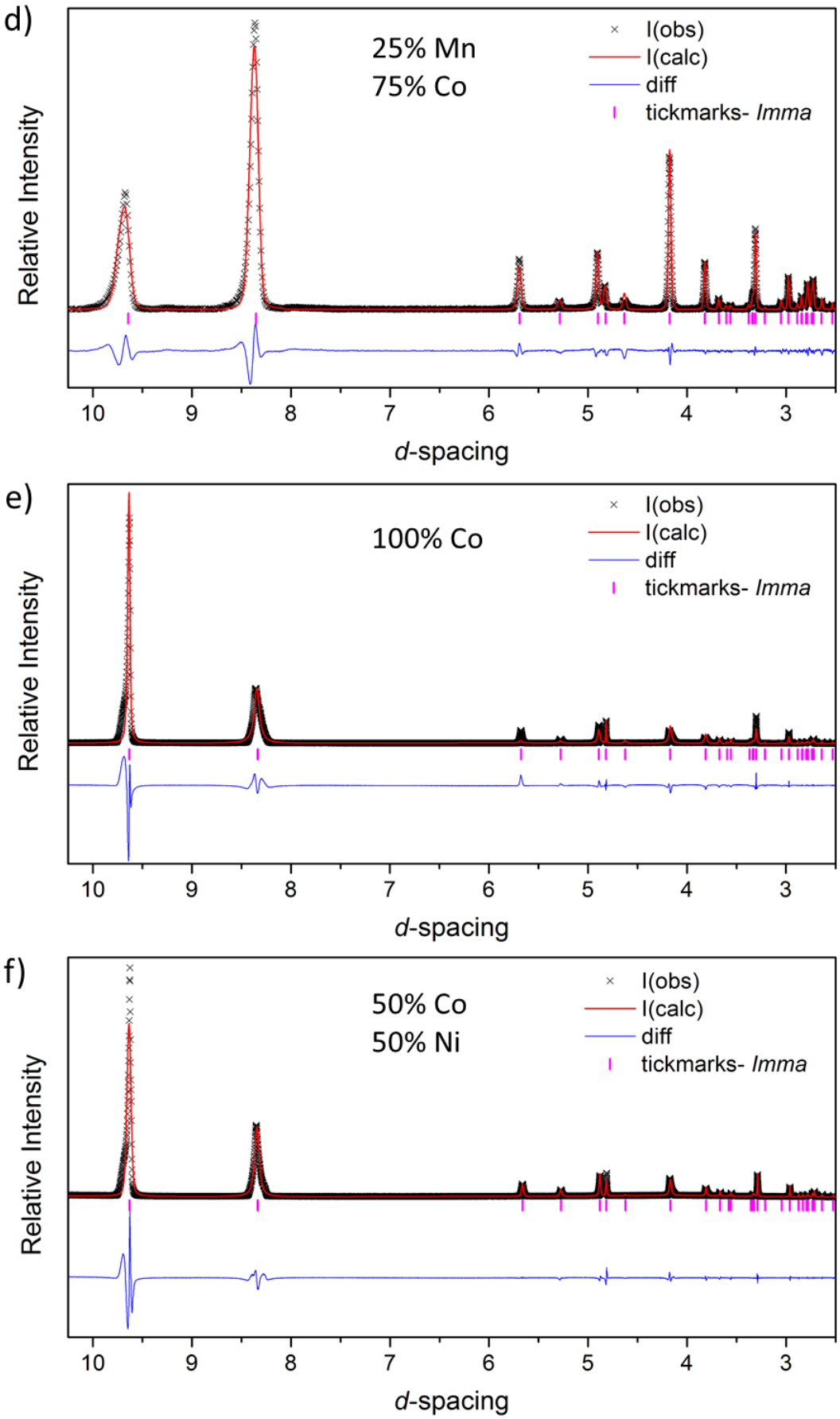
d)
25% Mn
75% Co
I(obs)
I(calc)
diff
tickmarks- Imma
Relative Intensity
10
9
8
7
6
5
4
3
d-spacing
e)
100% Co
I(obs)
I(calc)
diff
tickmarks- Imma
Relative Intensity
10
9
8
7
6
5
4
3
d-spacing
f)
50% Co
50% Ni
I(obs)
I(calc)
diff
tickmarks- Imma
Relative Intensity
10
9
8
7
6
5
4
3
d-spacing

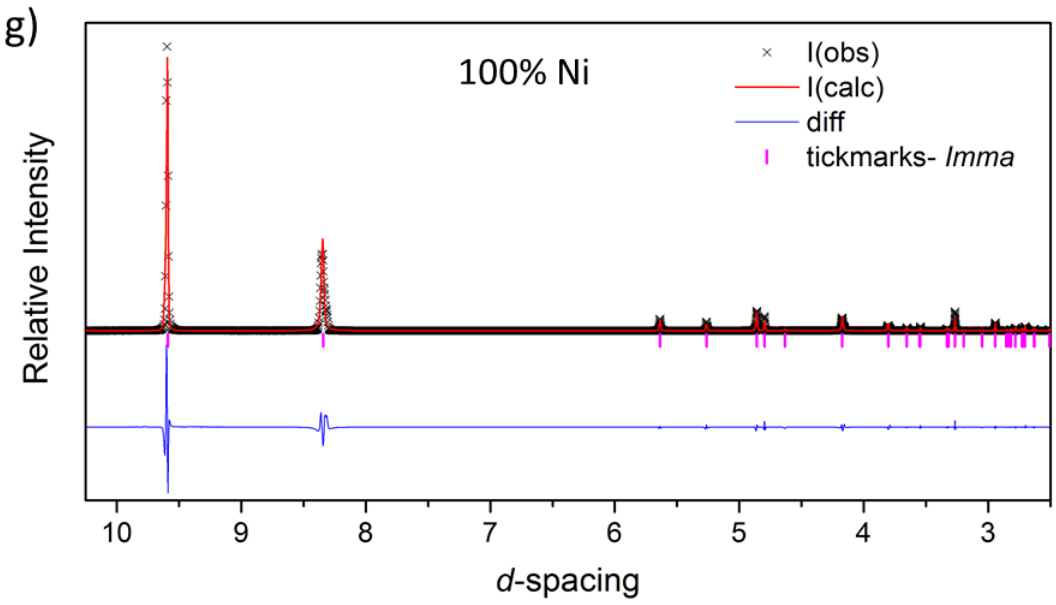

Figure 5.11: PXRD Le Bail profile fits for a) Mn(bdc)(PNO), b)$Mn_{0.75}Co_{0.25}$(bdc)(PNO), c) $Mn_{0.5}Co_{0.5}$(bdc)(PNO), d) $Mn_{0.25}Co_{0.75}$(bdc)(PNO), e) Co(bdc)(PNO), f) $Ni_{0.5}Co_{0.5}$(bdc)(PNO), and g) Ni(bdc)(PNO). Data were recorded using various X-ray diffractometers as indicated in the text.

The differences in the relative intensities of the first two peaks in the graphs shown in Figure 5.11 are due to preferred orientation. Graphs a, b and d were recorded using a fixed flat holder whereas the c, e, f and g were recorded in capillaries which are constantly spinning; removing the effects of preferred orientation.

To investigate whether the products were genuine mixed-metal frameworks, rather than just a mixture of two phases, a test experiment was performed. A sample containing 50% Co(bdc)(PNO) and 50 % Mn(bdc)(PNO) was created by mixing together the two pure materials to make a physical mixture. The resulting PXRD pattern, shown in Figure 5.12, highlights that the two different cells can be distinguished; the splitting of the peaks indicates the presence of two materials with different unit cells. The peaks appearing at lower angles belong to the larger unit cell of the Mn framework.

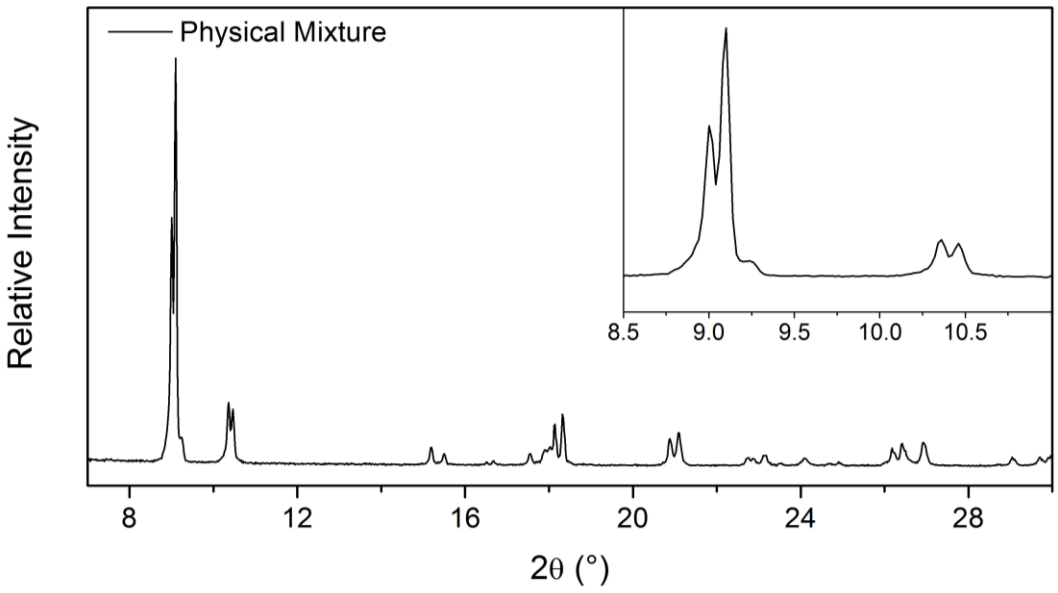

Figure 5.12: XRD pattern of the physical mixture of Co(bdc)(PNO) (50%) and Mn(bdc)(PNO) (50%)

The XRD pattern of the physical mixture verifies that the XRD patterns recorded for the mixed-metal frameworks show only a single unit cell. This data, along with the observation of the trend in the colour change of the materials (Figure 5.13), gives evidence for the conclusion that the mixed-metal materials do contain two different metals; the colour change provides evidence that the single unit cell is not a consequence of only one metal coordinating with the organic linkers and the other remaining in solution, and the purity of the colours would suggest genuine single phases.

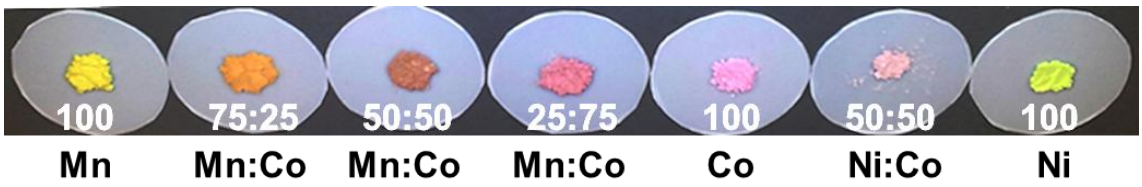

Figure 5.13: Colour change across the series of pure and mixed-metal materials.

Elemental analysis was recorded for the pure- and mixed-metal materials and the experimental and predicted results are shown in

Table 5.3. Analysis of the metal content of the mixed-metal materials shows a lower percentage of Mn than expected from the ratios used in the synthesis. Slower reaction kinetics of Mn^{II} compared to Co^{II} is one possible explanation for this result. The metal composition of the mixed-metal materials was calculated to reflect the elemental analysis results and these are shown in Table 5.3. The unit cell parameters from the individual Le Bail fits are also shown in the table, the lattice parameters for the mixed-metal materials show a decrease from pure Mn to pure Co and from pure Co to pure Ni. This is consistent with the change in ionic radii, which decrease across the 1^{st} row transition metals *i.e.* Mn^{II}> Co^{II}> Ni^{II}.

Table 5.3: Predicted and experimental elemental analysis results for the mixed-metal materials. The unit cell parameters, obtained from a Le Bail profile fit using the orthorhombic Imma space group, for all PNO frameworks are shown. XRD data were recorded at room temperature.

Metal Content (reagent ratio)	Expected CHN and M content (%)	**Experimental CHN and M content (%)**	Metal Content (elemental analysis ratio)	Expected CHN and M content (%)	*a* / Å	*b* / Å	*c* / Å	*V* / Å^3
Mn	-	-	-	-	19.601(1)	7.3805(7)	9.2986(4)	1345.2(2)
$Co_{0.25}Mn_{0.75}$	Co: 4.68 Mn: 13.07 C: 49.54 H: 2.88 N: 4.45	**Co: 6.48** **Mn: 11.26** **C: 48.24** **H: 2.85** **N: 4.46**	$Co_{0.35}Mn_{0.65}$	Co: 6.48 Mn: 11.32 C: 49.48 H: 2.88 N: 4.44	19.515(2)	7.3010(5)	9.2818(6)	1322.5(2)
$Co_{0.50}Mn_{0.50}$	Co: 9.32 Mn: 8.69 C: 49.39 H: 2.87 N: 4.43	**Co: 11.88** **Mn: 6.58** **C: 47.09** **H: 3.04** **N: 4.20**	$Co_{0.64}Mn_{0.36}$	Co: 11.91 Mn: 6.24 C: 49.30 H: 2.86 N: 4.42	19.3038(1)	7.2376(1)	9.2560(1)	1293.18(3)

$Co_{0.75}Mn_{0.25}$	Co: 13.94 Mn: 4.33 C: 49.23 H: 2.86 N: 4.42	**Co: 15.68** **Mn: 2.62** **C: 47.94** **H: 2.96** **N: 4.43**	$Co_{0.84}Mn_{0.16}$	Co: 15.59 Mn: 2.77 C: 49.17 H: 2.86 N: 4.41	19.287(1)	7.2062(4)	9.2662(6)	1287.8(2)
Co	C: 49.08 H: 2.85 N: 4.40	**C: 47.36** **H: 2.58** **N: 4.67**	-	-	19.2622(2)	7.1883(2)	9.2448(3)	1280.07(5)
$Co_{0.50}Ni_{0.50}$	Co: 9.27 Ni: 9.23 C: 49.09 H: 2.85 N: 4.41	**Co: 9.16** **Ni: 9.29** **C: 48.11** **H: 2.81** **N: 4.50**	$Co_{0.50}Ni_{0.50}$	-	19.2586(1)	7.1573(10)	9.2451(2)	1274.34(2)
Ni	C: 49.11 H: 2.85 N: 4.41	**C: 47.57** **H: 2.83** **N: 4.77**	-	-	19.18051(9)	7.09935(9)	9.2643(1)	1261.51(2)

The relationship of the unit cell parameters between each series of mixed-metal MOFs, Co:Mn and Co:Ni, is shown in Figure 5.14. The dashed lines indicate the expected values based on Vegard's law, which predicts a linear relationship between crystal lattice parameters and the concentration of the constituent components. The measured metal content is shown in these graphs. Good agreement can be seen, which confirms the results of elemental analysis that showed the Mn^{II} content to be lower than expected. It is noteworthy that the change in lattice parameters with changing Co content is not isotropic across each series: the largest percentage change is seen for *b* (> 3% for Co:Mn and > 1% for Co:Ni), which corresponds to the inorganic chain axis and is therefore most affected by the M^{II}–O distance. Smaller percentage changes are seen for *a*, which is determined by the geometry of the bdc linkers and is less dependent on the M^{II}–O distance. The changes in the *c* parameter are very small and can be considered as constant, allowing for discrepancies due to experimental errors, across the two series.

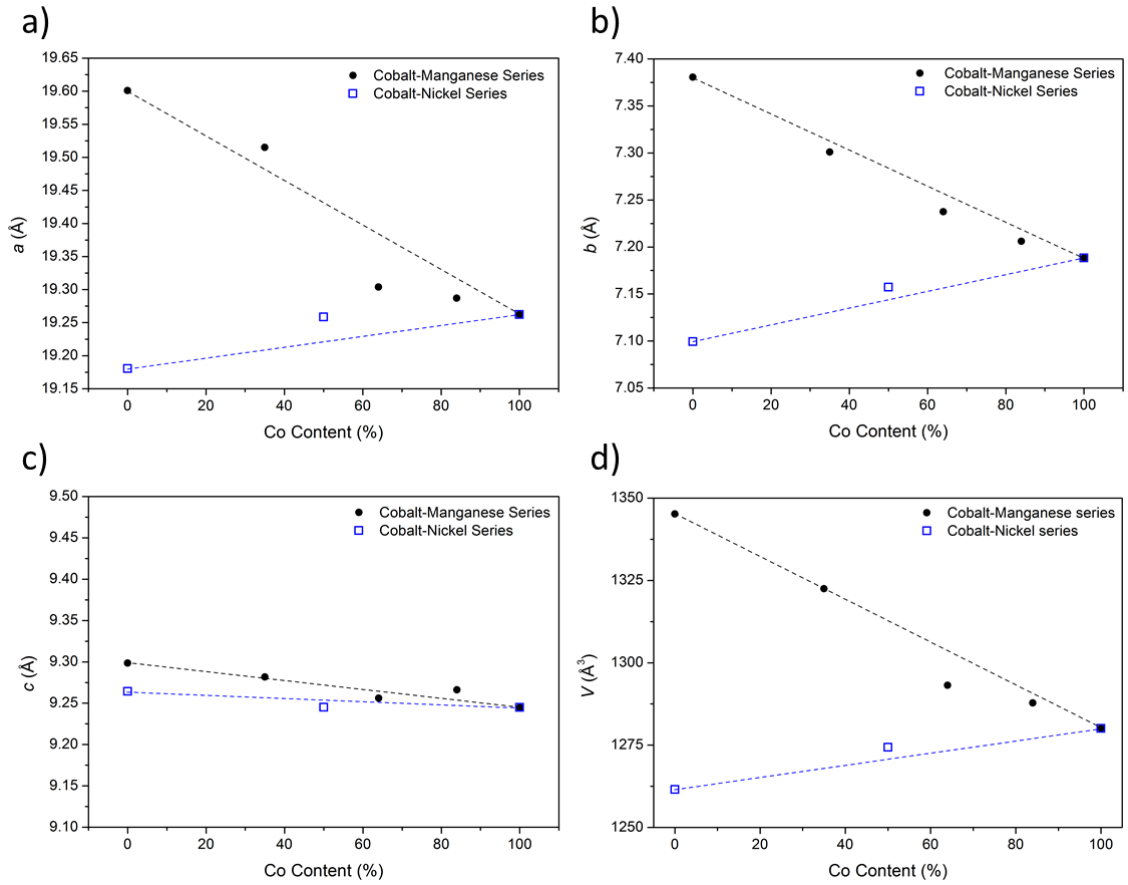

Figure 5.14: Calculated Le Bail volumes as a function of increasing cobalt content. The percentage cobalt content calculated from elemental analysis has been used in this graph.

5.3.2 Thermogravimetric Analysis

Thermogravimetric analysis was performed for the mixed-metal samples; the data for the pure metal samples were presented in Section 5.2.2. As before, the inflection points were calculated to identify the mass loss that corresponds to the step in the data and comparisons have been made with predicted mass losses. The ratios determined from elemental analysis were used for these calculations.

Figure 5.15a, b and c shows the TG data for the three Co/Mn mixed frameworks; the calculated metal ratios for these materials are, 84:16, 64:36 and 35:65. All of the samples show very similar decomposition profiles; there is no evidence for occluded

molecules and the decomposition occurs in a two stages. The percentage mass loss of the first step was found to be 26.1%, 22.0% and 23.6% respectively. These agree well with the predicted mass loss of C_5H_5N; 24.9%, 25.0% and 25.1% respectively. Complete decomposition to a mixture of metal oxides, Co_3O_4 and MnO_2, was seen above 400 °C for each sample. The total percentage mass losses were recorded as 74.4%, 73.8% and 74.1% respectively. These also agree well with the calculated values of 74.4%, 73.9% and 73.2% respectively.

The TG data for $Co_{0.50}Ni_{0.50}$(bdc)(PNO) is shown in Figure 5.15d. The decomposition profile is similar to the observed profile for the pure Ni sample; there is no evidence for occluded molecules and the decomposition occurs in only one step. The onset of complete decomposition of the framework, to a mixture of Co_3O_4 and NiO, is seen above 300 °C. The percentage mass loss of this step was found to be 71.9% which agrees well with the calculated percentage mass loss of 75.6%.

The two-step decomposition seen for the Co/Mn samples is the same as was seen for the single metal samples; the sample cannot be isolated after the first mass loss. The loss of the framework pyridine pendant ligands leads to the decomposition of the framework.

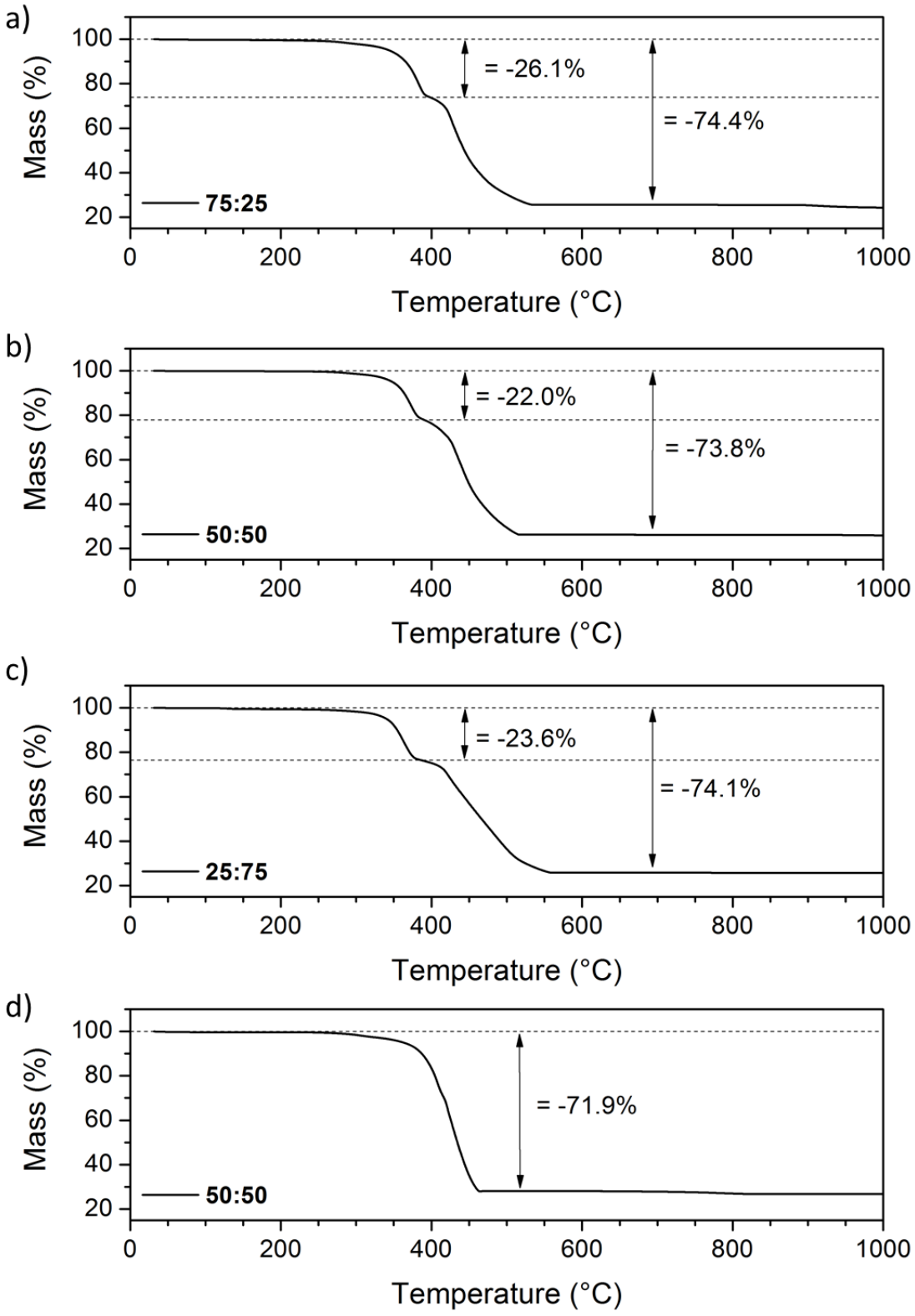

Figure 5.15: Thermogravimetry data for a) $Co_{0.75}Mn_{0.25}$(bdc)(PNO), b) $Co_{0.5}Mn_{0.5}$(bdc)(PNO), c) $Co_{0.25}Mn_{0.75}$(bdc)(PNO) and d) $Co_{0.5}Ni_{0.5}$(bdc)(PNO)

5.3.3 Magnetic Studies

A Superconducting Quantum Interference Device (SQUID) magnetometer was used to perform temperature and magnetic field dependence experiments. The mixed-metal frameworks were studied and the results of the parent frameworks are shown again for comparison. Figure 5.16 shows the magnetisation as a function of temperature under an applied magnetic field of 0.01 T. All the materials show paramagnetic behaviour at high temperatures. Although the Ni^{II} and Mn^{II} parent frameworks exhibit evidence for some antiferromagnetic ordering at low temperatures, as described in Section 5.2.4, the mixed frameworks are dominated by the response of Co^{II} and only exhibit paramagnetic behaviour.

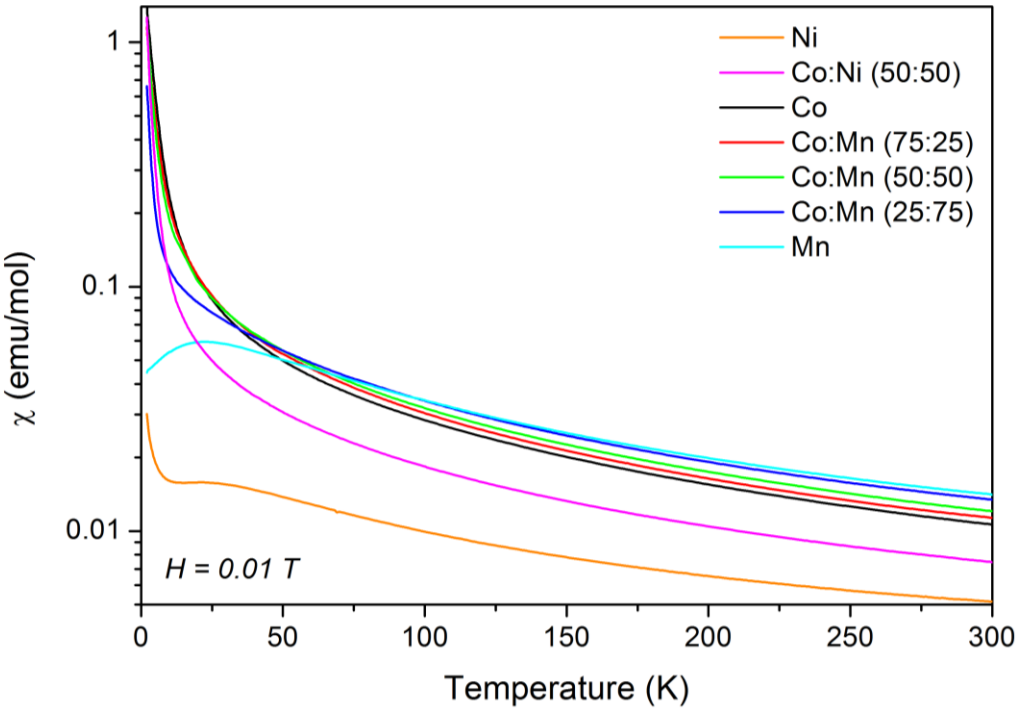

Figure 5.16: Magnetic susceptibility, χ, as a function of temperature for the mixed-metal materials. Applied magnetic field = 0.01 T.

Figure 5.17a shows the magnetisation versus applied field recorded at 300 K. The mixed-metal materials are paramagnetic and the magnetisation of each sample is between that of the two respective parent materials. The field dependence experiment

was repeated at 5 K; the mixed-metal materials are dominated by the response of Co^{II} as they all show some antiferromagnetic behaviour. The mixed-metal materials do not reach the same level of saturation at 5 T as the parent Co^{II} material and the small amount of coercivity seen for these materials decreases with decreasing cobalt content.

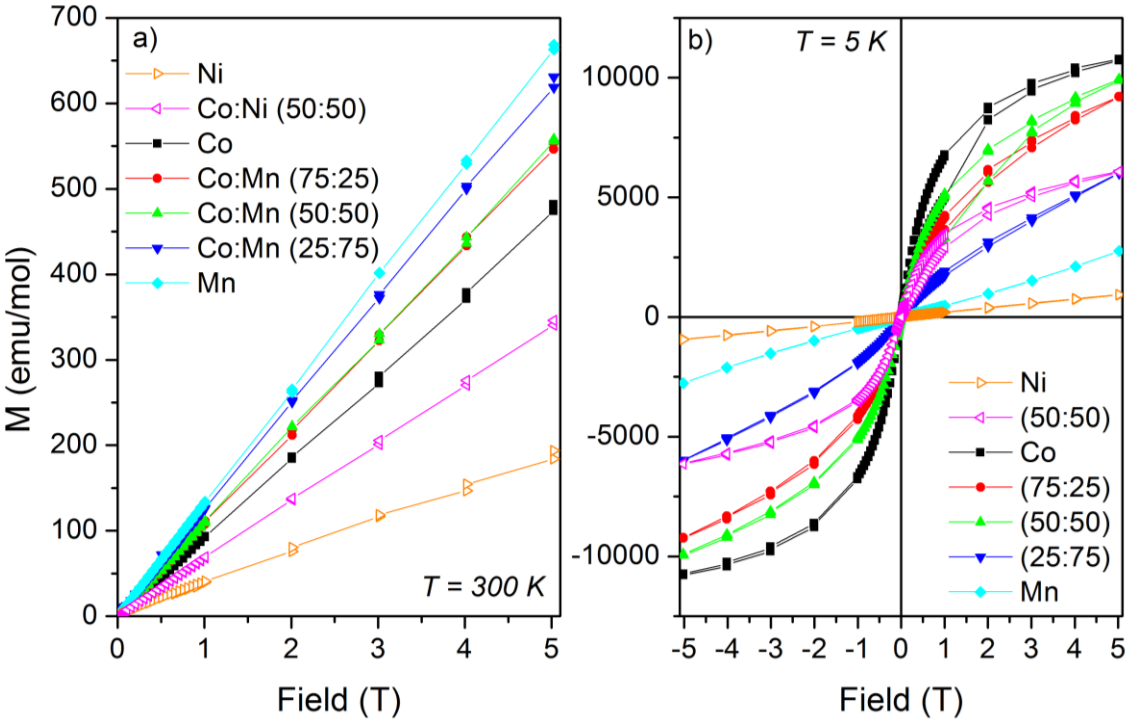

Figure 5.17: Magnetisation versus magnetic field recorded at two temperatures a) 300 K and b) 5 K.

These magnetic studies of the mixed-metal materials were performed to investigate the interactions between the two magnetic centres. Further investigations are needed as the results presented above were unable to provide information about the distribution of the two metal centres throughout the framework.

The results in this section have presented the successful synthesis of a series of cobalt-containing mixed-metal MOFs. X-ray diffraction studies were used to show that each material was a single-phase product. Magnetism studies showed that the magnetic

behaviour of each material was a combination of the two parent cations where the response of Co^{II} dominated.

5.4 MOFs with Functionalised Pyridine-*N*-Oxide Ligands

The pyridine *N*-oxide framework, described in section 5.2.1, is analogous to the MIL-53 framework. The differences are due to the substitution of the electronegative bridging OH group of MIL-53 with a neutral, O-bonded, pyridine-*N*-oxide (PNO) ligand. The metal cations in the PNO framework are in the +2 oxidation state which is balanced by the -2 charge on each terephthalate anion, resulting in a neutral framework. It has been shown that the MIL-53 framework can expand in response to external stimuli. This inherent flexibility is due to the specific connectivity between framework components, which is still believed to be present in these PNO frameworks. The aim of the synthetic experiments presented in this section was to increase the size of the bridging pendant pyridine-*N*-oxide ring to investigate whether the M^{II}(bdc)(PNO) framework would expand to incorporate the larger ligands. To investigate this flexibility, functionalised pyridine-*N*-oxides were purchased from chemical vendors. Several functionalised pyridine *N*-oxides, with different reactivities, were chosen to investigate the size and type of ligand that could be accommodated by the framework. Figure 5.18 shows the different ligands that were considered for the synthesis of new MOF materials: **L1** = 3-bromopyridine-*N*-oxide, **L2** = 4-methoxypyridine-*N*-oxide, **L3** = isoquinoline-*N*-oxide, **L4** = 4-phenylpyridine-*N*-oxide, **L5** = 4-pyridinecarboxaldehyde-*N*-oxide, **L6** = 4-nitropyridine-*N*-oxide, **L7** = nicotinamide-*N*-oxide, **L8** = 4-(3-phenylpropyl)pyridine-*N*-oxide, **L9** = 2,2-dipyridyl-*N*-oxide, **L10** = 2,2-dipyridyl-*N,N'*-dioxide and **L11** = 4,4-dipyridyl-*N,N'*-dioxide.

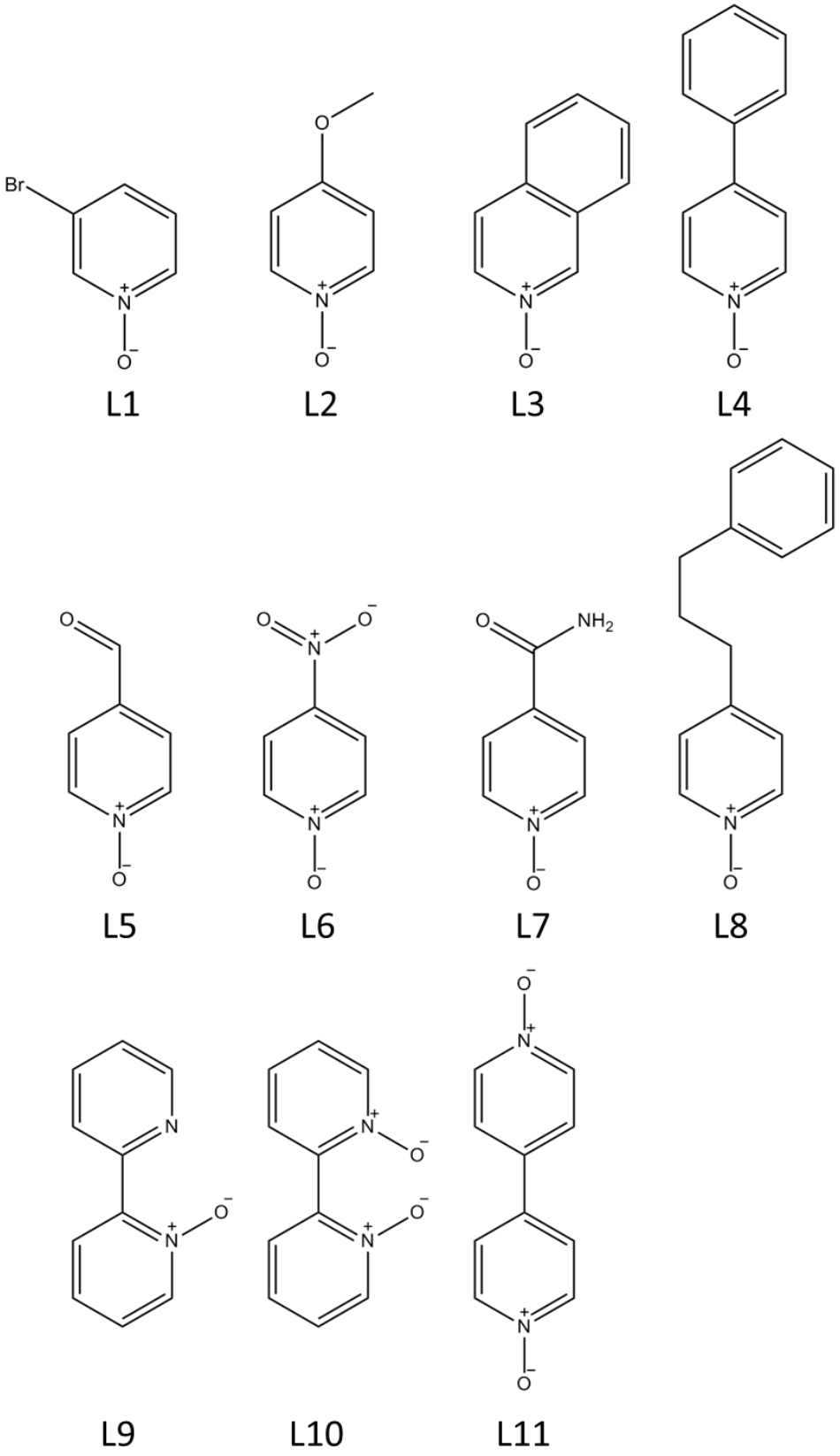

Figure 5.18: Pyridine-N-oxide functionalised with various groups used for the preparation of M^{II}(bdc)(PNO-X) MOFs

The control experiment was performed where the pyridine *N*-oxide was left out of the synthesis. The product formed was identified as Co(bdc)(DMF) and had previously been published by Fu *et al.*.[12] This phase has the same topology as the Co(bdc)(PNO) framework but the pendant ligand is *N*,*N*-dimethylformamide (Figure 5.19).

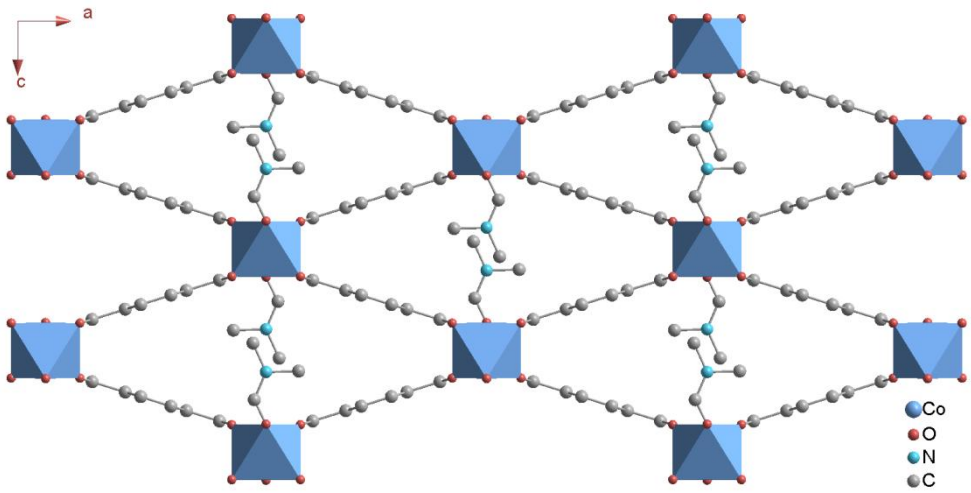

Figure 5.19: View along the b-axis of Co(bdc)(DMF). N,N-dimethylformamide bridges between neighbouring Co^{II} centres.

Knowing the structure that the materials form when no pyridine-*N*-oxide is present is important as it will be possible to identify if the functionalised ligands have had an effect on how the synthesis proceeds.

Experimentation with all eleven ligands showed that not all the ligands gave frameworks with the MIL-53 topology. Out of the eleven ligands that were chosen only four gave a MIL-53-type framework: **L1-L4**. Ligands **L5-L8** all gave the same framework, but this framework did not include the PNO ligand and it also did not crystallise with the same structure as the reference material (Figure 5.19). **L5** gave two variations on the same structure, where the resultant structure was dependent upon the linker concentrations and ratios. The bidentate ligands, **L9-L11,** gave 3 new structures

that were related, but not analogous to, the monodentate structures. All ligand and product numbers are shown in Table 5.4.

Table 5.4: Different ligands that were used to synthesise new metal-organic frameworks. Corresponding ligand number and related product number are shown.

Ligand Number	PNO linker	Product Number	
L1	3-bromopyridine-*N*-oxide	**1**	(Section 5.4.1)
L2	4-methoxypyridine-*N*-oxide	**2**	(Section 5.4.1)
L3	Isoquinoline-*N*-oxide	**3**	(Section 5.4.1)
L4	4-phenylpyridine-*N*-oxide	**4**	(Section 5.4.1)
L5	4-pyridinecarboxaldehyde-*N*-oxide	**5/6**	(Section 5.4.2)
L6	4-nitropyridine-*N*-oxide	**6**	(Section 5.4.2)
L7	Nicotinamide-*N*-oxide	**6**	(Section 5.4.2)
L8	4-propylphenylpyridine-*N*-oxide	**6**	(Section 5.4.2)
L9	2,2-dipyridyl-*N*-oxide	**7**	(Section 5.4.3)
L10	2,2-dipyridyl-*N,N'*-dioxide	**8**	(Section 5.4.3)
L11	4,4-dipyridyl-*N,N'*-dioxide	**9**	(Section 5.4.3)

5.4.1 MIL-53-type frameworks

Ligands **L1-L4** (Table 5.4) gave novel MIL-53-type frameworks. Four different products were obtained (**1**-**4**). They were all synthesised under similar conditions as those used for the unfunctionalised PNO material. $Co(NO_3)_2 \cdot 6H_2O$, 1,4-benzenedicarboxylic acid and the functionalised PNO ligand (**L1**-**L4**) were dissolved in 10 mL of *N*,*N*-dimethylformamide and heated in a Teflon-lined autoclave. The temperature and duration was varied depending on the PNO ligand used (Table A.9 gives the synthetic conditions that gave products suitable for single crystal analysis). Experimental PXRD patterns are shown in Figure A.10, which show the purity of the bulk materials.

5.4.1.1 Single-Crystal X-ray Diffraction

Frameworks **1-4** all have the same basic structure. They are all constructed from one dimensional chains of $Co^{II}O_6$ octahedra bridged by the pyridine-*N*-oxide ligands, which are coordinated via the oxygen group. These ligands may be described as pendant ligands as they are mono-coordinated and do not bridge between different metal chains. The terephthalate anions are four-coordinated; each acid group (COO^-) bridges neighbouring Co^{II} centres and the whole molecule bridges between chains of $Co^{II}O_6$. The structural connectivity remains the same as for Co(bdc)(PNO): I^1O^2. This three-dimensional coordination results in a three-dimensional framework with one-dimensional pores which are filled by the pendant pyridine-*N*-oxide ligands.

Framework **1** was determined to have monoclinic symmetry, $P2_1/c$, with a refined unit cell volume of 1356.3(3) $Å^3$. Comparing this structure with the structure for the unfunctionalised PNO framework it can be seen that the large bromo groups have forced the PNO groups further apart; increasing the pore length in the *b*-direction. However, due to the functional group being in the 3- position the pendant groups tilt away from the centre to accommodate the electron density of the large bromine atom, minimising the expansion of the pore size. There is also a small twist of the terephthalate linkers which is due to the framework accommodating a large pendant ligand. Representations of the framework along the *a*- and *c*-axes are shown in Figure 5.20. When viewed along the *a*-axis it can be seen that the pendant pyridine-*N*-oxide groups are blocking the diamond-shaped pores. The four metal oxide chains that form the corners of one diamond-shaped pore have been labelled as *1* and *2* in accordance with their relative positions. The PNO groups are shown in Figure 5.20b where it can be seen that the bromo groups cause a slight twisting of the rings. Similarly, in Figure

5.20c there is a slight twist of the terephthalate groups when compared to the unfunctionalised Co-PNO framework.

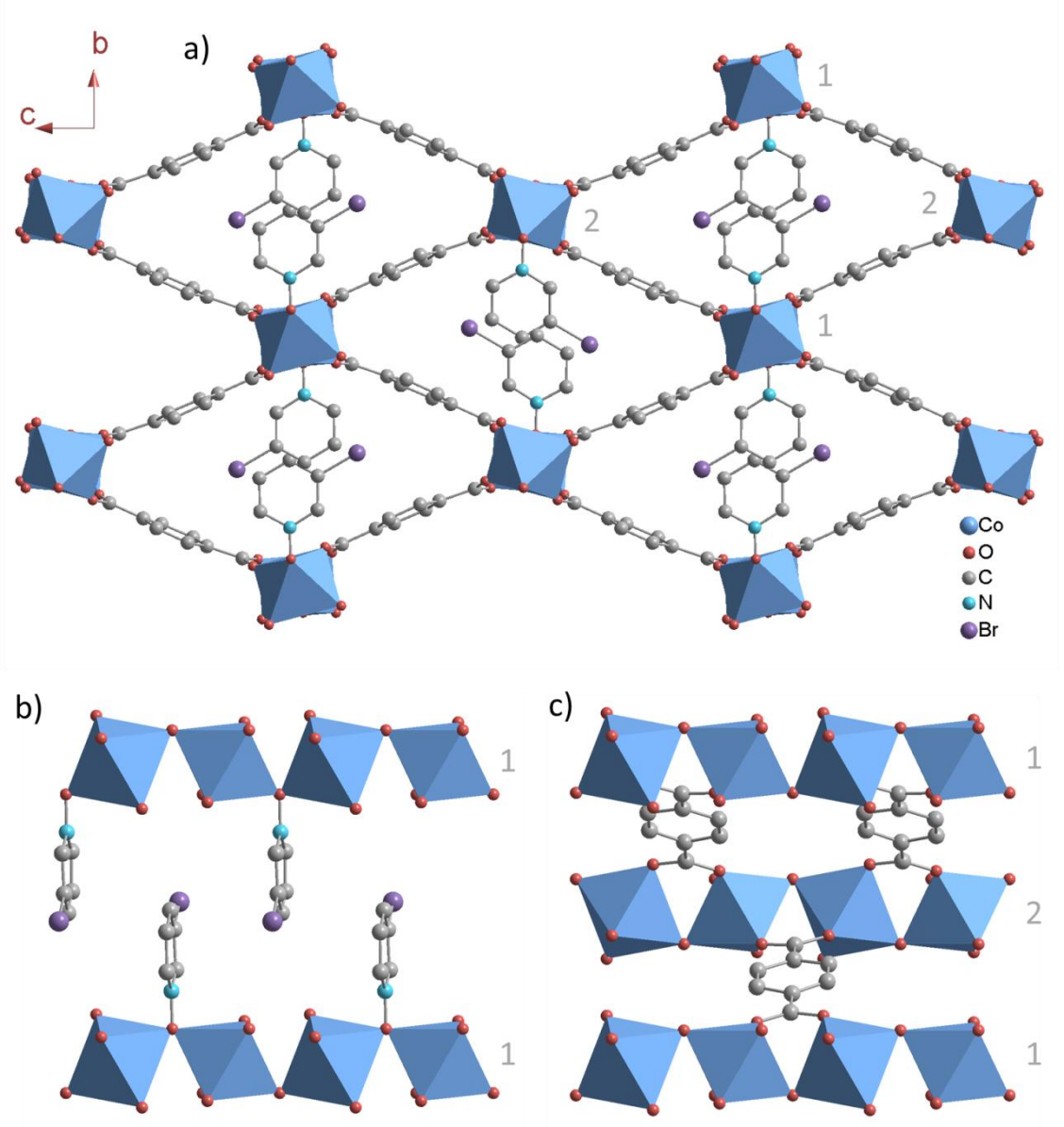

Figure 5.20: Structure of Co(bdc)(3-bromoPNO). a) Viewed along the a-axis, b) PNO groups viewed along the c-axis (the metal oxide chain labelled '2' and the terephthalate linkers have been omitted) and c) terephthalate groups viewed along the c-axis (the PNO-Br groups have been omitted). Hydrogen atoms are omitted for clarity.

Framework **2** was determined to have orthorhombic symmetry, *Pnma*, with a refined unit cell volume of 1510.09(7) $Å^3$. The 4-methoxypyridine-*N*-oxide group was found to be disordered about the mirror plane. It was refined to have two components each with a

partial occupancy of 0.5; the different orientations are shown in Figure 5.21b. The pendant ligands tilt away from the centre of the pores to accommodate the electronegative oxygen atom. There is a large degree of twisting of the terephthalate rings in this framework due to the larger functional group. Representations of the framework along the *a*- and *b*-axes are shown in Figure 5.21. When viewed along the *a*-axis it can be seen that pendant pyridine-*N*-oxide groups are blocking the available pore volume. The four metal oxide chains that form the corners of one diamond-shaped pore have been labelled as *1* and *2* in accordance with their relative positions (Figure 5.21a). Figure 5.21d shows that the structure has accommodated the large functional groups by twisting the octahedral and consequently the terephthalate linkers.

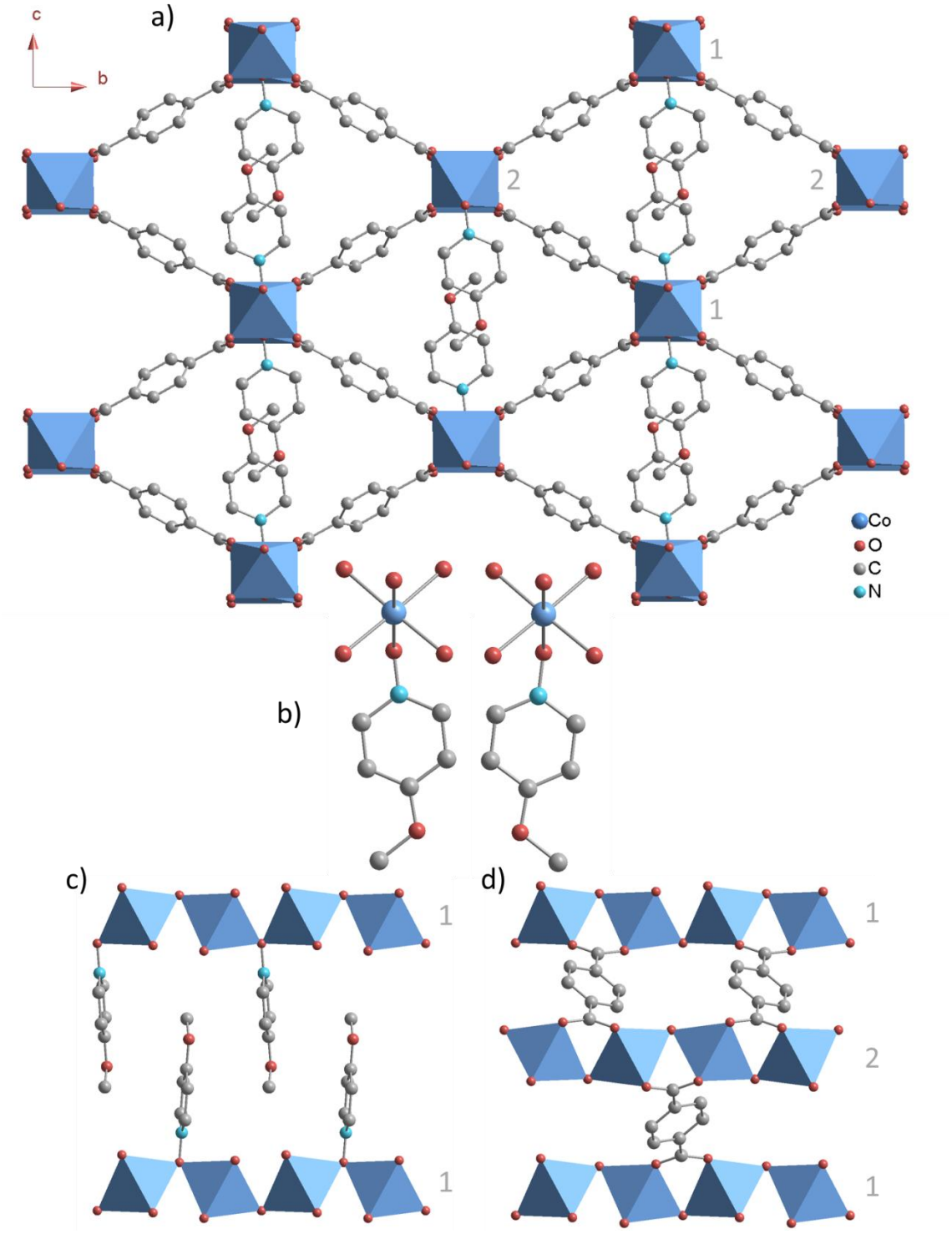

Figure 5.21: Structure of Co(bdc)(4-methoxyPNO). a) viewed along the a-axis, b) the different orientations of the PNO-OMe ligand, c) viewed along the b-axis with the terephthalate groups removed and c) viewed along the b-axis with the PNO groups removed. Hydrogen atoms are omitted for clarity.

Framework **3** was determined to have orthorhombic symmetry, *Pnma*, with a refined unit cell volume of 1542.0(2) $Å^3$. The unit cell volume of the framework has increased

due to the increased size of the functional group. The terephthalate ligand in this structure was found to be disordered around its mirror plane. It was refined to have two components each with a partial occupancy of 0.5; the two orientations are shown in Figure 5.22c. A small amount of residual electron density was refined as water molecules located in the pores of the framework. Representations of the framework along the *b*- and *a*-axes are shown in Figure 5.22. When viewed along the *b*-axis it can be seen that pendant pyridine-*N*-oxide groups are blocking the diamond-shaped pores. The four metal oxide chains that form the corners of one diamond-shaped pore have been labelled as *1* and *2* in accordance with their relative positions. Figure 5.22b highlights that the PNO groups are parallel to each other in the same way the unmodified PNO groups were arranged; in the absence of an electronegative group the rings do not need to tilt. The larger functional group is accommodated by a small twist of the octahedral and terephthalate linkers.

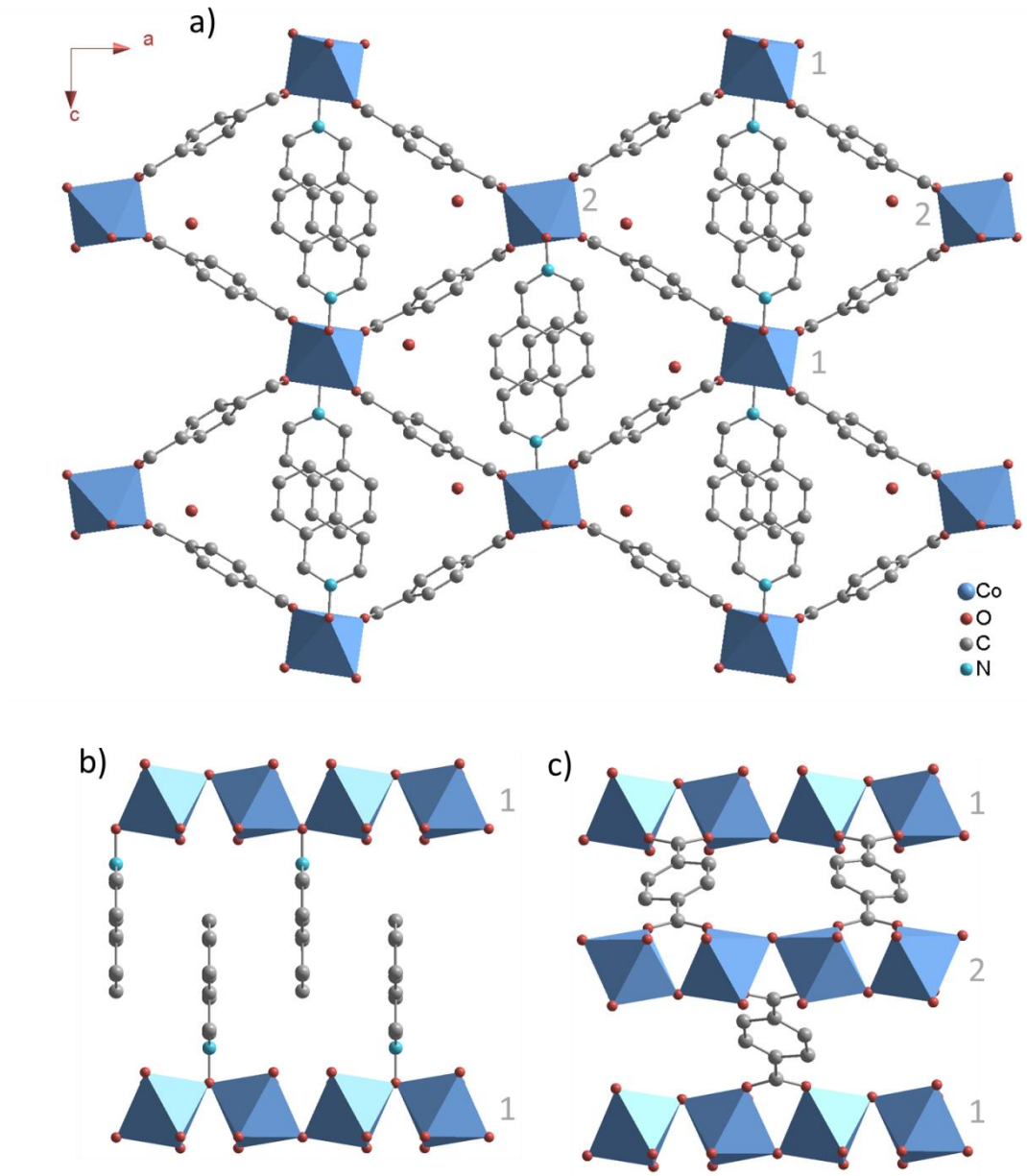

Figure 5.22: Structure of Co(bdc)(isoquinoline-N-oxide). a) Viewed along the b-axis, b) viewed along the a-axis with the terephthalate groups removed and c) viewed along the a-axis with the PNO groups removed, showing the two orientations of the terephthalate linker. Hydrogen atoms are omitted for clarity.

Framework **4** was determined to have monoclinic symmetry, *C2/c*, with a refined unit cell volume of 1497.32(16) $Å^3$. The expansion of the pores in the *b*- direction, due to the functionalised PNO group, is greater than has been seen for the analogous MIL-53 materials that expand and contract upon addition of guest molecules. This very large expansion in the *b*-direction has been achieved by a large degree of twisting of the

terephthalate ligands. When viewed along the *c*-axis it can also be seen that the CoO_6 chains have twisted to accommodate this large ligand. Representations of the framework along the *c*- and *a*-axes are shown in Figure 5.23. When viewed along the *c*-axis it can be seen that pendant pyridine-*N*-oxide groups are blocking the available pore volume. Figure 5.23b and c show that there is only a small twist of the PNO ring whereas the chains of the framework have been offset from each other by a large distance and the terephthalate rings have been twisted by almost 90 ° from the position seen for the terephthalates in the unmodified framework.

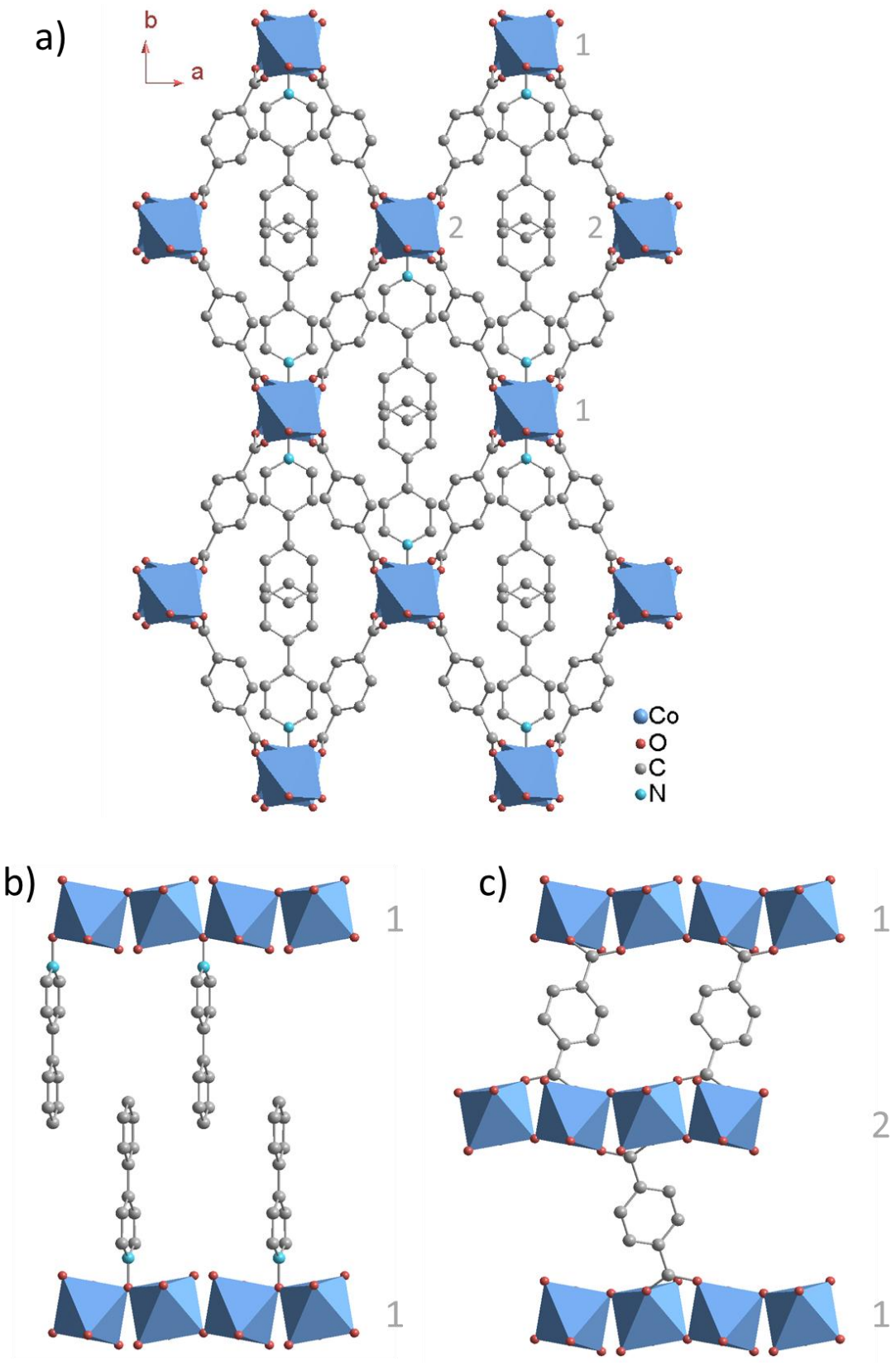

Figure 5.23: Structure of Co(bdc)(4-phenylPNO) a) Viewed along the c-axis, b) viewed along the a-axis terephthalate groups have been omitted for clarity and c) viewed along the a-axis where the PNO groups have been omitted for clarity. Hydrogen atoms are omitted for clarity.

The crystallographic data for products **1-4** is tabulated below in Table 5.5.

*Table 5.5: Crystallographic data for frameworks **1-4***

	Framework			
	1	**2**	**3**	**4**
Functionalised PNO	C_5H_4NO-Br	C_5H_4NO-OMe	C_5H_4NO-C_4H_4	C_5H_4NO-C_6H_5
Temperature/ K	296	100	100	100
a/ Å	7.1962(8)	7.1507(2)	18.025(16)	12.9936(8)
b/ Å	10.0563(13)	18.1353(4)	7.184(6)	17.9026(8)
c/ Å	18.748(3)	11.6447(3)	11.906(11)	7.1797(4)
β/ °	91.548	90	90	116.294(8)
V/ Å^3	1356.3(3)	1510.09(7)	1542(2)	1497.32(16)
Space Group	*P2/c*	*Pnma*	*Pnma*	*C2/c*

As shown above, products **1-4** all have frameworks with a MIL-53-type topology, which was also seen for the unfunctionalised pyridine-*N*-oxide framework. It is believed that these functionalised pyridine-*N*-oxide ligands all gave similar structures because they have similar chemical reactivities as the unfunctionalised pyridine-*N*-oxide ligand. Stabilisation of the N^+–O^- bond, which allows the coordination of these ligands within the framework, is a key factor in the successful formation of these MOF materials. Resonance and inductive effects can be used to rationalise the results reported here.

Ligands **L2-L4** are substituted in the 4-position and the functional groups all have a net electron donating effect on the ring. As these groups are electron donating the possible resonance structures (Figure 5.24a) show that the donated electron charge can be stabilised in either the ortho or the para positions. It may be proposed that N^+ is able to stabilise this extra charge, increasing the nucleophilicity of the oxygen atom, which

promotes coordination to the metal centres. In contrast, ligand **L1** (bromo-PNO) is substituted in the 3-position and the bromo group has a net electron withdrawing effect on the ring. Halogen groups are a special case where, although they are weakly electron withdrawing due to the inductive effects of the electronegative halogen atom, the lone pairs are donated into the ring resulting in these groups being para/ortho directing, in contrast to other electron withdrawing groups.[13] Therefore, the donated electron charge is stabilised on the carbons either side of the nitrogen atom as shown in Figure 5.24b. It may be proposed that the N^{+}–O^{-} bond is more greatly affected by the resonance effects of the bromo group, where the donating effect allow the ligand to behave in a similar way to the unfunctionalised pyridine-*N*-oxide.

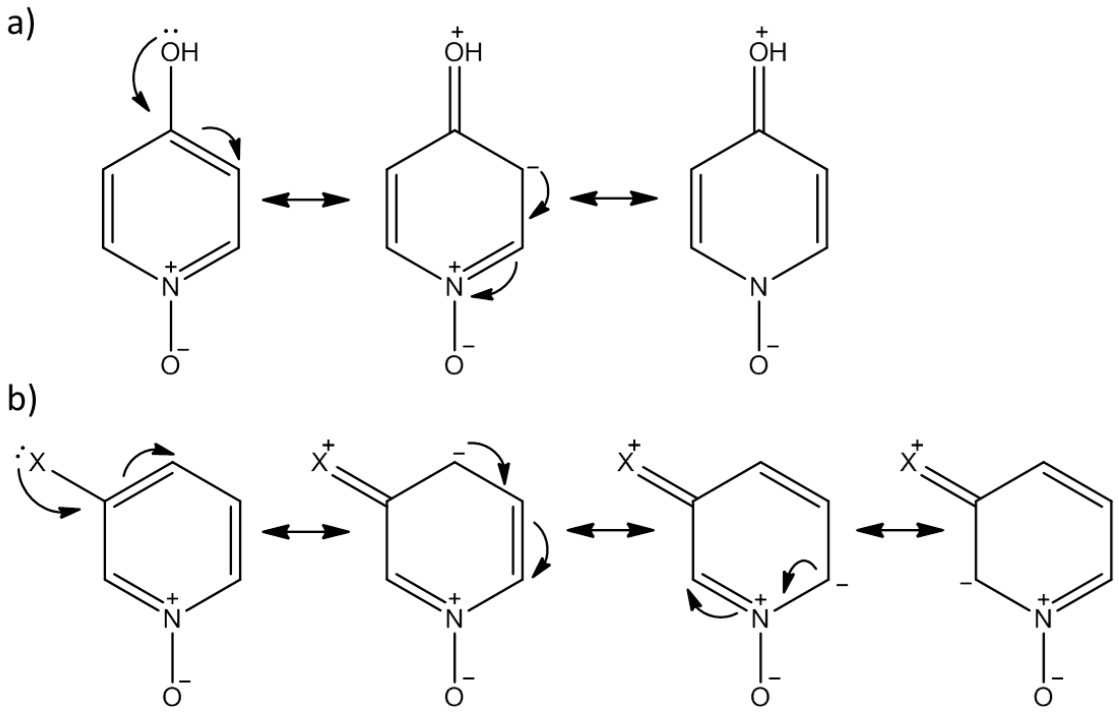

Figure 5.24: Example resonance diagrams for electron donating groups in a) the 4-position and b) the 3-position.

5.4.1.2 Thermogravimetric Analysis

Thermogravimetric analysis (TGA) was performed on products **1**-**4**. This allowed the stability of the framework to be found and it also allowed the empirical formula of the material, calculated from the single-crystal refinement data, to be confirmed. Inflection points in the data were used to calculate the mass loss corresponding to the steps observed in the decomposition.

Product **1**, was calculated to have the empirical formula $Co(C_8H_4O_4)(C_5H_4NO\text{-}\mathbf{Br})$. The TGA results for product **1** are shown in Figure 5.25a. The results show that there is no mass loss until above 250 °C which agrees well with the structural data that showed that there was no solvent trapped within the pores. Above 250 °C the framework gradually decomposes, the first inflection point, a loss of 37.6%, corresponds well with the theoretical percentage mass loss of the functionalised pyridine group, C_5H_4N-Br, 36.3%. Complete decomposition to Co_3O_4 is observed above 600 °C, the experimental percentage mass loss, 79.3%, agrees well with the theoretical percentage mass loss of 79.8%. Co_3O_4 is reduced to CoO above 850 °C

Product **2** was calculated to have the empirical formula $Co(C_8H_4O_4)(C_5H_4NO\text{-}\mathbf{OCH_3})$. No additional electron density was located within the pores of the framework therefore no mass loss was expected at low temperatures during the TGA experiment. The TGA results are shown in Figure 5.25b. However, they show that there is a small mass loss below 50 °C after which the mass stabilises until the sample is heated above 250 °C. Above this temperature the sample gradually decomposes to Co_3O_4. Due to the initial mass loss being complete below 50 °C it was assumed that this mass loss was due to residual water on the surface of the framework as no evidence was found for anything in the pores during the XRD studies. Also assuming that after this initial mass loss the

framework stabilises to $Co(C_8H_4O_4)(C_5H_4NO\text{-}OCH_3)$ between 100 – 250 °C the moles of surface water can be calculated. At room temperature the framework was calculated to include $0.5H_2O$ on the surface of the material. From this point, the pure framework (no water molecules) will be assumed to be equal to the first plateau observed in the data at approximately 97%. All subsequent calculations will use this as their reference point. During the decomposition there is an inflection point observed at approximately 350 °C which corresponds to a percentage mass loss of 16%, assuming the new calculated empirical formula. This mass loss does not agree with either of the theoretical percentage mass losses of $–OCH_3$ (8.6%) or $–C_5H_4N\text{-}OCH_3$ (31.3%). There is also a second inflection point which occurs at approximately 410 °C which corresponds to a percentage mass loss of 38.2%. This more closely relates to the theoretical percentage mass loss of $–C_5H_4N\text{-}OCH_3$ (31.3%). Complete decomposition to Co_3O_4 is observed above 500 °C, the experimental percentage mass loss, 76.2%, agrees well with the theoretical percentage mass loss of 76.9%. Co_3O_4 is reduced to CoO above 850 °C.

Product **3** was calculated to have the empirical formula $Co(C_8H_4O_4)(C_5H_3NO\text{-}\mathbf{C_4H_4})\cdot 0.25H_2O$; a small amount of water was located within the pores of the framework. The TGA results are shown in Figure 5.25c and they agree well with the calculated empirical formula. The experimental number of waters lost below 100 °C was calculated to be 0.26. From this point the first plateau is assumed to correspond to the empty framework, $Co(C_8H_4O_4)(C_5H_3NO\text{-}C_4H_4)$, all subsequent calculations will use this as their reference point. The framework is stable up to approximately 250 °C. There is an inflection point during the decomposition which occurs at approximately 410 °C and corresponds to the percentage mass loss of 34.5% which agrees well with the calculated percentage mass loss of $C_5H_3N\text{-}C_4H_4$, 35.1%. Complete decomposition to

Co_3O_4 occurs above 550 °C. The experimental percentage mass loss, 78.0%, agrees well with the theoretical percentage mass loss, 78.2%.

Product **4** was calculated to have the empirical formula $Co(C_8H_4O_4)(C_5H_4NO\text{-}\mathbf{C_6H_5})$. The TGA results, shown in Figure 5.25d, agree well with the calculated formula. No mass loss is seen until the sample is heated above 300 °C, which makes this product the most stable of the functionalised pyridine-*N*-oxide frameworks. Above 300 °C the framework decomposes to Co_3O_4, the experimental percentage mass loss of 79.3% agrees very well with the theoretical percentage mass loss of 79.6%. There is an inflection point during the decomposition at approximately 410 °C which corresponds to a percentage mass loss of 38.7% which agrees well with the theoretical percentage mass loss for the ligand, $C_5H_4N\text{-}C_6H_5$, 39.4%

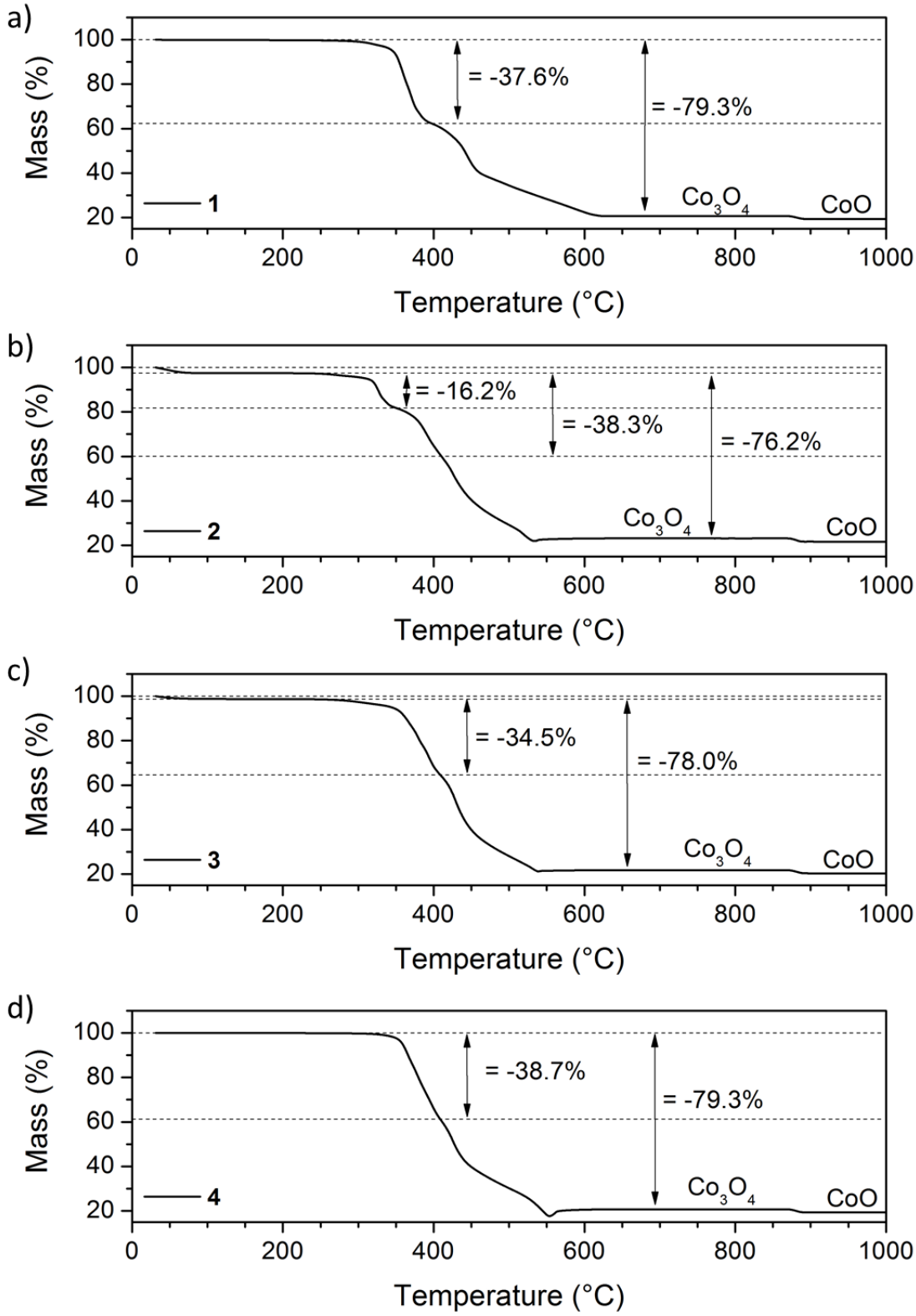

Figure 5.25: TGA of Co(bdc)(PNO-X) materials where X = a). –Br, b) –OMe, c) –C_4H_4 and d) –C_6H_5.

All of the experimental results show a step in the decomposition. For the theoretical calculations this inflection point was assumed to be due to the loss of the functionalised pyridine ring leaving the oxygen as a μ-O^{2-} group which bridges the Co oxide chains, as seen for the calcined MIL-47(V)[14]. To balance the charge the Co^{II} would be oxidised to Co^{IV}. This reaction is unlikely to occur therefore it is expected that it is not possible to isolate this stage in the decomposition process and that decomposition will continue immediately to give Co_3O_4.

5.4.2 New MOFs using PNO Directing Agents

Synthesis of new MOFs using functionalised pyridine-*N*-oxides where these molecules do not coordinate within the final product has also been achieved. These molecules will be described here as directing agents as their presence is necessary for the production of the specific framework however they do not form part of the final product.

5.4.2.1 Single-Crystal X-ray Diffraction

Using the aldehyde functionalised pyridine-*N*-oxide ligand (**L5**) two different MOFs can be synthesised (**5 and 6**). Both products were synthesised using $Co(NO_3)_2 \cdot 6H_2O$, 1,4-benzenedicarboxylic acid (bdc) and 4-pyridinecarboxaldehyde-*N*-oxide (CHO-PNO) solvothermally treated in DMF at 120 °C. The final product can be controlled by changing the ratio of the starting materials. Using a ratio of 1:3:3 (Co:bdc:PNO) the framework that was synthesised had the empirical formula, $[Co_3(C_8H_4O_4)_4] \cdot DMA^+ \cdot$solvent (**5**), using a ratio of 1:2:2 (Co:bdc:PNO) results in a framework with the empirical formula, $[Co_3(C_8H_4O_4)_3(DMF)_2] \cdot$solvent (**6**). Both frameworks contain Co^{II} centres therefore product **5** ($Co^{2+}{}_3(C_8H_4O_4)^{2-}{}_4$) has a charged framework found to be balanced by dimethylammonium (DMA^+) molecules in the pores. Dimethylammonium is formed as the product of the hydrolysis of *N*,*N*-

dimethylformamide (DMF) (Scheme 5.1), which has been reported in the synthesis of other MOFs.[15]

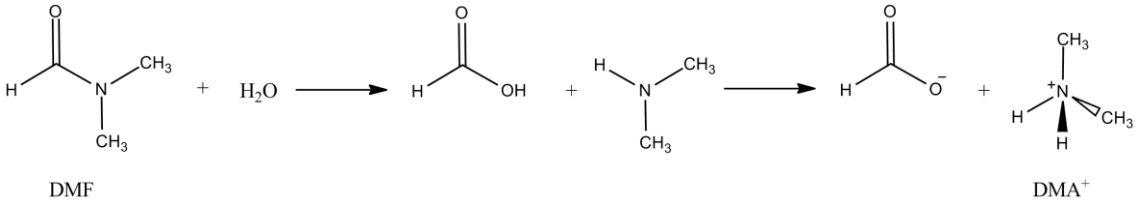

Scheme 5.1: Hydrolysis of N,N-dimethylformamide.

The synthesis of product **5** has been reported in the literature on a number of occasions. It was first synthesised by Poulsen *et al.*[16] in 2006 using $Co(NO_3)_2 \cdot 6H_2O$ as the metal salt and DEF as the solvent which resulted in DEA^+ as the charge balancing ion. It was then reported by Clausen *et al.*[17] in 2008; the product was the same but they used the hydrated chloride salt and DEF in the synthesis, and Luo *et al.*[18] in 2009; they also used the chloride salt but the solvent was a mixture of DMF and MeOH where DMA^+ was the charge balancing ion. In 2010 the framework was reported again by Zhang *et al.*[19] in their study of urothermal syntheses; tetramethyl-urea (tm-urea) was used as the solvent and $Co(NO_3)_2 \cdot 6H_2O$ was used as the metal salt. The framework was reported as neutral with the empirical formula $Co_3(bdc)_3$ but upon investigation of the crystallographic information it was determined to be identical to product **5**, therefore it is suggested that the charge is balanced by the tm-urea cation. This framework was called URO-44. Product **5** crystallised as purple hexagonal plates suitable for single-crystal analysis. The framework is shown in Figure 5.27a viewed along the *b*-axis showing the largest pores. The framework is made up of cobalt trimers which are bridged in three dimensions by terephthalate ligands. The structural connectivity is therefore described as I^0O^3; there are no infinite chains of inorganic connectivity. Figure 5.27b shows the coordination of the eight terephthalate ligands to a trimer of octahedral cobalt centres

(the eighth terephthalate is positioned behind the cobalt centres). Two coordination modes of the terephthalate linker are present in the structure; six of the eight terephthalates bridge between two cobalt centres (Figure 5.26a) and the O–C–O groups of terminal terephthalate linkers chelate with the terminal cobalt centre (Figure 5.26b).

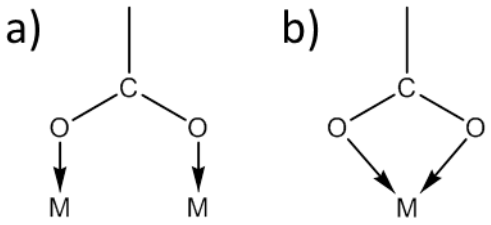

*Figure 5.26: Different coordination modes of the terephthalate linker in product **5** a) bridging and b) chelating*

The three-dimensional linkage of the terephthalate linkers results in a two-dimensional pore system. Figure 5.27c and d show the space filling views of the framework along the *b*- and *c*-axes respectively; if all the occluded molecules can be removed from the pores then this MOF has the potential to be porous.

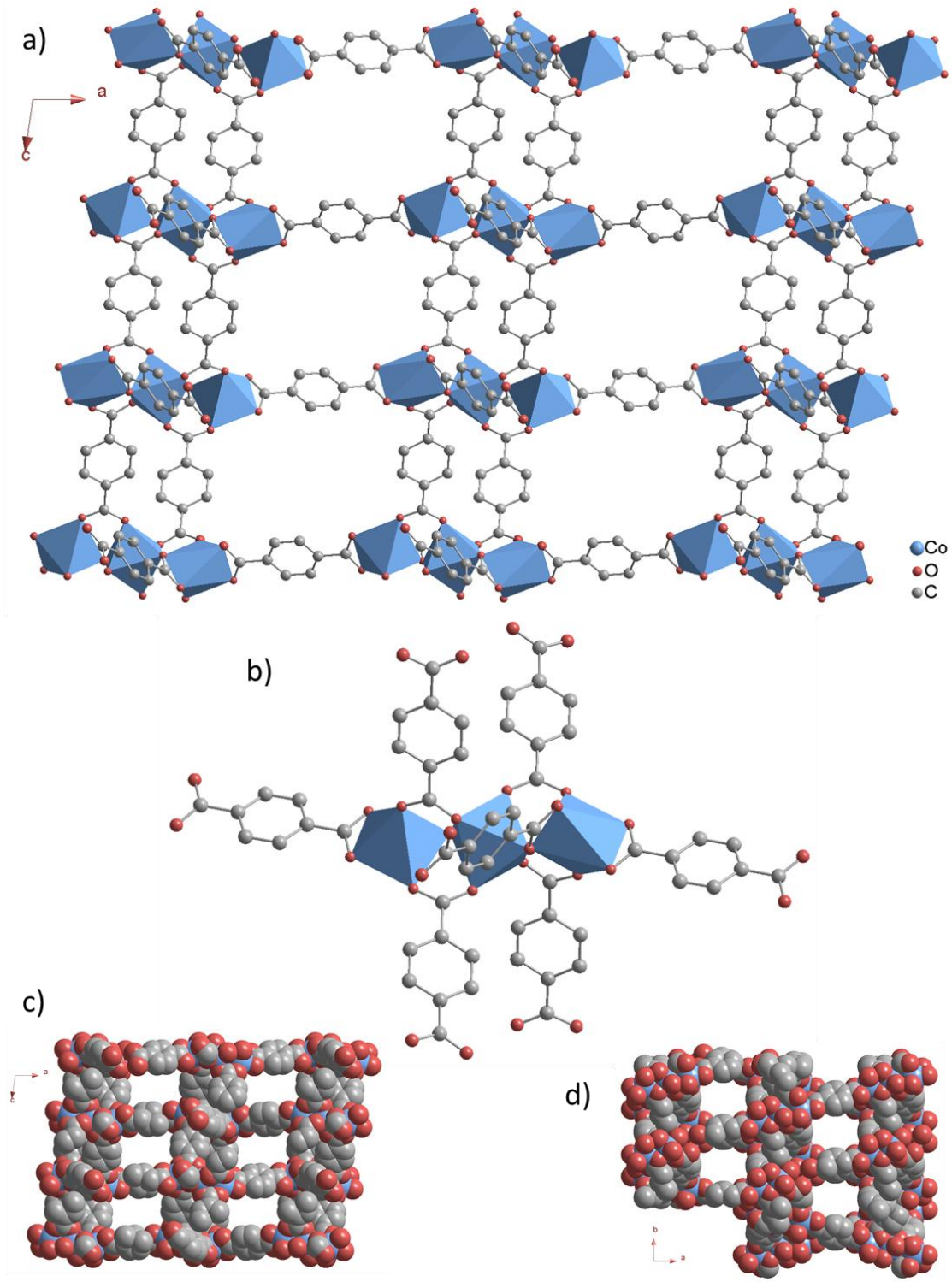

Figure 5.27: Three-dimensional MOF with empirical formula $Co_3(BDC)_4 \cdot [DMA^+]$, the DMA^+ molecules have been omitted for clarity. a) Shows the structure viewed along the b-axis, b) shows the eight terephthalate ligands bridging around the cobalt trimer c) space filling view along the b-axis and d) space filling view along the b-axis.

Computational studies on the framework, free of the charge-balancing cations, was performed by M. Lennox at the University of Edinburgh. These studies predicted that

the pores are suitable for the uptake of some gases such as N_2 and CO_2. The study confirmed that the MOF has a two-dimensional pore system. The pore windows are inaccessible to spheres larger than 4 – 4.5 Å and the pore channels intersect to give large quasi-ellipsoidal shaped cavities with a diameter of 8.5 – 9.5 Å and a length of 10 – 11 Å.

Product **6** crystallised as purple hexagonal plates however the crystals were always twinned and only a partial refinement of the structure was possible. This material, unlike structure **5**, is neutral. The material is also constructed from trimers of octahedral Co^{II} but these are coordinated to six terephthalate ligands and two neutral DMF molecules, resulting in a balanced framework. There is only one terephthalate coordination mode present in the structure, which is shown in Figure 5.28.

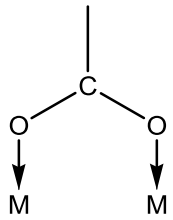

*Figure 5.28: Coordination mode of the terephthalate linkers in product **6**.*

The DMF molecules are not capable of bridging across cobalt centres therefore this framework is not coordinated in three dimensions; the cobalt trimers are terminated at either end by a DMF molecule, as shown in Figure 5.29b. As a consequence of the terminating DMF molecules this material has a layered structure where the DMF molecules of neighbouring trimers interdigitate allowing weak Van der Waals forces to hold the layers together (Figure 5.29c). The structural connectivity of this framework is described as I^0O^2; as seen for product **5** there are no infinite chains of inorganic connectivity.

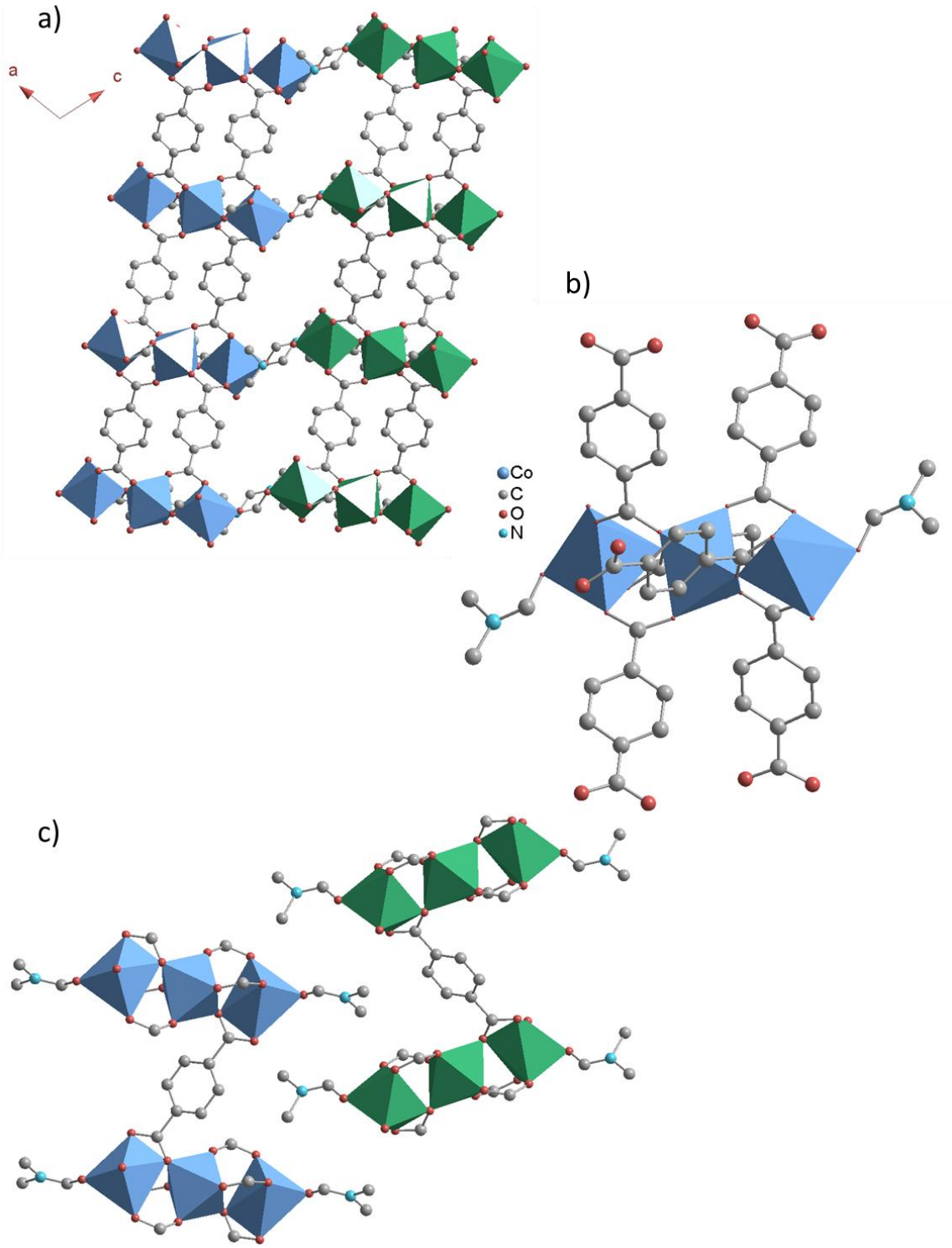

Figure 5.29: Structure of MOF with the empirical formula $Co_3(bdc)_3(DMF)_2$. a) The framework viewed along the b-axis, b) the terminating DMF groups and bridging terephthalate groups coordinated to the cobalt trimmers and c) interdigitated cobalt trimmers (terephthalate linkers have been omitted for clarity. The blue and green polyhedra have been used to distinguish the layers of the material.

The crystallographic data for frameworks **5** and **6** are tabulated below.

*Table 5.6: Crystallographic data for frameworks **5** and **6**.*

	Framework	
	5	**6**
Functionalised PNO	C_5H_4NO-CHO	C_5H_4NO-CHO
Dimensionality	3D	2D
a/ Å	33.149(5)	13.9766(10)
b/ Å	9.8224(14)	9.6910(4)
c/ Å	17.769(2)	16.6023(9)
β/ °	98.391(12)	108.742(7)
V/ Å^3	5723.7	2129.5
Space Group	*C2/c*	*P2$_1$/n*

Product **6** was also found to be synthesised when using various other functionalised PNO ligands in the synthesis. The other ligands that also gave $Co_3(bdc)_3(DMF)_2$ as the sole product, but without being themselves incorporated into the structure, were 4-nitropyridine-*N*-oxide (**L6**), nicotinamide-*N*-oxide (**L7**) and 4-(3-phenylpropyl)pyridine-*N*-oxide (**L8**). Figure 5.30 shows the powder X-ray diffraction patterns of the materials synthesised using these three ligands compared with the simulated pattern for product **6**.

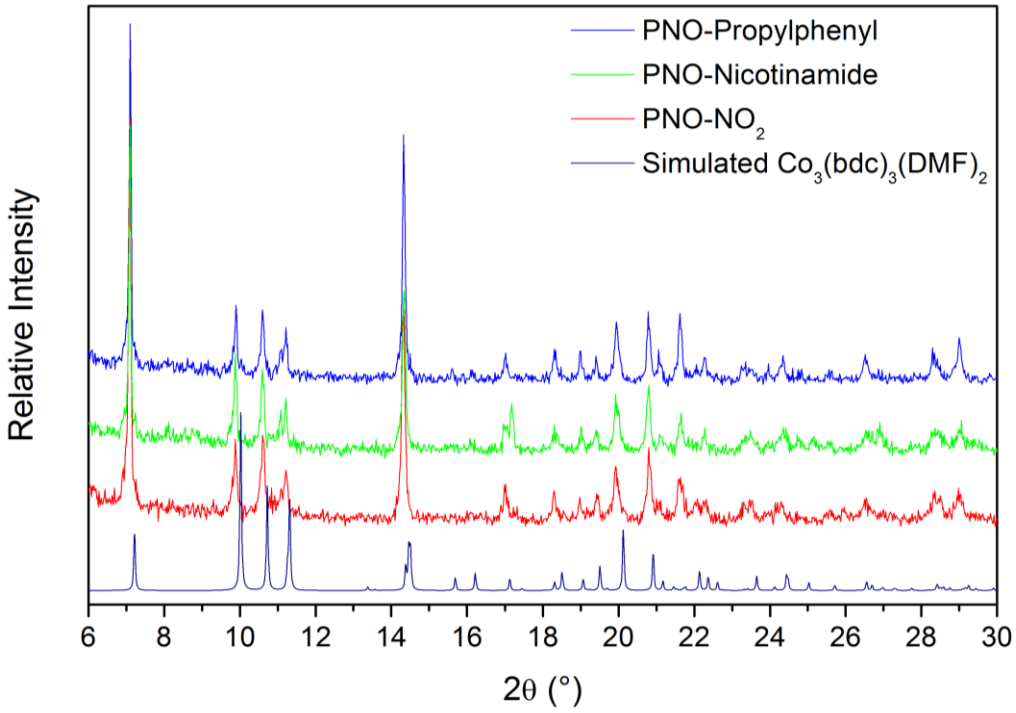

Figure 5.30: PXRD of the various PNO ligands that gave the MOF $Co_3(bdc)_3(DMF)_2$

Ligands **L5-7** are functionalised in the 4-position with electron-withdrawing groups. This has the net effect of destabilising the N^+–O^- bond through resonance effects. This destabilisation results in either a reduction in the nucleophilic character of the N^+–O^- bond or the breaking of this bond, both result in the ligand not coordinating with the metal ions to form part of the framework. In contrast, ligand **L8** is functionalised in the 4-position with a weakly electron-donating group. This ligand is believed not to coordinate with the framework due only to steric constraints; the ligand is too large to be accommodated in a MIL-53-type framework.

5.4.2.2 Thermogravimetric Analysis

Thermogravimetric analysis was performed for products **5** and **6**. The starting empirical formula was unknown at the start of these experiments. The single-crystal data gives evidence that these two frameworks are porous therefore the steps in the data are expected to be due to the loss of different occluded solvent molecules. The mass, and

hence the number of moles, of Co_3O_4 produced upon decomposition can be used to calculate the change in mass expected due to a change in the empirical formula. This method was used to predict the starting empirical formula and the formula for any plateaus visible in the data.

Figure 5.31a shows the TGA results for product **5**, the dashed lines indicate the predicted percentage mass changes. The predicted masses have been labelled 1-4 according to the following decomposition products. 1: $[Co_3(bdc)_4]\cdot 2DMA^+\cdot 1.5DMF\cdot 2H_2O$, 2: $[Co_3(bdc)_4]\cdot 2DMA^+\cdot 1.5DMF$, 3: $[Co_3(bdc)_4]\cdot 2DMA^+$ and 4: $Co_3(bdc)_4$. Each predicted mass agrees well with a step in the thermogravimetry (TG) data suggesting there is a good agreement between the predicted empirical formula and the experimental data.

The predicted percentage mass changes for product **6** have been labelled 1-3 according to the following decomposition products and are shown in Figure 5.31b. 1: $[Co_3(bdc)_3(DMF)_2]\cdot 2DMF\cdot 2H_2O$, 2: $[Co_3(bdc)_3(DMF)_2]\cdot 2DMF$ and 3: $Co_3(bdc)_3(DMF)_2$. There is good agreement between the predicted percentage mass changes and the mass losses seen in the TG data.

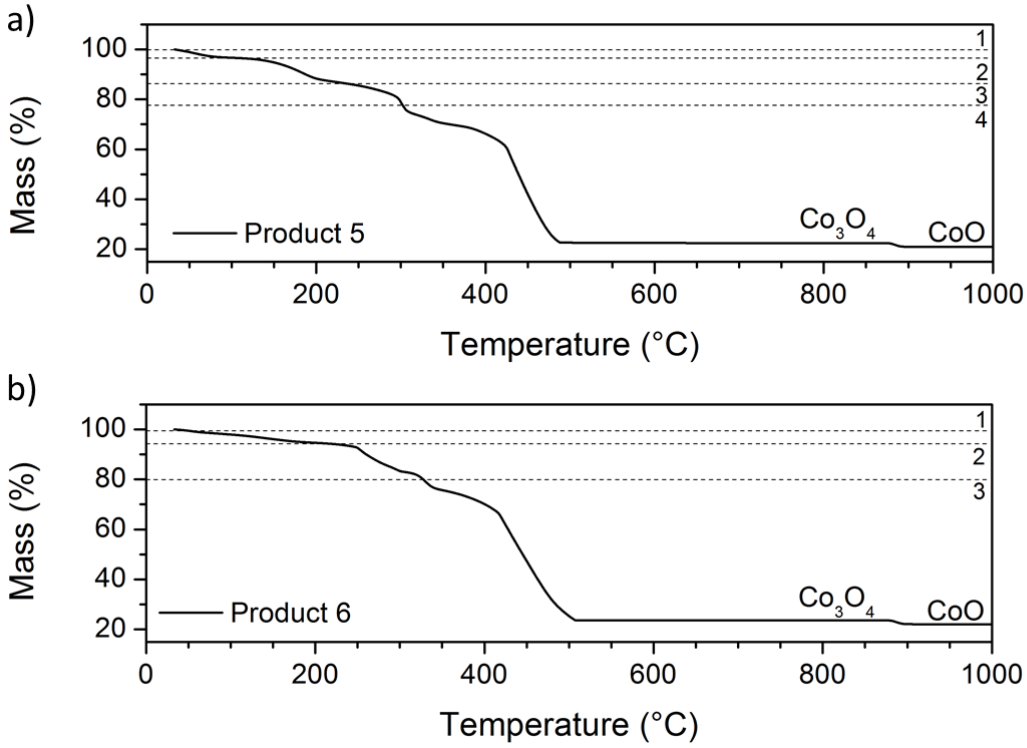

Figure 5.31: TGA data for a) $Co_3(bdc)_4$ and b) $Co_3(bdc)_3(DMF)_2$.

Adsorption isotherms, recorded at the Aix-Marseille Université, studied the uptake of CO_2 on both materials but neither was considered to have potential to perform as adsorbents. $[Co_3(bdc)_4]\cdot DMA^+$ showed an uptake of 2.33 mmol g^{-1} at 28 bar and 30 °C and $[Co_3(bdc)_3(DMF)_2]$ showed an uptake of 2.96 mmol g^{-1} under the same conditions. Due to the ionic nature of $[Co_3(bdc)_4]\cdot DMA^+$, poor activation is believed to be responsible for the low capacity seen in the adsorption studies; DMA^+ molecules are believed to still be present inside the pores. Activation at higher temperatures results in the decomposition of the framework. The $[Co_3(bdc)_3(DMF)_2]$ was not expected to show high adsorption capacities due to the small pore size which is a consequence of the interdigitated layers.

5.4.3 New MOFs using Bidentate Ligands

Continuing the work with pyridine-*N*-oxide ligands for MOF synthesis, PNO ligands containing two potential coordination sites were investigated. The ligands that were

chosen were, 2,2'-dipyridyl-*N*-oxide (**L9**), where the potential coordinating groups are the oxygen of the *N*-oxide group of one ring and the nitrogen atom on the other ring, 2,2'-dipyridyl-*N,N'*-dioxide (**L10**) and 4,4'-dipyridyl-*N,N'*-dioxide (**L11**), where the potential coordinating groups are the two oxygens of the two *N*-oxide groups. Three distinct MOF structures were obtained. Experimental PXRD patterns, for products **7** and **8**, are shown in Figure A.10, which confirm the purity of the bulk phase.

5.4.3.1 Single-Crystal X-ray Diffraction

Each of the three ligands studied gave a unique framework. Framework **7** was synthesised under solvothermal conditions at 120 °C in DMF. The starting reagents were $Co(NO_3)_2 \cdot 6H_2O$, 1,4-benzenedicarboxylic acid (bdc) and 2,2-dipyridyl-*N*-oxide (**L9**, 2,2'-dPNO). Framework **7** has the empirical formula $Co_3(bdc)_3(2,2'\text{-}dPNO)_2$, residual electron density within the pores was refined to be 2.5 H_2O and 4 DMF molecules. The topology of the framework is similar to structure **5** (Section 5.4.2); framework **7** contains trimers of CoO_6 octahedra which are bridged in three dimensions by terephthalate cross-links (Figure 5.33a) to give a two-dimensional pore system. Computational studies performed by M. Lennox calculated the pore diameter as between 4.8 – 5.5 Å. The Co^{II} centre in the middle of the trimer is bridged to the cobalt centre on both sides via the oxygen group of two 2,2'-dPNO ligands. The nitrogens in the pyridine rings are coordinated directly to the respective Co^{II} centre at either end of the trimer (Figure 5.33b). The coordination modes of the terephthalate and 2,2'-dPNO ligands are shown in Figure 5.32. Like product **5** and **6**, the structural connectivity of this framework is described as I^0O^3. At 100 K, this framework was determined to have triclinic symmetry, $P\bar{1}$, with a refined unit cell volume of 2885(3) $Å^3$.

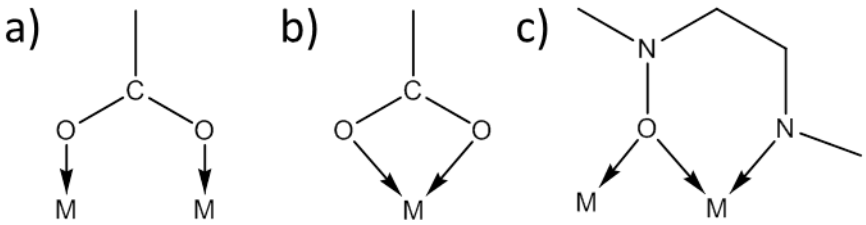

*Figure 5.32: Coordination modes of the ligands in product **7**.*

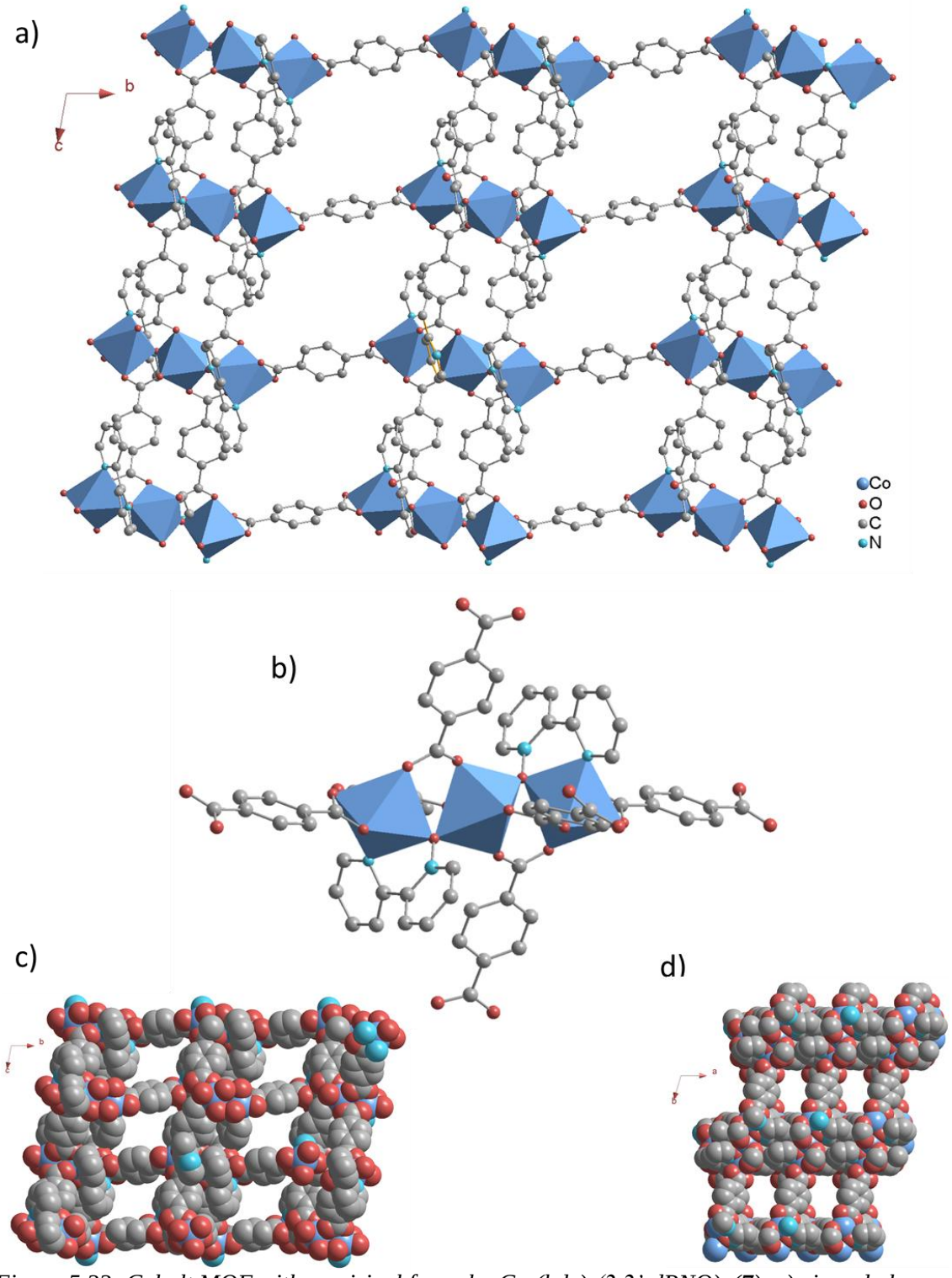

*Figure 5.33: Cobalt MOF with empirical formula, $Co_3(bdc)_3(2,2'\text{-dPNO})_2$ (**7**), a) viewed along the a-axis b) shows the bridging around the cobalt trimers, c) the space-filling view showing the pores in the a-direction and d) the space-filling view showing the pores in the c-direction.*

Structure **8** was synthesised using $Co(NO_3)_2 \cdot 6H_2O$, 1,4-benzenedicarboxylic acid and 2,2'-dipyridyl-*N,N'*-dioxide (**L10**, 2,2'-dPNdO) in DMF and MeOH, in the ratio 1:4, solvothermally heated to 100 °C. This reaction gave a product suitable for single-crystal

analysis. This MOF crystallised as small pink rectangular prisms which were determined to have the monoclinic space group *P2/c* and a refined unit cell volume of 1611.5(3) $Å^3$ at room temperature. Data were also collected at 150 K after the material had been soaked in methanol, the symmetry was determined to be triclinic, $P\bar{1}$, and the refined unit cell volume was 1589.07(18) $Å^3$. It is not possible to deduce if the decrease in volume is due purely to thermal contraction or if the framework shows some flexibility upon guest adsorption as these data could not be recorded at room temperature. The framework consists of infinite one-dimensional CoO_6 chains containing alternating *trans* and *cis* linkages. These chains are cross-linked by 1,4-benzenedicarboxylate groups in two dimensions creating a three-dimensionally coordinated framework (Figure 5.35a). The 2,2'-dipyridyl-*N,N'*-dioxide ligands bridge along the chains of CoO_6 centres, they do not bridge between chains. There are two distinct Co centres that alternate along each chain; the first is bridged to both of its neighbouring octahedra via the two N-oxide groups of the same PNO ligand, the second is bridged to its neighbours via the N-oxide groups from two different PNO ligands (Figure 5.35b). Computational studies (performed by M. Lennox) were used to determine that this framework only had a one-dimensional pore system; the bdc linkers create a channel with a width of 4.9 Å, but the dipyridyl ligands protrude into these channels causing a constriction of the diameter to 3.9 Å. The different coordination modes of the two organic linkers are shown in Figure 5.34. There is one coordination mode observed for the terephthalate linkers, where the acid groups bridge two metal centres, and one coordination mode for the 2,2'-dPNdO linker, where each oxide group bridges between two metal centres and one of these metal centres is coordinated to both oxide groups, forming a chelate ring. The structural connectivity is described as I^1O^2.

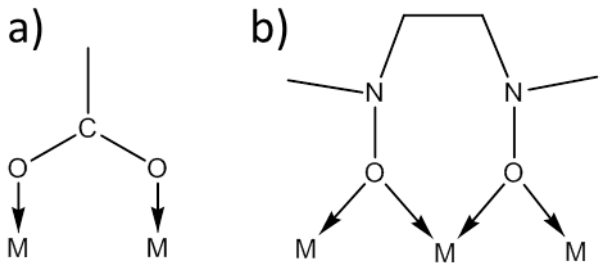

Figure 5.34: Coordination modes of the bridging ligands in product 8. a) Bridging mode of terephthalate, and b) bridging/chelating mode of 2,2'-dPNdO.

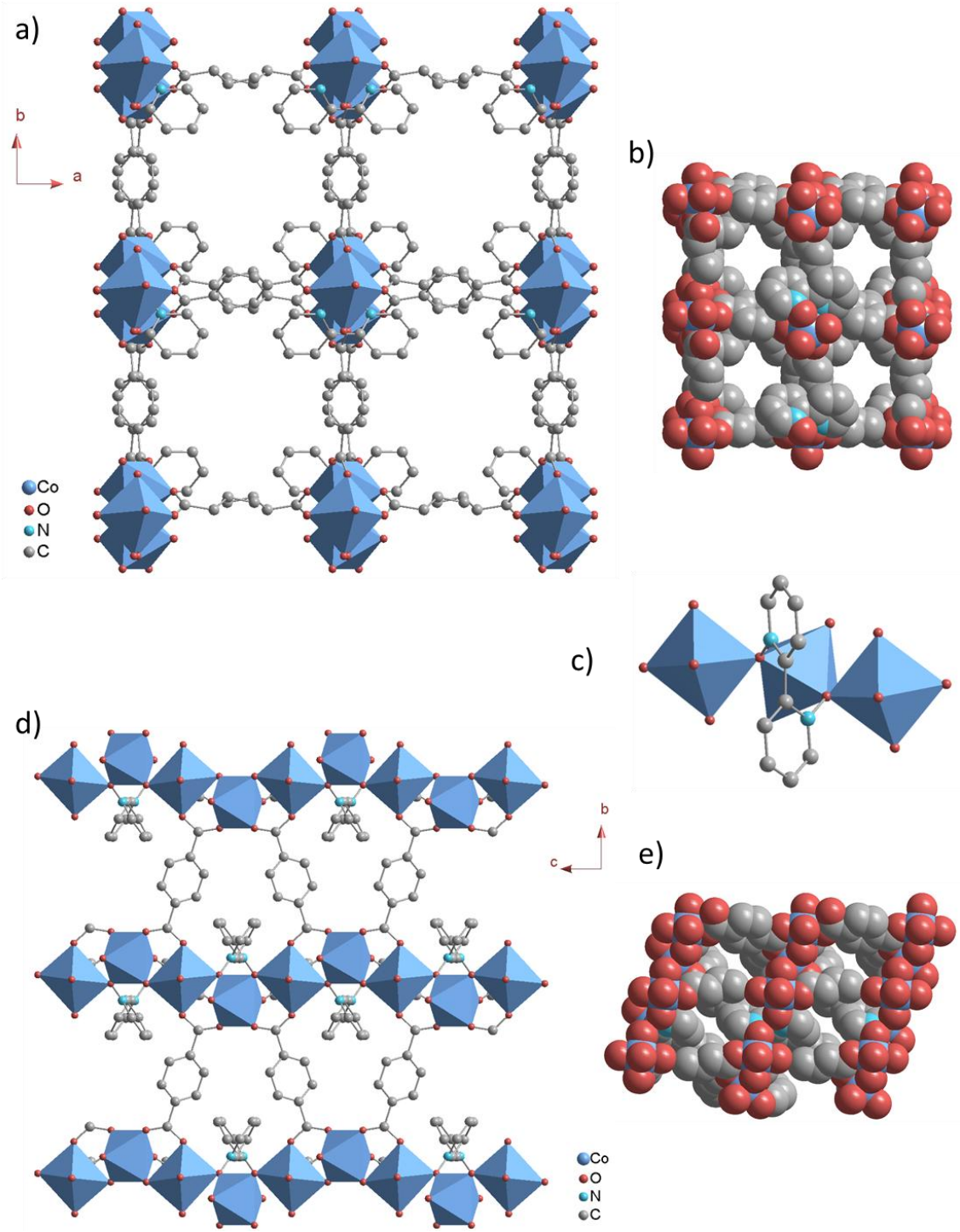

*Figure 5.35: The structure of $Co_2(bdc)_2(2,2'\text{-dPNdO})$ (**8**). a) shows the view along the c-axis b) shows the space-filling view of the c-axis, c) shows the bridging of the 2,2'-dPNdO ligand, d) shows the view along the a-axis and e) shows the space-filling view along the b-axis.*

Structure **9** (Figure 5.37) was synthesised using $Co(NO_3)_2 \cdot 6H_2O$, 1,4-benzenedicarboxylic acid and 4,4'-dipyridyl-*N,N'*-dioxide (**L11**, 4,4'-dPNdO) solvothermally heated to 90 °C in DMF for 10 days. This framework contains infinite

one-dimensional chains of CoO_6 octahedra which contain alternating *trans* and *cis* linkages. These chains are cross-linked by 1,4-benzenedicarboxylate and 4,4'-dipyridyl-*N,N'*-dioxide ligands. It is the different coordination modes of the two linkers, Figure 5.36, which creates the alternating trans/cis linkages of the CoO_6 octahedra. The two ligands alternate along the walls of the pores. The structural connectivity of this framework is described as I^1O^2.

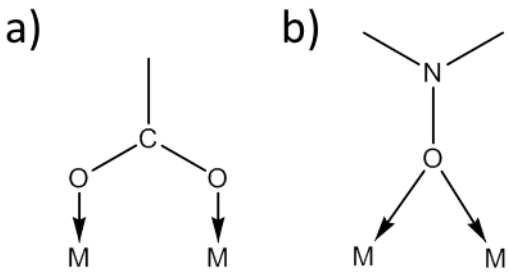

*Figure 5.36: Coordination modes of the organic linkers in product **9**. a) Bridging mode of terephthalate and b) bridging mode of 4,4-dPNdO.*

This framework was published previously by Liu *et al.*[20] using similar synthesis conditions: DMF/MeOH (solvent), 120 °C, 3d. The Mn analogue has also been published by Xu *et al.*[1] Therefore, no further analysis was performed on this material.

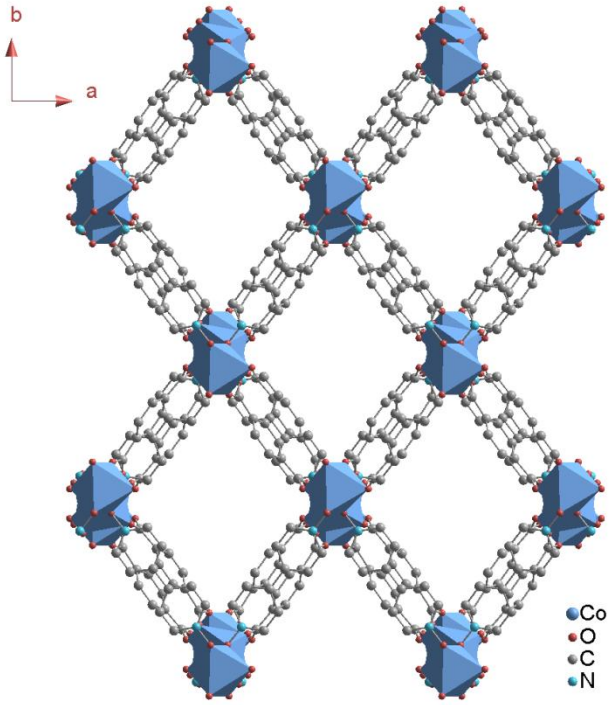

Figure 5.37: Structure of $Co_2(bdc)_2$(4,4'-dPNdO) viewed along the c-axis

The crystallographic data for the three frameworks presented in this section are shown in Table 5.7.

*Table 5.7: Crystallographic data for frameworks **7**-**9**.*

	Framework			
	7	**8**	**8**	**9**
Functionalised PNO	2,2'-dPNO	2,2'-dPNdO	2,2'-dPNdO	4,4'-dPNdO
Temperature/ K	100	296	150	120
a/ Å	9.650(6)	11.3517(2)	11.3407(5)	13.5101(4)
b/ Å	17.270(12)	11.3956(10)	11.3847(9)	17.2795(6)
c/ Å	18.274(12)	13.2806(12)	13.1908(7)	14.1141(4)
α/ °	99.057(11)	90	88.868(6)	90
β/ °	90.485(9)	110.274(11)	69.339(5)	98.448(3)
γ/ °	106.122(10)	90	85.726(5)	90
V/ Å^3	2884.84	1611.54	1589.07	3259.15
Space Group	$P\bar{1}$	*P2/c*	$P\bar{1}$	*I2/a*

5.4.3.2 Thermogravimetric Analysis

Thermogravimetry data were collected for the two new MOFs, $Co_3(bdc)_3(2,2\text{-dPNO})_2$ (**7**) and $Co_2(bdc)_2(2,2\text{-dPNdO})$ (**8**). Data were collected for each MOF both before ("as-made") and after washing. Both frameworks are porous and therefore are expected to contain occluded molecules, consequently, the final mass recorded for Co_3O_4 was used to predict the empirical formula of the MOF and the occluded molecules and the corresponding percentage mass changes.

Figure 5.38a shows the TGA data collected for the as-made $Co_3(bdc)_3(2,2\text{-dPNO})_2$. The predicted starting empirical formula is $[Co_3(bdc)_3(2,2\text{-dPNO})_2]\cdot DMF\cdot 3H_2O$, the predicted percentage mass is labelled as *1* on the graph. The mass labelled *2* = $[Co_3(bdc)_3(2,2\text{-dPNO})_2]\cdot DMF$ and *3* = $Co_3(bdc)_3(2,2\text{-dPNO})_2$. After washing the sample in ethanol, thermogravimetric analysis was repeated and the result is shown in Figure 5.38b. After washing it can be seen that there is only one step in the data before complete decomposition of the framework. The predicted percentage masses are labelled 1 and 2. 1 = $[Co_3(bdc)_3(2,2\text{-dPNO})_2]\cdot EtOH$ and 2 = $Co_3(bdc)_3(2,2\text{-dPNO})_2$. It can be seen that the predicted masses for both experiments agree well with the experimental mass losses.

Figure 5.38c shows the TG data for the as-made form of $Co_2(bdc)_2(2,2\text{-dPNdO})$. Labelled on the graph are the predicted percentage mass changes for three suggested empirical formulas, labelled 1-3. 1 = $[Co_2(bdc)_2(2,2\text{-dPNdO})]\cdot H_2bdc\cdot 2MeOH$, 2 = $[Co_2(bdc)_2(2,2\text{-dPNdO})]\cdot H_2bdc$ and 3 = $Co_2(bdc)_2(2,2\text{-dPNdO})$. After washing the sample in methanol and recording the TG data again it can be seen that there is only one mass loss before the complete decomposition of the framework. The predicted percentage masses have been labelled as 1 and 2. 1 = $[Co_2(bdc)_2(2,2\text{-dPNdO})]\cdot 2MeOH$

and 2 = $Co_2(bdc)_2$(2,2-dPNdO). The predicted formulae and experimental data for the washed sample agree well whereas there is less agreement for the as-made data. This is assumed to be due to the pores being able to take up various molecules from the reaction synthesis that were not included in the predictions.

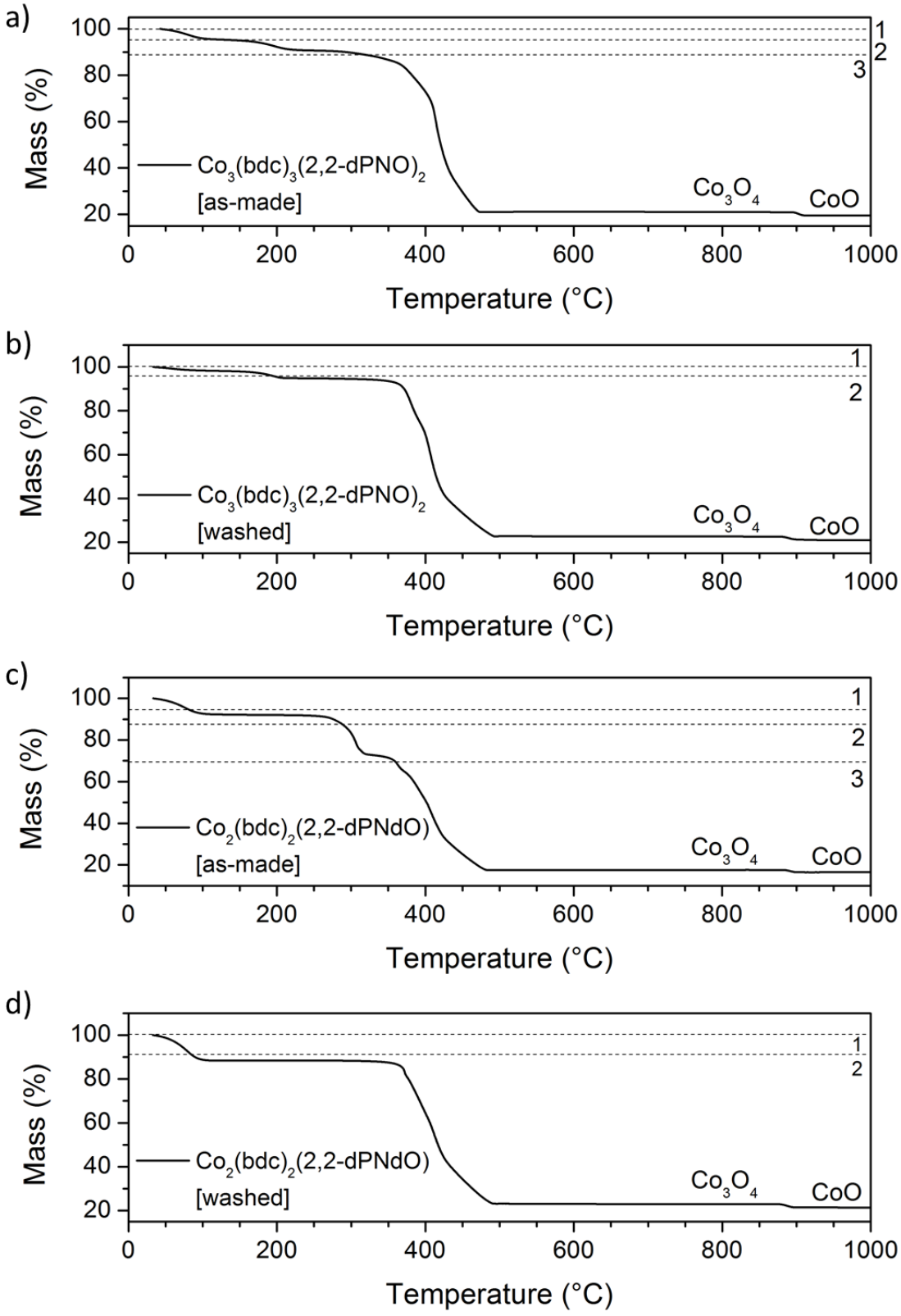

Figure 5.38: Thermogravimetry data collected in air in the range 30 – 1000 °C. a) As-made sample of $Co_3(bdc)_3(2,2\text{-}dPNO)_2$, b) $Co_3(bdc)_3(2,2\text{-}dPNO)_2$ previously washed, c) as-made $Co_2(bdc)_2(2,2\text{-}dPNdO)$ and d) $Co_2(bdc)_2(2,2\text{-}dPNdO)$ previously washed.

Preliminary adsorption isotherms recorded at 30 °C have shown that product **7** can only adsorb 1.6 and 0.4 mmol g^{-1} of CO_2 and CH_4 respectively, at pressures greater than 25 bar. However, product **8** was shown to be much more promising as a potential adsorbent as the preliminary studies showed that the material could adsorb between 4 – 5 mmol g^{-1} of CO_2 and 2 – 3 mmol g^{-1} of CH_4 above 9 bar. These data were recorded at the Aix-Marseille Université. Table 5.8 shows the CO_2 uptake for these two materials and comparable results from MIL-53(Al) and HKUST-1, the highest recorded CO_2 capacity for a MOF is also shown (MOF-200). The TG results presented above show that unreacted reagents and solvent molecules can be removed from the pores by washing the materials in volatile solvents; subsequent adsorption studies will be performed on these *clean* materials to ensure that after the materials are activated, prior to the adsorption studies, the pores are completely free of guest molecules.

Table 5.8: CO_2 adsorption at high pressures for selected MOFs

MOF	CO_2 uptake/ mmol g^{-1}	Pressure/ bar	Temperature/ K
$Co_3(bdc)_3(2,2\text{-dPNO})_2$	1.6	30	303
$Co_2(bdc)_2(2,2\text{-dPNdO})$	5.5	30	303
MIL-53(Al)[21]	10.4	30	304
HKUST-1[22]	10.7	35	298
MOF-200[23]	54.5	50	298

Presented in this section are nine different MOFs which were synthesised using functionalised pyridine-*N*-oxide ligands. The topology of the framework was found to be affected by the electron donating properties of the functional group. The functional

groups which are able to donate electrons into the pyridine ring promote coordination through the N–O bond and are subsequently coordinated within the resulting framework (**L1**-**L4**). The functional groups which withdraw electrons from the ring system, or are too bulky, act as directing agents and are not coordinated within the final product (**L5**-**L8**). Ligands **L1**-**L4** formed MIL-53-type frameworks, the pyridine-*N*-oxide groups were found to block any potential pore space therefore these materials are not porous. Ligand L**5** resulted in the formation of two related frameworks where the product was dependent upon ligand concentration and ligands **L6**-**L8** all gave the same product as the low concentration experiments with **L5**. These frameworks show low capacities towards CO_2 gas and other small molecules. PNO ligands functionalised with pyridyl and pyridyl-*N*-oxide (**L9**-**L11**) produce three potentially porous materials. Adsorption studies were performed on the two novel materials but only $Co_2(bdc)_2$(2,2-dPNdO) was shown to have a good CO_2 adsorption capacity: 5.5 mmol g^{-1}. The adsorption properties of this MOF need further investigation.

5.5 References

1. G. Xu, X. Zhang, P. Guo, C. Pan, H. Zhang and C. Wang, *JACS*, 2010, **132**, 3656-3657.

2. A. K. Cheetham, C. N. R. Rao and R. K. Feller, *Chem. Commun.*, 2006, **0**, 4780-4795.

3. F. A. Cotton and G. Wilkinson, *Advanced Inorganic Chemistry*, Fith edn., John Wiley & Sons, Inc., 1988.

4. S. S.-Y. Chui, S. M.-F. Lo, J. P. H. Charmant, A. G. Orpen and I. D. Williams, *Science*, 1999, **283**, 1148-1150.

5. K. S. Park, Z. Ni, A. P. Côté, J. Y. Choi, R. Huang, F. J. Uribe-Romo, H. K. Chae, M. O'Keeffe and O. M. Yaghi, *Proceedings of the National Academy of Sciences*, 2006, **103**, 10186-10191.

6. F. Millange, N. Guillou, R. I. Walton, J. M. Greneche, I. Margiolaki and G. Férey, *Chem. Commun.*, 2008, 4732-4734.

7. N. Guillou, R. I. Walton and F. Millange, *Z. Kristallogr. - Cryst. Mater.*, 2010, **225**, 552-556.

8. D. Ulku, B. P. Huddle and J. C. Morrow, *Acta Crystallogr. Sect. B: Struct. Sci.*, 1971, **27**, 432-436.

9. T. Bunič, M. Tramšek, E. Goreshnik and B. Žemva, *Acta Chimica Slovenica*, 2008, **55**, 788-792.

10. C. Kittel, *Introduction to Solid State Physics*, Fifth edn., John Wiley & Sons, Inc., New York, 1976.

11. C. Kittel, *Elementary Solid State Physics: a short course*, John Wiley & Sons, Inc., New York, 1962.

12. Y.-L. Fu, J.-L. Ren and S. W. Ng, *Acta Crystallogr. Sect. Sect. E: Struct. Rep. Online*, 2004, **60**, m1507-m1509.

13. D. R. Klein, *Organic Chemistry*, John Wiley & Sons, Inc., 2011, vol.

14. K. Barthelet, J. Marrot, D. Riou and G. Férey, *Angew. Chem. Int. Ed.*, 2002, **41**, 281-284.

15. A. D. Burrows, K. Cassar, R. M. W. Friend, M. F. Mahon, S. P. Rigby and J. E. Warren, *CrystEngComm*, 2005, **7**, 548-550.

16. R. Damgaard Poulsen, A. Bentien, M. Christensen and B. Brummerstedt Iversen, *Acta Crystallogr. Sect. B: Struct. Sci.*, 2006, **62**, 245-254.

17. H. F. Clausen, J. Overgaard, Y. S. Chen and B. B. Iversen, *JACS*, 2008, **130**, 7988-7996.

18. F. Luo, Y. X. Che and J. M. Zheng, *Cryst. Growth Des.*, 2009, **9**, 1066-1071.

19. J. Zhang, J. T. Bu, S. Chen, T. Wu, S. Zheng, Y. Chen, R. A. Nieto, P. Feng and X. Bu, *Angew. Chem. Int. Ed.*, 2010, **49**, 8876-8879.

20. D. Liu, Y. Liu, G. Xu, G. Li, Y. Yu and C. Wang, *Eur. J. Inorg. Chem.*, 2012, **2012**, 4413-4417.

21. S. Bourrelly, P. L. Llewellyn, C. Serre, F. Millange, T. Loiseau and G. Ferey, *JACS*, 2005, **127**, 13519-13521.

22. A. R. Millward and O. M. Yaghi, *JACS*, 2005, **127**, 17998-17999.

23. H. Furukawa, N. Ko, Y. B. Go, N. Aratani, S. B. Choi, E. Choi, A. Ö. Yazaydin, R. Q. Snurr, M. O'Keeffe, J. Kim and O. M. Yaghi, *Science*, 2010, **329**, 424-428.

Chapter 6

Conclusions and Future Work

6 Conclusions

The conclusions and proposed future work, for the three experimental chapters presented in this thesis, are detailed in this chapter. Some of the results have been published.[1-5]

6.1 Summary

The use of energy dispersive X-ray diffraction (EDXRD) enabled the transitions of the flexible MIL-53(Fe) material in response to small liquid-phase alcohols to be followed *in situ*. These studies revealed the conditions necessary to stabilise a transient phase, the structure of which was solved subsequently from high-resolution X-ray diffraction data and shown to be a *half-open* form of the structure. The results of these studies were applied to the industrially relevant problem of removing S- and N- compounds from petrochemicals. The experimental techniques established for the adsorption of alcohols were used to follow the uptake of benzothiophene, benzothiazole and indole from solution. The solvent was found to affect the rate of guest uptake; it was shown that the non-polar solvent heptane promoted guest uptake and that there was a guest concentration threshold to be exceeded when the polar solvent, isopropanol, was used. At low guest concentrations, conditions which are more representative of real applications, MIL-53(Fe) favourably adsorbed molecules containing hydrogen-bond acceptors over those containing hydrogen-bond donors. The ability of MIL-53(Fe) to act as an adsorbent in response to low concentrations of guest molecules is beneficial for the removal of pollutants which are normally present as minor components in a mixture of chemicals. Unlike many MOFs used for the adsorption of N/S-containing

compounds, MIL-53 does not have any coordinatively unsaturated sites. Therefore, recycling of this material will be easier as there are no direct M-guest interactions.

Comparable gas phase studies following the uptake of methanol vapour by MIL-53(Fe) showed that the expansion pathway was the same as was seen during the liquid phase experiments; expansion from the hydrated phase to the fully-open phase occurred via an intermediate half-open phase. The stability of this half-open phase was found to be dependent upon the flow rate of the carrier gas used to add the methanol. Thermogravimetry experiments were used to determine that two molar equivalents of methanol can be accommodated within the pores of MIL-53(Fe) independent of the starting phase of MIL-53(Fe), *i.e.* hydrated or dehydrated. It was also determined by TGA and inelastic neutron scattering that the adsorption of methanol using the hydrated phase of MIL-53(Fe) did not result in the displacement of the occluded water molecules but the co-adsorption of the methanol molecules inside the pores.

The adsorption properties of eight materials, based on the MIL-53(Al) framework, were found to be affected by the different modifications made to the phenyl ring of the terephthalate linkers. The material modified with two hydroxyl groups was found, in contrast to most of the other materials, to contract upon thermal dehydration. The amino modified material was found to have no flexibility in response to the studies performed in this work. And the material which was modified with a cyclohexyl ring showed no uptake of the polar guest molecules that were studied, *i.e*. methanol and excess water. However, among the six frameworks with modified phenyl rings (the amino framework has been excluded), little selectivity was shown towards guest molecules; all six materials adsorbed methanol and the nitro and methyl modified materials both adsorbed heptane. These results highlight that modifications to MOFs can change the behaviour

of these materials but also that more work is needed to understand the exact nature of the interactions which govern guest adsorption.

The neutron scattering studies of the local structure of MIL-53(Cr) are still in their infancy but the preliminary analysis shows that there is the potential for this type of technique to provide valuable information about the intricacies of the framework, which are responsible for the breathing phenomena and the differences seen between framework analogues.

A series of mixed-metal MOFs that include cobalt were successfully synthesised; X-ray diffraction was used to determine their structures and demonstrate that the materials crystallised as a single phase. This series of MOFs have the same diamond-shaped pores as MIL-53 but thermodiffraction studies show they do not exhibit the same structural flexibility. Modification of the pendant, pyridine-*N*-oxide (PNO) linkers was used to investigate the inherent flexibility of the diamond-shaped pores. The synthesis of four MIL-53-type frameworks was achieved; the PNO ligand modified with a phenyl group showed that the diamond-shaped pores could expand to accommodate very large groups. Pyridine-*N*-oxide groups substituted with electron withdrawing groups in the 4-position or with very bulky substituents were all found to produce the same framework, which did not incorporate the functionalised PNO and did not have a MIL-53-type topology. Synthesis of new materials using functionalised PNOs which include two potential coordination sites resulted in the formation of three frameworks, two of which were found to be novel. The properties of these two frameworks were investigated and they were found to be porous, preliminary studies show that the $Co_2(bdc)_2$(2,2-dPNdO) material has the potential to be a good CO_2 adsorbent. Computational studies predict

that the narrow pore channels of this material may be conducive to separations of straight and branched molecules.

6.2 Future Work

The preliminary studies detailed in this work, such as the uptake of N/S compounds by MIL-53(Fe), the investigations of the local structure of MIL-53(Cr) and the synthesis of novel porous Co (II) materials, present opportunities for this work to be expanded upon in the future.

The use of MIL-53(Fe) as an adsorbent for S- and N- containing compounds was shown as a potential industrial application for this material. However, adsorption studies in the presence of competing aromatic molecules present in crude petrochemicals, such as toluene, should also be investigated. Commercially viable MOFs are normally shaped into pellets for industrial applications and this presents problems for the performance of the MOF as the polymer binder used for making pellets normally results in a loss of adsorption capacity. The structural integrity of the pellet, which could be affected by the 50% volume increase upon the adsorption of guest molecules, presents an additional problem for MIL-53. These problems need to be explored to prove the feasibility of using MIL-53(Fe) as an industrial adsorbent.

Investigative work to identify the specific modifications that enhance the uptake of particular guest molecules requires high through-put adsorption methods where screening of guest uptake in small-scale experiments is possible. However, the initial work presented in this thesis that showed a strong interaction at low guest concentrations between H_2S and the thiol modified MIL-53(Al) needs to be investigated further. The reliability of the synthesis and the crystallinity of the sample need to be

improved and the structure ideally needs to be solved. The adsorption studies should be expanded to include various S-containing compounds, such as thiophene and benzothiophene, to explore the potential of this MOF to be used for industrial applications.

As mentioned in Section 4.4, where the local structure of MIL-53(Cr) was investigated, multi-phase modelling is not yet available and complementary X-ray techniques are still in the design phase, therefore, this work should be resumed when these tools are available. When achievable, this investigation, which will include ideally additional MIL-53 analogues, will provide detailed information regarding the differences and similarities in the local structure of these frameworks. This could ultimately enable a greater understanding of the mechanics of the unusual flexibility of MIL-53.

The newly synthesised MOF $Co_2(bdc)_2$(2,2-dPNdO) has shown promise as an adsorbent for CO_2 and computational studies have identified the architecture of the pores as promising for the separation of straight and branched molecules. Further adsorption studies are required to identify further applications where this MOF may excel. The synthesis of this MOF using different metal cations should be studied to explore the effect upon the adsorption of CO_2 and other guest molecules. The scale-up of this MOF and the activation process also need to be optimised for the ease of future studies.

6.3 References

1. R. I. Walton, A. S. Munn, N. Guillou and F. Millange, *Chem. Eur. J.*, 2011, **17**, 7069-7079.

2. B. Van de Voorde, A. S. Munn, N. Guillou, F. Millange, D. E. De Vos and R. I. Walton, *PCCP*, 2013, **15**, 8606-8615.

3. A. S. Munn, A. J. Ramirez-Cuesta, F. Millange and R. I. Walton, *Chem. Phys.*, 2013, **In Press**.

4. A. S. Munn, G. J. Clarkson, F. Millange, Y. Dumont and R. I. Walton, *CrystEngComm*, 2013, **DOI: 10.1039/C3CE41268G**.

5. A. S. Munn, G. J. Clarkson and R. I. Walton, *Acta Crystallogr. Sect. B: Struct. Sci.*, 2013, **In Press**.

Appendix

A. Appendix

A.1 Liquid Phase Adsorption

Table A.1: Experimental and simulated d-spacings with the associated hkl labels for the EDXRD data recorded for ethanol adsorption at various concentrations.

Figures 1.1-1.4		Energy/ keV	d_{exp}/ Å	d_{cal}/ Å	hkl
a) EtOH-100%	(Hydrated- *C2/c*)	49.44	9.579	9.580	200
		66.484	7.124	7.099	110
	(Fully-open- *Imcm*)	44.276	10.697	10.657	110
		59.204	7.999	8.104	200
b) EtOH-75%	(Hydrated- *C2/c*)	49.492	9.569	9.580	200
		66.536	7.118	7.099	110
	(Fully-open- *Imcm*)	44.321	10.686	10.657	110
		59.313	7.985	8.104	200
c) EtOH-25%	(Hydrated- *C2/c*)	25.416	9.364	9.580	200
		34.011	6.998	7.099	110
	(Half-open- *C2/c*)	25.804	9.223	9.434	200
		29.409	8.093	8.303	110
	(Fully-open- *Imcm*)	22.795	10.441	10.657	110
		30.357	7.840	8.104	200
d) EtOH-25%	(Hydrated- *C2/c*)	24.028	9.553	9.580	200
		32.127	7.145	7.099	110
	(Half-open- *C2/c*)	24.299	9.446	9.434	200
		27.937	8.216	8.303	110

Table A.2: Experimental and simulated d-spacings with the associated hkl labels for the EDXRD data recorded for propan-1-ol adsorption at various concentrations.

Figures 1.5-1.7		Energy/ keV	d_{exp}/ Å	d_{cal}/ Å	hkl
a) ^{n}PrOH-100%	(Hydrated- *C2/c*)	49.496	9.568	9.580	200
		66.532	7.118	7.099	110
	(Half-open- *C2/c*)	50.329	9.410	9.373	200
		55.368	8.554	8.570	110
	(Fully-open- *Imcm*)	44.733	10.587	10.249	110
		57.906	8.179	8.569	200
b) ^{n}PrOH-25%	(Hydrated- *C2/c*)	25.242	9.429	9.580	200
		33.782	7.045	7.099	110
	(Half-open- *Imcm*)	25.808	9.222	9.373	200
		28.308	8.408	8.570	110
	(Fully-open- *Imcm*)	23.077	10.313	10.249	110
		28.906	8.234	8.569	200
c) ^{n}PrOH-20%	(Hydrated- *C2/c*)	23.92	9.596	9.580	200
		31.945	7.185	7.099	110
	(Half-open- *C2/c*)	24.317	9.439	9.373	200
		26.751	8.580	8.570	110

Table A.3: Experimental and simulated d-spacings with the associated hkl indices for the EDXRD data recorded for propan-2-ol adsorption.

Figure 1.8		Energy/ keV	d_{exp}/ Å	d_{cal}/ Å	hkl
a) ^{i}PrOH-100%	(Hydrated- *C2/c*)	49.459	9.576	9.580	200
		66.505	7.121	7.099	110
	(Half-open- *C2/c*)	50.882	9.308	9.305	200
		54.097	8.755	8.768	110

Table A.4: Experimental and simulated d-spacings with the associated hkl indices for the EDXRD data recorded for the uptake of heterocycle guest molecules from hydrated MIL-53(Fe) in isopropanol

Figure 1.13		Energy/ keV	d_{exp}/ Å	d_{cal}/ Å	hkl
a) Benzothiophene	(Hydrated- *C2/c*)	29.832	9.593	9.580	200
		40.845	7.007	7.099	110
	(Fully-open- *Imcm*)	26.481	10.807	10.713	110
		36.509	7.839	7.901	200
b) Benzothiazole	(^{i}POH half-open- *C2/c*)	30.763	9.303	9.305	200
		32.678	8.757	8.768	110
	(Fully-open- *Imcm*)	26.747	10.700	10.724	110
		35.365	8.092	7.886	200
c) Indole	(Hydrated- *C2/c*)	29.726	9.627	9.580	200
		40.871	7.002	7.099	110
	(Fully-open- *Imcm*)	26.587	10.764	10.666	110
		35.764	8.002	8.032	200

Table A.5: Experimental and simulated d-spacings with the associated hkl indices for the EDXRD data recorded for the uptake of heterocycle guest molecules from dehydrated MIL-53(Fe) in isopropanol

Figure 1.14		Energy/ keV	d_{exp}/ Å	d_{cal}/ Å	hkl
a) Benzothiophene	(^{i}POH half-open - *C2/c*)	37.201	9.300	9.305	200
		39.269	8.811	8.768	110
	(Fully-open- *Imcm*)	32.36	10.692	10.713	110
		43.288	7.993	7.901	200
b) Benzothiazole	(^{i}POH half-open- *C2/c*)	37.295	9.277	9.305	200
		39.457	8.769	8.768	110
	(Fully-open- *Imcm*)	32.760	10.561	10.724	110
		42.512	8.1399	7.886	200
c) Indole	(^{i}POH half-open - *C2/c*)	37.271	9.283	9.305	200
		39.387	8.784	8.768	110
	(Fully-open- *Imcm*)	-	-	10.666	110
		-	-	8.032	200

Table A.6: Experimental and simulated d-spacings with the associated hkl indices for the EDXRD data recorded for the uptake of heterocycle guest molecules from dehydrated MIL-53(Fe) in heptane

Figure 1.15		Energy/ keV	d_{exp}/ Å	d_{cal}/ Å	hkl
a) Benzothiophene	(Dehydrated- *C2/c*)	36.496	9.480	9.656	200
		55.155	6.273	6.425	110
	(Fully-open- *Imcm*)	32.901	10.516	10.713	110
		44.557	7.765	7.901	200
b) Benzothiazole	(Dehydrated - *C2/c*)	36.332	9.523	9.656	200
		54.779	6.316	6.425	110
	(Fully-open- *Imcm*)	32.830	10.539	10.724	110
		43.452	7.962	7.886	200
c) Indole	(Dehydrated - *C2/c*)	36.355	9.517	9.656	200
		54.850	6.308	6.425	110
	(Fully-open- *Imcm*)	-	-	10.666	110
		-	-	8.032	200

Table A.7: Experimental and simulated d-spacings with the associated hkl indices for the EDXRD data recorded for the uptake of heterocycle guest molecules from hydrated MIL-53(Fe) in isopropanol

Figure 1.16		Energy/ keV	d_{exp}/ Å	d_{cal}/ Å	hkl
a) Benzothiophene	(^{i}POH half-open - *C2/c*)	36.0283	9.339	9.305	200
		38.288	8.788	8.768	110
	(Fully-open- *Imcm*)	31.485	10.687	10.713	110
		42.133	7.986	7.901	200
b) Benzothiazole	(^{i}POH half-open- *C2/c*)	36.122	9.315	9.305	200
		38.265	8.793	8.768	110
	(Fully-open- *Imcm*)	31.811	10.577	10.724	110
		40.991	8.208	7.886	200
c) Indole	(^{i}POH half-open - *C2/c*)	35.982	9.351	9.305	200
		38.195	8.809	8.768	110
	(Fully-open- *Imcm*)	-	-	10.666	110
		-	-	8.032	200

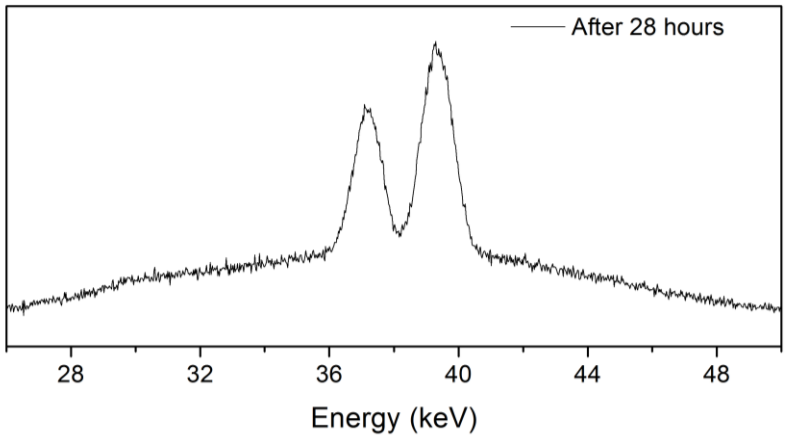

Figure A.1: Individual EDXRD pattern of dehydrated MIL-53(Fe) in a solution of indole and isopropanol, 28 hours after complete addition.

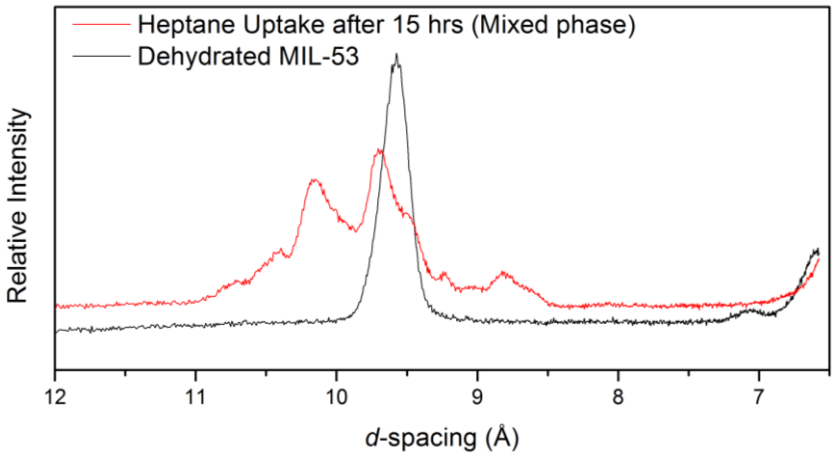

Figure A.2: EDXRD patterns showing the adsorption of heptane by MIL-53(Fe)

A.2 Gas Phase Adsorption

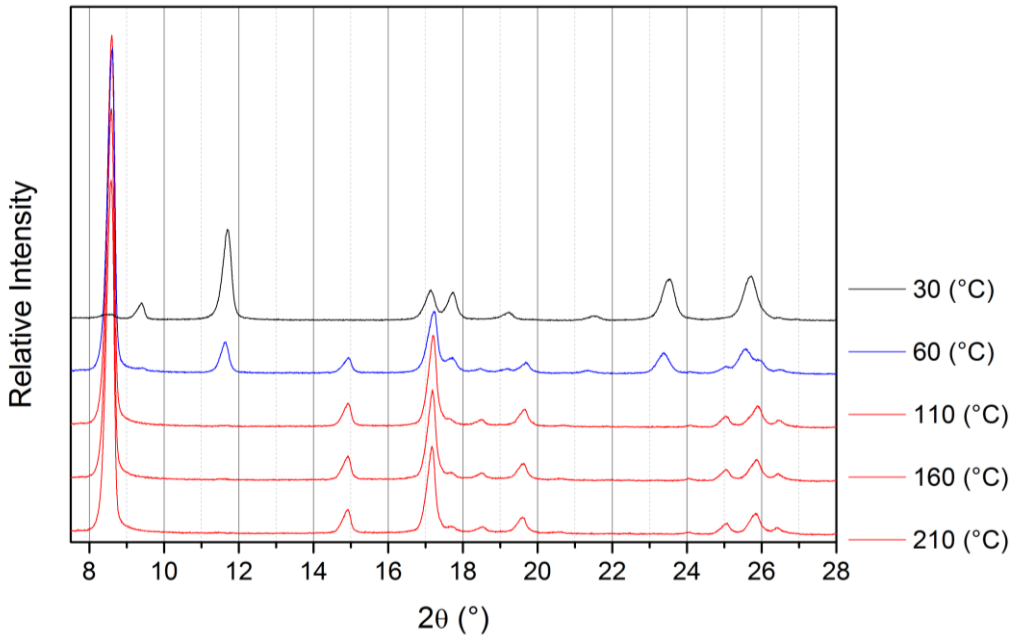

Figure A.3: Behaviour of dehydrated MIL-53(Al)-NO_2 upon cooling from 210°C to 30°C. Red = dehydrated phase, blue = mixed phase and black = hydrated phase.

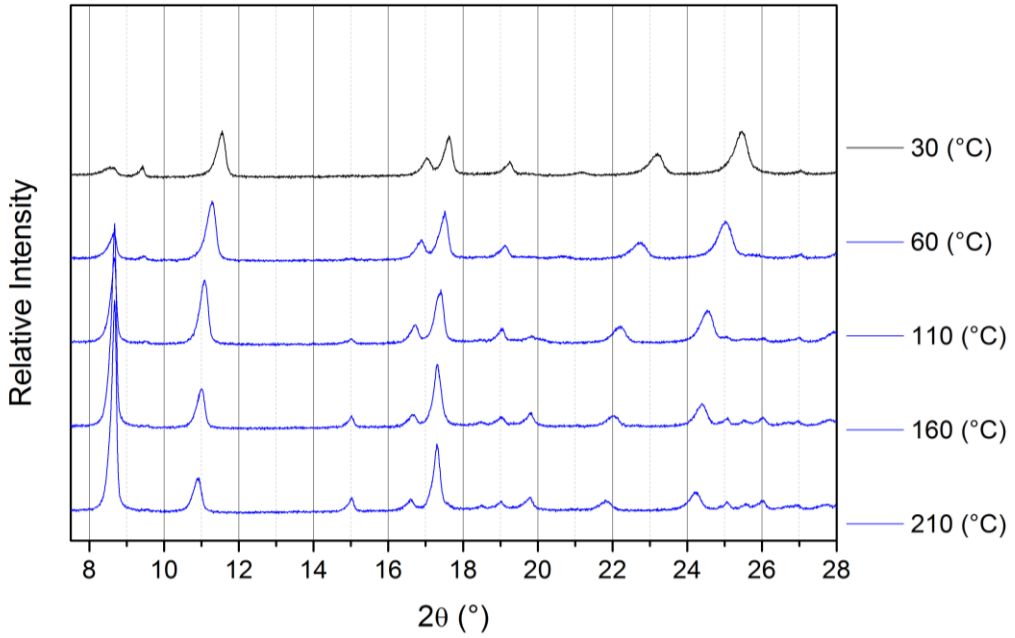

Figure A.4: Behaviour of dehydrated MIL-53(Al)-Br upon cooling from 210°C to 30°C. Blue = mixed phase and black = hydrated phase.

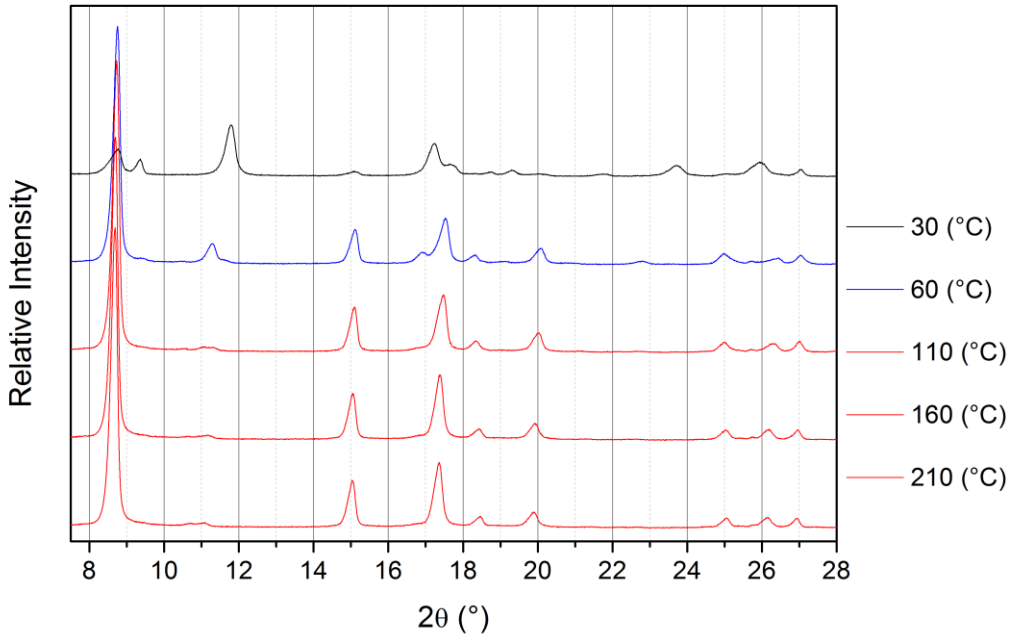

Figure A.5: Behaviour of dehydrated MIL-53(Al)-CH_3 upon cooling from 210°C to 30°C. Red = dehydrated phase, blue = mixed phase and black = hydrated phase.

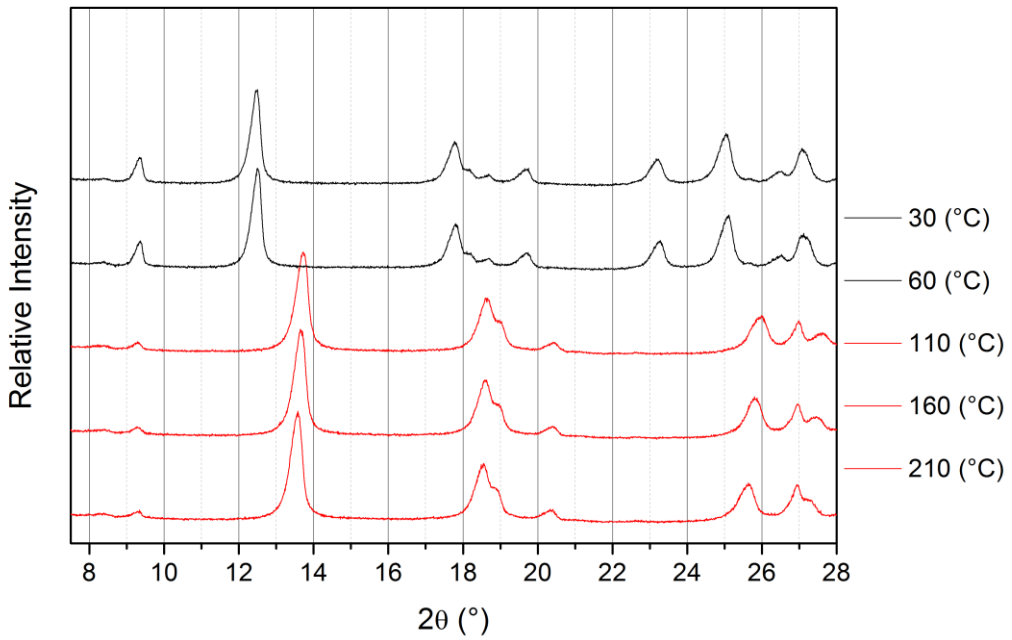

Figure A.6: Behaviour of dehydrated MIL-53(Al)–$(OH)_2$ upon cooling from 210°C to 30°C. Red = dehydrated phase, blue = mixed phase and black = hydrated phase.

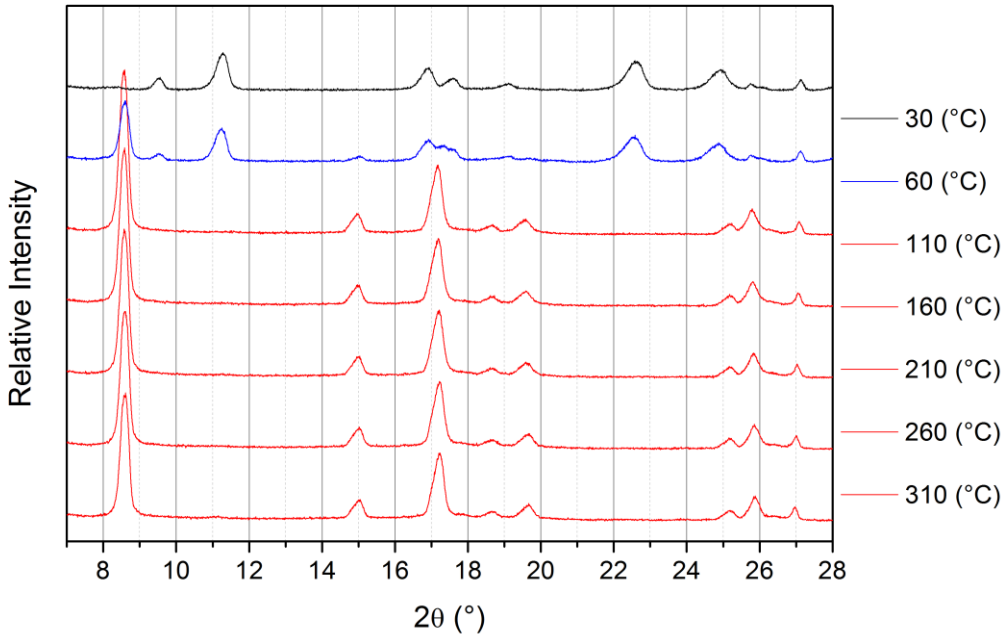

Figure A.7: Behaviour of dehydrated MIL-53(Al)–COOH upon cooling from 210°C to 30°C. Red = dehydrated phase, blue = mixed phase and black = hydrated phase.

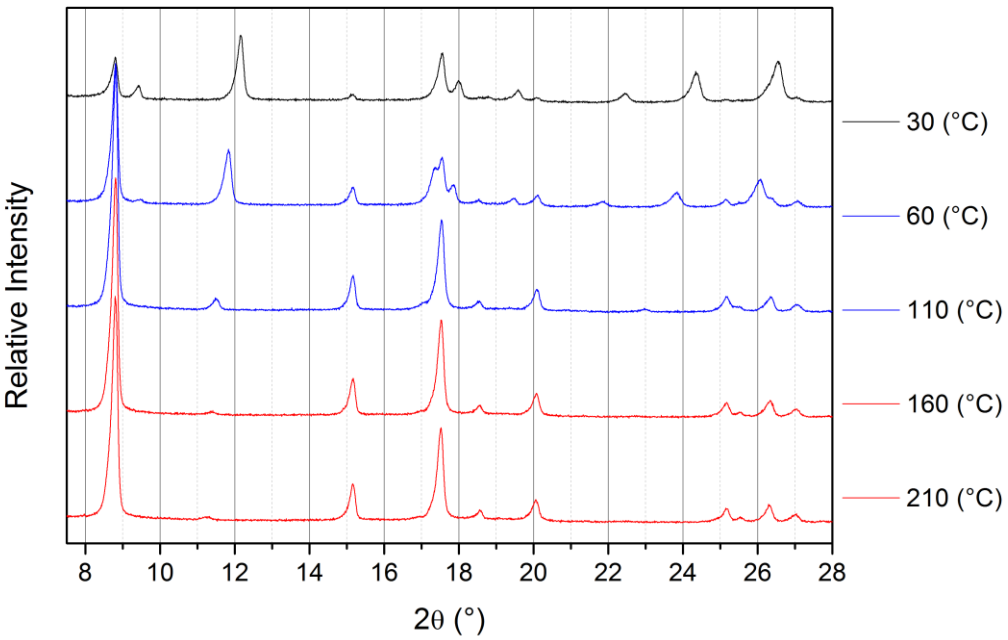

Figure A.8: Behaviour of dehydrated MIL-53(Al)-Cl upon cooling from 210°C to 30°C. Red = dehydrated phase, blue = mixed phase and black = hydrated phase.

Table A.8: Predicted and experimental percentage mass changes for the TG data of the thiol modified MIL-53(Al) samples presented in Section 4.3.3

Product Number	Predicted Empirical Formulae	Predicted Percentage Mass (%)	Experimental Percentage Mass (%)
A	$Al(C_8H_4O_4S_2)(OH)\cdot[H_2O]$ $Al(C_8H_4O_4S_2)(OH)$	97.6 91.4	100 90.4
B	$Al(C_8H_4O_4S_2)(OH)$	99.6	100 95.3

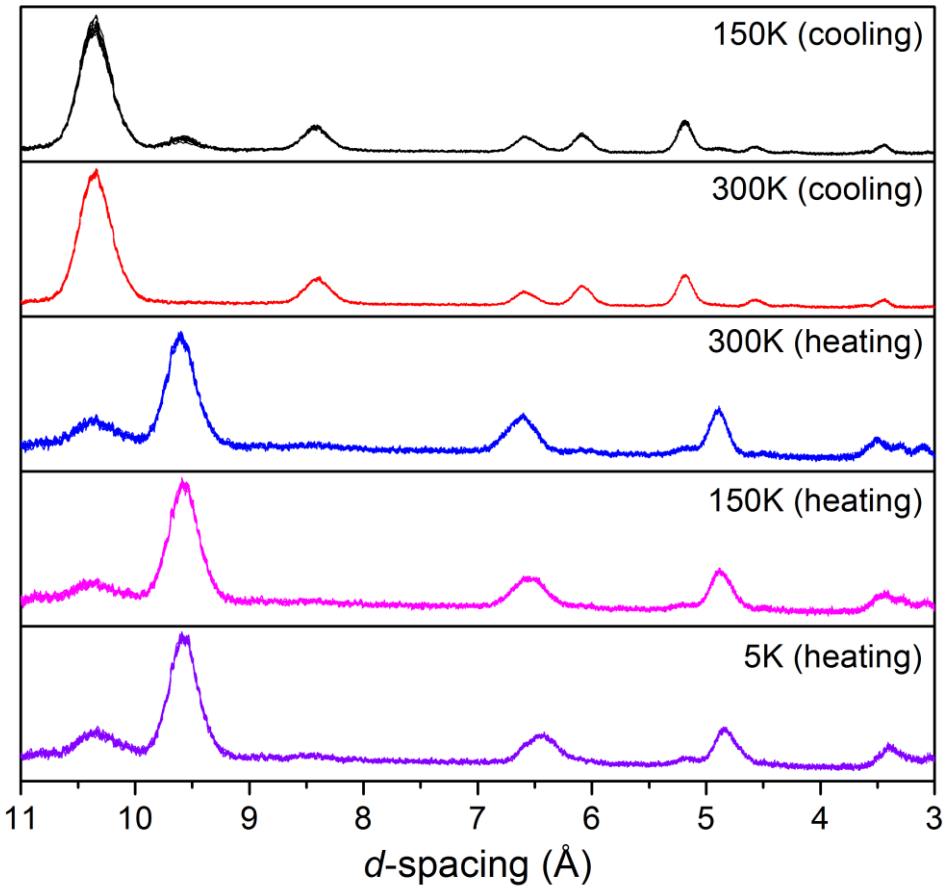

Figure A.9: Neutron diffraction data. One hour accumulations that show no change in the positions of the Bragg peaks

A.3 Synthesis

*Table A.9: Synthesis conditions for products **1-9***

Material		Conditions			Molar equivalents of reagents			
		Temp (°C)	Time	$Conc^n$ (M)	Co^{2+}	bdc	PNO	Solvent
MIL-53(PNO-Br)	**1**	120	7 d	0.07	1	3	3	DMF
MIL-53(PNO-MeO)	**2**	120	2 d	0.07	1	2	2	DMF
MIL-53(PNO-iso)	**3**	100	6 d	0.03	1	3	3	DMF
MIL-53(PNO-phenyl)	**4**	120	7 d	0.07	1	3	3	DMF
$Co_3(bdc)_4$	**5**	120	5 h	0.07	1	2	0.5	DMF
$Co_3(bdc)_3DMF_2$	**6**	120	7 d	0.07	1	3	3	DMF
$Co_3(bdc)_3$(2,2-dPNO)	**7**	90	2 d	0.07	1	2	2	DMF
$Co_2(bdc)_2$(2,2-dPNdO)	**8**	100	7 d	0.07	1	2	2	DMF/MeOH
$Co_2(bdc)_2$(4,4-dPNdO)	**9**	120	3.5 d	0.03	1	1	1	DMF

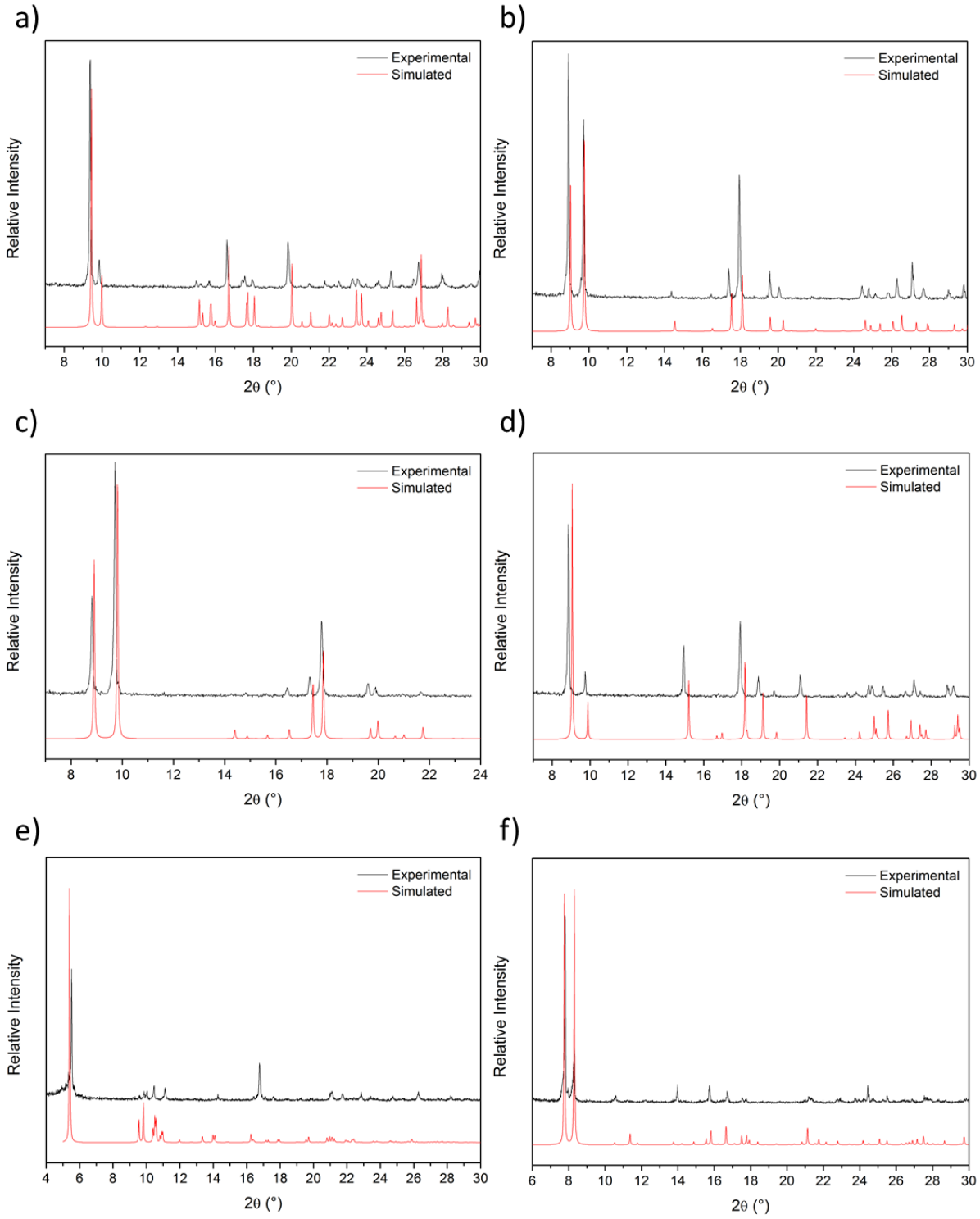

Figure A.10: PXRD patterns for a) Co(bdc)(PNO-Br), b) Co(bdc)(PNO-OMe), c) Co(bdc)(PNO)(isoquinoline), d) Co(bdc)(PNO-phenyl), e) $Co_3(bdc)_3(2,2\text{-dPNO})_2$ and f) $Co_2(bdc)_2(2,2\text{-dPNdO})$

Cell parameters and atomic coordinates for the crystal structures presented in Chapter 5

$Co(C_8H_4O_4)(C_5H_5NO)$

Cell length a	19.2841(15) Å
Cell length b	7.1837(7) Å
Cell length c	9.2835(9) Å
Cell angle α	90.00 °
Cell angle β	90.00 °
Cell angle γ	90.00 °
Cell volume	1286.1(2) $Å^3$
Symmetry cell setting	orthorhombic
Symmetry space group	*Imma*
Cell measurement temp.	296 K

Atomic Coordinates

Co1	Co	0.5000	0.0000	0.5000
O1	O	0.5000	0.2500	0.6175(7)
N2	N	0.5000	0.2500	0.7583(9)
C3	C	0.4395(5)	0.2500	0.8287(10)
H3	H	0.3981	0.2500	0.7775
C4	C	0.4387(5)	0.2500	0.9761(10)
H4	H	0.3969	0.2500	1.0260
C5	C	0.5000	0.2500	1.0485(14)
H5	H	0.5000	0.2500	1.1487
O7	O	0.42101(16)	0.0942(4)	0.3664(4)
C8	C	0.3933(3)	0.2500	0.3503(7)
C9	C	0.3187(3)	0.2500	0.2986(8)
C10	C	0.2837(3)	0.0872(7)	0.2741(9)

H10	H	0.3060	-0.0256	0.2902

$Co(C_8H_4O_4)(C_5H_5NO)_{0.65}(F)_{0.35}$

Cell length a	20.4413(15) Å
Cell length b	9.2327(7) Å
Cell length c	7.1660(5) Å
Cell angle α	90.00 °
Cell angle β	109.147(4) °
Cell angle γ	90.00 °
Cell volume	1277.6 (2) $Å^3$
Symmetry cell setting	monoclinic
Symmetry space group	*C2/c*
Cell measurement temp.	-

Atomic Coordinates

Co1	Co	0.0000	0.5000	0.0000
O1	O	0.0000	0.6175	0.2500
N2	N	0.0000	0.7610	0.2500
C3	C	0.0599	0.8310	0.3280
H3	H	0.1019	0.7785	0.3817
C4	C	0.0602	0.9779	0.3297
H4	H	0.1025	1.0286	0.3867
C5	C	0.0000	1.0535	0.2500)
H5	H	0.0000	1.1564	0.2500
O6	O	0.0837	0.3787	0.1680
O7	O	0.0747	0.3540	0.4710
C7	C	0.1061	0.3495	0.3490

C8	C	0.1806	0.2986	0.4255
C9	C	0.2114	0.2571	0.6273
H9	H	0.1852	0.2632	0.7148
C10	C	0.2213	0.2915	0.3041
H10	H	0.2022	0.3211	0.1702

$Co(C_8H_4O_4)(C_5H_4NO\text{-}Br)$

Cell length a	7.1962(8) Å
Cell length b	10.0563(13) Å
Cell length c	18.748(3) Å
Cell angle α	90.00 °
Cell angle β	91.548 °
Cell angle γ	90.00 °
Cell volume	1356.3(3) $Å^3$
Symmetry cell setting	monoclinic
Symmetry space group	*P2/c*
Cell measurement temp.	296(2) K

Atomic Coordinates

Co1	Co	-0.5000	0.5000	0.5000
Co2	Co	0.0000	0.5000	0.5000
O1	O	-0.1070(8)	0.6558(7)	0.4394(3)
O2	O	-0.4131(8)	0.6340(7)	0.4249(3)
C2	C	-0.2582(12)	0.6674(9)	0.4034(5)
C3	C	-0.2520(11)	0.7294(10)	0.3305(5)
C4	C	-0.4137(12)	0.7512(14)	0.2914(5)
H4	H	-0.5274	0.7293	0.3107

C5	C	-0.4093(13)	0.8053(13	0.2236(5)
H5	H	-0.5200	0.8178	0.1978
C6	C	-0.2433(12)	0.8410(10)	0.1937(5)
C7	C	-0.0830(13)	0.8267(13)	0.2352(5)
H7	H	0.0301	0.8558	0.2180
C8	C	-0.0903(12)	0.7691(12)	0.3023(5)
H8	H	0.0197	0.7573	0.3287
O9	O	-0.3917(8)	0.8924(8)	0.0838(3)
C9	C	-0.2393(12)	0.8894(10)	0.1175(5)
O10	O	-0.0837(8)	0.9204(7)	0.0949(3)
O11	O	-0.2488(7)	0.3928(6)	0.4868(3)
N12	N	-0.2450(11)	0.2659(11)	0.4844(6)
C13	C	-0.2658(14)	0.1949(12)	0.5441(8)
H13	H	-0.2871	0.2394	0.5866
Br14	Br	-0.2821(3	-0.0329(2)	0.62917(14)
C14	C	-0.2569(16)	0.0591(14)	0.5446(8)
C15	C	-0.2397(17)	-0.0041(16)	0.4840(9)
H15	H	-0.2392	-0.0965	0.4833
C16	C	-0.2217(18)	0.0680(16)	0.4191(9)
H16	H	-0.2089	0.0233	0.3761
C17	C	-0.2236(16)	0.2019(14)	0.4209(8)
H17	H	-0.2105	0.2504	0.3791

$Co(C_8H_4O_4)(C_5H_4NO\text{-}OMe)$

Cell length a	7.1507(2) Å
Cell length b	18.1353(4) Å
Cell length c	11.6447(3) Å
Cell angle α	90.00 °
Cell angle β	90.00°
Cell angle γ	90.00 °

Cell volume	1510.09(7) Å^3
Symmetry cell setting	orthorhombic
Symmetry space group	*Pnma*
Cell measurement temp.	100(2) K

Atomic Coordinates

Co1	Co	0.22106(9)	0.7500	0.24179(5)
O1	O	0.1264(4)	0.66666(16)	0.3479(3)
O2	O	-0.1838(4)	0.66827(15)	0.3686(3)
C2	C	-0.0250(5)	0.6408(2)	0.3801(4)
C3	C	-0.0135(5)	0.5673(2)	0.4425(4)
C4	C	0.1395(7)	0.5221(3)	0.4274(6)
H4	H	0.2366	0.5367	0.3765
C5	C	-0.1530(7)	0.5442(3)	0.5145(6)
H5	H	-0.2607	0.5742	0.5247
O6	O	-0.0343(4)	0.7500	0.1599(3)
N7	N	-0.0485(5)	0.7414(2)	0.0481(3)
C8	C	-0.0432(9)	0.8029(2)	-0.0233(3)
H8	H	-0.0297	0.8507	0.0088
C9	C	-0.0578(9)	0.7942(2)	-0.1415(3)
H9	H	-0.0542	0.8362	-0.1903
C10	C	-0.0776(7)	0.7242(3)	-0.1885(3)
C11	C	-0.0828(10)	0.6628(2)	-0.1172(3)
H11	H	-0.0963	0.6149	-0.1493
C12	C	-0.0683(9)	0.6714(2)	0.0011(3)
H12	H	-0.0719	0.6294	0.0498
O13	O	-0.0922(9)	0.7116(4)	-0.3012(5)
C14	C	-0.0802(12)	0.7739(5)	-0.3774(7)
H14A	H	-0.0996	0.7575	-0.4567
H14B	H	0.0436	0.7966	-0.3705
H14C	H	-0.1765	0.8100	-0.3569

Co($C_8H_4O_4$)(Isoquinoline-*N*-oxide)

Cell length a	18.025(16) Å
Cell length b	7.184(6) Å
Cell length c	11.906(11) Å
Cell angle α	90.00 °
Cell angle β	90.00°
Cell angle γ	90.00 °
Cell volume	1542(2) $Å^3$
Symmetry cell setting	orthorhombic
Symmetry space group	*Pnma*
Cell measurement temp.	100(2) K

Atomic Coordinates

Co1	Co	0.5000	0.5000	0.5000
O1	O	0.4077(2)	0.5945(6)	0.5862(4)
C2	C	0.3795(4)	0.7500	0.6053(6)
C3	C	0.3051(4)	0.7500	0.6632(6)
C4	C	0.2795(16)	0.908(3)	0.718(3)
H4	H	0.3091	1.0174	0.7125
C5	C	0.2132(15)	0.921(4)	0.780(3)
H5	H	0.1976	1.0327	0.8156
C4A	C	0.2613(15)	0.912(3)	0.672(3)
H4A	H	0.2763	1.0244	0.6361
C5A	C	0.1964(17)	0.906(3)	0.733(4)
H5A	H	0.1678	1.0167	0.7391
C6	C	0.1711(4)	0.7500	0.7850(6)
C7	C	0.0986(4)	0.7500	0.8528(7)
O8	O	0.0727(2)	0.9057(6)	0.8770(4)
O9	O	0.4900(3)	0.2500	0.5878(4)
N10	N	0.4861(4)	0.2500	0.7019(5)

C11	C	0.5475(5)	0.2500	0.7614(7)
H11	H	0.5945	0.2500	0.7254
C12	C	0.5424(6)	0.2500	0.8814(7)
C13	C	0.6072(8)	0.2500	0.9466(10)
H13	H	0.6541	0.2500	0.9103
C14	C	0.6043(11)	0.2500	1.0599(10)
H14	H	0.6488	0.2500	1.1027
C15	C	0.5350(9)	0.2500	1.1138(9)
H15	H	0.5325	0.2500	1.1936
C16	C	0.4711(8)	0.2500	1.0520(8)
H16	H	0.4244	0.2500	1.0888
C17	C	0.4744(7)	0.2500	0.9339(8)
C18	C	0.4112(7)	0.2500	0.8651(9)
H18	H	0.3632	0.2500	0.8981
C19	C	0.4183(6)	0.2500	0.7511(9)
H19	H	0.3751	0.2500	0.7054
O10	O	0.694(3)	0.7500	0.461(4)

$Co(C_8H_4O_4)(C_5H_4NO$-phenyl)

Cell length a	12.9936(8) Å
Cell length b	17.9026(8) Å
Cell length c	7.1797(4) Å
Cell angle α	90.00 °
Cell angle β	116.294(8) °
Cell angle γ	90.00 °
Cell volume	1497.32(16) $Å^3$
Symmetry cell setting	monoclinic
Symmetry space group	*C2/c*

Cell measurement temp. 100(2) K

Atomic Coordinates

Co1	Co	0.5000	0.0000	0.0000
O1	O	0.60170(14)	0.08775(10)	0.1862(2)
C2	C	0.64355(18)	0.10289(14)	0.3759(4)
C3	C	0.7008(2)	0.17830(15)	0.4404(4)
O4	O	0.64022(13)	0.06302(9)	0.5180(3)
C4	C	0.6533(2)	0.24064(15)	0.3120(4)
H4	H	0.5867	0.2346	0.1837
C5	C	0.7979(2)	0.18898(15)	0.6300(4)
H5	H	0.8306	0.1477	0.7200
O6	O	0.5000	-0.05720(13)	0.2500
N7	N	0.5000	-0.13221(16)	0.2500
C8	C	0.4023(2)	-0.16891(15)	0.2079(4)
H8	H	0.3338	-0.1418	0.1765
C9	C	0.4009(2)	-0.24579(15)	0.2099(4)
H9	H	0.3316	-0.2712	0.1836
C10	C	0.5000	-0.2872(2)	0.2500
C11	C	0.5000	-0.3696(2)	0.2500
C12	C	0.4016(2)	-0.41010(15)	0.2196(4)
H12	H	0.3337	-0.3840	0.1992
C13	C	0.4013(2)	-0.48719(16)	0.2186(5)
H13	H	0.3335	-0.5137	0.1965
C14	C	0.5000	-0.5260(2)	0.2500
H14	H	0.5000	-0.5790	0.2500

$Co_3(C_8H_4O_4)_4[DMA^+]$

Cell length a 33.149(5) Å

Cell length b 9.8224(14) Å

Cell length c 17.769(2) Å

Cell angle α	90.00 °
Cell angle β	98.391(12) °
Cell angle γ	90.00 °
Cell volume	5723.7(15) $Å^3$
Symmetry cell setting	monoclinic
Symmetry space group	*C2/c*
Cell measurement temp.	-

Atomic Coordinates

Co1	Co	0.1499(0)	0.8182(0)	0.468
Co2	Co	0.2500	0.7500	0.5000
O101	O	0.1500(1)	0.6856(2)	0.5542(1)
O102	O	0.2123(0)	0.6130(2)	0.5393(1)
C102	C	0.1823(1)	0.6185(3)	0.5747(1)
C103	C	0.1846(1)	0.5378(3)	0.6467(1)
C104	C	0.1498(1)	0.5196(3)	0.6817(2)
H104	H	0.1244	0.5561	0.6590
C105	C	0.1525(1)	0.4491(3)	0.7489(2)
H105	H	0.1287	0.4358	0.7722
C106	C	0.1895(1)	0.3970(3)	0.7831(1)
C107	C	0.2238(1)	0.4146(3)	0.7483(1)
H107	H	0.2493	0.3783	0.7713
C108	C	0.2214(1)	0.4848(3)	0.6802(1)
H108	H	0.2451	0.4964	0.6566
O109	O	0.2275(1)	0.2907(2)	0.8889(1)
C109	C	0.1926(1)	0.3212(3)	0.8571(1)
O110	O	0.1592(1)	0.2942(2)	0.8798(1)
O201	O	0.2047(0)	0.9100(2)	0.5081(1)
C202	C	0.1987(1)	1.0156(3)	0.4647(2)
O202	O	0.1697(1)	1.0179(2)	0.4115(1)
C203	C	0.2259(1)	1.1366(3)	0.4826(1)

C204	C	0.2214(1)	1.2498(3)	0.4349(2)
H204	H	0.2017	1.2489	0.3904
C205	C	0.2544(1)	1.1366(3)	0.5478(2)
H205	H	0.2573	1.0593	0.5803
O301	O	0.1114(1)	0.9576(3)	0.5355(1)
O302	O	0.0880(1)	0.8388(3)	0.4344(1)
C302	C	0.0824(1)	0.9181(4)	0.4876(2)
C303	C	0.0395(1)	0.9602(4)	0.4944(2)
C304	C	0.0321(1)	1.0588(5)	0.5452(3)
H304	H	0.0543	1.0992	0.5773
C305	C	0.0069(1)	0.9000(5)	0.4495(2)
H305	H	0.0115	0.8298	0.4149

$Co_3(bdc)_3(2,2\text{-}dPNO)_2$

Cell length a	9.650(6) Å
Cell length b	17.270(12) Å
Cell length c	18.274(12) Å
Cell angle α	99.057(11) °
Cell angle β	90.485(9) °
Cell angle γ	106.122(10) °
Cell volume	2885(3) $Å^3$
Symmetry cell setting	triclinic
Symmetry space group	$P\bar{1}$
Cell measurement temp.	100(2) K

Atomic Coordinates

Co1	Co	0.5	0	0.5
Co2	Co	0	0	1
Co3	Co	-0.16403(10)	-0.21059(5)	0.95073(5)
Co4	Co	0.45115(10)	-0.21070(5)	0.45201(5)
O1C	O	0.0200(5)	-0.1793(3)	0.8947(2)
O2C	O	0.0704(5)	-0.0434(3)	0.8997(2)
C2C	C	0.0725(7)	-0.1134(4)	0.8697(4)
C3C	C	0.1437(7)	-0.1201(4)	0.7962(4)
C4C	C	0.1972(7)	-0.0494(4)	0.7647(4)
H4C	H	0.1903	0.0018	0.7899
C5C	C	0.2603(7)	-0.0541(4)	0.6964(4)
H5C	H	0.2965	-0.0061	0.6751
C6C	C	0.2704(7)	-0.1296(4)	0.6593(4)
C7C	C	0.2243(7)	-0.1984(4)	0.6921(3)
H7C	H	0.2374	-0.2488	0.6687
C8C	C	0.1587(7)	-0.1940(4)	0.7595(4)
H8C	H	0.1238	-0.2421	0.7808
O9C	O	0.3454(5)	-0.0707(3)	0.5531(2)
C9C	C	0.3356(7)	-0.1328(4)	0.5865(4)
O10C	O	0.3734(5)	-0.1945(3)	0.5578(3)
O1D	O	0.2981(5)	-0.1789(3)	0.3961(2)
O2D	O	0.3817(5)	-0.0424(3)	0.4002(3)
C2D	C	0.3094(7)	-0.1136(4)	0.3709(3)
C3D	C	0.2320(7)	-0.1204(4)	0.2968(4)
C4D	C	0.1528(8)	-0.1968(4)	0.2560(4)
H4D	H	0.1472	-0.2451	0.2759
C5D	C	0.0847(8)	-0.2028(4)	0.1895(4)
H5D	H	0.0288	-0.2545	0.1639
C6D	C	0.0974(7)	-0.1325(4)	0.1591(4)
C7D	C	0.1765(8)	-0.0551(4)	0.1975(3)
H7D	H	0.1848	-0.0073	0.1763
C8D	C	0.2420(8)	-0.0497(4)	0.2668(4)
H8D	H	0.2937	0.0022	0.2938
O9D	O	0.0833(5)	-0.0732(3)	0.0520(3)
C9D	C	0.0313(8)	-0.1356(4)	0.0829(4)
O10D	O	-0.0715(5)	-0.1978(3)	0.0558(3)
O1F	O	-0.2077(5)	-0.3385(3)	0.9364(3)
O2F	O	-0.3661(5)	-0.2795(3)	0.9924(3)
C2F	C	-0.3248(9)	-0.3421(5)	0.9723(4)
C3F	C	-0.4166(9)	-0.4248(4)	0.9886(4)
C4F	C	-0.3663(9)	-0.4942(5)	0.9677(5)
H4F	H	-0.2769	-0.4896	0.9449
C5F	C	-0.5481(9)	-0.4296(5)	1.0185(5)
H5F	H	-0.5808	-0.3822	1.0298
O1A	O	0.6011(5)	-0.0975(3)	0.4705(2)
N2A	N	0.7361(6)	-0.1035(3)	0.4769(3)

C3A	C	0.8120(8)	-0.0734(5)	0.5429(4)
H3A	H	0.7703	-0.0468	0.5825
C4A	C	0.9491(8)	-0.0812(5)	0.5531(5)
H4A	H	1.0017	-0.0605	0.5996
C5A	C	1.0082(9)	-0.1194(5)	0.4946(5)
H5A	H	1.1032	-0.1244	0.5001
C6A	C	0.9305(8)	-0.1498(5)	0.4293(5)
H6A	H	0.9718	-0.1766	0.3895
C7A	C	0.7925(8)	-0.1430(4)	0.4188(4)
C8A	C	0.7054(8)	-0.1779(4)	0.3472(4)
C9A	C	0.7737(9)	-0.1711(5)	0.2798(4)
H9A	H	0.8724	-0.1409	0.2802
C10A	C	0.6992(10)	-0.2073(5)	0.2143(4)
H10A	H	0.7449	-0.2036	0.1686
C11A	C	0.5540(9)	-0.2502(5)	0.2158(4)
H11A	H	0.4992	-0.2763	0.1708
C12A	C	0.4894(9)	-0.2547(4)	0.2834(4)
H12A	H	0.3909	-0.285	0.284
N13A	N	0.5640(6)	-0.2167(3)	0.3488(3)
O1B	O	-0.1983(5)	-0.0971(3)	0.9740(3)
N2B	N	-0.3390(7)	-0.1015(4)	0.9804(4)
C3B	C	-0.3812(10)	-0.0750(7)	1.0497(5)
H3B	H	-0.3125	-0.0511	1.0903
C4B	C	-0.5278(11)	-0.0846(8)	1.0581(6)
H4B	H	-0.5601	-0.0671	1.1052
C5B	C	-0.6260(11)	-0.1188(8)	0.9994(6)
H5B	H	-0.726	-0.1254	1.0056
C6B	C	-0.5782(9)	-0.1438(8)	0.9310(5)
H6B	H	-0.6466	-0.1661	0.89
C7B	C	-0.4347(8)	-0.1374(5)	0.9203(4)
C8B	C	-0.3831(8)	-0.1691(4)	0.8486(4)
C9B	C	-0.4443(8)	-0.1577(5)	0.7827(4)
H9B	H	-0.5134	-0.1276	0.7843
C10B	C	-0.4034(8)	-0.1905(5)	0.7159(4)
H10B	H	-0.4452	-0.1852	0.6704
C11B	C	-0.2993(9)	-0.2315(5)	0.7170(4)
H11B	H	-0.2668	-0.2534	0.6716
C12B	C	-0.2433(8)	-0.2408(4)	0.7820(4)
H12B	H	-0.1747	-0.2711	0.7806
N13B	N	-0.2804(6)	-0.2089(3)	0.8492(3)
O1E	O	0.3645(5)	-0.3386(3)	0.4413(3)
O2E	O	0.5839(5)	-0.2792(3)	0.4949(3)
C2E	C	0.4792(8)	-0.3419(4)	0.4734(4)
C3E	C	0.4912(8)	-0.4236(4)	0.4870(4)
C4E	C	0.3886(9)	-0.4969(4)	0.4489(4)
H4E	H	0.3159	-0.4937	0.4151

C5E	C	0.6020(9)	-0.4271(5)	0.5375(4)
H5E	H	0.6691	-0.3782	0.5617

$Co_2(bdc)_2(2,2\text{-dPNdO})$

Cell length a	11.3517(12) Å
Cell length b	11.3956(10) Å
Cell length c	13.2806(12) Å
Cell angle α	90.00 °
Cell angle β	110.274(11) °
Cell angle γ	90.00 °
Cell volume	1611.5(3) $Å^3$
Symmetry cell setting	monoclinic
Symmetry space group	$P2_1/c$
Cell measurement temp.	296.15 K

Atomic Coordinates

Co1	Co	0	0.11810(7)	0.75
O1	O	-0.0475(3)	-0.0219(3)	0.8319(2)
Co2	Co	0	0	1
N2	N	-0.1202(4)	-0.1075(4)	0.7777(3)
C3	C	-0.2437(5)	-0.1058(5)	0.7619(4)
H3	H	-0.2772	-0.0452	0.7905
C4	C	-0.3199(5)	-0.1925(5)	0.7042(4)
H4	H	-0.4053	-0.1912	0.6933
C5	C	-0.2706(6)	-0.2813(5)	0.6621(4)
H5	H	-0.3223	-0.3409	0.6229
C6	C	-0.1454(6)	-0.2825(5)	0.6779(4)
H6	H	-0.1119	-0.3425	0.6486
C7	C	-0.0683(4)	-0.1948(4)	0.7370(4)
O8	O	0.1844(3)	-0.0019(3)	1.0119(2)

C9	C	0.2333(4)	0.0458(4)	0.9499(3)
O9	O	0.1811(3)	0.1047(3)	0.8680(2)
C10	C	0.3731(4)	0.0240(4)	0.9787(3)
C11	C	0.4353(4)	-0.0570(5)	1.0549(3)
H11	H	0.3918	-0.0966	1.0923
C12	C	0.4396(4)	0.0812(4)	0.9228(3)
H12	H	0.3993	0.1358	0.8701
O13	O	0.0629(3)	0.2393(3)	0.6701(2)
C14	C	0.0231(4)	0.2569(4)	0.5714(4)
O14	O	-0.0085(3)	0.1814(2)	0.4980(2)
C15	C	0.0111(4)	0.3839(4)	0.5349(3)
C16	C	0.0849(5)	0.4694(4)	0.5974(4)
H16	H	0.1426	0.4502	0.6645
C17	C	-0.0747(5)	0.4151(4)	0.4380(4)
H17	H	-0.1271	0.3581	0.395

Table A.10: Crystallographic Information Files are given on the CD provided

CD File name	Abbreviated Chemical Formula	
ASM1a	Co(bdc)(PNO)	Room Temperature
ASM1b	Co(bdc)(PNO)	Low temperature
ASM2	Co(bdc)(PNO/F)	
ASM3	$Co_{0.35}Mn_{0.65}$(bdc)(PNO)	
ASM4a	$Co_{0.84}Mn_{0.16}$(bdc)(PNO)	Room Temperature
ASM4b	$Co_{0.84}Mn_{0.16}$(bdc)(PNO)	Low temperature
ASM5	Co(bdc)(PNO-Br)	
ASM6	Co(bdc)(PNO-OMe)	
ASM7	Co(bdc)(Iso-NO)	
ASM8	Co(bdc)(PNO-Phenyl)	
ASM9	$Co_3(bdc)_4[DMA^+]$	
ASM10	$Co_3(bdc)_3(2,2\text{-}dPNO)_2$	
ASM11a	$Co_2(bdc)_2$(2,2-dPNdO)	Room Temperature
ASM11b	$Co_2(bdc)_2$(2,2-dPNdO)	Low Temperature

Table A.11: Predicted and experimental percentage mass changes for the TGA data of the novel cobalt MOFs presented in Chapter 5

Product Number	Predicted Empirical Formulae	Predicted Percentage Mass (%)	Experimental Percentage Mass (%)
5	$Co_3(bdc)_4 \cdot [DMA^+]_2[DMF]_{1.5}[H_2O]_2$	99.9	100
	$Co_3(bdc)_4 \cdot [DMA^+]_2[DMF]_{1.5}$	96.5	96.6
	$Co_3(bdc)_4 \cdot [DMA^+]_2$	86.3	87.2
	$Co_3(bdc)_4$	77.7	75.1
6	$Co_3(bdc)_3(DMF)_2 \cdot [DMF]_2[H_2O]_2$	99.5	100
	$Co_3(bdc)_3(DMF)_2 \cdot [DMF]_2$	94.2	94.6
	$Co_3(bdc)_3(DMF)_2$	79.9	82.8
7	$Co_3(bdc)_3(2,2\text{-dPNO})_2 \cdot [DMF][H_2O]_3$	100.0	100
	$Co_3(bdc)_3(2,2\text{-dPNO})_2 \cdot [DMF]$	95.2	95.3
	$Co_3(bdc)_3(2,2\text{-dPNO})_2$	88.8	90.6
7 (washed)	$Co_3(bdc)_3(2,2\text{-dPNO})_2 \cdot [EtOH]$	100.2	100
	$Co_3(bdc)_3(2,2\text{-dPNO})_2$	95.8	94.8
8	$Co_2(bdc)_2(2,2\text{-dPNdO}) \cdot [H_2bdc][MeOH]_2$	94.6	100
	$Co_2(bdc)_2(2,2\text{-dPNdO}) \cdot [H_2bdc]$	87.6	92.2
	$Co_2(bdc)_2(2,2\text{-dPNdO})$	69.5	72.7
8 (washed)	$Co_2(bdc)_2(2,2\text{-dPNdO}) \cdot [MeOH]_2$	100.4	100
	$Co_2(bdc)_2(2,2\text{-dPNdO})$	91.2	88.4